Approved for public release; distribution is unlimited.

Dynamics of Transport and Variability in the Denmark Strait Overflow

by James B. Girton

Technical Report
APL-UW TR 0103
August 2001



Applied Physics Laboratory University of Washington
1013 NE 40th Street Seattle, Washington 98105-6698

NSF Grants OCE9712313 and OCE0099275

Dynamics of Transport and Variability in the Denmark Strait Overflow

James Bannister Girton

A dissertation submitted in partial fulfillment
of the requirements for the degree of

Doctor of Philosophy

University of Washington

2001

Program Authorized to Offer Degree: Oceanography

©Copyright 2001
James Bannister Girton

In presenting this dissertation in partial fulfillment of the requirements for the Doctoral degree at the University of Washington, I agree that the Library shall make its copies freely available for inspection. I further agree that extensive copying of this dissertation is allowable only for scholarly purposes, consistent with "fair use" as prescribed in the U.S. Copyright Law. Requests for copying or reproduction of this dissertation may be referred to Bell and Howell Information and Learning, 300 North Zeeb Road, Ann Arbor, MI 48106-1346, to whom the author has granted "the right to reproduce and sell (a) copies of the manuscript in microform and/or (b) printed copies of the manuscript made from microform."

Signature James B. Gibson

Date 7 May 2001

University of Washington
Graduate School

This is to certify that I have examined this copy of a doctoral dissertation by

James Bannister Girton

and have found that it is complete and satisfactory in all respects,
and that any and all revisions required by the final
examining committee have been made.

Chair of Supervisory Committee:

Thomas B. Sanford

Reading Committee:

Rolf H. Käse

John L. Bullister

Date: 7 May 2001

University of Washington

Abstract

Dynamics of Transport and Variability in the Denmark Strait Overflow

by James Bannister Girton

Chair of Supervisory Committee:

Professor Thomas B. Sanford
School of Oceanography

The overflow of dense water from the Nordic Seas through the Denmark Strait is one of the primary sources of the deep water in the world's oceans. In 1998, a rapid high-resolution survey on the F/S *Poseidon* with expendable profilers (XCP/XCTD) collected velocity, temperature and salinity data from the region of the Denmark Strait sill to study the initial descent of the overflow into the deep North Atlantic. The major results from this and an earlier, more modest, survey in 1997 on the R/V *Aranda*, along with additional analysis of satellite and current meter data, can be summarized as follows:

- The flow near the sill is characterized by a strongly barotropic structure associated with a nearly-vertical temperature front. As the denser water descends the Greenland slope, it develops the bottom-intensified structure characteristic of a gravity current.

- Initial transport of $\sigma_\theta > 27.8$ water at the sill is measured by the synoptic sections to be 2.7 ± 0.6 Sv, essentially identical both in mean and variability to that measured in 1973 by a 5-week current meter array deployment.

- Despite large spatial and temporal variability in velocity, thickness and transport, the overflow's pathway and descent with distance from the sill are remark-

ably steady.

- Measurements of near-bottom shear stress (from logarithmic velocity fits) confirm the importance of bottom friction in controlling the rate of overflow descent.

- Satellite sea-surface temperature images confirm the birth and downstream propagation of cyclonic eddies starting at approximately 125 km southwest of the sill. This same point is also marked by a change in the rate of overflow entrainment and a maximum in overflow speed.

- The presence of subsurface eddies upstream of the appearance of the surface features suggests a geographical separation between the region of flow instability and the site of eddy generation and vortex stretching. These two distinct processes occur in the approach to the sill and over the steepest descent, respectively.

TABLE OF CONTENTS

List of Figures v

List of Tables ix

Chapter 1: Introduction 1

1.1 High-Latitude Overflows 1

1.2 Past Observations of the DSO 3

1.2.1 Overflow 3

1.2.2 Sources 4

1.2.3 Products 4

1.2.4 Eddies 6

1.3 Modeling and Theory 7

1.3.1 Streamtubes 7

1.3.2 Hydraulic Theory and Experiment 7

1.3.3 Instability Calculations 8

1.3.4 Process Models 8

1.3.5 GCMs 9

1.4 Present Work 9

1.5 Velocity Profiling 10

Chapter 2: Instruments and Methods 12

2.1 Bathymetry 12

2.1.1 Echo Sounder Correction by CTD and Thermosalinigraph 13

2.1.2 Comparison with Smith and Sandwell and ETOPO-5 bathymetry 16

2.2 Expendable Probes and Their Calibration 16

2.2.1 Depth Correction 20

2.2.2 XCTD 21

2.2.3 XCTD Temperature-Conductivity (T/C) Lag 22
2.2.4 XCP/CTD 23
2.3 LADCP 24
2.3.1 Compass Calibration 25
2.4 Velocity Profiling with Electromagnetic Induction 26
2.5 Absolute Velocity 30
2.5.1 GPS Navigation 30
2.5.2 Rotating and Referencing the ADCP 33
2.5.3 Construction of referenced XCP profile 42
2.5.4 Techniques Used 48
2.5.5 Operations and Error Computations 49
2.5.6 Final Error Estimate 55
2.5.7 Remaining inconsistencies 56
2.6 Combining XCP and ADCP for data visualization 62
2.7 Estimating Bottom Stress 65

Chapter 3: *Aranda* Experiment **68**
3.1 Cruise 68
3.2 Measurements 70
3.3 Summary of Data 71
3.4 Interpretation 76
3.5 Hydrographic Survey 79
3.5.1 Northern Basin 79
3.5.2 Irminger Basin 80
3.5.3 Sill Repeats 80
3.6 Other observations 81

Chapter 4: *Poseidon* Experiment **83**
4.1 Cruise 83
4.2 Survey 85
4.3 Summary of Data 85

4.3.1 Part I 88
4.3.2 Part II 90
4.3.3 Part III 92
4.4 Interpretation 94

Chapter 5: Transport and Variability **97**
5.1 Near-sill Transport 97
5.2 Historical Variability 101
5.3 Subsampling 103
5.4 Model Comparison 104
5.5 Hydraulic Control 106
5.6 Tides 108
5.6.1 OVERFLOW '73 108
5.6.2 FES94 108
5.7 Atmospheric Pressure 109
5.8 Conclusions 110

Chapter 6: Overflow Path, Momentum Budget and Energetics **111**
6.1 Streamtube Theory 111
6.2 Observed Quantities 113
6.3 Pathway and Descent 117
6.3.1 Drag Coefficient 118
6.3.2 Slippery Boundary Layers 119
6.3.3 Other mechanisms for cross-isobath transport 121
6.4 Mixing and Momentum 121
6.4.1 Density Changes 122
6.4.2 Energy Changes 125
6.4.3 Entrainment Stress 126
6.5 Energy Flux 128
6.5.1 Inertial Wave Drag 134
6.6 Conclusions 134

Chapter 7: Eddies 137
7.1 Surface Eddies in Satellite IR . . . 137
7.1.1 Form and Evolution . . . 137
7.1.2 Eddy Birth . . . 140
7.1.3 Sill and Upstream Features . . . 141
7.2 Surface Eddies in In-situ Survey . . . 142
7.2.1 Appearance in Thermosalinigraph . . . 142
7.2.2 Appearance in ADCP . . . 143
7.3 Deep Eddy Signature . . . 145
7.4 Eddy Positions and Speeds . . . 145
7.5 A Composite Eddy . . . 148
7.5.1 Upper-Layer Composite . . . 149
7.5.2 Deep-Layer Composite . . . 152
7.6 Conclusions . . . 153

Chapter 8: Conclusions 154
8.1 Velocity Structure . . . 154
8.2 Transport . . . 155
8.3 Energetics . . . 156
8.4 Eddies . . . 156

Glossary 159

Bibliography 162

Appendix A: Magnetotelluric Contamination 171
A.1 Electromagnetic Frequency Window . . . 171
A.2 Sources—aurora! . . . 172
A.3 XCP Offsets and magnetogram rate of change . . . 174
A.4 1-D transfer function estimates of apparent shear . . . 176

Appendix B: Atlas of Sections 178

LIST OF FIGURES

2.1 Calibration of the SST proxy 14
2.2 Distributions of differences between various depth measurements 15
2.3 Comparison between corrected ES and SS97 gridded bathymetry 17
2.4 Comparison between corrected ES and ETOPO-5 gridded bathymetry . 18
2.5 Comparison between ETOPO-5 and SS97 gridded bathymetries 19
2.6 Linear stretching applied to XCP profiles 21
2.7 XCTD 11 temperature *vs.* conductivity coherence 22
2.8 Comparisons between XCP and CTD temperatures in surface and bottom mixed layers 24
2.9 LADCP compass calibration 26
2.10 XCP probe and surface float/transmitter 27
2.11 Using ADCP and GPS to reference an XCP velocity profile 31
2.12 Example of GPS comparison showing residual E-W and N-S positions . 33
2.13 φ_{A-G} as a function of time and heading 36
2.14 ADU, ADCP and gyrocompass mounting angles 37
2.15 A comparison of two determinations of φ_{A-G} 38
2.16 Three estimates of φ_{mount} 40
2.17 Illustration of velocity determination method about 10 min after XCP 4135 51
2.18 XCP/ADCP velocity comparison 53
2.19 Profile of ADCP minus XCP 4135 velocity 55
2.20 Scatter in water velocities over the 7 minutes surrounding each XCP . . 56
2.21 XCP/ADCP combination for data visualization 63
2.22 Reference layer and final velocity 64
2.23 Logarithmic velocity fit 66

3.1 Locations of XCP sections from the *Aranda* cruise in August 1997 69
3.2 Difference between 3DF and gyrocompass headings 69
3.3 Temperature, salinity and velocity sections from the *Aranda* 72
3.4 Temperature profiles from the *Aranda* CTD 73
3.5 T-S plot of Aranda CTD data 74
3.6 Velocity at 40 m above the bottom and friction velocity 75
3.7 ADCP velocity averaged over the layer 50–150 m below the surface . . . 78
3.8 Potential density section in the northern basin 80

4.1 Environmental variables recorded during *Poseidon* 244 84
4.2 Locations of XCP drops 86
4.3 TSG sea-surface temperature 87
4.4 Part I near-surface temperature and velocity 88
4.5 Part I near-bottom temperature and velocity 89
4.6 Part II near-surface temperature and velocity 91
4.7 Part II near-bottom temperature and velocity 91
4.8 Part III near-surface temperature and velocity 92
4.9 Part III near-bottom temperature and velocity 93
4.10 Effective downstream ship speed 95

5.1 Locations of 1998 XCP/XCTD drops 98
5.2 Seven snapshots of XCP/ADCP velocity 99
5.3 O73 transport and current meter timeseries 102
5.4 $\theta < 2°C$ transport distributions 103
5.5 Cumulative probability distribution functions 104
5.6 M2 tide amplitude 109

6.1 Streamtube illustration 112
6.2 Balance of forces on a 1-D overflow 113
6.3 Illustration of streamtube quantities in a measured section 114
6.4 Decomposition of density into mean, background and anomaly contributions 115

6.5 Descent of the overflow with distance from the sill 118
6.6 Positions of overflow center of mass (X) and half-width ($W_{0.5}$) 119
6.7 C_D from linear fit of u_*^2 *vs.* u_{50}^2 120
6.8 Evolution of plume density ($\overline{\sigma_\theta}$) and density anomaly ($\overline{\rho'}$) 122
6.9 Dense water transport (Q) *vs.* distance from the sill 124
6.10 Variability of plume velocity (V) and cross-sectional area (A) 125
6.11 Evolution of energy terms with distance from the sill 127
6.12 Through-section energy flux *vs.* downstream distance 132
6.13 Total energy flux ($\int\int_A (\mathbf{F^{tot}} \cdot \hat{\mathbf{j}}) dz dx$) 133
6.14 Topographic slopes at each section 135

7.1 Satellite image (Sep 13, 1998) 138
7.2 Satellite image (Sep 14, 1998) 139
7.3 Satellite image (Sep 15, 1998) 139
7.4 Eddy birth 140
7.5 Sill eddies 141
7.6 Thermosalinigraph (TSG) and ADCP during Part III 143
7.7 Examples of subjective eddy fits to ADCP 144
7.8 Eddy positions 146
7.9 Downstream motion of eddies 147
7.10 Estimated eddy speeds 148
7.11 Composite eddy picture 149
7.12 Decomposition of eddy velocities into radial and azimuthal components 151
7.13 Properties of the deep layer in the composite eddy 152

8.1 Cartoon illustrating the separate processes at work in generating the surface eddies observed in the DSO satellite imagery. 158

A.1 EM skin depth 171
A.2 Ultraviolet emissions from the *aurora borealis* 173
A.3 XCP 4210 and XCP 4196 profiles 174
A.4 Electric current at each XCP drop location 175

A.5 Correlation between XCPs and nearby magnetograms 177

LIST OF TABLES

2.1 Statistics of different methods of estimating depth 14
2.2 XCP–CTD temperature differences in surface and bottom mixed layers . 25
2.3 Equivalent notation used in bottom track calibration methods 41
2.4 Estimated measurement errors 45
2.5 Diagnostic statistics to evaluate all XCPs 57
2.6 Average statistics for XCP absolute velocity 61

4.1 Station numbers and times used to divide *Poseidon* 244 cruise up into 3 parts 88

5.1 Transport in 7 near-sill sections 100

ACKNOWLEDGMENTS

I am deeply grateful my advisor, Tom Sanford, for all of his advice and wisdom over the years. I can only hope to someday follow his example as an observational physical oceanographer. Much of the work in this dissertation could not have been done without the assistance of committee member Rolf Käse, who has always been a source of fascinating ideas and good humor.

The core of my work came out of substantial ship time on two cruises that were part of programs to study the high-latitude North Atlantic: VEINS (EU) and SFB-460 (Germany). The opportunities to join these cruises were provided by Bob Dickson and Rolf Käse, respectively.

Essential data were provided by Bert Rudels (from the *Aranda* hydrographic observations), Charlie Ross (from the OVERFLOW '73 current meters) and Rolf Käse (from both the *Poseidon* hydrography and his numerical model results).

My first few years of graduate school were funded by an ONR graduate fellowship, without which I would not have had the freedom to consider embarking on such an adventurous program of field observations. Additional grants and fellowships from NSF and APL have kept me going.

And finally, my wife Sabine Mecking has shown truly remarkable patience and restraint during the trials of the past few months of completing this dissertation. Without her it would have been much harder and much less pleasant.

DEDICATION

This dissertation is dedicated to my parents, John E. and Sheila J. Girton who may have wondered when but never really doubted that it would be finished.

Chapter 1

INTRODUCTION

Through the Denmark Strait flows one of the most remarkable currents of the world's oceans. Roughly 3 million cubic meters per second of dense water formed in the Nordic and Arctic Seas spills over the ridge between Greenland and Iceland and cascades more than 2000 m downwards into the North Atlantic, supplying a deep boundary current system that extends through the Labrador Sea, down the eastern coast of North America, across the equator and into the South Atlantic. Recognizable characteristics of the resulting North Atlantic Deep Water (NADW) are seen throughout the Pacific and Indian oceans, making up the lower limb of the "great ocean conveyor belt" [*Broecker*, 1991]. The Denmark Strait is one of the most geographically-confined locations along this entire path, and so is a region of great interest to researchers interested in understanding the forcing and modifications of the overturning circulation by its individual components, as well as to those interested in monitoring the strength of the circulation on long timescales. In addition, physical processes such as entrainment and bottom drag occur in many similar density currents and overflows, so that knowledge obtained in one can often be applied to others. In this dissertation I will first outline the justifications for and results of previous work and then describe the results of a new set of measurements designed to illuminate some of the details of processes at work in the Denmark Strait Overflow (DSO).

1.1 High-Latitude Overflows

Deep water is only formed in a few locations throughout the world's oceans. Many of these are in confined marginal seas separated from the major ocean basins by narrow straits and shallow sills. Dense water formed through thermohaline processes at the sea surface (primarily evaporation at low latitudes and sensible and latent

cooling at high latitudes, although brine rejection during ice formation also plays a role) accumulates in the sea and then flows through the constriction as a bottom-trapped density current. In the North Atlantic, the exchange of warm northward-flowing surface waters with these cold deep outflows from the Nordic Seas carries an important fraction of the poleward heat transport in the ocean-atmosphere system. In addition, the dense overflows through the Denmark Strait and across the Iceland–Scotland ridge carry the signature of surface heat and chemical content into the deep oceans, forming a mechanism for the ocean's participation in global processes with durations corresponding to the overturning timescale of the entire system—up to 2000 years.

In fact, a leading theory to explain the rapid climate oscillations observed in ice and sediment-core records of the last ice-age (the so-called Dansgaard/Oeschger cycles between 12,000 and 80,000 years ago [*Dansgaard et al.*, 1993]) involves the repeated shutoff and resumption of deep water formation and oceanic heat transport, possibly triggered by freshwater input to the high-latitude seas. While the paleoceanographic picture is a sparse one, not easily able to map bottom currents or water properties with sufficient resolution to pinpoint the overflows, some records have suggested deep oceanic changes synchronized with surface variability [e.g., *Bond et al.*, 1993]. A number of coupled ocean-atmosphere models have also highlighted the importance of deepwater formation processes in the ocean's response to and effect on climate [*Manabe and Stouffer*, 1988; *Schiller et al.*, 1997; *Fanning and Weaver*, 1997].

The ultimate properties of the deep water being formed are determined not only by the direct processes of air-sea interaction that create the initial overflowing water, but also by the mixing with and entrainment of surrounding fluid during the density current's descent. For this reason, the location and mechanism of entrainment is of vital importance to the ability to simulate deep water changes in ocean models. This combination of localized small-scale physics and global importance presents a particularly difficult situation for the large-scale numerical models used to study the ocean and global climate. Even with continual improvements in computational power, the resolution needed to simulate overflow processes will not be available on a global scale in the foreseeable future, and so a realistic approach to subgrid-scale parameterization (based on observations) is needed.

1.2 Past Observations of the DSO

1.2.1 Overflow

While the importance of deep overflows from the Nordic Seas was suspected by Scandinavian oceanographers including Knudsen, Nielsen, Nansen and Helland-Hansen during the first decade of the 20th century (and the role of the polar regions in general even earlier by Count Rumford in 1800), the importance of the Nordic overflows' contributions to NADW was discounted or ignored by most investigators until revived by *Cooper* [1955] and subsequently taken up by others [*Dietrich*, 1961; *Lee and Ellett*, 1965]. The first detailed study focusing on the Denmark Strait was made in 1967 by the C.S.S. *Hudson* [*Mann*, 1969] as part of an attempt to quantify the DSO with moored current meters [*Worthington*, 1969]. While a failure of the majority of the moorings in the unexpectedly-strong currents made the transport measurements unsuccessful, the survey did reveal a number of important features of the overflow, including the way that the dense water is banked against the Greenland side of the strait due to the effects of the earth's rotation and the presence of highly-variable currents of up to $1.4\,\mathrm{m\,s^{-1}}$.

The ICES "OVERFLOW '73" expedition [described in *Ross*, 1984; *Smith*, 1976, and hereafter referred to as O73] was far more successful and has remained the most comprehensive set of mooring and hydrographic section data from the Denmark Strait region until very recently. The 37-day long mooring deployment in O73 showed that the DSO is highly variable on timescales of 2–5 days but steady over longer periods, with a mean transport of 2.9 Sv of water colder than 2°C. Tides play only a small role in the variability, accounting for 2–10% of the variance in the current meter velocities. These data form a large part of the historical context for the new measurements presented in this dissertation. The year-long MONA array about 100 km downstream from the O73 location corroborated these conclusions and revealed a lack of variability on seasonal timescales [*Aagaard and Malmberg*, 1978].

Since 1993 the Nordic WOCE and EC-VEINS programs have undertaken a number of cruises to the Denmark Strait sill and nearby regions. Two of these cruises on the Finnish R/V *Aranda* are described by *Fristedt et al.* [1999] and *Rudels et al.* [1999a]. In recent years the German government has also undertaken a number of

cruises with the F/S *Poseidon* and other vessels to the region, some of which have been briefly described by *Krauss and Käse* [1998]. I was fortunate enough to have the opportunity to participate in the deployment of velocity profiling instruments from two of the above-mentioned cruises on the *Aranda* and *Poseidon*, the data from which are described in Chapters 3 and 4 and form the basis for most of this dissertation.

1.2.2 Sources

While the most dramatic air-sea interaction and deep convection in the Nordic Seas occurs in the center of the ice-free Greenland Sea gyre, the majority of the very dense Greenland Sea Water (GSW) so produced lies too deep to get over the ridge separating the Nordic Seas from the North Atlantic proper. For this reason the primary source waters for the DSO are the various intermediate waters of the Nordic Seas, and their locations of formation have been the subject of some debate. *Swift et al.* [1980] found winter mixed layers in the Iceland Sea (to the north of Iceland) with properties similar to the desired Arctic Intermediate Water (AIW) in the DSO and so concluded that this must be an important source region. A substantial revision of this view was presented by *Mauritzen* [1996a] based on the analysis of a set of hydrographic sections tracking the evolution of incoming Atlantic Water as it is modified in the Norwegian Current, branches into three separate pathways involving the Barents Sea, Arctic Ocean and southern Fram Strait, and then is reassembled in the East Greenland Current (EGC) with the properties necessary to supply the overflows both through the Denmark Strait and to the southeast of Iceland. According to this picture, supplemented by *Rudels et al.* [1999b], the primary regions of transformation are the Norwegian Current and the Arctic Ocean boundary current. An additional possibility, presented by *Strass et al.* [1993] and substantiated by *Swift* [1999], includes significant ventilation from the Greenland Sea gyre through isopycnal mixing intensified by baroclinic instability in the EGC.

1.2.3 Products

The fate of the DSO and other Nordic Seas outflows has been studied extensively using hydrographic measurements throughout the North Atlantic during the 1950s through 1970s as summarized by *Swift* [1984]. Later measurements [*Smethie and*

Swift, 1989; *Livingston et al.*, 1985] added a more comprehensive set of tracers to the mix, but definitive estimates of transport and the evolution of the overflows from violent sill flow to (more-or-less) steady boundary current were not available until the deployment of a set of moorings by the UK Lowestoft laboratories at 3 sites along the southeast coast of Greenland [*Dickson and Brown*, 1994]. These moorings showed the increase in transport of the DSO from 3 to 5 Sv through entrainment during its initial descent as well as subsequent increases to 10 Sv due to the joining of the Iceland–Scotland overflows and eventually to 13 Sv at the southern tip of Greenland after gradual additional mixing.

A somewhat different picture of the overflows' effects is given by the consideration of the spreading rates of atmospheric tracers [*Doney and Jenkins*, 1994] and tracer inventories [*Smethie and Fine*, 2001]. While the direct pathways of boundary currents are clearly important, the spreading of tracers seems to give almost equal weight to lateral processes such as isopycnal stirring and mixing by eddies. The integrating effects of tracers is clearly useful in preventing aliasing by high-frequency variability, but does make conclusions about time-dependent effects difficult.

Another major contribution of the Lowestoft arrays was to reveal a lack of seasonal or interannual variability in the transport of the overflow waters. This led to an apparent contradiction, given the substantial changes in Greenland Sea convective activity throughout the year and from year to year. The contradiction has been partially explained by the more gradual transformation process described by *Mauritzen* [1996b] but the question does remain as to what timescale of forcing the overflow will respond to. Recent efforts have focused on the possibility of connections between the Overflow and convective processes in the Nordic Seas, possibly related to decadal forcing by the North Atlantic Oscillation [*McCartney et al.*, 1998; *Bacon*, 1998; *Dickson et al.*, 1999]. Clearly, if the dramatic changes in deepwater formation suggested by the paleo records were to occur, the dense overflows should be one of the first places that the effects would be apparent.

1.2.4 Eddies

The nature of the short-term variability in the initial descent of the DSO is a puzzle that has received attention since some of the earliest speculations about the Nordic outflows [*Cooper*, 1955]. Mooring deployments near the sill [*Stein*, 1974; *Ross*, 1978] have given detailed information about the temporal characteristics of velocity and temperature at a few fixed locations (and are consistent with the results of a simple model of baroclinic instability [*Smith*, 1976]) but are unable to reveal the spatial structure of the observed variability. The wider coverage of the Lowestoft moorings did shed some additional light on the nature of the variability. While the mean kinetic energy (KE) measured by the current meters at the Angmagssalik array was trapped to the bottom in the form of the dense overflow, the fluctuating (eddy) KE increased upwards towards the shallowest meters (500–800 m above the bottom). Unfortunately these moorings did not reach into the upper water column so the extent of the upward eddy KE increase was not known.

A definitive answer has been elusive due to the complexity of the region and difficulty of obtaining comprehensive measurements, but a substantial advancement came with the study by *Bruce* [1995], revisiting the O73 measurements in the light of satellite infrared images. Hydrographic measurements simultaneous with the O73 current meters showed that pulses in transport were often associated with discrete intermediate-depth salinity minima. In addition the satellite measurements of surface temperature showed a persistent train of cyclonic eddies with similar spatial and temporal scale to transport pulses and salinity minima. Knowledge of the characteristics of these surface eddies has been augmented by surface drifter studies [*Krauss*, 1996] which allowed the tracking of individual eddies for long distances—something not possible with satellite measurements, given the infrequency of clear-weather days in the Denmark Strait. The conclusion that the eddies are a surface manifestation of the variability in the deep plume is supported by laboratory experiments showing the generation of strongly barotropic vortices by the impulsive entrance of dense bottom-water flow onto a slope [*Whitehead et al.*, 1990; *Griffiths*, 1983].

1.3 Modeling and Theory

1.3.1 Streamtubes

The mean characteristics of the DSO have been investigated through several modeling approaches. *Smith* [1975] described many of the plume-averaged features of the overflow using a simple reduced-gravity, streamtube model. This basic one-dimensional approach, which will be discussed further in Chapter 6, has proven highly-successful in simulating a number of observed oceanic density currents. *Price and Baringer* [1994] extended the streamtube description through improved friction and entrainment schemes and applied it to a number of both high- and low-latitude outflows. Of all of these, the DSO is possibly the most problematic because of its highly-variable nature and full-water-column flow.

1.3.2 Hydraulic Theory and Experiment

Although large-scale budgets require the inclusion of flows on the opposite side of Iceland, the local dynamics in the Denmark Strait can be approximated as a two-layer exchange (with a substantial amount of interfacial tilt due to rotation). The thin deep layer of dense Norwegian Sea Water flows out rapidly while the upper layer flows in slowly. The rate of outflow can be modeled as a hydraulically controlled system, but the transports so derived are generally too large [*Whitehead*, 1989, 1998]. To some extent, this may be because the hydraulic value is a theoretical "maximal" limit *Killworth and MacDonald* [1993], although it is unclear to exactly what extent the idealized theory applies to the Denmark Strait (or, perhaps more properly, the entire Nordic Seas basin). The discrepancy may also be because of frictional effects or the deficiencies of the simplified hydraulic theory in dealing with unsteady flow. As an additional effect of the hydraulics, rotating laboratory experiments by *Borenäs and Whitehead* [1998] indicated a persistent separation of upstream flow from the right-hand wall of a channel with a sill, and *Whitehead and Salzig* [1999] have further studied the combined effects of contraction and shoaling on flow approaching a sill.

1.3.3 Instability Calculations

Theoretical studies [*Smith*, 1976; *Swaters*, 1991; *Mooney and Swaters*, 1996] have emphasized the possibility for baroclinic instability of the dense overflow to generate variability (either waves or coherent vortices) at temporal and spatial scales consistent with the variability observed in current meters and satellite images. For example, an analytical two-layer, quasi-geostrophic model for baroclinic instability in the strait itself produces unstable motions at wavenumbers and frequencies similar to those observed [*Smith*, 1976]. However, the idealized nature of such models makes the process difficult to pick out of real data, and it is particularly questionable, given the strong overflow speeds, whether these instability mechanisms would have time to act during the sudden descent of the plume. Calculations of the instability growth rates generally suggests that they would not. Motivated by the existence of strong barotropic flow at the sill, *Fristedt et al.* [1999] have postulated a barotropic instability mechanism, suggesting that the variability might even originate upstream of the sill.

1.3.4 Process Models

More thorough numerical modeling efforts [*Jungclaus and Backhaus*, 1994; *Jiang and Garwood*, 1996; *Spall and Price*, 1998; *Krauss and Käse*, 1998] have explored the effects of topography, background stratification and intermediate-layer outflows, each arriving at different explanations for the variability and different interpretations of the essential dynamics. This is no-doubt partly due to differences in forcing, boundary conditions, topography and model complexities used, as well as to the number of different processes simultaneously active in the DSO. Most recently, *Käse and Oschlies* [2000] have configured a primitive-equation sigma-coordinate model with realistic topography of the Denmark Strait region to simulate both the approach to the constriction and the subsequent overflow. This model has been successful in reproducing many of the features contained in observational studies and laboratory modeling, and will be described further in Chapter 5.

1.3.5 GCMs

The ocean modeling community has focused on the DSO as represented in several general circulation models of the North Atlantic, but transport estimates from these have not been in good agreement [*DYNAMO Group*, 1997; *Willebrand et al.*, 1999]. This is not too surprising, considering the low horizontal and vertical resolution of these models in the Strait region, as well as their inadequate parameterizations of bottom friction [Marotzke and Willebrand, 1996]. In fact, a current top priority of the ocean modeling community is to find an effective way to parameterize unresolved overflow processes in coarse resolution models [*Beckmann and Döscher*, 1997; *Winton et al.*, 1998; *Killworth and Edwards*, 1999; *Song and Chao*, 2000; *Yang and Price*, 2000].

1.4 Present Work

Due to the combined effects of variability on short temporal and spatial scales, we chose to undertake a rapid, high-resolution survey of the Denmark Strait region using ship-lowered (CTD) and expendable (XCP, XCTD) profiling instruments to measure velocity, temperature and salinity. The expendable instrumentation allowed for faster sampling and a greater opportunity to conduct measurements in a region where rough weather often limits ship operations.

A summary of the chapters in this dissertation is as follows:

Chapter 2 describes some of the various techniques used in acquiring and processing the data from these two cruises, including the method for deriving absolute velocity by combining the velocity profiles from the XCP and ADCP along with GPS navigation information.

Chapters 3 and 4 describe the surveys undertaken on the *Aranda* and *Poseidon*, respectively, and give an initial examination of the data collected on each.

Chapter 5 uses the 7 sections closest to the Denmark Strait sill to both quantify the transport of dense water and to evaluate the comparability between the data from the surveys and previous measurements of the DSO.

Chapter 6 examines the mean characteristics of the overflow using all of the cross-sections from the two surveys seen in the light of a streamtube-type approach. In addition, I have attempted to explain some deviations from streamtube behavior by looking at the energy flux through each section.

Chapter 7 investigates the connection between eddies seen in satellite infrared imagery and those sampled in the in-situ surveys.

Chapter 8 sets forth concluding remarks.

1.5 Velocity Profiling

The direct measurement of instantaneous profiles of oceanic velocity is a remarkably underutilized and underexploited activity. This is curious, since a major stated goal of physical oceanography is the determination of flow magnitudes and pathways. The primary reasons for this underutilization have included the historical difficulties and disappointments in obtaining direct velocity measurements combined with difficulties in the interpretation of instantaneous profiles. Early attempts to measure velocity profiles from ship-lowered current meters suffered from large errors due to the ship tethering. Later, free-falling, acoustically-tracked dropsondes succeeded in measuring velocity but required large investments in ship time to set up the tracking arrays. With the advent of electromagnetic profiling techniques, an autonomous method of measuring velocity profiles became viable, but has still received only limited acceptance from the oceanographic community, due in part to the lack of commercially-available user-friendly products and the high degree of specialized technical knowledge required to design the instruments themselves. The most widely-used technique for direct velocity profiling, the LADCP, is vulnerable to its own set of difficulties, including the accumulation of random errors induced by package motion, the inability to measure close to the bottom and the lack of absolute velocity in rapidly-changing environments.

The biggest obstacle to the pursuit of a more effective and more accessible velocity profiling method has been the wide range of processes, operating on many different timescales, that can produce velocity signals, and the difficulties in interpretation

that arise from trying to distinguish among them in instantaneous measurements. Barotropic motions driven by wind and tides, propagating inertial motions, internal gravity waves and topographic Rossby waves all add their signature on top of the often-weak mean current that is the measurement target of many observational programs. To counteract these problems, fixed-point timeseries from moorings and Lagrangian trajectories from floats have become the methods of choice for flow measurement, while instantaneous profiles continue to be regarded with some puzzlement.

There are certain situations, however, which cry out for instantaneous profile measurements. These include the study of processes which exhibit a large degree of identifiable structure in the vertical, as well as those in which the velocity signal is so large that it dwarfs all other contributions. The study of internal wave generation and propagation has made wide use of the former variety, while surveys of energetic boundary currents and eddies often fall into both categories. In fact, other than to the degree that currents and eddies include solely geostrophic velocities, the *only* way to learn about the vertical structure of such entities is through velocity profiling.

While successful profiling studies have been made of oceanographic subjects as varied as internal wave dynamics, the equatorial undercurrent, the Florida Current, the Mediterranean outflow and eddies and now the Denmark Strait Overflow, velocity profiles continue to be low on the list of the oceanographic community's priorities, particularly in the growing descriptions of operational oceanographic programs like GOOS, ARGO and various coastal systems. The small number of currently active velocity profiling groups simply reinforces this trend. Perhaps the greatest utility of the instantaneous velocity profile is in its exploratory character, as an aid to developing the phenomenology of oceanic processes. However, it seems to be a mistake to ignore it in favor of satellite monitoring, fixed-depth measurements and profiling floats that measure only T and S. Velocity measurements, complicated though they may be, are a direct indicator of many physical processes active in the ocean and are certain to be a vital component in the diagnosis of future changes in the dynamics of those processes.

Chapter 2

INSTRUMENTS AND METHODS

In the rapidly-changing environment of the Denmark Strait, conventional deep-water hydrographic measurements and geostrophic calculations are inadequate to characterize the flow and variability. In addition, many of the instruments and techniques designed for high-resolution work in the dynamic coastal zone can operate only to limited depths or at reduced ship speeds. For the purposes of this study, then, it was necessary to evolve a new approach allowing rapid surveying of oceanographic properties from a ship underway to, at times, 2000 m depth. By combining expendable profilers with underway ADCP measurements and improved navigation (including GPS heading) we have been able to construct full water column profiles of absolute velocity with accuracy comparable to or better than other available techniques.

In support of the expendable probe measurements it has also been necessary to develop methods for correcting echo sounder data, calibrating probe fall rates and comparing simultaneous profiles. This chapter primarily describes the application of these methods to the data collected from the F/S *Poseidon* in September 1998 (described more fully in Chapter 4) although some of the techniques have also been applied to the *Aranda* dataset from 1997 (Chapter 3). A list of abbreviations and a brief description of some of the instruments can be found in the Glossary.

2.1 Bathymetry

Because of the bottom-trapped nature of the Denmark Strait Overflow current, and the importance of bottom shape in defining the path and dynamics of the Overflow, it is important that we know as much about the bathymetry as possible. This includes both the along-track bathymetry as measured by the ship's echo sounder and the regional bathymetry available in gridded datasets. In addition, it is useful to know how well the gridded datasets compare with the echo-sounder depths. Along-track

bathymetry is also particularly useful for determining the maximum depth attained by expendable probes, since these have no independent depth measurement.

2.1.1 Echo Sounder Correction by CTD and Thermosalinigraph

The *Poseidon's* echo sounder (ES) was in operation throughout the cruise and was recorded through the PC log system. It recorded "uncorrected" depth values, using an assumed soundspeed of $1500\,m\,s^{-1}$. The actual soundspeed was almost always less than this, however, leading to depth errors of 20 m or more in the uncorrected data. Although accurate soundspeed profiles can be constructed from the CTD data, when available, a method was needed for correcting the bathymetry over the entire cruise. Since the biggest variation in the soundspeed profile is caused by the large temperature variation across the nearly-vertical Polar Front, it seems useful to adopt the continuously-recorded measurement of sea-surface temperature (SST) from the *Poseidon*'s thermosalinigraph (TSG) as a proxy for the depth-averaged soundspeed. Of course, this method fails at times when either a thin layer of cold fresh water crosses to the warm side of the front or a thin warm layer extends over the cold side, as does sometimes happen over eddies or in the interleaving region at the sill. At such times, depths could be in error by as much as 2%. The locations at which CTD profiles are available serve to calibrate this estimate and also provide a measure of its reliability. Table 2.1 shows the mean difference and scatter between various depth-correction methods and the best estimate from integrating the CTD specific volume *vs.* pressure.

The SST proxy (calibrated using the quadratic curve in Figure 2.1) performs very well, leading to a one-standard-deviation error estimate of just over ±5 m. Figure 2.2 shows histograms of the error distribution for the various correction estimates, including the best corrected (using CTD profiles), uncorrected and proxy-corrected methods. The proxy correction clearly removes the bi-modal nature of the uncorrected estimates, and ends up looking very similar to the best correction. In a few periods of time, the ship's echo sounder failed to record usable data, and these periods had to be filled in by linear interpolation (when short enough) or by interpolation using the gridded bathymetry plus an offset and trend (when the interval was too long). This last method is clearly inferior to real data, but preferable to missing

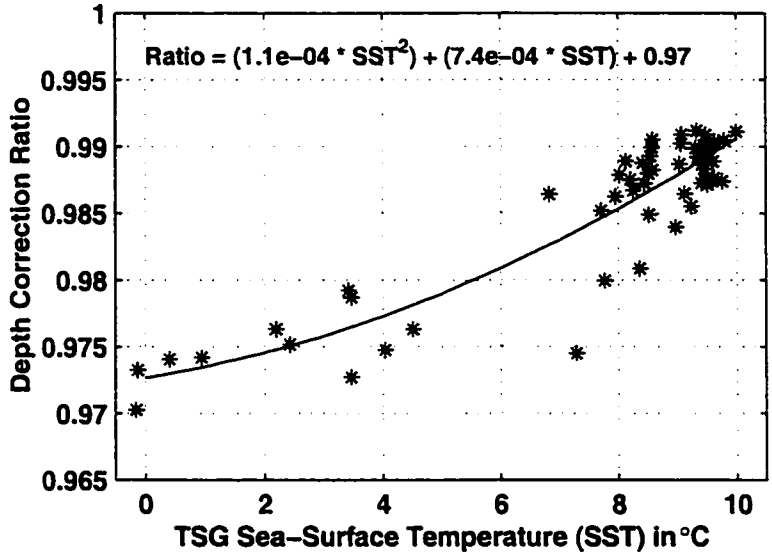


Figure 2.1: Calibration of the SST proxy: The graph shows the relationship between the "depth correction ratio," (corrected depth)/(uncorrected depth) computed by averaging the inverse soundspeed at each CTD profile, and simultaneous sea-surface temperatures (SST) measured by the *Poseidon*'s thermosalinigraph (TSG). Also plotted is a quadratic best fit of the data. The same procedure performed with XCTD profiles gives a very similar relationship (not shown here), albeit with more scatter.

Table 2.1: Statistics of different methods of estimating depth using the *Poseidon*'s echo sounder (ES) compared to the best estimate, derived from the maximum CTD pressure converted into depth using the integrated specific volume profile (and assuming a CTD stopping altitude of 12 m above the bottom, estimated from the 15 m warning line and a brief (~3 s) delay in stopping the winch). 57 CTD stations were used for comparison.

Depth Measurement	Mean Difference (m)	St. Dev. (m)
Uncorrected ES	15.70	7.89
ES corrected by a single average depth ratio	0.90	6.30
ES corrected by each CTD soundspeed profile	3.21	4.52
ES corrected by SST proxy	3.07	5.13
Smith and Sandwell bathymetry	16.85	54.15

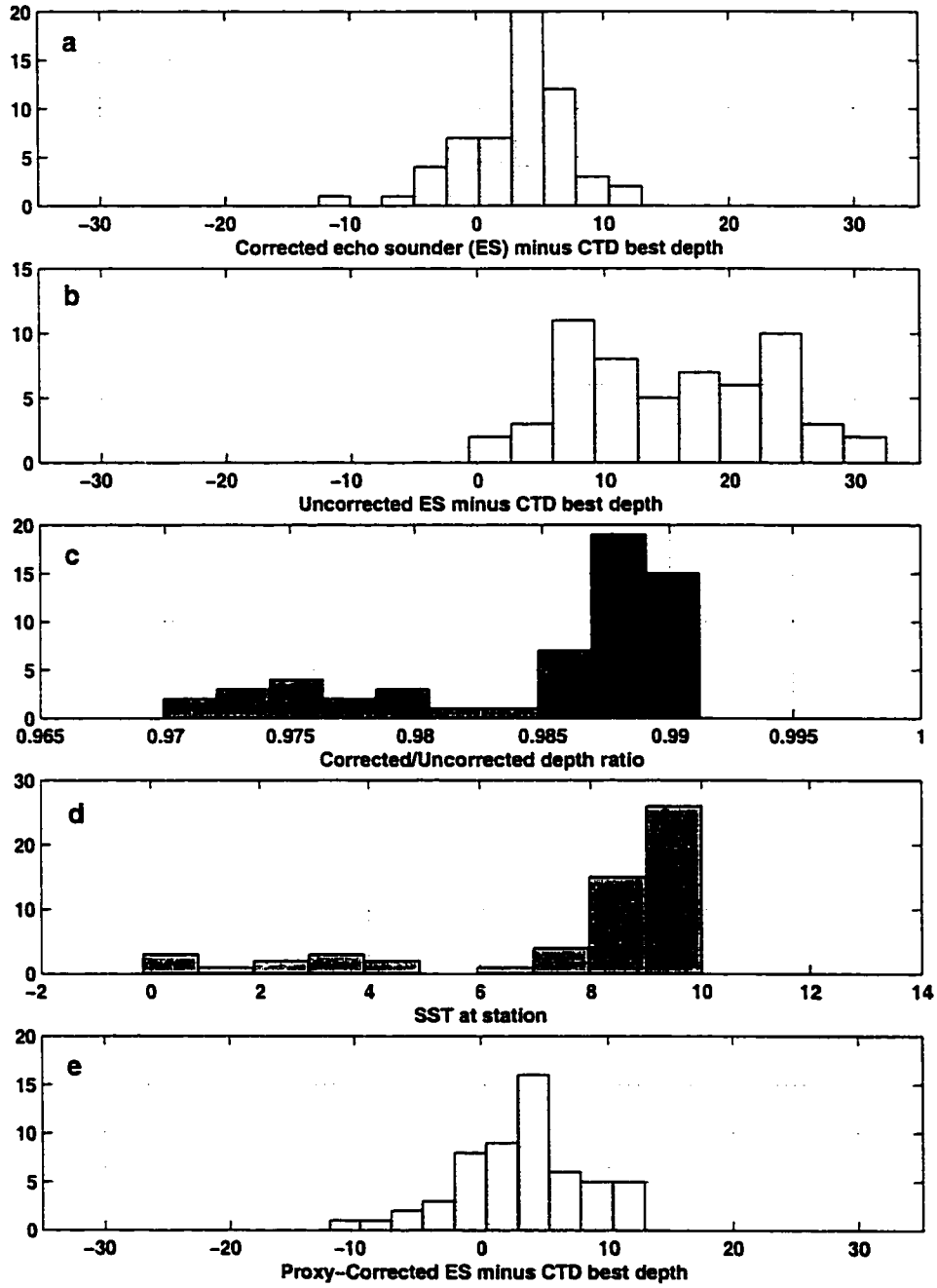


Figure 2.2: Distributions of differences between various depth measurements. The tightest distribution is obtained in panel a) (also the third line of Table 2.1) from the two methods using individual CTD profiles—direct computation of depth from integrated specific volume and ES correction from the CTD soundspeed profile. The middle three panels show the bimodal distributions of b) the uncorrected ES (corresponding to the first line in Table 2.1), c) the CTD-determined correction ratio (see Figure 2.1) and d) SST. This distribution results from the presence in the Denmark Strait region of two main watermasses generally separated by a front identifiable in surface temperature. Panel e) shows the improvements over b) made by using the SST proxy to correct the depth (also reflected in the fourth line of Table 2.1).

intervals. Taking the error in the CTD-integration estimate of depth to be small, the value of ±5 m can serve as an error estimate for all of the bathymetry measurements.

2.1.2 Comparison with Smith and Sandwell and ETOPO-5 bathymetry

Given the likely importance of topography on the dynamics of the overflow, it would be useful to have some sort of independent measure of the accuracy of the gridded products used to generate bathymetric maps and constrain numerical models of the region. Two such popular products are the high-resolution (2' longitude Mercator grid) data from *Smith and Sandwell* [1997] (hereinafter SS97) and the coarser (5' latitude, 5' longitude) ETOPO-5. A comparison between these two data products, interpolated to the cruise track, and the corrected echo sounder bathymetry measured by the *Poseidon* reveals some interesting differences. The best comparison is between the *Poseidon's* echo sounder and the SS97 database, shown in Figure 2.3, although even this exhibits a substantial scatter of 51 m and mean difference of 11.7 m. ETOPO-5 essentially compares equally poorly with each of the other two records: the mean difference from the echo sounder is 13.3 m, standard deviation 99 m (Figure 2.4)); the mean difference from the higher-resolution SS97 is 25.0 m, with a standard deviation of 106 m (Figure 2.5). It is encouraging that the newer, higher-resolution SS97, incorporating additional ship measurements as well as satellite data, agrees more closely with the *Poseidon's* measurements than the older ETOPO-5. If we can assume that the echo sounder measurements are nearly correct (to the 5 m accuracy claimed above), then this comparison clearly argues in favor of using the SS97 database for studies of the Denmark Strait region, albeit with substantial caution given the large inconsistencies that still remain.

2.2 Expendable Probes and Their Calibration

The use of expendable probes, while often worthwhile for its convenience and the added flexibility in survey planning and platform choice, tends to entail a substantial reduction in measurement accuracy. Reasons for this include necessarily cheaper components, noise introduced by the thin wire and the lack of pressure sensors to determine depth. In attempt to estimate the resulting accuracy of our probes, we have

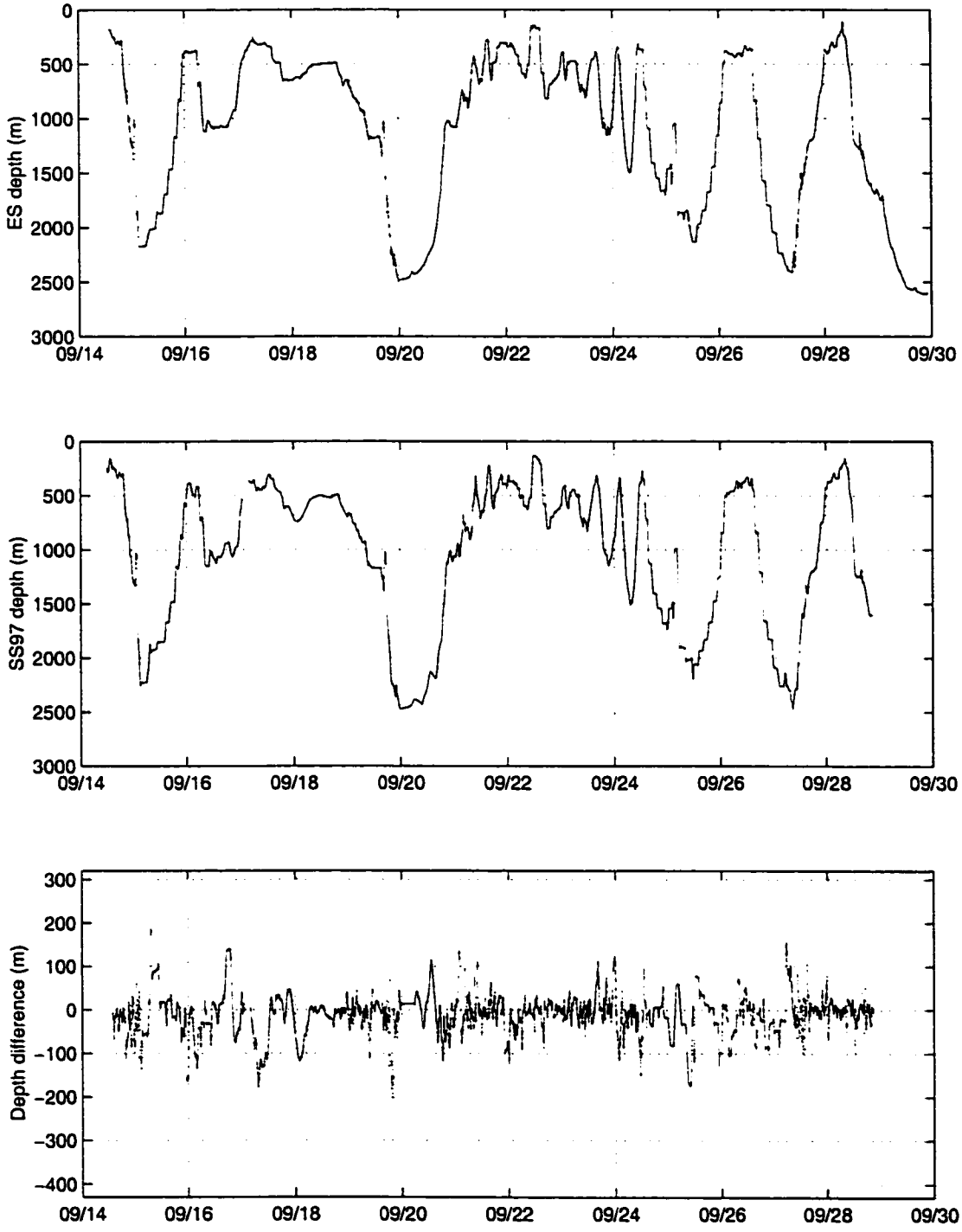


Figure 2.3: Comparison between corrected echo sounder (ES) measurements and gridded bathymetry from *Smith and Sandwell* [1997] (SS97) interpolated to the cruise track. The bottom panel shows the difference between the two, with positive values indicating shallower depths in SS97.

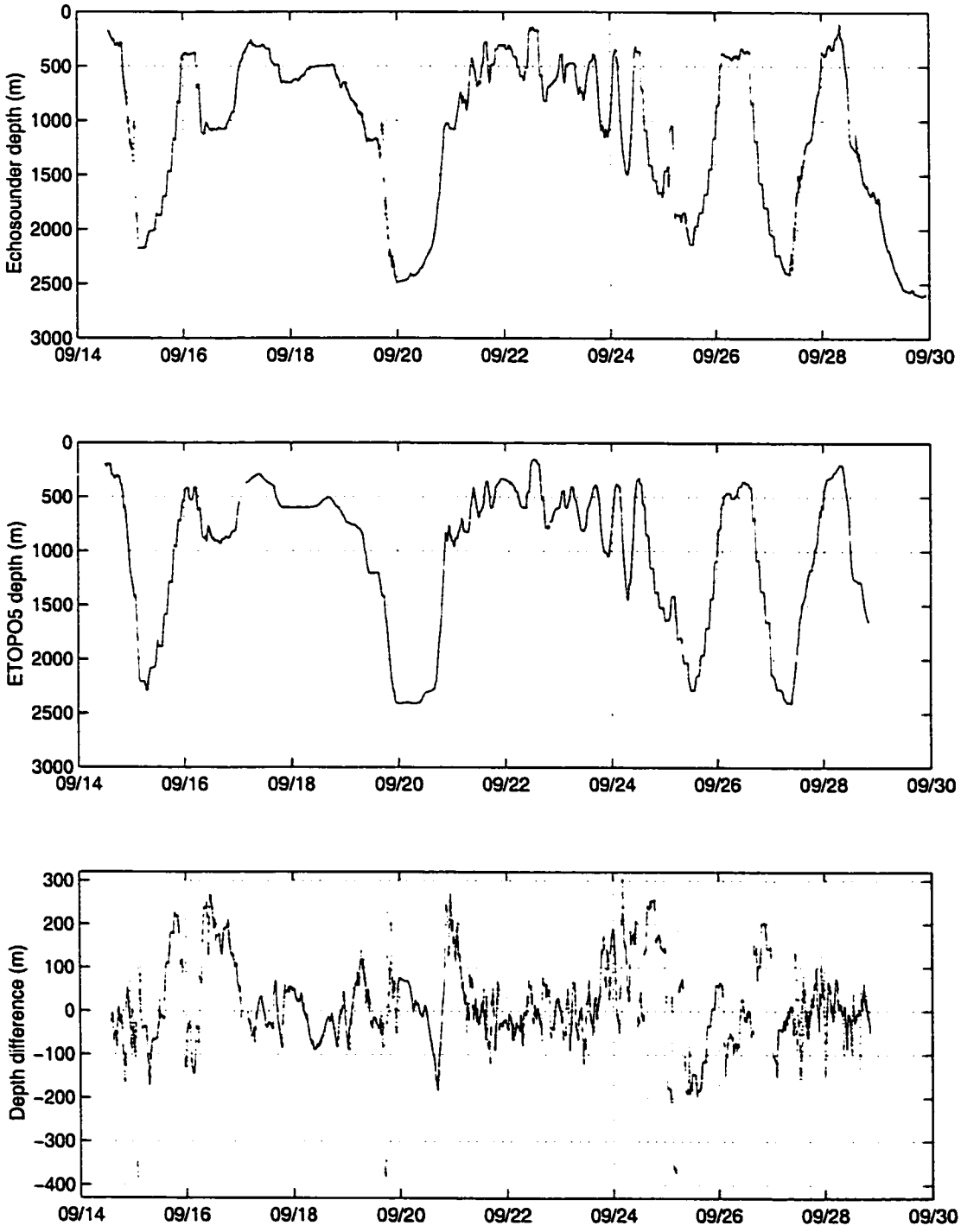


Figure 2.4: Comparison between corrected ES measurements and gridded bathymetry from ETOPO-5 interpolated to the cruise track. The bottom panel shows the difference between the two, with positive values indicating shallower depths in ETOPO-5.

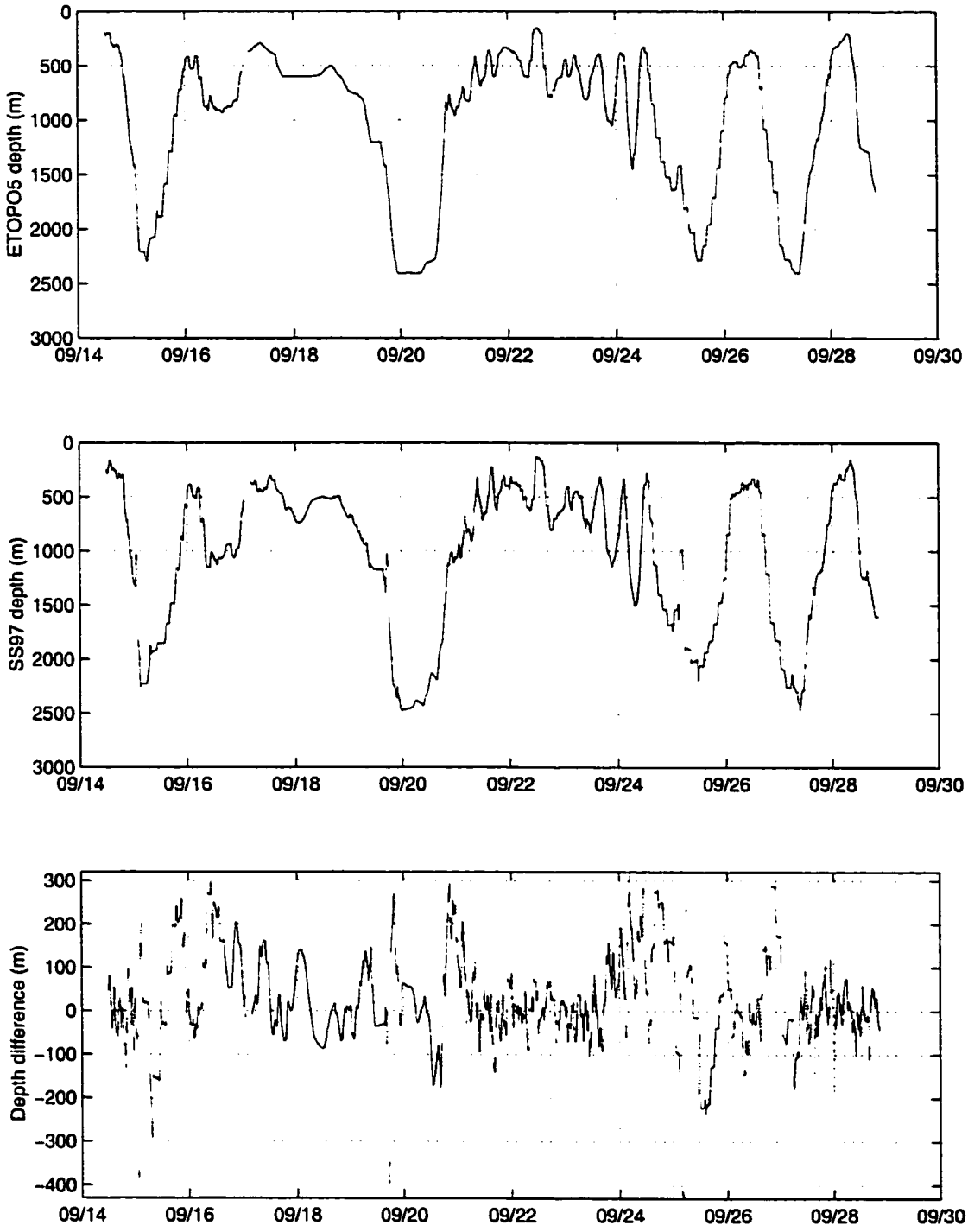


Figure 2.5: Comparison between ETOPO-5 and SS97 along the cruise track. The bottom panel shows the difference between the two, with positive values indicating shallower depths in ETOPO-5.

made comparisons between as many redundant measurements as possible. Over the course of *Poseidon* 244, simultaneous drops include 31 CTD/XCP pairs, 7 CTD/XCTD pairs, and 76 XCP/XCTD pairs. In addition, near-surface water velocity is measured by both the XCP and ADCP, and water depth can be estimated from the ship's echo sounder as well as from the free-fall time of each probe. Issues relating to the XCP and water velocity are, in some ways, the most critical and are discussed extensively throughout this chapter. In the following section I focus on other expendable measurements, including calibrations for fall rates, temperature and salinity.

2.2.1 Depth Correction

An accurate bathymetry record, combined with an accurate record of the expendable probe start and stop times, allows us to estimate fall rate corrections for each of the XCP and XCTD probes. The depths are initially estimated using an empirically-determined equation of the form:

$$-z = z_0 + z_1 t + z_2 t^2, \tag{2.1}$$

where z is the vertical coordinate (negative depth). Several versions of the coefficients z_0, z_1, and z_2 have been obtained from different studies, including some by the probes' manufacturer, Sippican. The values used in the initial processing of the *Poseidon* data were the revised ones published by *Prater* [1991]: $z_0 = 4.68$, $z_1 = 4.377$, and $z_2 = -0.00044$ for time in seconds and depth in meters. Since probe performance appears to differ from experiment to experiment due to variations over time in manufacturing procedure, design modifications or simply oceanographic environment, I have decided to apply a stretching procedure to every probe when possible, or to apply an experiment-wide batch average to those which cannot be individually calibrated. For probes which struck the bottom (almost all in our surveys) a linear stretching is applied so that the depth of bottom contact (determined for the XCTDs by a conductivity spike and for the XCPs by a sudden decrease in rotation rate) matches the echo-sounder depth.

The stretching terms applied to each of the XCP probes is shown in Figure 2.6. For those probes which did not span the entire water column (i.e., the top or the bottom of the profile is missing or the water was too deep) the remaining portion of the profile

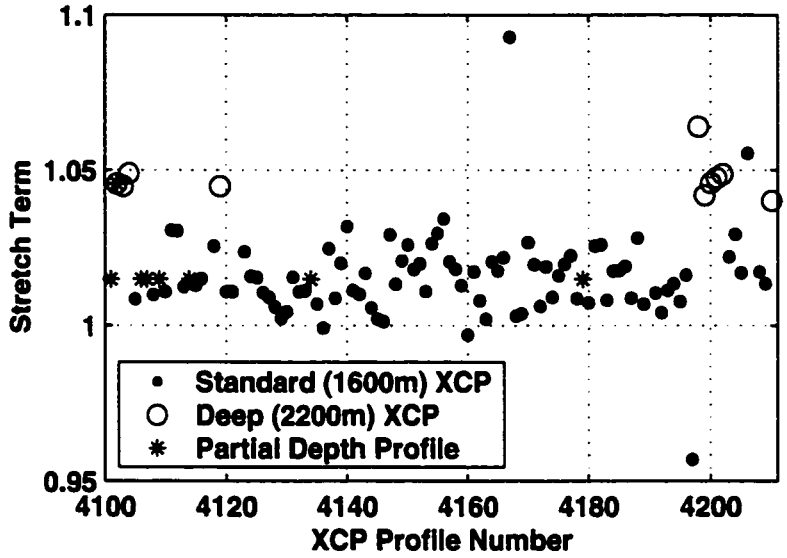


Figure 2.6: Linear stretching applied to the computed XCP profile depths, determined from comparison of XCP bottom hit with concurrently-measured corrected depth from the ES. Deep XCPs should require a systematically larger stretching term since they carry more wire and, hence, fall faster. Partial depth profiles are missing the top or bottom part of the profile, and so are stretched by an average value determined from other probes of the same type. The scatter is most likely due to inter-probe differences, but variability in the ES correction (see Section 2.1.1) plays some role.

is stretched by an average value for the type of probe. Average stretching values were 1.0149 ± 0.0085 (one standard deviation) for regular XCPs and 1.0456 ± 0.0033 for deep probes.

Similar stretching has been applied to the XCTD profiles, for which the original depth coefficients are not known (due to the direct output depth rather than time from the MK-12 processing software). Stretching values used for regular and deep XCTDs were 1.01 and 1.04, respectively.

2.2.2 XCTD

According to the manufacturer's specifications, the XCTD is accurate to 0.035°C and $0.035\,\mathrm{mS\,cm^{-1}}$, translating to approximately 0.06 PSU salinity accuracy.

Alberola et al. [1996] report comparisons of XCTDs with CTD casts with uncertainties of 0.02°C and 0.004 S/m, agreeing with Sippican's specifications. On the *Poseidon* cruise, several XCTDs were dropped immediately after lowered CTD profiles, but nat-

ural variability even on this short timescale made these difficult to compare directly (due to clear changes in the shape of the profile or depth of the thermocline). The 3 most directly comparable of these profiles revealed consistent biases of -0.029°C and +0.0012 S/m in the XCTDs, but a scatter of only 0.016°C and 0.0001 S/m. Visual inspection of these comparisons indicates that the XCTD is usually accurate to 0.02 PSU and 0.02°C (corresponding to a density uncertainty of 0.02 $kg\,m^{-3}$) after correction for temperature *vs.* conductivity sensor time lags and removal of the systematic temperature and conductivity biases.

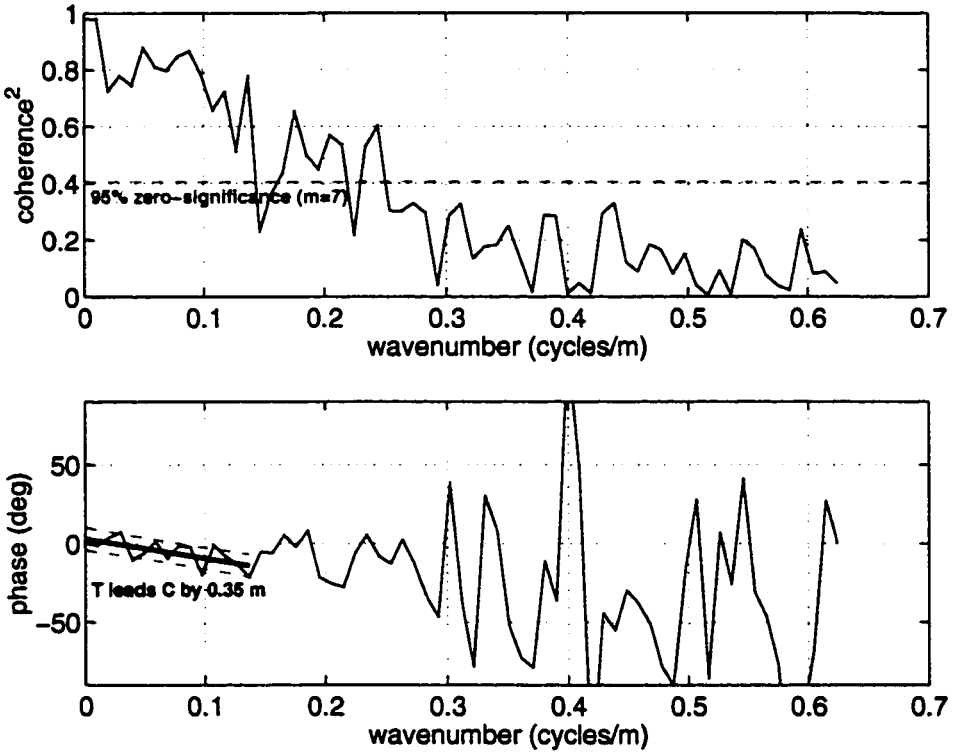


Figure 2.7: XCTD 11 temperature *vs.* conductivity coherence (squared) and phase, along with linear fit to significantly coherent wavenumbers below 0.15 cycles per meter.

2.2.3 XCTD Temperature-Conductivity (T/C) Lag

The XCTD salinity data are vulnerable to errors caused by delays in the conductivity *vs.* temperature measurements which appear to vary from probe to probe. To correct

for this, I have used the slope in phase *vs.* vertical wavenumber (frequency) of the conductivity-temperature coherence to estimate the delay for each probe. Figure 2.7 shows an example of this estimation. The mean delay determined from 75 XCTDs corresponds to T leading C by 0.33 m (or approximately 0.1 s at a fall rate of $3\,m\,s^{-1}$), with a standard deviation of 0.16 m. Although the sampling interval for the XCTD is around 0.8 m, the T/C delay is clearly identifiable from the phase slope. In addition, shifting T by the delay thus determined and then interpolating back to the same grid as C does appear to improve the character of the calculated salinity and density values. The degree of improvement is difficult to gauge, however, since the few XCTD/CTD comparisons available contain oceanic variability that is substantially larger than the changes produced by incorporating the T/C shift.

Alternatively, since the effects of T/C delays are most apparent in salinity and density (through salinity spikes and spurious density overturns) another approach to determining the delay is to find the shift which, when applied to T, minimizes density overturns (or, more specifically, the RMS difference between the sorted and unsorted density profiles). This produces similar results to the phase slope method: T leads C by a mean of 0.25 m with a standard deviation of 0.16 m over the 75 profiles. However, while the mean delay determined by each of these methods is similar, the probe-to-probe variations are not well correlated between the two methods. In fact the correlation coefficient (r) between the two is only 0.33, barely above the 95% zero-significance level of 0.23 for 75 points. This low correlation could be an indication that probe-to-probe variations in T/C delay are due mostly to random peculiarities in the noise of each profile and not to actual systematic differences between each probe. On the other hand, the low correlation could simply be due to the differences between the two methods of determination, while the fact that the correlation is positive and significant (if only barely) argues that applying individual delays to each profile is meaningful.

2.2.4 XCP/CTD

Figure 2.8 shows the range of temperature differences obtained from comparing XCP and CTD data. In order to remove differences due to vertical gradients, only data from homogeneous mixed layers near the surface or bottom were compared. Com-

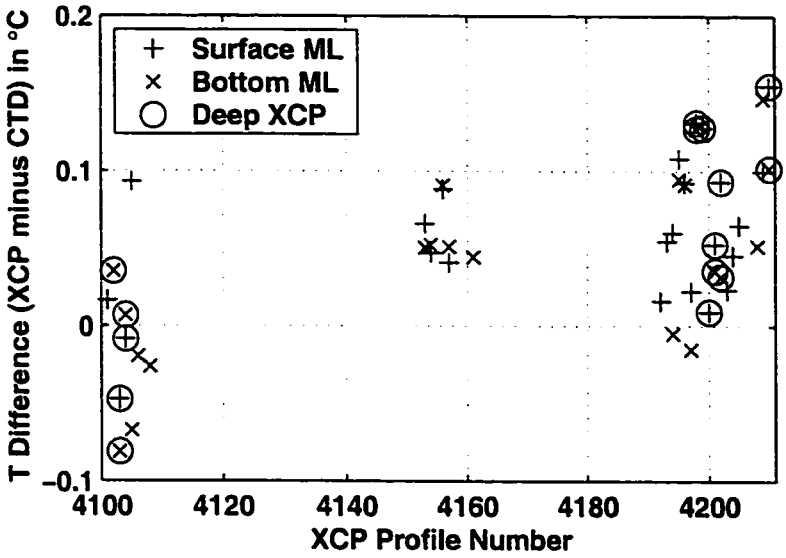


Figure 2.8: Comparisons between XCP and CTD temperatures in surface and bottom mixed layers. Only stations for which both XCP and CTD profiles were available are shown. Since the manufacturer claims XCP temperature accuracy of 0.2°C, the performance demonstrated here is better than expected.

parisons from surface and bottom layers, separately, are shown in Table 2.2. The scatter in these values can probably be largely explained by the substantial separation in space and/or time between these supposedly "simultaneous" drops. The most puzzling characteristic of these numbers is the apparent grouping, especially among the first 5 or 6 comparisons, in which the XCP measured consistently lower temperatures than the CTD. Comparison with electronic thermometers on the CTD rosette indicates that the CTD drifted less than 0.005°C over the duration of the cruise—not enough to cause this grouping.

2.3 LADCP

A broadband lowered ADCP (LADCP) provided by the University of Hawaii was included in the instrument package on the *Poseidon* and recorded data on all but 2 of the CTD stations. Although these measurements have not yet been incorporated into the dataset described here, they will eventually provide additional velocity estimates on those stations without simultaneous XCP drops. Initial comparisons indicate that

Table 2.2: XCP/CTD temperature differences in surface and bottom mixed layers.

	Mean Difference (°C)	St. Dev. (°C)
Surface ML	0.061	0.048
Bottom ML	0.038	0.060
All Estimates	0.050	0.054

the LADCP underestimated the strong shears often present in the overflow layer and therefore may be better suited to less energetic regions. In addition, larger package tilts may have caused a substantial amount of lost data on some of the profiles.

2.3.1 Compass Calibration

The LADCP compass was tested on Monday, November 2, 1998 (after the cruise) at NOAA-PMEL in a magnetically quiet environment on a rigid rotating platform. Overall, the instrument appears to have performed very well during the test. The output precision of the LADCP's compass is only 1 degree, but within that resolution the data are quite reasonable. There was no detectable effect from moving the battery relative to the LADCP. However, after completing the calibration, when the APL pickup truck was moved close and the tailgate put down maybe 2 feet from the LADCP, the heading changed by about 4 degrees! Figure 2.9 shows the heading-dependent error curve determined during the testing with sine fit peak-to-peak amplitude of 4.3 degrees and residual root-mean-squared deviation of 0.7 degrees (with a possible $\sin 2\theta$ dependence). The maximum error was at a compass reading of 354 degrees. The measurement line of the LADCP compass appears to be oriented in the direction of transducer #3, but this was not measured precisely.

The purpose of the test was to see how well the KVH compass in the LADCP performs under the best of circumstances. Clearly, the smaller horizontal magnetic field, the magnetism of nearby material on the CTD cage and the variable tilt of the package will give a completely different picture for the field deployment in the Denmark Strait. However, the reasonable post-calibration values for heading-dependent

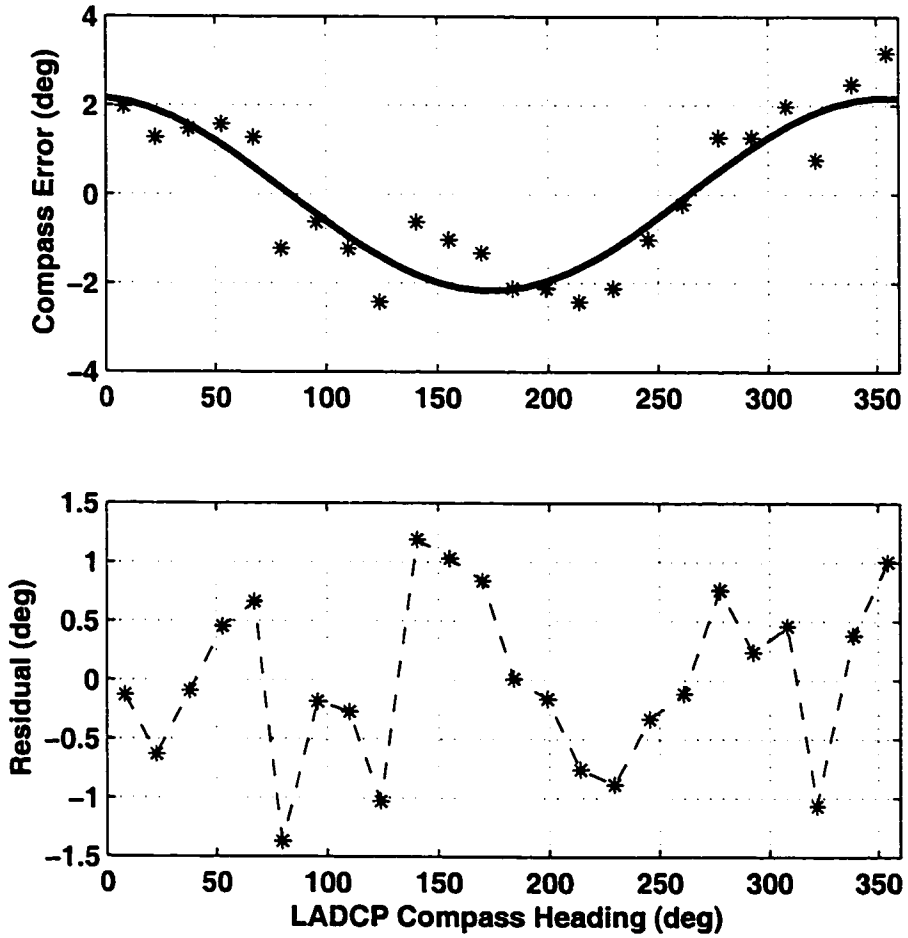


Figure 2.9: The upper panel shows the data (*) and sine fit from the calibration of the LADCP compass at the NOAA-PMEL turntable. A mean compass offset has been removed since the orientation of the instrument on the turntable was not precisely determined at the time of the test. The lower panel shows the residual error after the sine fit has been subtracted.

error acquired on the NOAA turntable give confidence that, at least, the compass was operating satisfactorily to the best of its ability throughout the cruise.

2.4 Velocity Profiling with Electromagnetic Induction

The XCP, manufactured by Sippican, Inc., is a self-contained, free-falling profiler based on the principles of geomagnetic induction [*Sanford et al.*, 1993]. The instrument consists of a surface float/transmitter and a free-falling probe containing electrodes, a thermistor, compass coil, and electronics (Figure 2.10). The small size of the

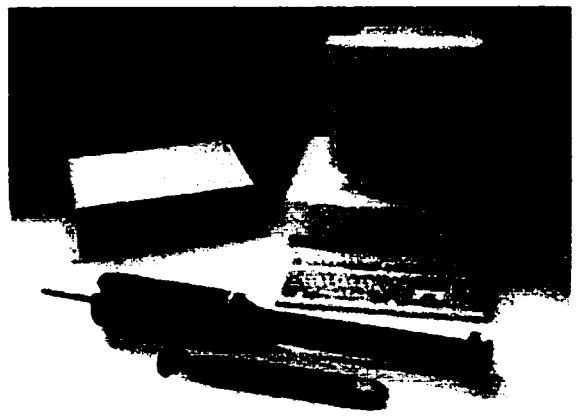


Figure 2.10: Photo from Sippican brochure, showing XCP probe and surface float/transmitter along with computer and MK-10 signal processor/receiver. More info available at `http://www.sippican.com/expendable_probes.html`

probe gives the XCP the ability to measure to within less than a meter from the ocean bottom, allowing resolution of the turbulent boundary layer. Voltage, temperature and heading information are encoded as audio frequencies and sent from the probe to the surface float via a thin conducting wire (with spools in both the probe and float to eliminate pull on either). This frequency-modulation technique gives a signal-to-noise performance far superior to that of the raw voltages used in, for example, XBT measurements. In the float, the audio data are impressed onto a radio-frequency carrier and sent to the ship in real time, where they can be recorded on any audio device (with digital tapes being the currently-preferred medium). The autonomous nature of the XCP makes deployment possible in a wide range of weather conditions and allows for rapid surveying at full vessel speed. The XCP can be used in conjunction with either lowered CTD stations or expendable CTD (XCTD) drops for simultaneous profiles of temperature, salinity and velocity. XCTDs are most useful in situations, like the DSO, where rapid sampling is important, allowing for continuous ship motion as well as operation in rough weather. On the 1997 *Aranda* cruise described in Chapter 3, the XCP profiles were made either shortly before or shortly after lowered CTD stations, while on the 1998 *Poseidon* cruise (Chapter 4) a combination of XCTD and lowered CTD profiles was used.

The XCP exploits the fact that the measured electrical voltage is proportional to the difference between a depth-independent quantity ($\bar{\mathbf{v}}^*$) and the horizontal velocity ($\mathbf{v}(z)$) of the instrument itself, as described below.

The motion of conducting seawater through the earth's magnetic field ($\mathbf{F}$) generates electric currents ($\mathbf{J}$). These currents result from a combination of the local horizontal motion ($\mathbf{v}$) and the large-scale electric field ($-\nabla\Phi$) produced by motion over a broad (compared to the water depth) region:

$$\mathbf{J} = \sigma(\mathbf{v} \times \mathbf{F} - \nabla\Phi), \tag{2.2}$$

where σ is the seawater conductivity. The magnitude of the large-scale electric field depends on the conductivity-weighted depth-averaged horizontal water velocity ($\bar{\mathbf{v}}^*$)[1] as well as the local and depth-averaged vertical vorticity ($\zeta = \partial v/\partial x - \partial u/\partial y$ and $\bar{\zeta}^* = \partial \bar{v}^*/\partial x - \partial \bar{u}^*/\partial y$) and the vertical and horizontal components of the geomagnetic field (F_z and F_h):

$$\nabla\Phi = F_z \bar{\mathbf{v}}^* \times \hat{\mathbf{k}} + (\int_z^0 F_z(\zeta - \bar{\zeta}^*)dz + F_y u)\hat{\mathbf{k}}, \tag{2.4}$$

where $\hat{\mathbf{k}}$ is the vertical unit vector, so that only the first term contributes to the horizontal part of $\nabla\Phi$. Due to the horizontal nature and thin aspect ratio of most oceanographic phenomena the horizontal part of the large-scale electric field is depth-independent.

An instrument in the water will distort the local electric currents around its body somewhat, introducing a scale factor C_1, with a value that depends on both the shape of the instrument and the position of the electrodes relative to the body. For example, a free-floating instrument moving with the seawater's horizontal velocity that has electrodes mounted flush against a cylindrical body measures a horizontal voltage:

$$\Delta\phi = -\frac{(1 + C_1)}{\sigma}\mathbf{J} \cdot \mathbf{s} \tag{2.5}$$

$$\approx -F_z(1 + C_1)((\mathbf{v} - \bar{\mathbf{v}}^*) \times \hat{\mathbf{k}}) \cdot \mathbf{s} \tag{2.6}$$

[1]Actually, $\bar{\mathbf{v}}^*$ is a quantity close, but not exactly equal, to $\bar{\mathbf{v}}$, the true depth-averaged velocity. The asterisk indicates the influences of variations in seawater conductivity, as well as conducting sediments:

$$\bar{v}^* = \frac{\int_{-H}^0 v\sigma dz}{\int_{-H_S}^0 \sigma dz}, \tag{2.3}$$

where H is the water depth and H_S is a basement depth where conductivity vanishes. In most situations where these effects could be measured, $\bar{\mathbf{v}}^*$ has been within 10% of $\bar{\mathbf{v}}$.

where s is the (horizontal) electrode separation vector. A vertically-falling probe adds an additional voltage in the magnetic east direction proportional to the fall rate, w_p, of the probe (and an additional scale factor, C_2, due to the distortion of vertical currents and fluid flow relative to the body), so that

$$\Delta\phi = -F_z(1+C_1)((\mathbf{v}-\bar{\mathbf{v}}^*)\times\hat{\mathbf{k}})\cdot\mathbf{s} + w_p F_h(1+C_2)\hat{\mathbf{i}}\cdot\mathbf{s}, \tag{2.7}$$

where $\hat{\mathbf{i}}$ is the magnetic east unit vector.

In the case of the XCP, w_p is known from an empirically-determined formula ($w_p = -z_1 - z_2 t$ from Equation 2.1) and C_1 and C_2 are approximately 1 and 0, respectively, based on analytical calculations [*Sanford et al.*, 1978, 1982]. Variations with depth in the remaining term are due entirely to variations in velocity, so that a profile of $\Delta\phi$ can be converted into a profile of velocity relative to $\bar{\mathbf{v}}^*$ (which is generally unknown but constant over the water depth). This relative velocity profile will be referred to as $\mathbf{v_{EF}}$:

$$\mathbf{v_{EF}} = (u_{\mathrm{EF}}, v_{\mathrm{EF}}) \tag{2.8}$$

$$= (u-\bar{u}^*, v-\bar{v}^*) \tag{2.9}$$

$$= \mathrm{rot}(\mathbf{v_{EF,mag}}, \varphi_{\mathrm{decl}}) \tag{2.10}$$

$$u_{\mathrm{EF,mag}} = \frac{\Delta\phi_{y,\mathrm{mag}}}{F_z(1+C_1)s} \tag{2.11}$$

$$v_{\mathrm{EF,mag}} = -\frac{\Delta\phi_{x,\mathrm{mag}}}{F_z(1+C_1)s} + \frac{F_h(1+C_2)}{F_z(1+C_1)}w_p \tag{2.12}$$

Note that because of the importance of flow relative to the earth's magnetic field, many of the source quantities will arise naturally in geomagnetic coordinates. In general, geomagnetically-oriented vector components will be denoted by the subscript "mag" and will need to be rotated into geographical coordinates by the magnetic declination, φ_{decl}.

Additional information is then needed to get absolute flows from $\mathbf{v_{EF}}$ (as required, for instance, to estimate volume transport). This can be accomplished using near-surface velocity from a vessel-mounted ADCP combined with accurate GPS navigation, as described in Section 2.5.

Further discussion of the theory of motional induction and its application to profiling instruments can be found in *Sanford* [1971] and *Sanford et al.* [1978]. In particular, issues such as conducting sediments, non-local electrical currents and horizontal

motion of a free-falling probe relative to the water are discussed. More detailed description of the XCP, including an additional correction due to probe tilt, can be found in *Sanford et al.* [1993].

2.5 Absolute Velocity

Since the XCP measures relative velocity, additional information is needed to determine the flow of the water relative to the earth. We have chosen to use the procedure illustrated in Figure 2.11. The XCP measures a velocity profile, $v_{EF}(z)$, relative to an unknown constant, $\bar{v}^*$; the ADCP measures a near-surface velocity profile, $v_{r2s}(z)$, relative to the ship; and GPS navigation measures the ship's own velocity, $v_{ship}(t)$ (later called $v_{GPS}(t)$), relative to the earth. In the upper part of the water column, the XCP and ADCP profiles overlap and the resulting difference can be used to determine the XCP's unknown offset:

$$v_{EF} = v_{water} - \bar{v}^* \tag{2.13}$$

$$v_{r2s} = v_{water} - v_{ship} \tag{2.14}$$

$$\bar{v}^* = v_{water} - v_{EF} \tag{2.15}$$

$$= v_{r2s} + v_{ship} - v_{EF} \tag{2.16}$$

Once determined, the constant $\bar{v}^*$ can be added to $v_{EF}(z)$ to give absolute velocity. In addition, $\bar{v}^*$ itself is an interesting quantity to know for some applications, representing the large-scale horizontal electric field in the ocean. In most situations, $\bar{v}^*$ is very close to the depth-averaged velocity over the full water column, but is also affected by electrically-conducting sediments and external electric fields. For the purposes of this dissertation, however, $\bar{v}^*$ will simply be treated as an unknown constant to be removed and ignored.

2.5.1 GPS Navigation

GPSPACE

Post-processing GPS corrections were purchased from the Canadian Geodetic Survey in the hopes that the resulting positioning would be more precise than the single-station DGPS corrections that were received on board the *Poseidon*. The corrections,

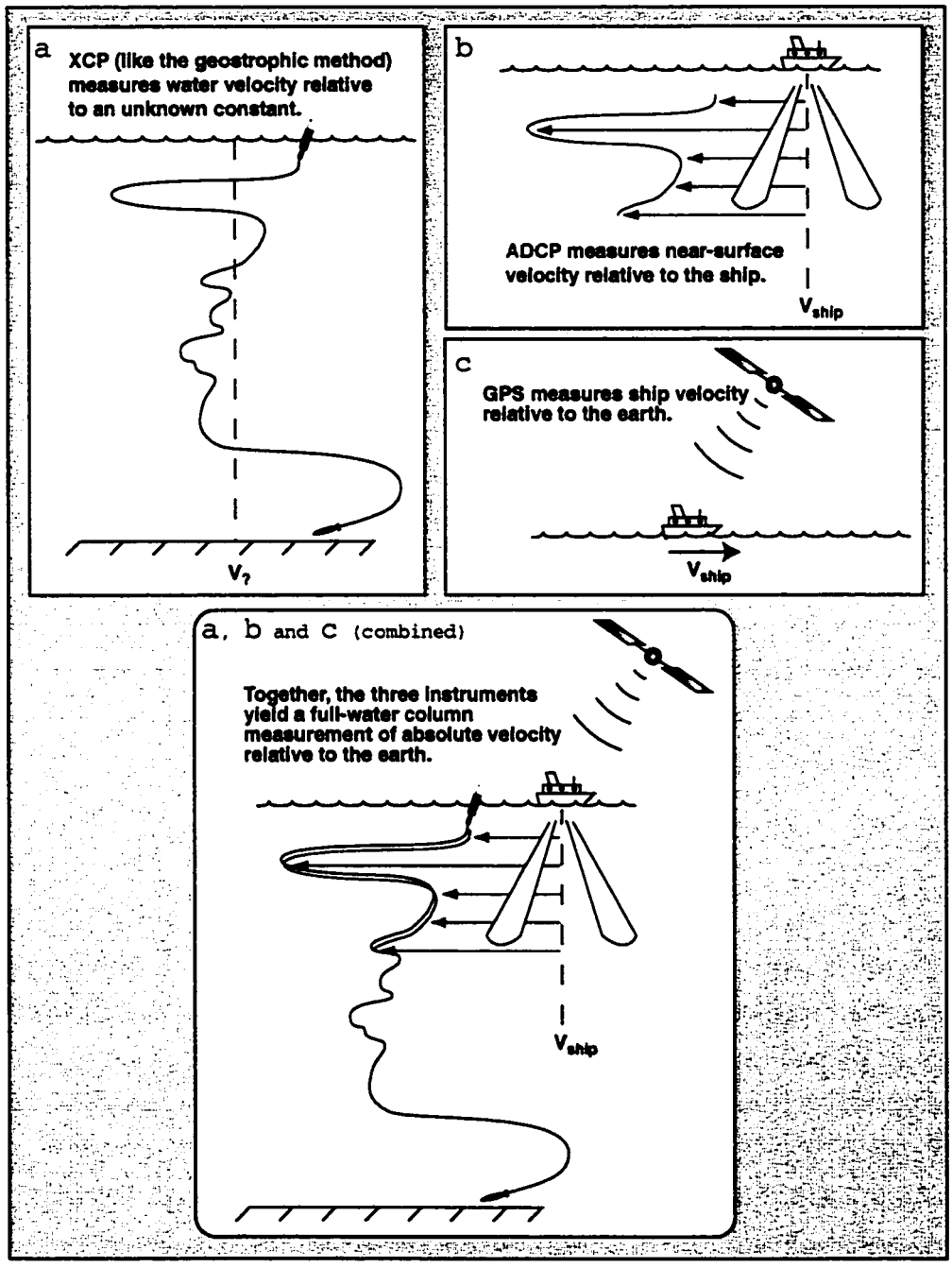


Figure 2.11: Using ADCP and GPS to reference an XCP velocity profile.

derived from receiving stations in the Canadian Active Control System (CACS) network, allow determination of precise satellite ephemerides (GPS orbits) and precise satellite clock corrections to remove the degrading effects of Selective Availability (SA). In fact, this wide area network may produce superior orbits to those broadcast by the satellite in real time, resulting in improvements beyond the SA removal. The corrections are applied by a software program called GPSPACE, which allows considerable flexibility in the choice of satellites used to reconstruct the positions.

Customized Constellations

Problems with the GPSPACE data arise when the satellite constellation in view changes too rapidly, as was frequently the case with the 6-channel Ashtech 3DF receiver used on the *Poseidon*. More satellite channels have helped relieve this problem in later cruises, but for the *Poseidon* data the best solution came from constructing customized 4-satellite constellations around the period of each XCP drop. By restricting the solution to the same 4 satellites over a 7-min period, a substantially more stable velocity estimate can be made.

Comparison to DGPS

It is not obvious, given the broadband nature of the SA degradation, how to compare different GPS "improvement" techniques. Two ways to compare GPSPACE and DGPS are 1) by looking at raw position scatter relative to a constant-steered course or constant-held position (Figure 2.12) or 2) by comparing GPS-referenced acoustic Doppler current profiler (ADCP) water velocities, which should be markedly smoother than the ship's own motion. The first method works if the ship's actual changes in position are smaller than the GPS noise, as they definitely are for the raw GPS under SA. The second method, although removing the effect of the ship's own motion, is only as good as the ADCP measurements themselves, which may have a large scatter or bias in rough conditions. An example of this water velocity comparison is shown in Figure 2.20. A possible reason for the advantage of DGPS over GPSPACE in some of our drops is that the Icelandic DGPS station may be better able to correct for local ionospheric and tropospheric variability than the Canadian global average. If a large part of the GPS uncertainty was caused by ionospheric disturbances, say through

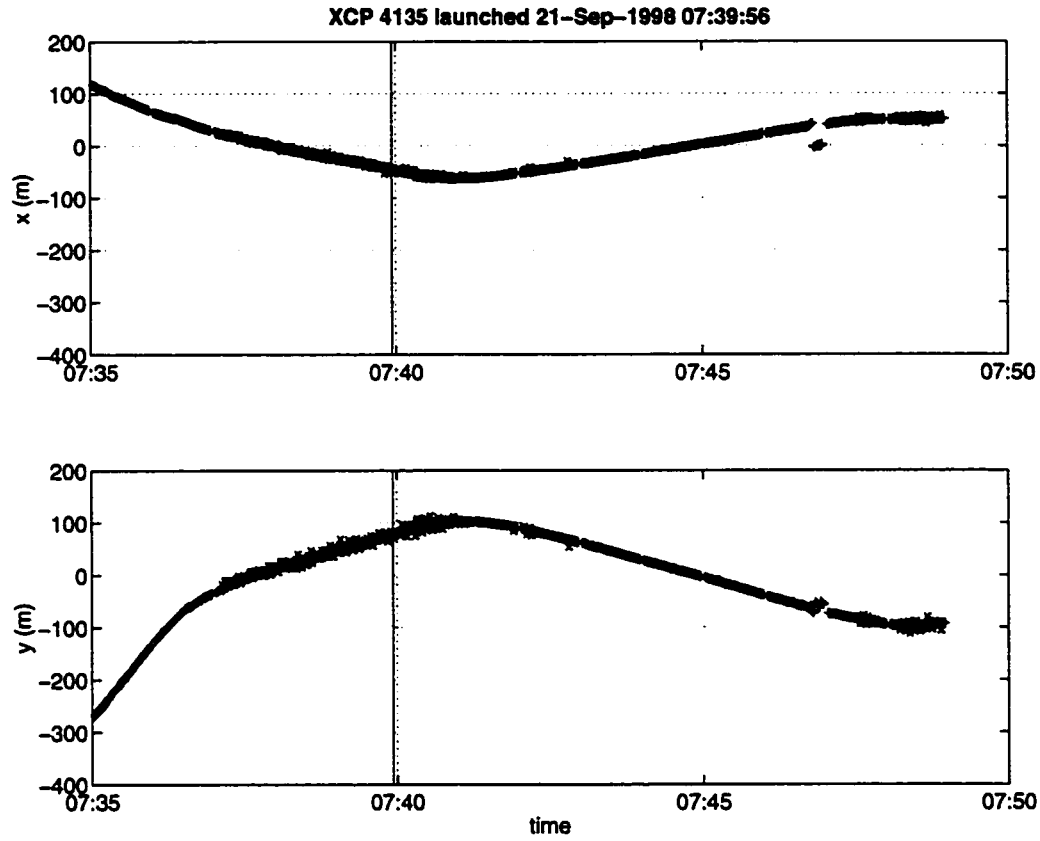


Figure 2.12: Example of GPS comparison showing residual E-W and N-S positions after removing most of the ship motion via a 2nd-order polynomial fit. Red pluses are the DGPS 1-second positions, which demonstrate somewhat less scatter than the GPSPACE positions (blue Xs) but are vulnerable to position discontinuities when switching satellites. PACE data are missing when any of the chosen set of 4 satellites is unavailable. The vertical line green line marks the time of an XCP drop.

the *aurora borealis*, rather than by the SA degradation, the DGPS method could be better. On the other hand, the global nature of the GPSPACE system should, in principle, produce superior corrections for each satellite, making the ionospheric and tropospheric contributions important only inasmuch as they change over the course of a velocity estimate.

2.5.2 Rotating and Referencing the ADCP

In order to be interpreted in oceanographic terms, ADCP velocities from a moving and rotating ship must be transformed into absolute velocities relative to the earth. This consists of two parts:

1. rotating the measured velocity ($\mathbf{v}_{\mathbf{ADCP}}$) into earth coordinates (by the angle φ_{Drot}) and

2. adding the vessel's own velocity ($\mathbf{v}_{\mathbf{GPS}}$) in these coordinates.

The combination of these gives:

$$\mathbf{v}_{\mathbf{water}} = \mathrm{rot}(\mathbf{v}_{\mathbf{ADCP}}, \varphi_{\mathrm{Drot}}) + \mathbf{v}_{\mathbf{GPS}} \tag{2.17}$$

or

$$\begin{bmatrix} u_{\mathrm{water}} \\ v_{\mathrm{water}} \end{bmatrix} = \begin{bmatrix} u_{\mathrm{ADCP}} \cos\varphi_{\mathrm{Drot}} + v_{\mathrm{ADCP}} \sin\varphi_{\mathrm{Drot}} + u_{\mathrm{GPS}} \\ v_{\mathrm{ADCP}} \cos\varphi_{\mathrm{Drot}} - u_{\mathrm{ADCP}} \sin\varphi_{\mathrm{Drot}} + v_{\mathrm{GPS}} \end{bmatrix}. \tag{2.18}$$

The Importance of Accurate Headings

If the quantities u_{ADCP}, v_{ADCP}, u_{GPS}, v_{GPS} and φ_{Drot} have respective uncertainties $\epsilon_{u\mathrm{D}}$, $\epsilon_{v\mathrm{D}}$, $\epsilon_{u\mathrm{P}}$, $\epsilon_{v\mathrm{P}}$ and ϵ_{φ}, then the uncertainties in u_{water} and v_{water} are given by:

$$\begin{aligned} \epsilon_{uw}^2 &= (\epsilon_{u\mathrm{D}} \cos\varphi_{\mathrm{Drot}})^2 + (\epsilon_{v\mathrm{D}} \sin\varphi_{\mathrm{Drot}})^2 + \\ &\quad (\epsilon_{\varphi} v_{\mathrm{ADCP}} \cos\varphi_{\mathrm{Drot}} - \epsilon_{\varphi} u_{\mathrm{ADCP}} \sin\varphi_{\mathrm{Drot}})^2 + \epsilon_{u\mathrm{P}}^2 \end{aligned} \tag{2.19}$$

$$\begin{aligned} \epsilon_{vw}^2 &= (\epsilon_{u\mathrm{D}} \sin\varphi_{\mathrm{Drot}})^2 + (\epsilon_{v\mathrm{D}} \cos\varphi_{\mathrm{Drot}})^2 + \\ &\quad (\epsilon_{\varphi} v_{\mathrm{ADCP}} \sin\varphi_{\mathrm{Drot}} + \epsilon_{\varphi} u_{\mathrm{ADCP}} \cos\varphi_{\mathrm{Drot}})^2 + \epsilon_{v\mathrm{P}}^2 \end{aligned} \tag{2.20}$$

For a ship underway, errors in φ_{Drot} will show up as errors in the velocity component perpendicular to the direction of ship's motion. This becomes apparent in the case of a ship steaming northwards ($\varphi_{\mathrm{Drot}} = 0$, $u_{\mathrm{ADCP}} \approx 0$ and $u_{\mathrm{GPS}} \approx 0$). Then Equation 2.19 becomes:

$$\epsilon_{uw}^2 = \epsilon_{u\mathrm{D}}^2 + (\epsilon_{\varphi} v_{\mathrm{ADCP}})^2 + \epsilon_{u\mathrm{P}}^2 \tag{2.21}$$

$$\epsilon_{vw}^2 = \epsilon_{v\mathrm{D}}^2 + (\epsilon_{\varphi} u_{\mathrm{ADCP}})^2 + \epsilon_{v\mathrm{P}}^2 \tag{2.22}$$

Since v_{ADCP} includes the ship's own velocity, which is very large compared to oceanic water velocities, ϵ_{uw} has the potential to be quite large. For example, if the ship moves at a typical cruising speed of $5\,\mathrm{m\,s^{-1}}$, a heading uncertainty of only 2 milliradians (mrad) will produce a $1\,\mathrm{cm\,s^{-1}}$ uncertainty in the perpendicular velocity component.

GPS Heading Measurements

The most accurate heading measurements currently available are from multi-antenna GPS instruments which use phase interferometry to very accurately determine relative antenna position (and, hence, the orientation of a fixed array of antennas). The ADU-II, a 4-antenna unit manufactured by Ashtech Corp., is specified to be accurate to a resolution of 1 mrad for an antenna spacing of 2.5 m [*Ashtech*, 1996]. This is approximately the spacing used for the ADU installation on the *Poseidon*, while the *Aranda* setup involved somewhat greater antenna separation. *King and Cooper* [1993] examined an earlier version of the Ashtech unit and concluded that the manufacturer's claims of 1 mrad accuracy were justified.

Gyrocompass Errors

In comparison, gyrocompasses often exhibit errors which vary considerably among different installations. On *Poseidon* cruise 244, the gyrocompass frequently differed from the ADU-II by 50 mrad or more! This included both heading-dependent and time-dependent components related to how a gyrocompass is affected by meridional velocities and accelerations (Figure 2.13). With the availability of accurate GPS heading sensors (like the ADU) which are immune to these problems, the nuances become less important.

Definitions

α_A ADU mounting angle to the ship's centerline

α_D Doppler (ADCP) mounting angle to the ship

α_G Gyrocompass mounting angle to the ship

φ_{hdg} "True" heading of vessel (*i. e.*, the clockwise angle between true north and the ship's centerline—not necessarily the direction the ship goes under forward thrust, neutral rudder and calm conditions, although it will normally be close)

φ_{ADU} Heading output from 4-antenna GPS heading sensor

φ_{gyro} Heading output from gyrocompass

See Figure 2.14 for illustration of these angles.

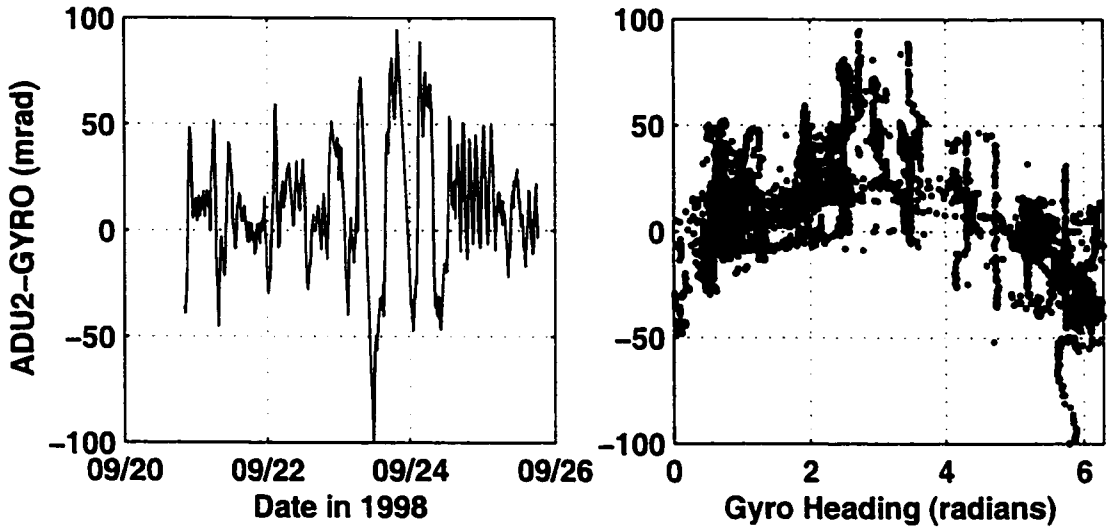


Figure 2.13: φ_{A-G} as a function of time (left panel) and of heading (right panel).

Application

Since the GPS heading measurements require a continuous lock on at least 4 satellites by all 4 of the antennas, they are often vulnerable to dropouts due to multipath effects and other sources of GPS disruption. For this reason, a common approach has been to use the continuous heading measurements from the gyrocompass to rotate individual ADCP pings as frequently as every second or two (to account for rapid changes in the vessel's orientation) while the GPS headings are applied to ensemble-averaged velocities over 1 minute or more to correct longer-period gyro errors. Using this scheme, then, horizontal velocities from the ADCP must be rotated clockwise by φ_{Drot}:

$$\varphi_{Drot} = \varphi_{gyro} + \varphi_{corr} \tag{2.23}$$

Ensemble velocities that have already been rotated into "earth" coordinates using the gyrocompass, *e.g.*, by RDI's DAS software, only need to be rotate by φ_{corr}:

$$\varphi_{corr} = \varphi_{A-G} + \varphi_{mount} \tag{2.24}$$

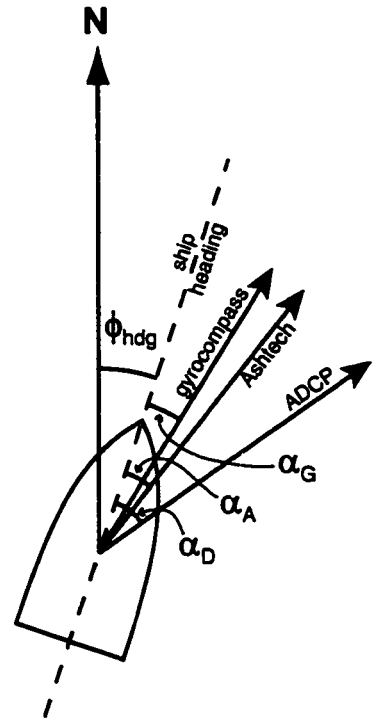


Figure 2.14: Mounting angles of ADU (Ashtech), ADCP and gyrocompass relative to ship heading.

where

$$\varphi_{A-G} = \langle \varphi_{ADU} - \varphi_{gyro} \rangle_t \tag{2.25}$$

and

$$\varphi_{mount} = \alpha_D - \alpha_A \tag{2.26}$$

A few things to note:

1. $\langle\rangle_t$ is an average over some interval of time, and is necessary to remove high-frequency noise present in the ADU data.

2. The parameter dh_avg_ue4 output by Eric Firing's UE4 addition to DAS is an estimate of φ_{A-G} obtained by averaging the ADU–gyrocompass heading differences over each 1-min ADCP ensemble. An alternative estimate can also

be determined from raw gyro and ADU data, if available, averaged over some suitable period. On the *Poseidon* cruise, raw gyro data were not recorded, and so only an average over each ensemble can be used. If gyro errors (ϵ_{gyro}) are relatively constant over the averaging interval, φ_{A-G} can still be estimated by $\langle\varphi_{\text{ADU}}\rangle_t - \langle\varphi_{\text{gyro}}\rangle_t$. Figure 2.15 shows that the UE4 estimate (green) is cleaner than the estimate from raw ADU and averaged gyro (blue).

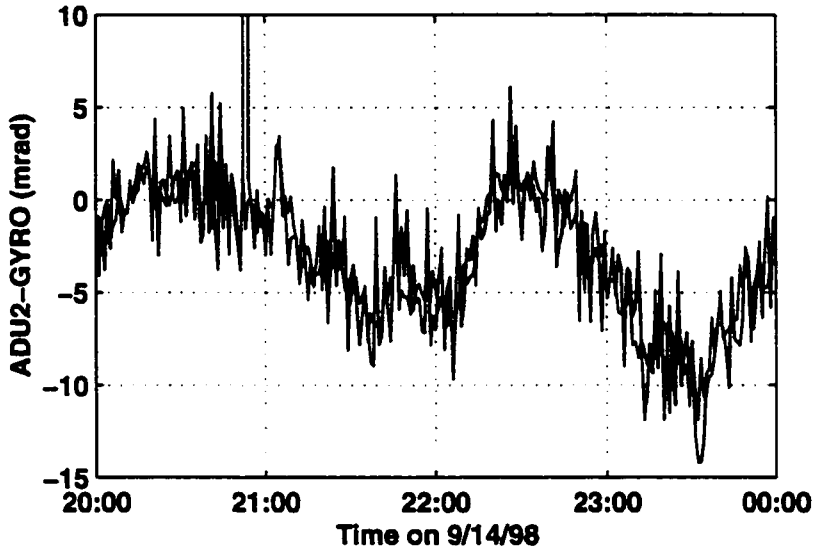


Figure 2.15: A comparison of two determinations of φ_{A-G}. The blue line is the difference between 1-min averages of ADU and gyrocompass (*i.e.*, $\langle\varphi_{\text{ADU}}\rangle_t - \langle\varphi_{\text{gyro}}\rangle_t$) and the green is dh_avg_ue4 from UE4 (*i.e.*, $\langle\varphi_{\text{ADU}} - \varphi_{\text{gyro}}\rangle_t$). The similarity confirms the sign of the UE4 output while the slightly lower noise level of the green line demonstrates the desirability of using the ADU–gyro difference from each ping. Note also the approximately 1.5 hour period of oscillation, corresponding to the Schuler oscillation of the gyrocompass.

3. Examples of φ_{A-G} are shown in Figures 2.13 and 2.15 as "ADU2–GYRO."

4. φ_{mount} can be determined via the *bottom track* or *water track* methods [*Joyce*, 1989; *Pollard and Read*, 1989].

Bottom Track Calibration

The bottom track method compares the course over ground[2] measured by GPS navigation,

$$\varphi_{\mathrm{GPS}} = \mathtt{atan2}(u_{\mathrm{GPS}}, v_{\mathrm{GPS}}), \tag{2.28}$$

with that measured by ADCP bottom-tracking,

$$\varphi_{\mathrm{BT}} = \mathtt{atan2}(-u_{\mathrm{BT}}, -v_{\mathrm{BT}}), \tag{2.29}$$

where $\mathbf{v}_{\mathrm{BT}}$ is the measured *bottom* velocity, rotated into earth coordinates by φ_{gyro} and output by DAS. This must be rotated further by φ_{corr} to give true course. The GPS and BT courses should then be equal:

$$\varphi_{\mathrm{GPS}} = \varphi_{\mathrm{BT}} + \varphi_{\mathrm{corr}} \tag{2.30}$$

$$= \varphi_{\mathrm{BT}} + \varphi_{\mathrm{A-G}} + \varphi_{\mathrm{mount}} \tag{2.31}$$

so that

$$\varphi_{\mathrm{mount}} = \varphi_{\mathrm{GPS}} - (\varphi_{\mathrm{BT}} + \varphi_{\mathrm{A-G}}). \tag{2.32}$$

Examples of φ_{mount} determined from successive 1-minute estimates of φ_{GPS}, φ_{BT}, and $\varphi_{\mathrm{A-G}}$ are shown in Figure 2.16 as "GPS–BTrack." Since bottom tracking was available in only three of the 4-hour ADCP acquisition intervals for the cruise, a separate average value was determined for each. Each ensemble gives an independent estimate of φ_{mount}. The timeseries of good points (containing both ADCP and GPS information) for each file is shown, along with the average φ_{mount} value and an estimate of standard error ($\sigma/\sqrt{N}$).

The fact that these three independent estimates of φ_{mount} are so similar implies that this angle really is known to an accuracy of about 1 mrad, allowing sub-cm s^{-1} ADCP velocity accuracy even while underway.

---

[2]Courses and directions in this dissertation follow the nautical bearing convention of measuring angles clockwise from north. In converting vector components I have used the MatLab function `atan2`, which yields a result in the range $[\pi, -\pi]$ radians. The expression $\mathtt{atan2}(u, v)$ is equivalent to:

$$\tan^{-1}(\frac{u}{v}) + \begin{cases} 0 & \text{for } v > 0 \\ \pi & \text{for } v < 0 \text{ and } u > 0 \\ -\pi & \text{for } v < 0 \text{ and } u < 0 \end{cases}. \tag{2.27}$$

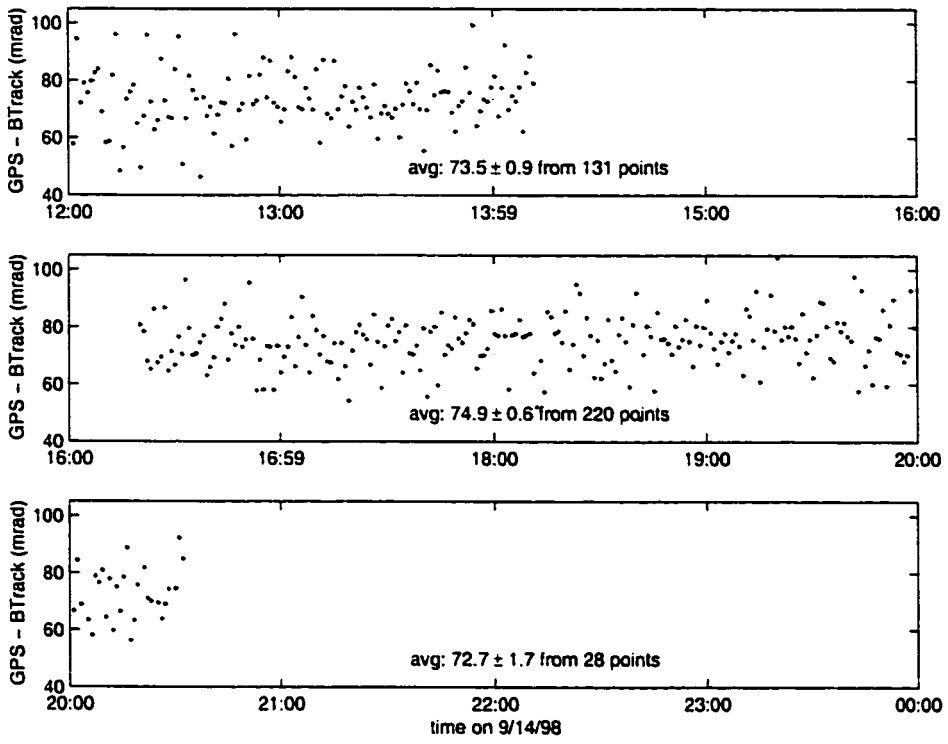


Figure 2.16: Three estimates of φ_{mount} determined from comparing ship course over ground from bottom tracking (corrected for gyro errors) with GPS navigation.

More Angles

For ADCP velocity determination, the only mounting angle that really needs to be determined is $\alpha_D - \alpha_A$, so φ_{hdg} and α_G, as well as the separate values of α_D and α_A, are unimportant. It is possible that other applications may need to know these other mounting angles or φ_{hdg}, so some additional relationships are presented here.

By definition:

$$\varphi_{\text{ADU}} = \varphi_{\text{hdg}} + \alpha_A + \epsilon_{\text{ADU}} \tag{2.33}$$

$$\varphi_{\text{gyro}} = \varphi_{\text{hdg}} + \alpha_G + \epsilon_{\text{gyro}} \tag{2.34}$$

where ϵ_{gyro} is both heading and time dependent and ϵ_{ADU} is primarily high-frequency

random error. Combining the two yields:

$$\varphi_{\text{gyro}} = \varphi_{\text{ADU}} - \alpha_A - \epsilon_{\text{ADU}} + \alpha_G + \epsilon_{\text{gyro}}, \tag{2.35}$$

so that

$$\varphi_{\text{A-G}} = \langle \alpha_A - \alpha_G + \epsilon_{\text{ADU}} - \epsilon_{\text{gyro}} \rangle_t . \tag{2.36}$$

A small amount of averaging should remove ϵ_{ADU} entirely (to an accuracy of 1 mrad, at least) but ϵ_{gyro} is a bit more problematic. With enough averaging, and perhaps after subtracting a heading-dependent component (*i. e.*, removing a sinusoidal fit and outliers from the right-hand panel of Fig. 2.13, then averaging), it might be reasonable to assume that ϵ_{gyro} will vanish, leaving an estimate of $\alpha_A - \alpha_G$.

α_G is likely to be small, due to the gyro's importance for navigation, so the remaining angle is probably a good estimate of α_A, but one can't be sure.

A possible option is to compare GPS-derived course over ground with φ_{ADU}, assuming that differences between course and heading will vanish in long averages. This is not a very solid assumption, though.

Equivalent Notation in References

Table 2.3 shows the equivalent notation used by *Joyce* [1989] and *Pollard and Read* [1989] for quantities described here. Note that *Joyce* [1989] prefers to define rotations as counterclockwise while *Pollard and Read* [1989] and use clockwise rotations, as adopted here. *Joyce* [1989] does not consider the possibility of a GPS heading sensor,

Table 2.3: Equivalent notation used in bottom track calibration methods.

This Work	*Joyce* [1989]	*Pollard and Read* [1989]
φ_{corr}	$-\alpha$	φ
u_{GPS}	u_{s}	u_{s}
v_{GPS}	v_{s}	v_{s}
u_{BT}	u'_{d}	u'_{d}
v_{BT}	v'_{d}	v'_{d}

and so assumes that the correction angle will be a time-dependent quantity, including both gyrocompass errors and the unknown ADCP and gyro mounting angles. His method of solution (Equation 10a) uses matrix methods to determine the bottom track and water track corrections, which may do a slightly better job of minimizing noise kinetic energy but is not as intuitive as simply adding angles. If the ADCP velocities used (u_s and v_s) have already been corrected by the ADU, then his solution for $-\alpha$ gives my constant value of φ_{mount}.

2.5.3 Construction of referenced XCP profile

We want to measure a profile of absolute velocity, $\mathbf{v_{abs}}$. The basic equations, reflecting the construction of absolute velocity from its component measurements, are (see Section 2.4 and below for definitions of terms):

$$\mathbf{v_{abs}}(z) = \mathbf{v_{EF}}(z) + \bar{\mathbf{v}}^* \tag{2.37}$$

$$\bar{\mathbf{v}}^* = \langle \mathbf{v_{watX}}(z) - \mathbf{v_{EF}}(z) \rangle_z \tag{2.38}$$

$$\mathbf{v_{EF}}(z) = \text{rot}(\mathbf{v_{EF,mag}}(z), \varphi_{\text{decl}}) \tag{2.39}$$

$$\mathbf{v_{EF,mag}}(z) = \begin{bmatrix} \frac{\Delta\varphi_{y,\text{mag}}(z)}{F_2(1+C_1)s} \\ -\frac{\Delta\varphi_{x,\text{mag}}(z)}{F_2(1+C_1)s} + \frac{F_h(1+C_2)}{F_2(1+C_1)} w'_p(z) \end{bmatrix} \tag{2.40}$$

$$\mathbf{v_{watX}}(z) = \langle \mathbf{v_{wat}}(z,t) \rangle_t \tag{2.41}$$

$$\mathbf{v_{wat}}(z,t) = \mathbf{v_{r2s}}(z,t) + \mathbf{v_{GPS}}(t) \tag{2.42}$$

$$\mathbf{v_{r2s}}(z,t) = \text{rot}(\mathbf{v_{ens}}(z,t), \varphi_{\text{corr}}(t)) \tag{2.43}$$

$$\mathbf{v_{ens}}(z,t) = \langle \text{rot}(\mathbf{v_{ADCP}}(z,t), \varphi_{\text{gyro}}(t)) \rangle_t \tag{2.44}$$

$$\varphi_{\text{corr}}(t) = \langle \varphi_{\text{ADU}}(t) - \varphi_{\text{gyro}}(t) \rangle_t + \varphi_{\text{mount}} \tag{2.45}$$

$$\mathbf{v_{GPS}}(t) = \left\langle \frac{d}{dt}\mathbf{x_{GPS}}(t) \right\rangle_t \tag{2.46}$$

where $\mathrm{rot}(v, \varphi)$ indicates clockwise rotation of a vector v by the angle φ:

$$\mathrm{rot}(\begin{bmatrix} u \\ v \end{bmatrix}, \varphi) = \begin{bmatrix} u\cos\varphi + v\sin\varphi \\ v\cos\varphi - u\sin\varphi \end{bmatrix}. \tag{2.47}$$

Combining all together, we get (first the horizontal vector, then its components):

$$\begin{aligned}
\mathbf{v_{abs}} = {} & \mathrm{rot}(\mathbf{v_{EF,mag}}(z), \varphi_{\mathrm{decl}}) + \langle (\mathrm{rot}(\langle \mathrm{rot}(\mathbf{v_{ADCP}}(z,t), \varphi_{\mathrm{gyro}}(t)) \rangle_t, \\
& \langle \varphi_{\mathrm{ADU}}(t) - \varphi_{\mathrm{gyro}}(t) \rangle_t + \varphi_{\mathrm{mount}}) + \left\langle \frac{d}{dt}\mathbf{x_{GPS}}(t) \right\rangle_t \rangle_t - \\
& \mathrm{rot}(\mathbf{v_{EF,mag}}(z), \varphi_{\mathrm{decl}}) \rangle_z
\end{aligned} \tag{2.48}$$

$$\begin{aligned}
u_{\mathrm{abs}} = {} & \frac{\Delta\phi_{y,\mathrm{mag}}\cos\varphi_{\mathrm{decl}}}{F_z(1+C_1)s} - \frac{\Delta\phi_{x,\mathrm{mag}}\sin\varphi_{\mathrm{decl}}}{F_z(1+C_1)s} + \frac{F_h(1+C_2)w_p\sin\varphi_{\mathrm{decl}}}{F_z(1+C_1)} + \\
& \langle \langle \langle u_{\mathrm{ADCP}}\cos\varphi_{\mathrm{gyro}} + v_{\mathrm{ADCP}}\sin\varphi_{\mathrm{gyro}} \rangle_t \cos(\langle \varphi_{\mathrm{ADU}} - \varphi_{\mathrm{gyro}} \rangle_t + \varphi_{\mathrm{mount}}) + \\
& \langle v_{\mathrm{ADCP}}\cos\varphi_{\mathrm{gyro}} - u_{\mathrm{ADCP}}\sin\varphi_{\mathrm{gyro}} \rangle_t \sin(\langle \varphi_{\mathrm{ADU}} - \varphi_{\mathrm{gyro}} \rangle_t + \varphi_{\mathrm{mount}}) + \left\langle \frac{d}{dt}x_{\mathrm{GPS}} \right\rangle_t \rangle_t \\
& - \frac{\Delta\phi_{y,\mathrm{mag}}\cos\varphi_{\mathrm{decl}}}{F_z(1+C_1)s} + \frac{\Delta\phi_{x,\mathrm{mag}}\sin\varphi_{\mathrm{decl}}}{F_z(1+C_1)s} - \frac{F_h(1+C_2)w_p\sin\varphi_{\mathrm{decl}}}{F_z(1+C_1)} \rangle_z
\end{aligned} \tag{2.49}$$

$$\begin{aligned}
v_{\mathrm{abs}} = {} & \frac{F_h(1+C_2)w_p\cos\varphi_{\mathrm{decl}}}{F_z(1+C_1)} - \frac{\Delta\phi_{x,\mathrm{mag}}\cos\varphi_{\mathrm{decl}}}{F_z(1+C_1)s} - \frac{\Delta\phi_{y,\mathrm{mag}}\sin\varphi_{\mathrm{decl}}}{F_z(1+C_1)s} + \\
& \langle \langle \langle v_{\mathrm{ADCP}}\cos\varphi_{\mathrm{gyro}} - u_{\mathrm{ADCP}}\sin\varphi_{\mathrm{gyro}} \rangle_t \cos(\langle \varphi_{\mathrm{ADU}} - \varphi_{\mathrm{gyro}} \rangle_t + \varphi_{\mathrm{mount}}) - \\
& \langle u_{\mathrm{ADCP}}\cos\varphi_{\mathrm{gyro}} + v_{\mathrm{ADCP}}\sin\varphi_{\mathrm{gyro}} \rangle_t \sin(\langle \varphi_{\mathrm{ADU}} - \varphi_{\mathrm{gyro}} \rangle_t + \varphi_{\mathrm{mount}}) + \left\langle \frac{d}{dt}y_{\mathrm{GPS}} \right\rangle_t \rangle_t \\
& - \frac{F_h(1+C_2)w_p\cos\varphi_{\mathrm{decl}}}{F_z(1+C_1)} + \frac{\Delta\phi_{x,\mathrm{mag}}\cos\varphi_{\mathrm{decl}}}{F_z(1+C_1)s} + \frac{\Delta\phi_{y,\mathrm{mag}}\sin\varphi_{\mathrm{decl}}}{F_z(1+C_1)s} \rangle_z
\end{aligned} \tag{2.50}$$

Some explanations:

RED text variables indicate measurements or other estimated or determined base quantities (possibly averaged or smoothed in some way), each of which introduces some error to the final estimate of $\mathbf{v_{abs}}$.

$\langle\rangle_z$ **or** $\langle\rangle_t$ indicates some kind of estimator operation in space or time, possibly using an average of nearby values, an interpolation using a weighted least-squares polynomial fit (*e.g.*, from the MatLab `lscov` function), a manual selection ("by eye") or something else (*e.g.*, Kalman filter). Currently the estimators for $\bar{\mathbf{v}}^*$ ($\langle\rangle_z$ in Eq. 2.38) and $\mathbf{v_{GPS}}$ ($\langle\rangle_t$ in Eq. 2.46) are handled by `lscov` while others are

simple averages or hand-picked. *Pierce et al.* [1999], in their outline of a possible ADCP processing procedure, use a polynomial smoother for the Eq. 2.46 estimator and two steps for the Eq. 2.41 estimator—first a moving outlier-removal procedure and second low-pass filtering with a Blackman window. The net result probably loses too much oceanic detail for the purposes of this study.

Boldface quantities are horizontal vectors: $\mathbf{v} = \begin{bmatrix} u \\ v \end{bmatrix}$ and $\mathbf{x} = \begin{bmatrix} x \\ y \end{bmatrix}$

$\mathbf{v}_{\mathbf{r2s}}$ is the ADCP-measured velocity relative to the ship.

$\mathbf{v}_{\mathbf{ens}}$ is the average of an ensemble of ADCP pings, each of which has been rotated by φ_{gyro} into "earth coordinates" before averaging.

$\mathbf{v}_{\mathbf{watX}}$ is the water velocity at the time of the XCP drop, either picked manually or interpolated or estimated somehow (via the $\langle\rangle_t$ in Eq. 2.41). For the purposes of the individual profiles, I have chosen to use a linear fit over a 15-min window of $\mathbf{v}_{\mathbf{wat}}$ data and interpolate the resulting line to the time of the XCP drop.

φ_{corr} is the correction required to bring the gyro-rotated $\mathbf{v}_{\mathbf{ens}}$ into true geographical coordinates. It consists of both constant and time-dependent parts. The constant part is φ_{mount}, described below. The time-dependent part, called $\varphi_{\text{A-G}}$, is often obtained from a 4-antenna GPS heading system such as the Ashtech ADU. For example, could be $\varphi_{\text{ADU}} - \varphi_{\text{gyro}}$ averaged by ue4 over each 1-min interval.

φ_{mount} is a constant angle offset resulting from the relative mounting angles of the ADCP and ADU. Its estimation is described in Section 2.5.2.

Errors in measured quantities

Typical (median or estimated) values of each measured quantity are given in Table 2.4, along with estimated error magnitudes. Some comments on each quantity are as follows:

ϵ_{ADCP} is derived from the high-wavenumber noise within individual ADCP profiles, on the premise that bin-to-bin scatter derives from a mapping of different depths

to different bins as the ship rolls, and that the resulting error is also the dominant contribution to ensemble-to-ensemble noise in time. I have used the standard deviation of the high-passed profile as an estimate of ϵ_{ADCP}. This could be an under-estimate.

ϵ_{GPS} is derived from the linear least-squares fitting used to determine velocity from one-second GPS fixes. An alternative would be to use the position residual output by the GPS set, which is derived from the known accuracy of individual satellite fixes combined with the current geometrical configuration of the satellites used to determine position (the so-called, "dilution of precision"). A further possibility might be the residuals generated by the use of more than 4 satellites to determine position.

ϵ_{gyro} is the gyrocompass error which is removed through the correction by the ADU.

Table 2.4: Estimated typical values and errors for measured quantities.

quantity	typical value	error	error estimate
$\mathbf{v}_{\mathrm{ADCP}}$	$5\,\mathrm{m\,s^{-1}}$	ϵ_{ADCP}	$0.03\,\mathrm{m\,s^{-1}}$
$\left\langle \frac{d}{dt}\mathbf{x}_{\mathrm{GPS}}(t)\right\rangle_t$	$5\,\mathrm{m\,s^{-1}}$	ϵ_{GPS}	$0.01\,\mathrm{m\,s^{-1}}$
φ_{gyro}	1 rad	ϵ_{gyro}	50 mrad
φ_{mount}	100 mrad	$\epsilon_{\mathrm{mount}}$	0.6 mrad
φ_{ADU}	1 rad	ϵ_{ADU}	1 mrad
φ_{decl}	0.4 rad	ϵ_{decl}	10 mrad
F_h	1×10^4 nT	ϵ_{F_h}	100 nT
F_z	5×10^4 nT	ϵ_{F_z}	100 nT
w_p	$5\,\mathrm{m\,s^{-1}}$	ϵ_{w_p}	$0.1\,\mathrm{m\,s^{-1}}$
$\lvert\mathbf{s}\rvert$	0.05 m	ϵ_s	0.001 m
C_1	1	ϵ_{C_1}	0.1
C_2	0	ϵ_{C_2}	0.1
$\Delta\phi$	$1\,\mu$V	$\epsilon_{\Delta\phi}$	25 nV

Since the gyro contributes to the heading measurement which rotates the full ship velocity (as do ϵ_{mount} and ϵ_{ADU}), the quality of the correction is important. Any remaining gyro error (*e.g.*, from a velocity/heading correlation which produces a net velocity vector rotation other than that of the mean heading) could contaminate the measurements while the ship is underway.

ϵ_{mount} is the uncertainty in the constant mounting angle offset of the ADU relative to the ADCP, estimated from repetitions of the water track or bottom track calibration methods.

ϵ_{ADU} is the accuracy of the 4-antenna GPS heading sensor, as stated by the manufacturer and verified by *King and Cooper* [1993].

ϵ_{decl} (the error in the magnetic declination derived from a geomagnetic reference field model) is primarily of concern if oceanic velocities are large (leading to significant errors in the cross-stream component due to direction errors). In addition *all* of the measurements affecting XCP measurements are particularly liable to cause errors if they contain significant variation with depth, as in the case of near-bottom magnetic anomalies, since the depth-varying component of velocity is solely dependent on the XCP.

ϵ_{F_h} has the potential to produce errors in the magnetic north velocity component due to the multiplication by the substantial velocity term w_p. For example, variations of the size listed in Table 2.4 (about 1%) will produce velocity errors of $0.01\,\text{m}\,\text{s}^{-1}$, while a large magnetic anomaly of 1000 nT will result in $0.1\,\text{m}\,\text{s}^{-1}$velocity errors. This size of anomaly is not at all unusual and could conceivably affect only the near-bottom region where ADCP verification is unavailable.

ϵ_{F_z} has a direct multiplicative effect on the XCP velocity measurement but the size of the steady field should overwhelm most anomalies. A change in F_z of 1000 nT (about as large as localized magnetic anomalies and time-varying magnetotelluric effects get) is still only a 2% effect and (because of the ADCP referencing) does not touch the depth-averaged component.

ϵ_{w_p} contributes to a sizeable term which can affect the magnetic north component but is probably less likely to vary considerably with depth. In addition, the multiplication by a factor of $\frac{F_h}{F_z}$ reduces the impact in the high latitudes, where F_z is much greater than F_h. In the Denmark Strait, an unanticipated change in fall rate of 1% produces approximately $0.01\,\mathrm{m\,s^{-1}}$velocity error.

ϵ_s will affect the *magnitude* of velocity measured and so does not itself have to change during the fall in order to produce errors. If shear is large, the resulting velocity change will be multiplied by the percent uncertainty in s, which might be substantial (a few %) due to the small size of s to begin with.

ϵ_{C_1} has not been well quantified except to the extent that different idealized analytical instrument shapes have been compared to give differences on the order of 0.1 [*Sanford et al.*, 1978]. Like ϵ_s, ϵ_{C_1} is unlikely to change during the course of a drop and probably has remained the same since Sippican started building the XCP. It has the potential to affect the observed shear in proportion to its magnitude relative to $1 + C_1$ ($\approx 5\%$), but the historically favorable agreement observed between the XCP and other velocity profiling methods may indicate that C_1 is, in fact, better constrained than this.

ϵ_{C_2} is probably even less well known than ϵ_{C_1}, but has less of an impact. Like ϵ_{C_1}, ϵ_{C_2} has probably been constant since the current configuration of the XCP probe was designed. However, the resulting error in the magnetic north velocity component is only on the order of $5 \times 10^{-4}\,\mathrm{m\,s^{-1}}$, due to the combined effects of the small change in w_p and the small magnitude of the term in which C_2 appears.

$\epsilon_{\Delta\phi}$ is probably component of the XCP that has been the subject of the most research, for obvious reasons. The quality of the signal depends very much on ability of the probe to hold a steady rotation rate, but errors of this kind are usually obvious. A significant possibility is the existence of non-oceanic electrical fields (for example, due to geomagnetic storm activity). In some situations these can be quite large (see Appendix A). Additional discussion of XCP error sources can be found in *Sanford et al.* [1982].

Net errors in the results are calculated somewhat differently depending on the desired resulting product, and the processing steps that go into it:

Each ADCP profile measures $v_{wat}(z)$ and can contain contributions from ϵ_{ADCP}, ϵ_{GPS}, ϵ_{gyro}, ϵ_{ADU} and ϵ_{mount}. Examples are shown in Section 2.5.2.

Each XCP profile of v_{abs} has contributions from all error quantities in Table 2.4 (where ocean variability also contributes over a 7-min or 15-min period while computing v_{wat} but then is reduced while fitting to the XCP profile in forming $\bar{v}^*$).

Each section has contributions from ϵ_{ADCP}, ϵ_{GPS}, ϵ_{ADU} and the various XCP constituents (combined and propagated via a formula for errors in trapezoidal integration), ϵ_{mount} (accumulated by direct integration because of its single-signed, though uncertain, nature), ϵ_{interp} and ϵ_{extrap} (quantities depending on the parameters used in the objective mapping of the data into regions near the bottom and extrapolation beyond the ends of the section).

An ensemble of sections contains contributions from each of the random error sources in each section, added in quadrature, as well as from ϵ_{mount}, added or subtracted depending on the direction of travel of each section.

2.5.4 Techniques Used

XCP velocity referencing is carried out by the MatLab script `xcpabs.m` (and later modified to `rtabs.m` for real-time operation on the RRS *Discovery* cruise to the Faroe Bank Channel in June 2000).

The primary tricky issues for estimating $\bar{v}^*$ in practice are: 1) determining the ship's velocity from discrete, noisy GPS positions; 2) deciding what averaging interval of noisy ADCP data is most appropriate for comparing to the instantaneous XCP profile; and 3) picking the depth interval of overlap for differencing the XCP and ADCP profiles. It is preferable to be able to allow for temporally and spatially-varying levels of error in all measurements.

In order to use as much available information as possible, while not being adversely affected by lower-quality data, a procedure of weighted averaging and least-squares fitting has been adopted. The weighted average ${}^{w}\overline{x}$ of a set of values x_i is found by:

$$ {}^{w}\overline{x} = \frac{\sum_i x_i \omega_i}{\sum_i \omega_i} \tag{2.51} $$

where ω_i are the weights corresponding to each data value. Larger values of ω will cause the corresponding x value to count more strongly towards the final average. In contrast, the weighted least-squares formalism assigns values of "known covariance" (or error estimates) to each data value, effectively creating an inverse weighting. The matrix formulation of the least squares problem solves for X in

$$ \mathsf{A}X = B + E, \tag{2.52} $$

where E is a normally-distributed, zero-mean error term. In general, B represents a column vector of data values and X represents the coefficients of the linear combination of columns of A that best reproduces B. The standard solution, $X = \mathsf{A}^{-1}B$ assumes a uniform error covariance in E. If the covariance of E is known to be C, then the solution is:

$$ X = (\mathsf{A}^T\mathsf{C}^{-1}\mathsf{A})^{-1}\mathsf{A}^T\mathsf{C}^{-1}B \tag{2.53} $$

In practice, this is performed by the MatLab function `lscov`, which finds the solution without actually inverting C.

2.5.5 Operations and Error Computations

The operations on raw data from the XCP, ADCP, GPS and ADU instruments on the *Poseidon* procede as follows (using only the geographical east-west component, u, for illustration):

1. GPS positions (x_{GPS}) from a single-antenna Ashtech 3DF with differential beacon receiver were recorded every second, along with diagnostics such as age (the time since the last update from the DGPS beacon), beacon status (available or not) and horizontal and vertical error estimates (`herr` and `verr`, from the residuals of the overdetermined position when more than 4 satellites are present). A

linear fit (weighted by the estimated error of each position) to GPS 1-sec positions *vs.* time is used to determine 1-min averages of ship velocity (u_{GPS}). The corresponding quantities from Equation 2.52 (dropping the "GPS" from x_{GPS}) are then:

$$\mathrm{A} = \begin{bmatrix} \vdots & \vdots \\ t_i & 1 \\ \vdots & \vdots \end{bmatrix}, B = \begin{bmatrix} \vdots \\ x_i \\ \vdots \end{bmatrix}, \mathrm{C} = \begin{bmatrix} \ddots & & 0 \\ & c_i & \\ 0 & & \ddots \end{bmatrix} \text{ and } X = \begin{bmatrix} u_{\mathrm{GPS}} & x_0 \end{bmatrix}.$$

The quantity minimized is simply

$$\sum_i \frac{(x_p - x_i)^2}{c_i},$$

where $x_p = u_{\mathrm{GPS}} t_i + x_0$ is the position predicted by the linear fit.

The covariance values, c_i, are determined from herr, verr, age and the beacon status, according to the following formula:

$$c_i = \mathrm{herr}_i^2 + \left(\frac{\mathrm{verr}_i}{2}\right)^2 + e_i^2 + 0.25(\mathrm{age}_i - 20)^2, \tag{2.54}$$

where age has been converted to distance via an estimated effective wander rate of $0.5\,\mathrm{m\,s^{-1}}$ for fixes older than 20 s and

$$e_i = \begin{cases} 100\,\mathrm{m} & \text{if no DGPS beacon available, or} \\ 0\,\mathrm{m} & \text{if DGPS available.} \end{cases} \tag{2.55}$$

An example of this linear fitting is shown in Figure 2.17, which includes just over 2 minutes' worth of GPS fixes (color-coded according to the covariance, c_i, used in the least-squares weighting) along with lines of constant velocity determined by the fit.

7-min PACE

With the customized constellation of the PACE data, quality is less of an issue but the weighted fitting is used nonetheless. The quantities used to determine c_i in this case are the standard deviations of N-S and E-W position, `sdlat` and `sdlon` (in meters), output by the wide-area differential processing:

$$c_i = \mathrm{sdlat}_i^2 + \mathrm{sdlat}_i^2 \tag{2.56}$$

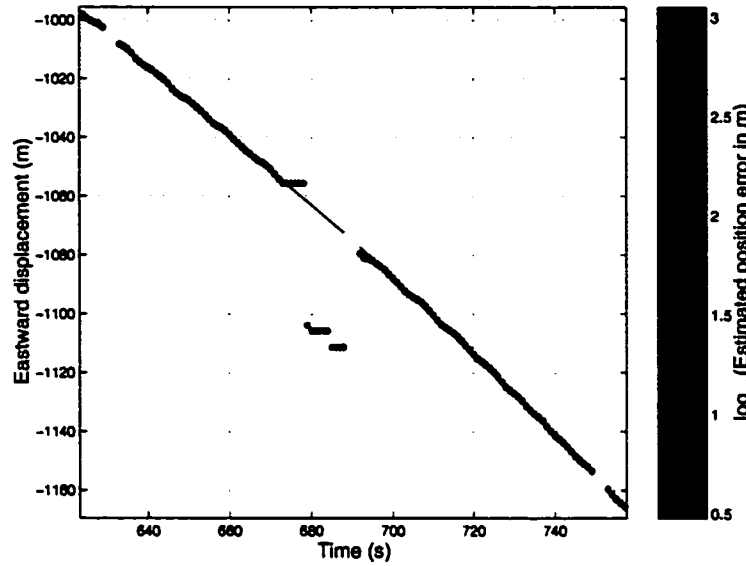


Figure 2.17: Illustration of velocity determination method about 10 min after XCP 4135. GPS fixes (longitude only, converted into meters) are plotted vs. time and color coded by log(c), where c is the covariance estimate used in the least-squares fitting. Black lines indicate the uniform velocity determined for each interval.

In the case of missing differential data, `sdlat` and `sdlon` are each set to 1000 m (effectively removing those uncorrected points from consideration), while if c_i is below a noise threshold of 9 m^2, it is set equal to the threshold value.

Errors

Standard error values are output by the MatLab `lscov` function, and are similar to those derived from the formula for the error of a linear fit, except that they incorporate the covariance weighting. The standard error in slope (u) of a linear least-squares fit of a straight line to N values of position (x_i) *vs.* time (t_i) is given by *Press et al.* [1995]:

$$\epsilon_u = \sqrt{\left(\frac{N}{N\sum_{i=1}^{N} t_i^2 - \left(\sum_{i=1}^{N} t_i\right)^2}\right)\left(\frac{\sum_{i=1}^{N} r_i^2}{N-2}\right)} \tag{2.57}$$

where $\sum_{i=1}^{N} r_i^2$ is the quantity being minimized in the fit, *i.e.*, the sum of the squared residuals, r_i, after the straight line has been subtracted from the data.

For example, the errors thus derived in the two 1-minute fits shown in Figure 2.17 are $0.1450\,\mathrm{m\,s^{-1}}$ and $0.0063\,\mathrm{m\,s^{-1}}$ (all of the bad points are in the first interval), while the `lscov` error output values (which downweight the bad points) are $0.0060\,\mathrm{m\,s^{-1}}$ and $0.0063\,\mathrm{m\,s^{-1}}$, respectively.

2. VM-ADCP velocities were recorded in one-minute averages output by the DAS software with Eric Firing's UE4 enhancement. The DAS/UE4 program uses the vessel's gyrocompass to rotate pings (every second) into earth coordinates before averaging these together. As described in Section 2.5.2, the 1-min ADCP ensemble velocities are rotated clockwise by

$$\varphi_{\mathrm{corr}} = \overline{\varphi_{\mathrm{A-G}}} + \varphi_{\mathrm{mount}}, \tag{2.58}$$

where $\overline{\varphi_{\mathrm{A-G}}}$ (given by UE4) is the 1-min averaged difference between the ADU and gyrocompass headings and φ_{mount} is the difference in mounting angle between the ADCP and ADU sensors, determined using bottom track data. Rotated ADCP velocities are then added to the ship velocity determined above to get absolute water velocity.

Errors

The error in φ_{mount} can be estimated by combining independent estimates, as shown in Figure 2.16. This gives a standard error ($\epsilon_{\mathrm{mount}}$) of 0.6 mrad, as presented in Table 2.4.

ϵ_{φ_r}, the error in $\overline{\varphi_{\mathrm{A-G}}}$ is more difficult to estimate, combining, as it does, errors in ADU and gyrocompass heading. The assumption is that the ADU measures heading perfectly and that $\overline{\varphi_{\mathrm{A-G}}}$ is simply a measure of gyro error which will be removed by the rotation. In reality, there must be *some* error in the ADU measurement (on the order of 1 mrad), and there is also a possibility that the value could become biased by the wild-point editing used in constructing the average from individual $\varphi_{\mathrm{A-G}}$ measurements. This editing attempts to throw out outliers but during periods of acceleration or turning might remove data of one sign more than the other.

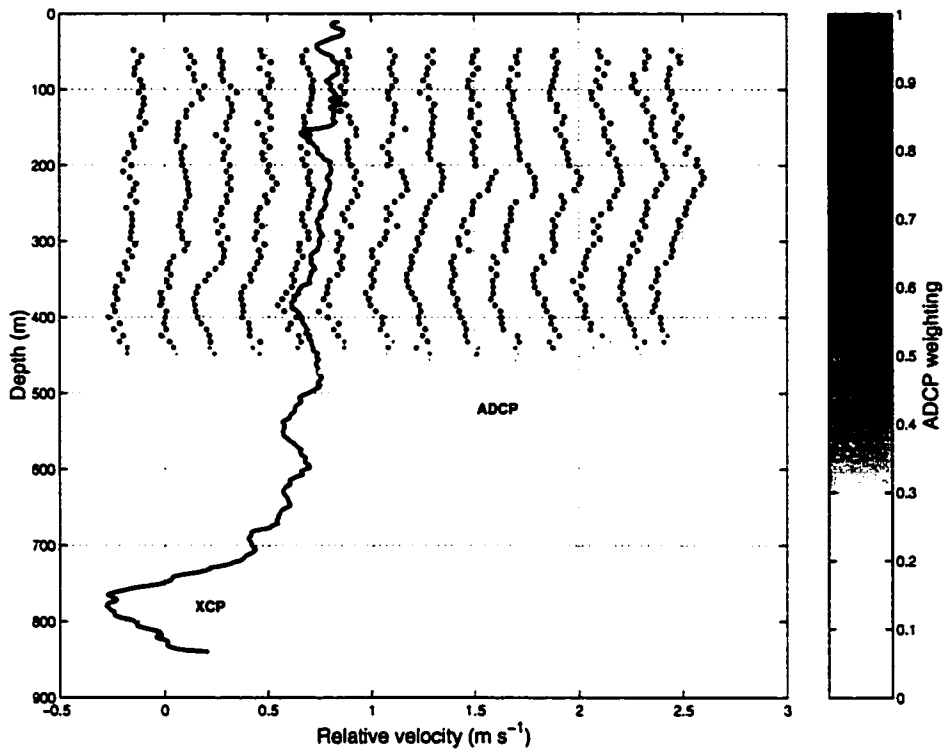


Figure 2.18: East component of relative velocity measured by XCP 4135 along with 1-min averages of ADCP east component from 5 min before until 10 min after the XCP drop (staggered sequentially by $0.2\,\mathrm{m\,s^{-1}}$). Color-coding indicates the weighting given the ADCP data when these are combined to form a single mean profile. Some of the ADCP variation over the 15 minutes does appear to be due to oceanic variability. This particular XCP extends into the strong velocity layer of the overflow, illustrating the importance of the full water column measurement. Note also the matching of many of the features between the XCP and ADCP measurements. This degree of similarity is seen in most of the XCP/ADCP comparisons.

3. 1-min absolute ADCP water velocities (u_{wat}) over the 15-min period surrounding each XCP drop (Figure 2.18) are combined into a single weighted mean profile (u_{watX}). Data are weighted according to the estimated error in the GPS fit of ship velocity and the ADCP's `percent good` (`%gd`) variable, derived from the single-ping signal-to-noise ratios:

$$\omega = \left(\frac{\%\mathrm{gd} - 25}{100 - 25}\right)\left(\frac{0.2 - \sqrt{\epsilon_u^2 + \epsilon_v^2}}{0.2 - 0.005}\right) \tag{2.59}$$

where ϵ_u and ϵ_v are the estimated u and v errors determined from the weighted least-squares fit in operation 1, above.

Errors

The error in the weighted mean profile is estimated by constructing a profile of "weighted RMS" for the 15-minute interval:

$$\texttt{UwatWRms} = \sqrt{\frac{\sum_i (u_{\text{wat},i} - u_{\text{watX}})^2 \omega_i}{\sum_i \omega_i}}. \tag{2.60}$$

The quantity `UwatWRms` is, in turn, used in the weighting of the ADCP data for comparison with the XCP profile.

4. The XCP velocity profile (u_{EF}) is rotated from geomagnetic to geographical coordinates using the `geomag` routine to interpolate from the IGRF90 geomagnetic field model.

5. The amount to shift the XCP profile to best match the averaged absolute ADCP is the quantity $\bar{u}^*$. This is now determined by minimizing the squared differences between u_{EF} and u_{watX}, weighted by estimated error, over the range from 40 m down to 500 m (or 85% of the bottom depth, whichever is less) as shown in Figure 2.19. The method is to again solve Equation 2.52 with the corresponding matrices being:

$$\mathsf{A} = \begin{bmatrix} \vdots \\ 1 \\ \vdots \end{bmatrix}, B = \begin{bmatrix} \vdots \\ (u_{\text{watX}} - u_{\text{EF}})_j \\ \vdots \end{bmatrix}, \mathsf{C} = \begin{bmatrix} \ddots & & 0 \\ & c_j & \\ 0 & & \ddots \end{bmatrix} \text{ and } X = \begin{bmatrix} \bar{u}^* \end{bmatrix}.$$

Now j indexes over depth and the covariances, c_j, are derived from `UwatWRms`, the (weighted) RMS of ADCP ensemble velocities, and N, the number of ensembles used, in operation 3, along with `xverr`, the XCP error velocity:

$$c = \frac{\texttt{UwatWRms}^2}{\sqrt{N}} + \texttt{xverr}^2 \tag{2.61}$$

In fact, this is identical to finding $\bar{u}^*$ using a weighted mean of $(u_{\text{watX}} - u_{\text{EF}})_j$ with the weights equal to $1/c_j$.

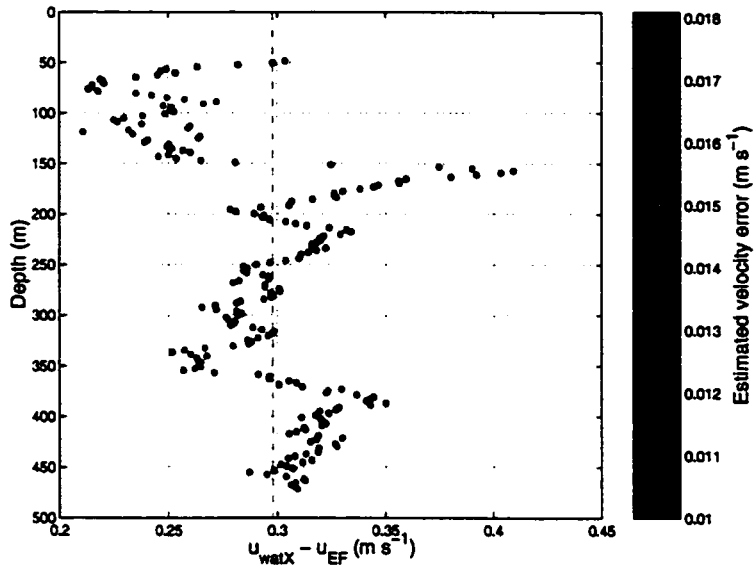


Figure 2.19: Profile of ADCP minus XCP 4135 velocity (east-west component only), color-coded by error estimates used in determining the final value (dashed line) by minimizing the RMS deviation weighted by the known covariances.

Errors

The uncertainty in $\bar{u}^*$ can be estimated from the standard deviation of the $u_{watX} - u_{EF}$ variations with depth. This is the quantity presented in Table 2.5 as `UVbsRms` (where the u and v components have been added in quadrature).

2.5.6 *Final Error Estimate*

The final product, then, is a profile of absolute velocity with the XCP's full range and resolution:

$$u_{abs} = u_{EF} + \bar{u}^* \tag{2.62}$$

As pointed out in Section 2.5.3, the final error estimate is constructed differently for individual profiles than for sections and ensembles of sections, partly due to the different treatment required of possible bias error in the ADCP mounting angle. The final uncertainty in each velocity profile can be estimated in two ways: either by propagating the uncertainty in the constituent measurements through the operations de-

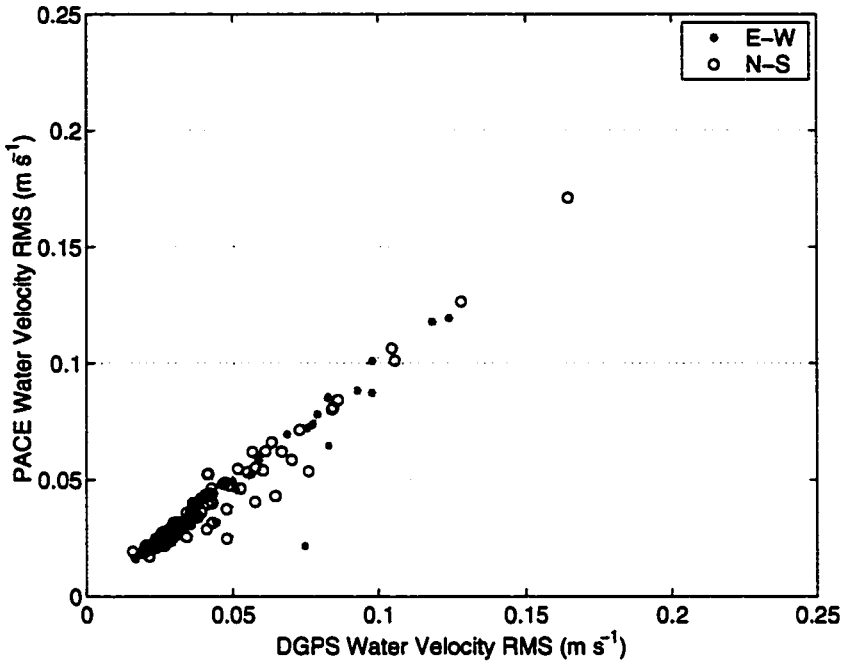


Figure 2.20: Scatter in reference-layer water velocities over the 7 minutes (7 samples of 1 minute duration each) surrounding each XCP drop (`UVwatWRms`). Velocity deviations have been weighted according to GPS quality determined from other parameters.

scribed above (and in equations 2.37–2.47) or by using the scatter in averaged quantities (operations 3 and 5, above) as an estimate of uncertainty. In fact, a number of situations exist in which we can compare estimates made in these two ways.

For example, the scatter of water velocities over the 7 minutes surrounding each drop (in Figure 2.20 and Table 2.5) can be compared with the expected uncertainty in each of these estimates. (Averages of some of these are presented in Table 2.6.) For the most part, the RMS of the measurements is substantially larger than the expected variance, which may be a result of the "red" nature of oceanic velocities, but may also indicate an underestimate of the true uncertainty in our velocity measurements.

2.5.7 *Remaining inconsistencies*

Diagnostics computed during the XCP/ADCP referencing procedure (shown in Table 2.5) can help identify which profiles are more trustworthy than others, as well as the possible sources of error. `UVbsRms` indicates the quality of the fit between ADCP and XCP profiles. A high `UVbsRms` could indicate the presence of magnetotelluric contamination in the XCP or some sort of depth-dependent ADCP error. `UVwatWRms` (u and v contributions to the weighted RMS of ADCP/GPS absolute water velocity added in quadrature) measures the apparent water velocity jitter and is a prime estimate of GPS reliability but could also indicate ADCP problems or simply be a record of naturally-occurring oceanic variability.

Table 2.5: Diagnostic statistics to evaluate all XCPs.

XCP #	St #	P/D	UVwatWRms	UVbsRms	ErrGPS	ErrADCP
4101	452	D	$0.068\,\mathrm{m\,s^{-1}}$	$0.021\,\mathrm{m\,s^{-1}}$	$0.004\,\mathrm{m\,s^{-1}}$	$0.022\,\mathrm{m\,s^{-1}}$
4102	453	P	0.041	0.024	0.005	0.023
4103	454	P	0.034	0.020	0.005	0.020
4104	455	P	0.039	0.026	0.002	0.022
4105	456	D	0.093	0.026	0.004	0.023
4106	457	P	0.038	0.046	0.003	0.024
4107	458	P	0.034	0.044	0.002	0.025
4108	459	D	0.058	0.034	0.002	0.023
4109	468	P	0.095	0.030	0.004	0.038
4110	469	P	0.129	0.113	0.003	0.045
4111	470	P	0.143	0.122	0.005	0.051
4112	471	P	0.139	0.075	0.005	0.045
4113	472	P	0.093	0.060	0.006	0.043
4114	473	D	0.157	0.082	0.005	0.042
4115	474	P	0.122	0.123	0.009	0.037
4116	475	D	0.184	0.101	0.005	0.041
4117	—	D	—	—	—	—
4118	476	P	0.132	0.058	0.011	0.043
4119	477	D	0.085	0.023	0.003	0.030

(continued)

XCP #	St #	P/D	UVwatWRms	UVbsRms	ErrGPS	ErrADCP
4120	478	P	0.048	0.033	0.006	0.027
4121	479	P	0.080	0.110	0.006	0.030
4122	—	D	—	—	—	—
4123	480	P	0.053	0.182	0.004	0.039
4124	481	P	0.091	0.050	0.003	0.027
4125	482	D	0.085	0.056	0.004	0.028
4126	483	P	0.042	0.081	0.004	0.026
4127	484	P	0.045	0.095	0.007	0.027
4128	485	P	0.079	0.040	0.008	0.025
4129	486	D	0.059	0.039	0.003	0.026
4130	487	D	0.073	0.032	0.005	0.026
4131	488	P	0.048	0.061	0.004	0.025
4132	489	P	0.042	0.035	0.005	0.028
4133	490	P	0.031	0.102	0.002	0.023
4134	491	P	0.046	0.066	0.006	0.024
4135	492	D	0.050	0.060	0.003	0.023
4136	493	D	0.075	0.062	0.005	0.023
4137	494	D	0.043	0.045	0.003	0.023
4138	495	D	0.136	0.058	0.005	0.027
4139	496	D	0.069	0.040	0.004	0.026
4140	497	P	0.041	0.041	0.004	0.024
4141	498	D	0.186	0.049	0.016	0.022
4142	499	P	0.036	0.062	0.004	0.025
4143	500	P	0.050	0.062	0.002	0.025
4144	501	P	0.093	0.044	0.011	0.022
4145	502	D	0.143	0.048	0.005	0.026
4146	503	P	0.032	0.041	0.005	0.022
4147	504	P	0.039	0.053	0.005	0.030
4148	505	P	0.044	0.032	0.004	0.026

(continued)

XCP #	St #	P/D	UVwatWRms	UVbsRms	ErrGPS	ErrADCP
4149	506	P	0.045	0.032	0.005	0.025
4150	507	P	0.032	0.031	0.003	0.026
4151	508	P	0.041	0.045	0.006	0.024
4152	509	P	0.288	0.031	0.004	0.029
4153	514	P	0.045	0.060	0.004	0.026
4154	517	P	0.035	0.055	0.001	0.030
4155	999	P	0.043	0.048	0.001	0.035
4156	518	P	0.033	0.040	0.004	0.030
4157	520	D	0.085	0.041	0.005	0.028
4158	521	P	0.063	0.054	0.004	0.025
4159	522	P	0.036	0.065	0.004	0.026
4160	523	P	0.032	0.030	0.004	0.027
4161	524	P	0.030	0.050	0.006	0.026
4162	525	P	0.040	0.057	0.005	0.026
4163	526	P	0.037	0.073	0.004	0.026
4164	527	D	0.137	0.090	0.012	0.029
4165	528	D	0.156	0.057	0.013	0.031
4166	529	D	0.102	0.069	0.004	0.043
4167	530	D	0.159	0.092	0.004	0.031
4168	531	P	0.070	0.058	0.004	0.033
4169	532	D	0.081	0.051	0.004	0.031
4170	533	P	0.067	0.059	0.004	0.028
4171	534	P	0.153	0.090	0.013	0.039
4172	535	D	0.093	0.088	0.003	0.034
4173	536	P	0.075	0.087	0.005	0.031
4174	537	P	0.054	0.044	0.005	0.031
4175	538	P	0.072	0.037	0.006	0.032
4176	539	P	0.061	0.042	0.004	0.028
4177	540	P	0.063	0.076	0.005	0.027

(continued)

XCP #	St #	P/D	UVwatWRms	UVbsRms	ErrGPS	ErrADCP
4178	541	P	0.088	0.148	0.007	0.033
4179	542	P	0.076	0.073	0.006	0.031
4180	543	D	0.108	0.057	0.006	0.028
4181	544	P	0.063	0.058	0.005	0.025
4182	545	P	0.072	0.123	0.004	0.030
4183	546	P	0.081	0.057	0.008	0.028
4184	547	P	0.066	0.057	0.004	0.026
4185	548	P	0.063	0.059	0.005	0.028
4186	549	D	0.565	0.035	0.009	0.024
4187	550	D	0.107	0.035	0.009	0.026
4188	551	P	0.095	0.071	0.004	0.027
4189	552	P	0.052	0.060	0.004	0.028
4190	—	D	—	—	—	—
4191	553	D	0.128	0.038	0.006	0.028
4192	554	P	0.052	0.045	0.005	0.026
4193	555	D	0.124	0.054	0.005	0.031
4194	556	D	0.113	0.036	0.005	0.027
4195	557	P	0.063	0.040	0.003	0.027
4196	558	P	0.042	0.020	0.002	0.024
4197	560	P	0.054	0.168	0.005	0.022
4198	563	P	0.031	0.032	0.004	0.023
4199	565	D	0.062	0.047	0.002	0.022
4200	566	D	0.046	0.034	0.002	0.020
4201	567	P	0.027	0.027	0.003	0.022
4202	568	P	0.023	0.019	0.002	0.022
4203	569	D	0.119	0.053	0.004	0.023
4204	570	P	0.037	0.023	0.005	0.021
4205	571	D	0.115	0.025	0.004	0.024
4206	573	D	0.118	0.049	0.003	0.032

(continued)

XCP #	St #	P/D	UVwatWRms	UVbsRms	ErrGPS	ErrADCP
4207	—	D	—	—	—	—
4208	582	P	0.033	0.034	0.003	0.023
4209	583	P	0.036	0.021	0.002	0.023
4210	584	D	0.177	0.065	0.005	0.025

Notes: P/D column indicates whether the GPS used was from a 7-min PACE custom constellation or from 15-min of DGPS data. UVwatWRms estimates water velocity scatter. UVbsRms estimates the XCP/ADCP fit quality.

Table 2.6: Average statistics for XCP absolute velocity.

processing #	UVwatWRms	UVbsRms	UErrGPS	UErrADCP
PACE	$0.063\,m\,s^{-1}$	$0.060\,m\,s^{-1}$	$0.005\,m\,s^{-1}$	$0.028\,m\,s^{-1}$
DGPS	0.119	0.051	0.005	0.028
all	0.081	0.057	0.005	0.028

Notes: Values are averaged from quantities in Table 2.5

2.6 Combining XCP and ADCP for data visualization

In order to take advantage of both the high spatial resolution of the shipboard ADCP in the upper water column and the full-depth capability of the XCP, I have found it useful to construct velocity sections by combining the two. Since the absolute XCP profiles have already been referenced to the ADCP in the upper layer, there is little need to preserve the independent character of the measurements there. Instead I have simply used the ADCP at high resolution in the upper 300–400 m of the water column and the XCP below this depth.

The dominant variability in both ADCP and XCP velocity sections seems to be barotropic, meaning that it requires only GPS-referenced ADCP data. However, bottom-intensified flows do play a role at times, necessitating the full water-column XCP profiles. In order to be able to take advantage of the full horizontal resolution of the ADCP while still including XCP shears below ADCP range, I have treated barotropic and baroclinic parts independently, as shown in Figure 2.21.

First, each velocity field is separated into a reference layer velocity (the average between 100 and 300 meters depth), and residual (baroclinic) velocity.

$$v_{\mathrm{XCP}}(x,z) = v_{\mathrm{XCP,refl}}(x) + v_{\mathrm{XCP,BC}}(x,z) \tag{2.63}$$

and

$$v_{\mathrm{ADCP}}(x,z) = v_{\mathrm{ADCP,refl}}(x) + v_{\mathrm{ADCP,BC}}(x,z). \tag{2.64}$$

The baroclinic XCP velocity is interpolated by objective mapping to fill in the spaces between profiles, yielding $\overline{v_{\mathrm{XCP,BC}}(x,z)}$, where the overbar will be used to indicate smoothed quantities. The choice of correlation scales used in this mapping has some effect on the outcome, primarily determining whether features tend to spread horizontally or vertically. In general, more vertical spreading appears to work better (again making the section appear more barotropic, even with the reference layer removed), but this can lead to losing the signature of XCP shear a short horizontal distance away. In some cases, the situation is complicated by sloping topography—it appears that isotachs or at least isopycnals should tend to follow the topography, but most interpolation methods don't want to do this, preferring vertical and horizontal operation.

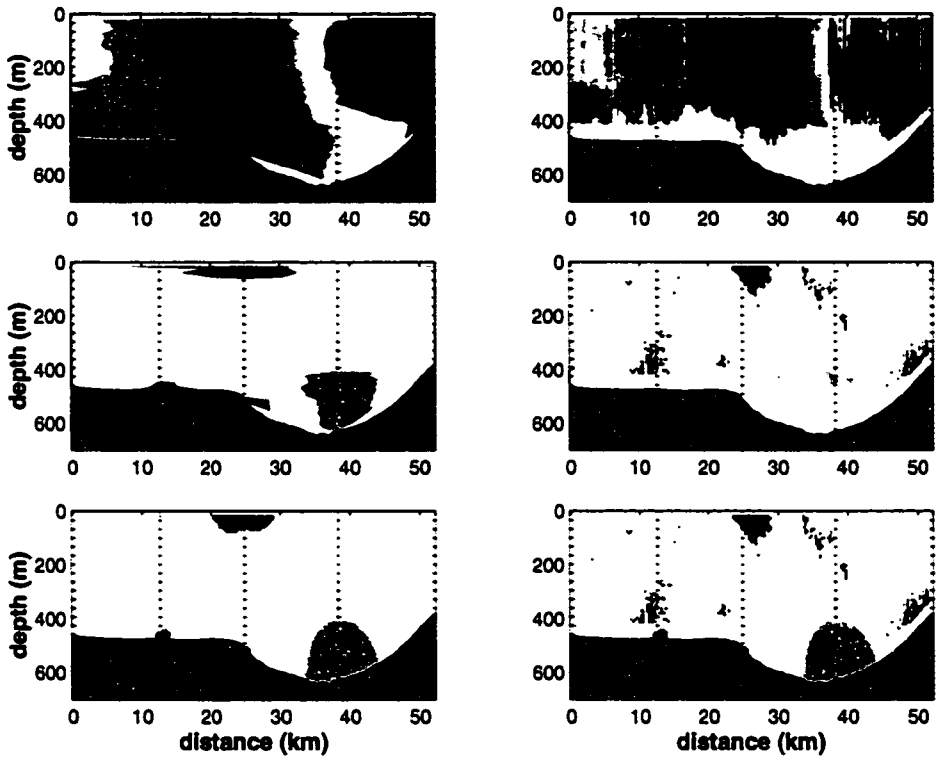


Figure 2.21: A) v_{XCP}; B) v_{ADCP}; C) $v_{XCP,BC}$; D) $v_{ADCP,BC}$; E) objectively-mapped $v_{XCP,BC}$; F) merged baroclinic fields. Panel A illustrates some of the difficulties in the use of widely-spaced measurements over variable topography. The algorithm interpolates between the bottom-most values but the resulting contours appear unrealistic. The addition of the higher-resolution barotropic velocity from the ADCP (panel B) does seem to sharpen gradients (see Figure 2.22)

The interpolated XCP baroclinic field is generally quite similar to the ADCP field, so I chose to simply make a mosaic: use the ADCP values where available, interpolated XCP everywhere else. This causes some discontinuities at the bottom of the ADCP range, but they are luckily fairly small. At this point, one option would be to smooth the mosaicked field, either along each profile or with some 2-D method such as another objective mapping, but this would lead to additional loss of resolution and so has not been done.

The reference layer velocity looks pretty noisy at this point so I decided to smooth it with a 10-minute boxcar applied using the MatLab function `filtfilt`, which effectively gives a 20-minute triangular filter, since it runs the filter (convolution) twice.

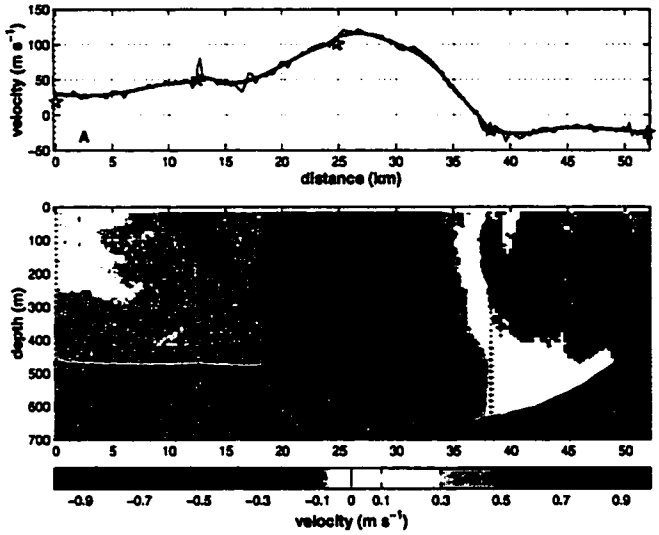


Figure 2.22: A) Reference layer velocity from ADCP (black line) and XCP (blue stars) profiles, along with smoothed version (red line); and B) final velocity section after adding smoothed $v_{\mathrm{ADCP,refl}}$ back into the combined field of Figure 2.21F.

This removes variability up to about a 5-km scale at the ship speeds generally used. I picked the filter length because a spectrum of reference layer velocity seems to have a noise floor at shorter than about 30 minute periods. The smoothed velocity is then added back into the combined XCP/ADCP residual field to get the final product (shown in Figure 2.22):

$$v_{\mathrm{final}}(x,z) = \overline{v_{\mathrm{ADCP,refl}}(x)} + \begin{cases} v_{\mathrm{ADCP,BC}}(x,z) & \text{where ADCP available} \\ \overline{v_{\mathrm{XCP,BC}}(x,z)} & \text{where no ADCP.} \end{cases} \tag{2.65}$$

The resulting section appears to retain the dominantly barotropic variability present in the original data as well as additional features provided by the full-depth XCPs. Although some discontinuities are evident, and the deep values are clearly smoother than the points within ADCP range, the final sections look reasonable.

Density contours were added to the plots using XCTD profiles. Each profile was sorted (since any inversions captured by the XCTD are probably just noise) and below-bottom points were filled with the densest value in preparation for contouring. The fields were then contoured using the default MatLab contouring program, which uses

linear interpolation. The resulting shapes of the contours between profiles are perhaps not what would be drawn by a skilled manual contour artist, but do appear to represent the data correctly.

Errors

The error values were derived by combining the noise present in the GPS, ADCP and XCP data with uncertainties obtained by using a range of interpolation and extrapolation parameters in the calculations. In general, the interpolation of velocity below ADCP range and between XCP drops tended to give an overestimate of transport when a larger horizontal correlation scale was used, and an underestimate with a larger vertical scale. In addition, sections which contained a non-zero transport of dense water at one or both ends were linearly interpolated to zero at some distance, estimating the unsampled portion of flow beyond the section. Using extreme values of vertical to horizontal correlation scale ratio differing by a factor of 100 and extrapolation scale ranging from 0 to 20 km gives ranges of transports attributable to different interpolation and extrapolation choices. Arbitrarily taking these extreme ranges as 95% confidence intervals, I have chosen to divide each by 4 to generate 1σ uncertainty estimates (so that $\pm 2\sigma$ returns the 95% confidence) and add them as uncorrelated errors. For most of the sections, this combined interpolation/extrapolation error is much larger than that estimated from instrumental RMS values, and in a few cases (XO2, XO3) the magnitudes are comparable.

2.7 Estimating Bottom Stress

Bottom stress is an important parameter affecting the path and speed of a bottom-intensified flow. In the DSO, where instantaneous near-bottom velocities often reach over $1\,\mathrm{m\,s^{-1}}$, bottom drag may be substantial.

In the turbulent constant-stress layer (or "log layer") near the bottom, the velocity profile assumes the form

$$u(z) = \frac{u_*}{\kappa} \ln\left(\frac{z}{z_0}\right). \tag{2.66}$$

Here, u_* is the friction velocity, $\kappa = 0.4$ the von Kármán constant and z_0 the roughness length. A linear fit to a plot of observed u *vs.* $\ln z$, then, allows a determination of u_*

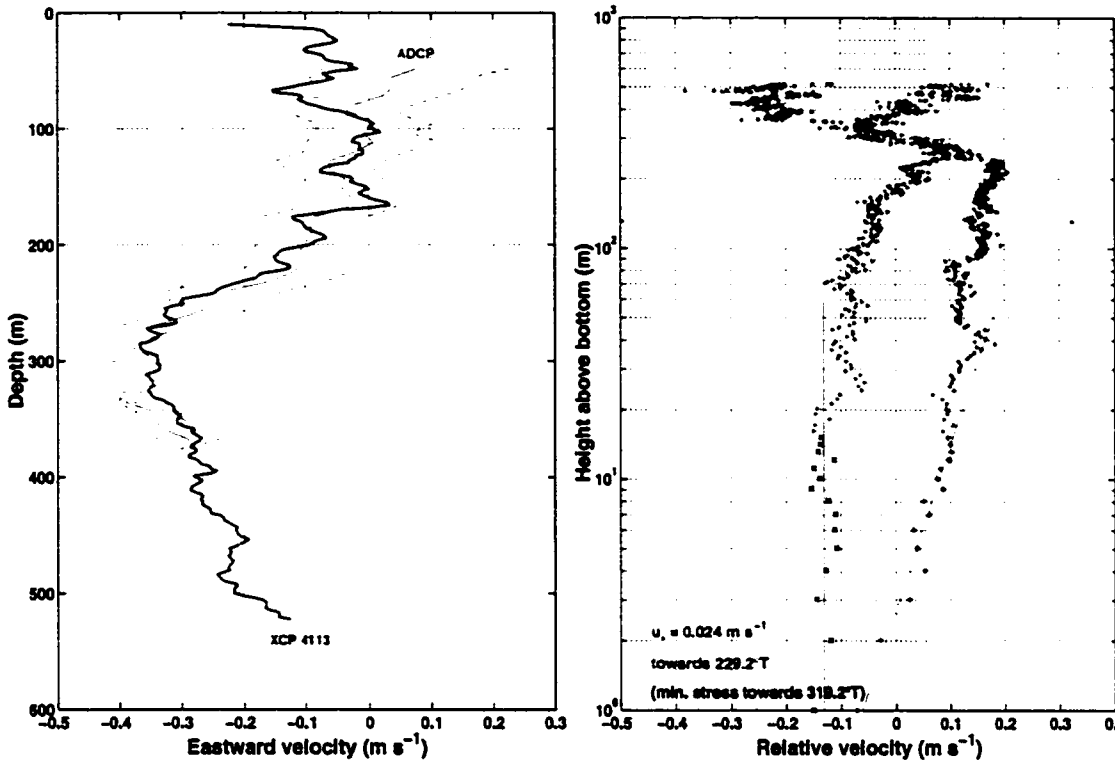


Figure 2.23: A sample profile showing the good match of XCP and ADCP velocities (left panel) and the logarithmic velocity fit to the bottom 15 m of the XCP (right panel). Both panels are from the same XCP drop (4113), but the left shows the (geographic) eastward component only while the right shows the components in the directions of maximum and minimum log-layer stress.

and, hence, shear stress ($\tau = \rho u_*^2$), as shown in Figure 2.23. The direction of the stress is determined by rotating the velocity components until all of the stress is in one component. Due to the velocity rotation in the planetary boundary layer, this direction is normally to the left of the maximum overlying velocity.

While theoretical and laboratory studies have derived the logarithmic velocity shape for time-averaged velocity profiles, rather than instantaneous ones, the technique has been successfully applied to XCP data a number of times, including in the Mediterranean Outflow [*Johnson et al.*, 1994] and the Faroe Bank Channel [*Johnson and Sanford*, 1992]. The reason for this success is attributed to the fact that, in general, deviations from the logarithmic shape should only be on the order of the magnitude of u_*, which is usually substantially smaller than the velocity range over the boundary layer. Figure 2.23 does appear to verify this.

The correct boundary layer height over which to fit remains the subject of some

debate. For example, *Sanford and Lien* [1999] have found systematic differences between stresses estimated from logarithmic fits over the 0–3 m layer *vs.* the 5–12 m layer, and suggest that the former is the "true" layer of boundary (or wall) turbulence while the latter is dominated by form drag and represents the actual force exerted by the bottom on the flow. If this is correct, 0–15 m should give an adequate value for estimating the energy balance of the overflow, and is thick enough so that the XCP yields a suitable number of points to fit.

Chapter 3

ARANDA EXPERIMENT

As a test of the suitability of XCP measurements to the Denmark Strait and in the hopes of getting a first look at the connection between overflow transport events, intermediate low-salinity patches, and cyclonic surface eddies, I made a set of velocity profiles (locations shown in Fig. 3.1) from the Finnish R/V *Aranda* during August 1997. Initial results from this survey were presented in a poster at the 1998 AGU Ocean Sciences meeting in San Diego [*Girton and Sanford*, 1998] and later presented in the International WOCE Newsletter [*Girton and Sanford*, 1999].

3.1 Cruise

The cruise was a part of both the Nordic WOCE effort and the European VEINS project, and included scientific teams from primarily Swedish and Finnish institutes. The chief scientists were Hannu Grönvall and Jouko Launiainen on two consecutive legs in the Denmark Strait. The major component of the cruise was a pattern of hydrographic stations including CTD and chemical tracers to span the extent of the overflowing plume and upstream basin. The CTD survey, led by Bert Rudels of the Finnish Institute for Marine Research and Peter Lundberg of Stockholm University, has been recently described by *Rudels et al.* [1999a].

For the purpose of providing improved ADCP data while underway, I installed a 4-antenna GPS array on the *Aranda* to measure heading, pitch and roll. The resulting correction to the ship's gyrocompass was similar in character and magnitude to that seen on other ships (see Figure 3.2). Water-track and bottom-track calibration methods gave consistent estimates for the constant mounting angle correction (only -2.5 milliradians, since the technical staff on the *Aranda* had apparently already entered a previously-determined calibration value into the Transect data acquisition program).

The weather and sea ice conditions during the cruise were extremely favorable,

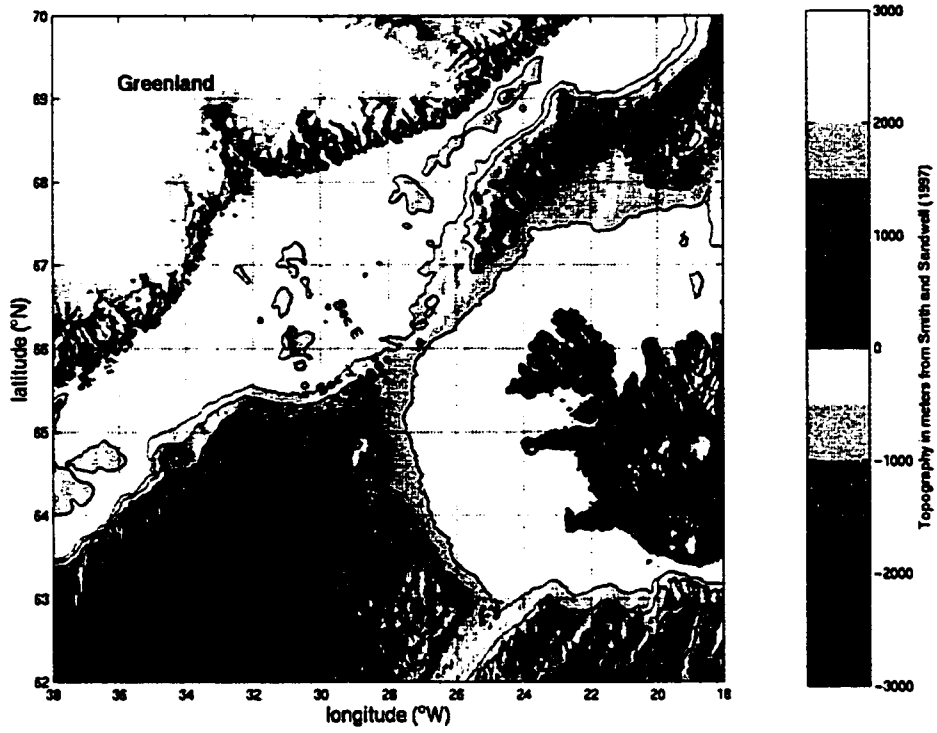


Figure 3.1: Locations of XCP sections from the *Aranda* cruise in August 1997. Water shallower than 500 m is shaded gray, and the 1000 m and 2000 m bathymetric contours from *Smith and Sandwell* [1997] are shown.

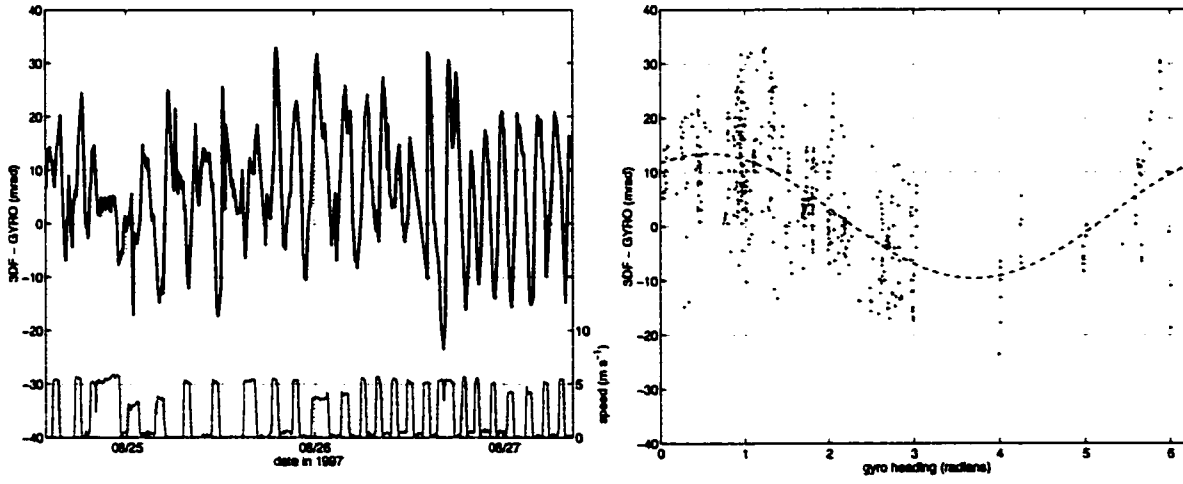


Figure 3.2: Difference between heading measured by multi-antenna GPS sensor (Ashtech 3DF) and ship's gyrocompass, plotted versus time and heading. The left-hand panel includes the ship's speed, illustrating the effect of accelerations on the gyro error. The right-hand panel also shows a best sinusoidal fit to the heading-dependent component.

with only one day lost to rough weather on my leg. This was fortunate, since the *Aranda* is not particularly suited to working in high winds and rough seas, as it is a smaller research vessel (60 m) with a low freeboard and an unusual enclosed CTD bay designed for comfortable working in very cold conditions, but leaving very little allowance for ship motion during instrument recovery. Other research vessels might have continued working in the 16 m s^{-1} winds that caused us to suspend operations, although the time lost was not excessive. In contrast to earlier cruises in the Denmark Strait that summer, no pack ice was sighted on the Greenland shelf, although several large icebergs did drift by.

3.2 Measurements

The basic theory of the expendable current profiler (XCP) has been described in Chapter 2, along with the methods used to generate a profile of absolute velocity. Only the ways in which the *Aranda* measurements differ from the standard procedure (as used on the *Poseidon*) will be described here.

In all, 22 of the 23 XCPs deployed from the *Aranda* returned usable data. The survey consisted of two sections across (D and E) and one along (J) the path of the overflow, as well as two additional profiles at the sill (Figure 3.1). The probes were deployed immediately before or immediately after CTD stations to allow comparisons between the velocity, temperature, salinity and density profiles. Section D was occupied first, moving offshore, followed by section J up the axis of the overflow and, finally, section E, also in the offshore direction. Sections D and E were separated by approximately 115 km in space and 40 hours in time. Repeated stations at the crossing points of the sections and at the sill give a hint as to the importance of time-variability, which can be considerable.

The fact that section J was occupied in the upstream direction implies that the wavelength of propagating features will be shortened by a ratio of:

$$\frac{\lambda_{\text{observed}}}{\lambda_{\text{original}}} = \frac{1}{1 + \frac{v_p}{v_s}}, \tag{3.1}$$

where v_p is the feature's propagation speed and v_s is the ship speed in the opposite direction. For example, with an upstream progress of 1.5–2 m s^{-1}, as applicable to J, a 100 km feature propagating at 0.5 m s^{-1} will shrink to 75–80 km in length. This

complication in interpretation becomes more difficult as the effective ship speed becomes comparable to or slower than the propagation speed, and especially difficult when the survey moves in the same direction as the flow.

The velocity measurements were referenced to the shipboard ADCP. However, since the quality of GPS and ADCP data was not quite as good as on the later *Poseidon* cruise, and since the survey was not done while continuously underway, the ADCP profile used for comparison to the XCP was the average of the absolute velocity over the time on station. In addition, a linear fit to the change over time of the average reference layer velocity (100–250 m) has been used to correct for the temporal separation between the XCP profile and the on-station measurements. This correction was rarely more than $0.05\,\mathrm{m\,s^{-1}}$, and, given the remaining ambiguities in referencing choices, produces a final velocity accuracy of $0.02\,\mathrm{m\,s^{-1}}$ or better.

3.3 Summary of Data

Contoured sections of temperature, salinity, density and velocity perpendicular to and parallel to each line are shown in Appendix B. T, S and v sections from the *Aranda* are also shown in Figure 3.3. They reveal the basic character of the DSO as a cold, dense layer flowing to the southwest beneath an interior of warm and salty Atlantic water (AW). Figure 3.4 illustrates the contrast between the AW and DSOW with a compilation of temperature profiles from the 22 XCPs, plotted over the envelope of temperature data from the OVERFLOW '73 (O73) expedition, the most comprehensive survey of the DSO to date.

At all depths below 200 m or so, water north of the sill is colder and denser than water at the same level south of the sill. The two XCPs at the sill span the range of available temperatures and provide the starting point for the descending overflow, which shows up as anomalously cold near-bottom water in the stations south of the sill. The speed of this bottom layer ranges from $0.3\,\mathrm{m\,s^{-1}}$ to $1\,\mathrm{m\,s^{-1}}$ and the thickness from 40 m to 400 m. Many of the largest overflow speeds and layer thicknesses were seen in conjunction with an overlying salinity minimum, indicating the presence of polar intermediate water (PIW, sometimes called upper Arctic intermediate water), distinct from the Arctic intermediate water (AIW) and Norwegian Sea deep water (NSW) which make up the bulk of the overflow. These three water types, shown

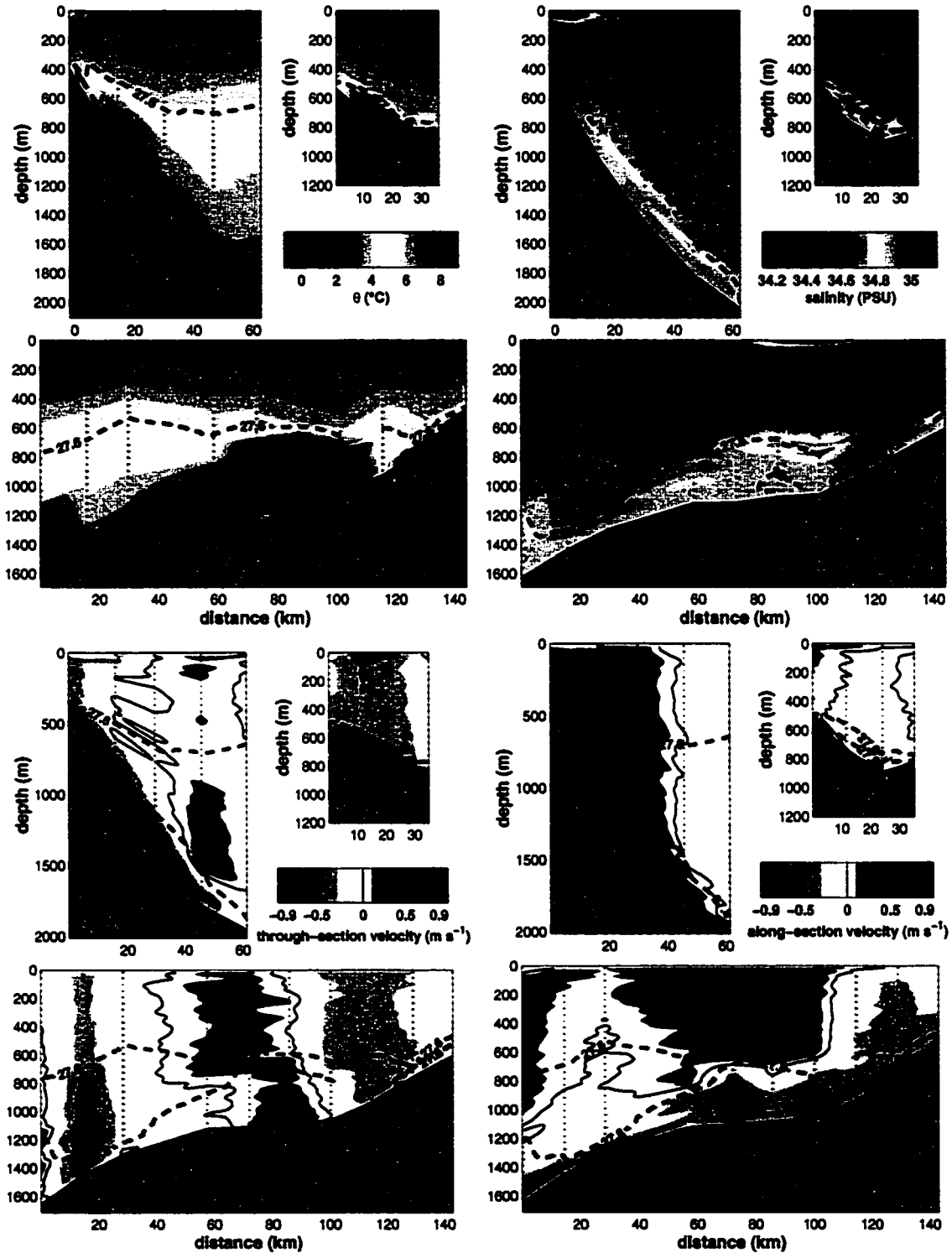


Figure 3.3: Temperature, salinity and velocity sections from the *Aranda* (locations shown in Figure 3.1). Sections D and E are shown looking to the northeast (upstream). Section J is shown looking to the northwest (towards Greenland).

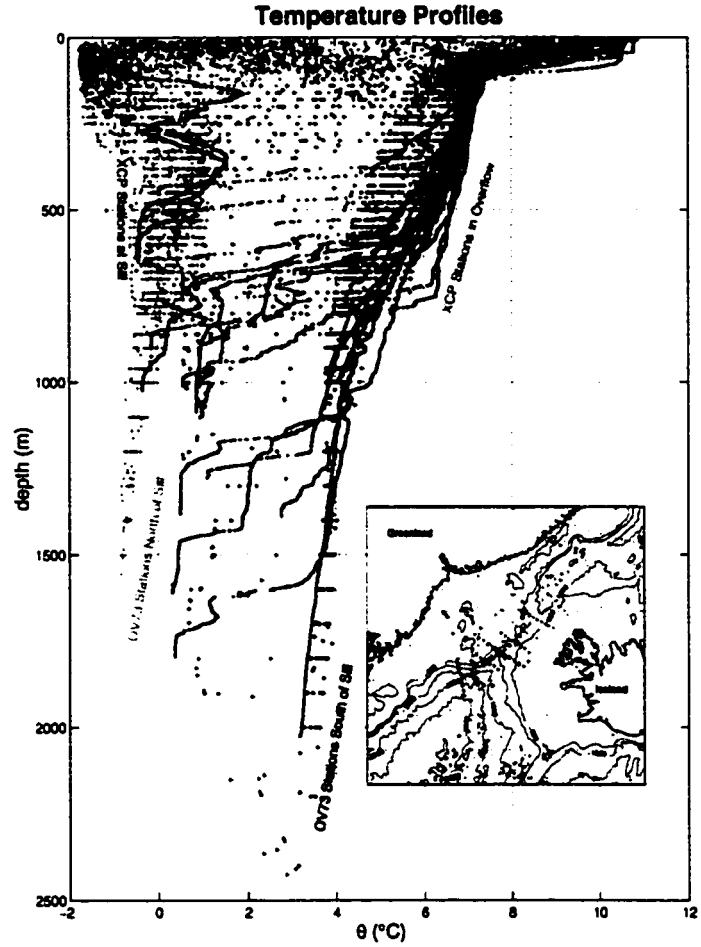


Figure 3.4: Temperature profiles from the *Aranda* CTD (red and green) along with data from the OVERFLOW '73 (O73) experiment (blue and magenta). The O73 stations are split into those in the northern and southern basins (see inset for locations). The position of the CTD profiles relative to the envelope of the O73 data appears to show that the upper intermediate depths (200–800 m) have warmed between 1973 and 1997.

in Figure 3.5 and known collectively as DSOW, give an interior stratification to the overflow which may act to inhibit mixing between its denser parts and the overlying Atlantic water, as suggested by *Rudels et al.* [1999a].

In fact, examples of overflow layers without the PIW or NSW components can be found south of the sill, as can various mixtures of the three water types. It is not immediately obvious, however, whether this is due to varying composition at the sill or to varying mixing and interleaving processes occurring during the plume's descent.

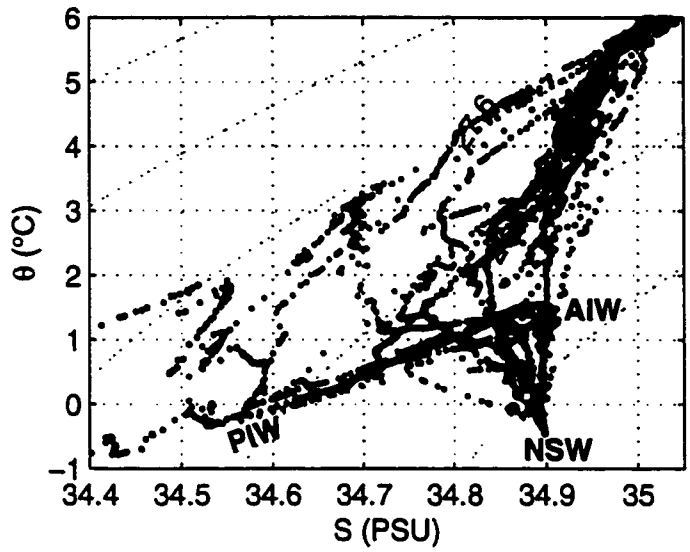


Figure 3.5: Temperature-Salinity plot of Aranda CTD data showing water mass characteristics of the dense overflow and surrounding waters. The two profiles in green are at the Denmark Strait sill, and illustrate the different type of water (salinity-stratified) found north of the Polar Front. The red profiles show the range of water masses present and trace the evolution of the intermediate salinity minimum layer as it encounters the Atlantic water. The three major water types that make up the "overflow water" are labeled. Also included are contours of potential density (σ_θ). In general, all water denser than 27.8 in the vicinity of the sill will be considered to be "DSOW."

Certainly, PIW, AIW and NSW can all be found at the sill, as evidenced by the typical structure of the dense water in the two sill stations (in green in Figure 3.5).

The velocity structure in the sections varies between primarily barotropic and baroclinic conditions, with the barotropic character most pronounced in the shallower water (generally less than 1000 m, *i. e.*, up on the Greenland shelf in section D, closer to the sill in section J and all of section E) and the baroclinic structure manifested as a bottom-intensified current in the deeper water, sometimes with an overlying counter-flow, as over the thick bottom layers in section J and D. Section E, which is entirely shallower than 1000 m, has a mostly barotropic structure, with the addition of a bottom-intensified jet. A similar structure appears in the last 30 km of section J, where it intersects E. In section D, however, the barotropic and baroclinic components appear to have split, with a clear progression from almost solely barotropic current at the shelf to a two-layer exchange flow at the offshore edge of the deep water.

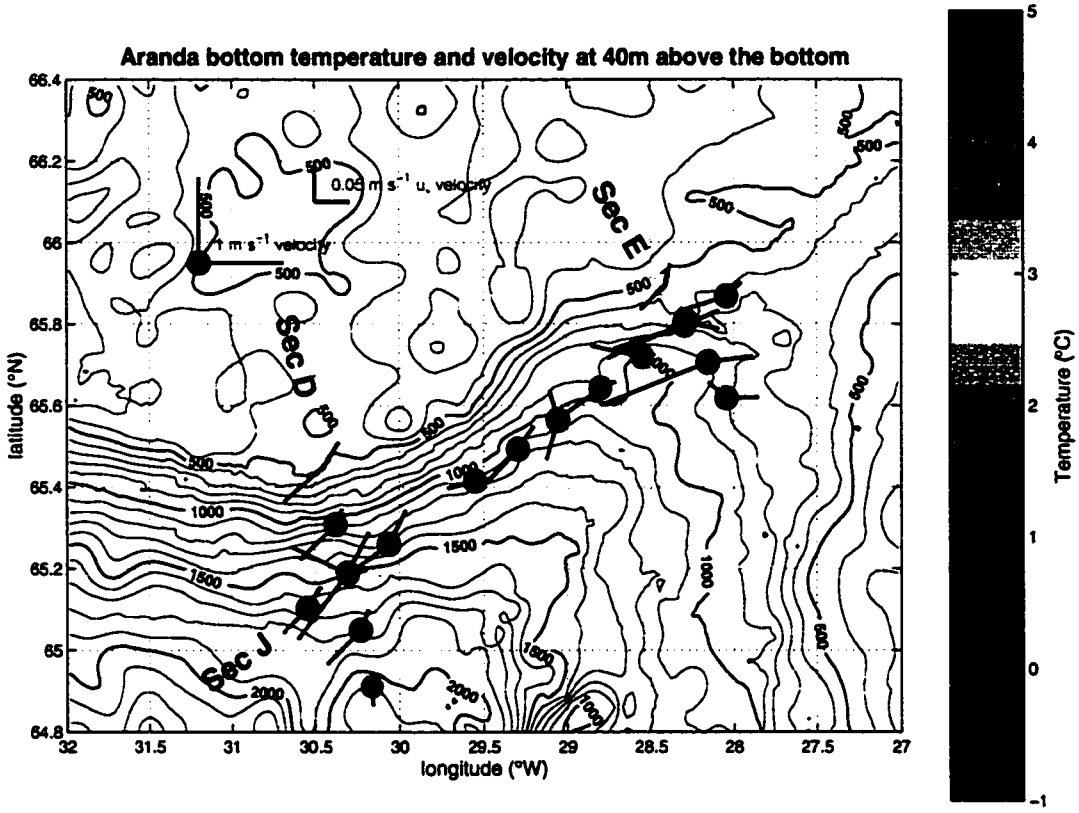


Figure 3.6: Vectors indicating the overflow plume velocity at 40 m above the bottom and friction velocity (u_*) magnitude and direction for each of the *Aranda* XCP profiles. Bathymetry in meters from *Smith and Sandwell* [1997] is shown.

Many of the profiles show a pronounced veering in their near-bottom velocity structure (appearing as an increase in cross-stream velocity approaching the bottom). In some cases, the profiles also reveal strong veering above and within the overflow, reminiscent of the frictional laboratory flows of *Johnson and Ohlsen* [1994]. Most also resolve part of the turbulent bottom boundary layer and can be used to estimate parameters of this layer, such as bottom stress. The method for calculating the bottom stress from a logarithmic fit to the boundary layer velocity profile is described in Chapter 6. The distribution of directions and magnitudes of friction velocity, (u_*, proportional to the square-root of the stress) over the XCP survey is shown in Figure 3.6, along with the bottom temperature and velocity 40 m above the bottom. The effect of the bottom Ekman layer veering is apparent here, with the u_* direction almost al-

ways lying opposite and slightly upslope of the 40 m velocity, indicating a downslope flow close to the bottom.

3.4 Interpretation

The sections appear to have sampled 3 distinct events of increased overflow transport (or "pulses" or "boluses"), separated by 2 low-transport periods. All three of the high-transport events include thick layers of DSOW (as defined by either the 2°C isotherm or the 27.8 $kg\,m^{-3}$ isopycnal), an overlying layer of low-salinity water, and strong bottom-layer velocities with a substantial downslope component.

The second event was transected in its entirety by section J, wherein it appears as a dome of DSOW between kilometers 20 and 110 (Figure 3.3). The structure of the dome is one of gradual increase in thickness on its leading edge followed by a rapid cutoff on its trailing edge. The gradual increase appears to occur again between kilometers 120 and 145, leading into the moderately thick DSOW layer in section E and the beginnings of the third transport event. The first transport event, most obvious in the thick DSOW layer spanning section D, reproduces the sharp trailing-edge cutoff sometime between the occupation of D and the repeat of station 457 only 15 hours later as station 461 in section J, at which time the DSOW has vanished completely. Interestingly, both of the stations immediately following DSOW cutoffs (461 and 467) contain warm bottom water flowing upslope, as if in a counter-flow of ambient fluid to balance the downward-flowing cold pulse that has just passed. Both stations also contain an increased amount of intermediate water, evident in the spreading of the 27.6 and 27.8 $kg\,m^{-3}$ isopycnals. This water is also moving upslope and appears, from it's T-S characteristics and reduced stratification, to be derived from similar water found at the same depth (~800 m) in the center of the Irminger Basin, supposed by *Rudels et al.* [1999a] to have been formed by local wintertime convection.

This pattern of upslope movement of warm water is also evident in Figure 3.6 (where the warm color green on station 461 at the intersection of D and J indicates the second occupation of the station, and is associated with the northwestward velocity vector and shorter u_*vector). The inflow of ambient water following a transport pulse is not unlike the situation that occurs in some numerical studies of eddy formation

in the DSO, in which deep cyclones are seen to wrap overflow water around ambient fluid [*Jungclaus et al.*, 2000].

It should be noted that an alternative explanation for the dome-like feature in section J is that of a meandering jet, which simply happens to intersect section J in such a way as to appear to thicken and thin. Although this interpretation is not inconsistent with the meandering character of the near-bottom velocity (Figure 3.6), it seems implausible in light of the width of the thick DSOW layers in sections D and E. If a hypothetical jet were to meander to such an extent to produce the extremes in thickness observed in section J while more-or-less retaining the shapes seen in section D and E, it would require excursions of more than 20 km in lateral direction and 400 m in height along the slope, which seems quite unlikely, given the strong topographic constraints on the overflow's position (see, for example, Section 6.3). The occurrence of temporal variability in the form of propagating pulses of overflow water is much more consistent with historical observations, although some combination of spatial and temporal variability in both thickness and path cannot be ruled out.

Since only one of the transport events was sampled from beginning to end, we have only one estimate of the spacing of such features. The separation of the two low-transport periods between the events was about 100 km. Given the *Aranda's* rate of upstream progress at $1.8\,m\,s^{-1}$ and a propagation speed of between 0.2 and $1.0\,m\,s^{-1}$, the true spacing could be as much as 150 km or as little as 110 km. Deep water velocities and eddy propagation speeds (Ch. 5) point towards the upper end of this range.

In addition to the strong bottom-layer plume velocities, section J shows evidence of a cyclonic surface eddy, of the sort observed by *Bruce* [1995], between kilometers 40 and 140 (see Figure 3.3), both in the low temperature and salinity of the top 50 m and in the cross-stream component of velocity in the top 800 m (above the dome in the bottom plume). Although the deep layer also has a cyclonic pattern, the upper-layer leads slightly. Section D shows a hint of a similar feature.

Both of these eddies also show up as cyclonic features in the near-surface velocity measured by the shipboard ADCP (Figure 3.7). The section J eddy (larger) appears to be centered just upslope of the cruise track, moving southwestward and descending over the course of stations 464–467. The offshore edge of the eddy carries spiral-

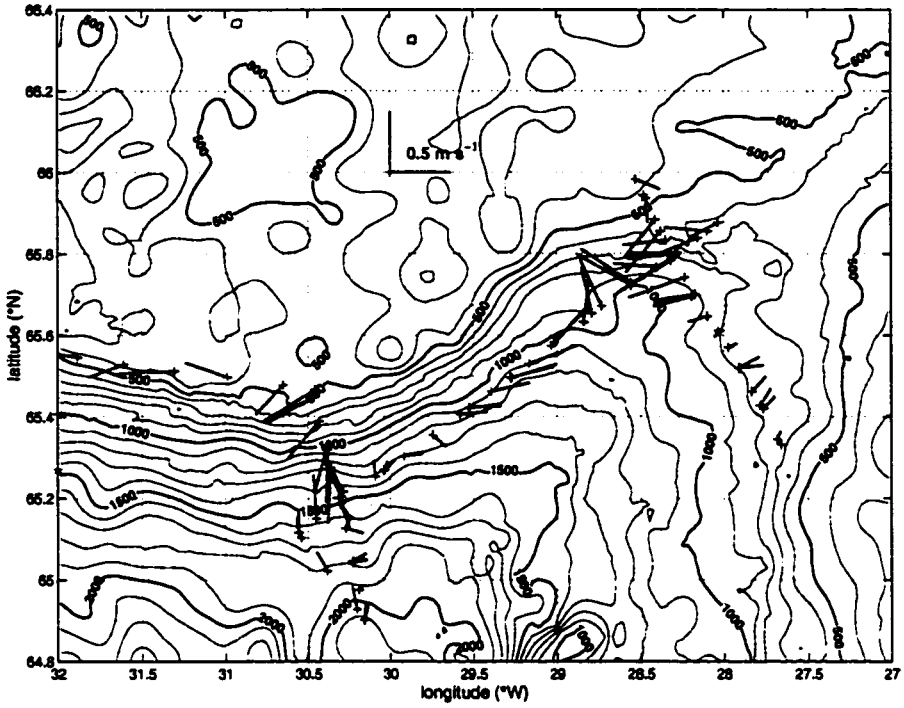


Figure 3.7: ADCP velocity averaged over the layer 50–150 m below the surface.

ing cold, fresh EGC surface water in a counter-flow over the thickest overflow layer (transport pulse), while the trailing edge of the eddy adds a barotropic component to the upslope inflow of warm Atlantic water.

The section D eddy is weaker and wider, occurring as it does after the overflow has spread considerably. Its interpretation is made even more complicated by time variability which is most evident in the complete reversal of the flow in the 15 hours between the occupations of stations 457 and 461. This reversal is nearly barotropic in the cross-slope component, and follows the same pattern as in the section J eddy, with downslope (southward) flow in and above the thick overflow layer of station 457 followed by a barotropic upslope (northward) inflow of warm water on station 461. In the interim between these two situations, the offshore edge of the eddy forms a northeastward counter-flow above the overflow layer. The progression of the velocity vector in the upper layer is, therefore, counter-clockwise, as would be expected from the passage of a cyclonic eddy north of the cruise track.

Section D also has surface velocities with an Ekman-like shear in the southern

part. This may indicate that a wind-driven current is present in addition to the overflow-generated events.

3.5 Hydrographic Survey

Descriptions of the full set of CTD measurements collected from the *Aranda* have been set forth in the FIMR cruise report and by *Rudels et al.* [1999a]. These descriptions provide an important complement to the XCP measurements, setting up the larger picture of the situation in effect at the time of the cruise. In addition, a few other investigators have published results of some relevance to the DSO in 1997.

3.5.1 Northern Basin

The sections in the northern basin (northeast of the sill) contained a subsurface temperature maximum of >1°C confined to the Greenland side of the basin. This is the AIW core of the water which flows over the sill.

At the same time, the deep water (<0°C) is banked against the Iceland side of the basin, with isopycnal slopes suggesting a deep northeastward flow. This structure, shown in Figure 3.8, is present in all of the regular occupations of the northern basin (Kögur section) by the Icelandic Marine Research Institute (MRI), as well as in the O73 hydrographic survey. In seeming contrast, current meter records from an ongoing set of Nordic WOCE moorings on the same section indicate that all waters over the 800 m isobath on the Iceland slope flow southwestwards, towards the sill [*Jónsson*, 1999]. In order to reconcile these two observations, it is clear that there must be a substantial southwestward barotropic flow over the Iceland slope.

The water on the Icelandic shelf is warm northeastward-flowing Atlantic Water, but a substantial amount of mixing occurs across the dividing front, as demonstrated by the tracks of surface drifters (Jerome Cuny, personal communication).

The geostrophic shear acts to retard the outflow velocity near the bottom, and it seems possible that the banking of deep water is due at least in part to upslope Ekman transport generated by the barotropic pressure gradient.

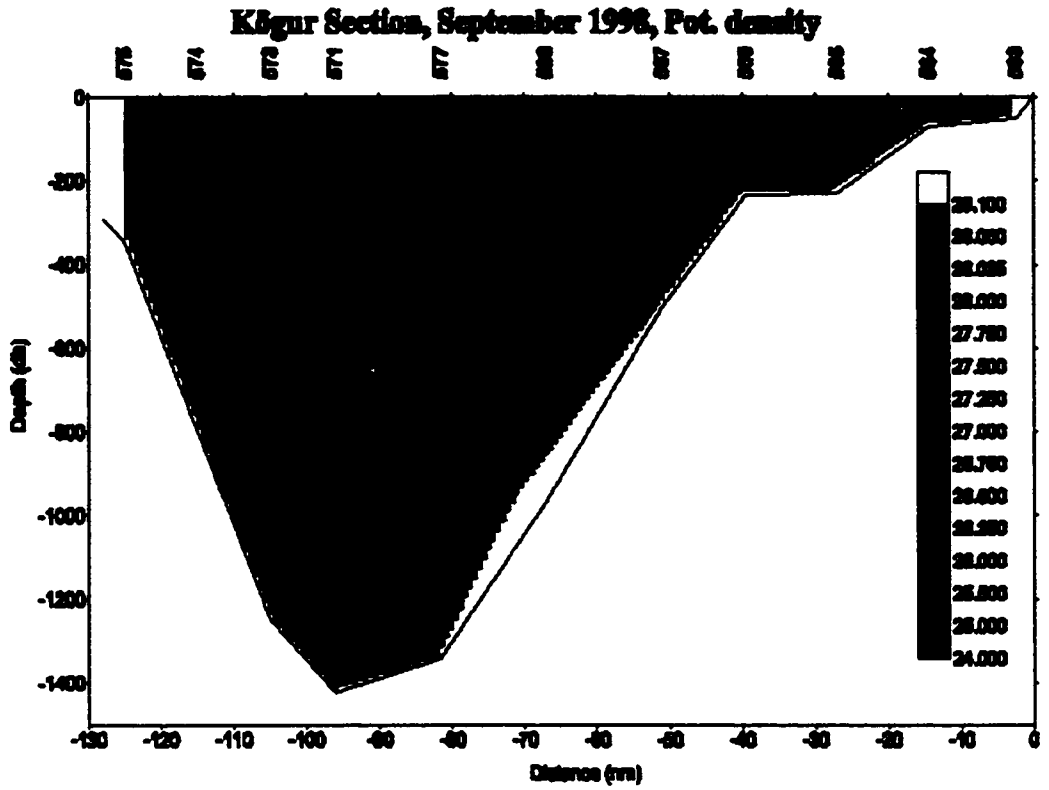


Figure 3.8: Potential density section in the northern basin occupied by the Icelandic Marine Research Institute (MRI). This and other sections regularly occupied by the MRI are available in cruise reports on their web page at `http://www.hafro.is/Sjora/index.htm`

3.5.2 Irminger Basin

The interior of the Irminger basin (southwest of the sill) contains an 800 m thick layer of low-salinity water that *Rudels et al.* [1999a] suppose originated in deep mixed layers formed the previous winter. They also point out examples of Labrador Sea Water and Northeast Atlantic Deep Water in the deep interior and Iceland side of the basin, respectively. These waters are not encountered in sections D, E or J.

3.5.3 Sill Repeats

The section across the Denmark Strait sill was occupied three times during the two legs of the cruise, with very different situations observed each time. During the first occupation, the sill was dominated by the Arctic waters, including a thick layer of

dense water and overlying cold and fresh waters. The second occupation saw the opposite situation, with Atlantic waters dominating and a much thinner layer of overflow water confined to the Greenland side of the sill. On the third occupation, both Arctic and Atlantic waters were present, with a substantial amount of interleaving between the two.

My section E was occupied approximately 1 full day before the first of these sill sections, leaving a great deal of uncertainty as to the relationship between the growing transport pulse observed in E and the large overflow at the first sill section. Given the distance (65 km) and time separating section E and the sill measurements, it seems likely that the large overflow observed was the *following* transport event, and not the one observed at E. In fact, a rough estimate using a 130 km spacing from section J together with a propagation speed of $0.6\,\mathrm{m\,s^{-1}}$ (derived from satellite imagery in Ch. 5) suggests that the next transport pulse will appear at the sill about 1.25 days after section E.

An important difference, according to *Rudels et al.* [1999a], between the sill occupations is the lack of the overlying low-salinity water (PIW) during the Atlantic-dominated case. This, then puts the AW in direct contact with the denser part of the overflow, allowing for direct entrainment. They claim that this situation is controlled by density at which the Atlantic and Arctic waters intersect, as well as by the amount and density of PIW present. While it is not clear what produces the variations in PIW, *Rudels et al.* [1999a] argue that the presence or absence of PIW is a determining factor in the amount and character of mixing permitted in the overflow's descent.

3.6 Other observations

Two other significant reports appeared in 1997 of events occurring further downstream in the overflow plume along the Greenland coast. While the delay time between the Denmark Strait sill and these downstream locations is not known for certain, these reports must be kept in mind when viewing our near-sill observations in a larger context.

McCartney et al. [1998] reported an increase in the transport of the deep boundary current along the southeast coast of Greenland between sections occupied in 1996

and 1997 and speculated that this might be related to changes in the North Atlantic oscillation (NAO). The estimates from geostrophic velocities referenced to a 1000 m level of no motion and to the near-surface ADCP velocity both give a factor of two increase in dense water transport. A number of processes unrelated to the DSO could be responsible for this increase, including aliasing of short-term variability, an increase in subpolar water content of the boundary current, or an increase in the overflows east of Iceland. However, there is a very real possibility that a similar change in the Denmark Strait was involved.

Dickson et al. [1999] find no evidence for significant interannual overflow variability in a set of long-term current meter and inverted echo-sounder records on the Greenland slope. However, these records do support the idea of short-term atmospheric changes propagating through the boundary current, as shown by a brief ($\sim$10 days) thinning and warming of the overflow plume in early 1997. While the evidence from this record (and from the temperature record from the Denmark Strait sill also presented by *Dickson et al.* [1999]) for persistent long-term changes is inconclusive, the records do emphasize that significant short-term variability is present even as far as 500 km downstream.

Chapter 4

POSEIDON EXPERIMENT

In order to better characterize the structure and evolution of the DSO, we conducted an extensive survey from the F/S *Poseidon* in September of 1998, using primarily expendable instruments to maximize synopticity. Some of the results from this survey have appeared in a poster at the WOCE North Atlantic workshop [*Girton et al.*, 2000] and in *Girton et al.* [2001].

4.1 Cruise

The cruise was the third of Prof. Rolf Käse's set of surveys of the Denmark Strait in three consecutive years as part of the German SFB-460 program (subproject A1—Overflow and Mixing Processes in the Irminger Sea). A group from APL (Tom Sanford, John Dunlap and I) were invited along to conduct our high-resolution survey with expendables while the remainder of the time was to be dedicated to a regional CTD survey.

As it turned out, the CTD survey was not as extensive as hoped, while the expendable survey underwent substantial modification. A continual sequence of low-pressure weather systems brought strong winds and large waves, leading to difficult working conditions. During several extended periods, the *Poseidon* experienced windspeeds of over $20\,\mathrm{m\,s^{-1}}$ (Figure 4.1), leading to the cessation of scientific activity, while at other times, wind and wave directions severely limited the available speeds and headings that the ship could hold. Fortunately, even when the winds and sea state made cable-lowered CTD operations impossible, we were often still able to launch the expendable probes from the O1 level and continue our survey, albeit at a slower pace due to the difficulty of maintaining headway. The result was that much less time was lost to the bad weather than would have been the case with a purely conventional CTD survey and the net data return was only slightly lower than originally intended.

Also shown in Figure 4.1 are several other variables recorded by the *Poseidon's*

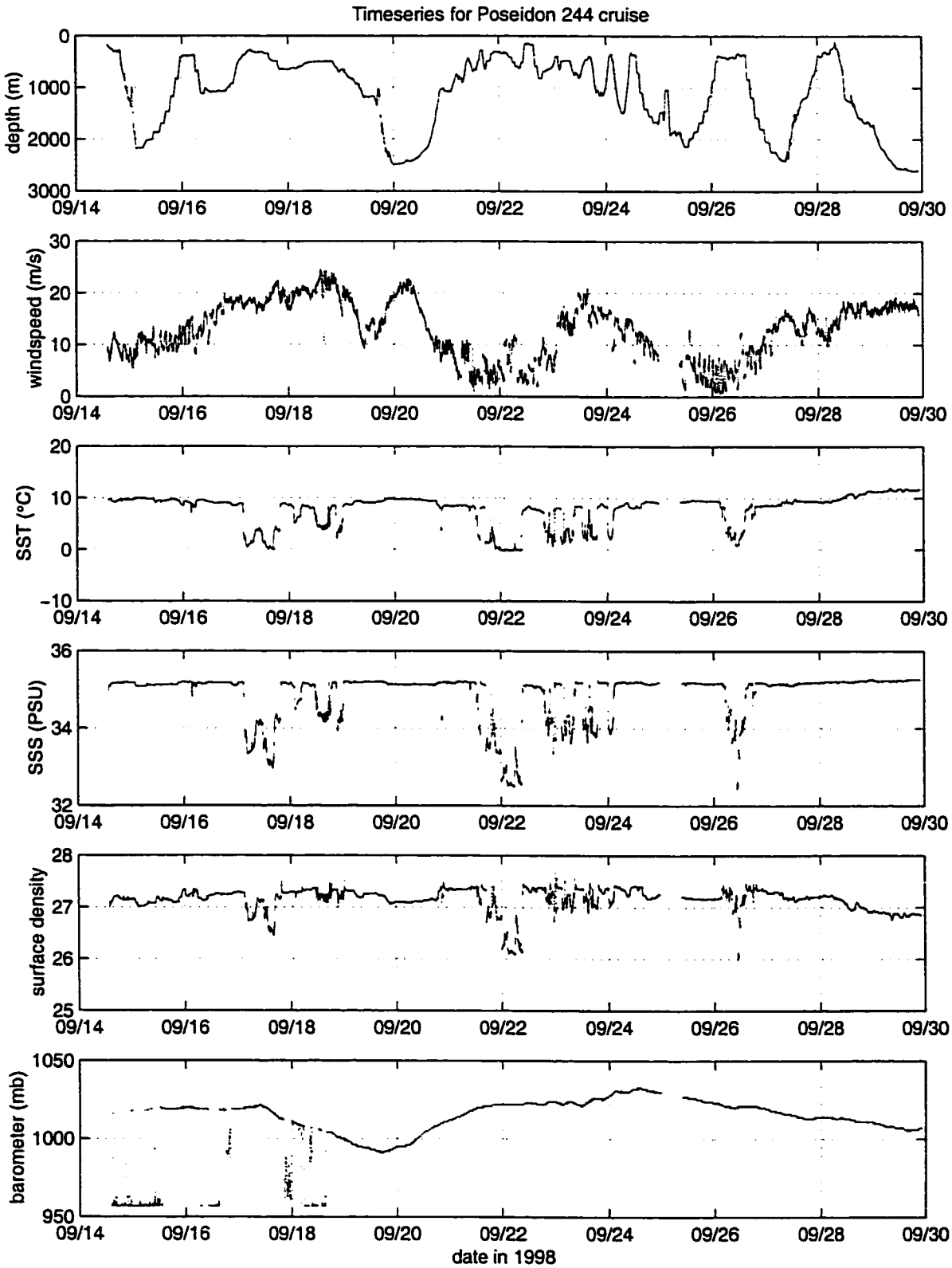


Figure 4.1: Environmental variables recorded during *Poseidon* 244.

PCLOG system. The sea-surface temperature (SST) and salinity (SSS) records show that the region is characterized by a strong front, leading to periods of very rapid SST and SSS change, interspersed with only gradual variability. The depth record points out the times that the *Poseidon* was over the Greenland continental shelf, and when it was in the deeper waters of the Irminger Basin. Unfortunately, the barometric pressure reading exhibited some rather strange behavior, and so it probably not trustworthy.

4.2 Survey

The main goals of the survey were to: 1) estimate the transport through several sections, 2) map the dynamical properties of the overflow plume, including Froude number and bottom stress, 3) determine the upstream condition for hydraulic considerations and 4) characterize the velocity and watermass structure of one or more surface eddies. The eventual pattern and timing of expendable current profiler (XCP) stations (shown in Figure 4.2) reflects these goals, but was also heavily influenced by weather conditions. In the end, repeat sections were run at the Denmark Strait sill (t1u, t2u, t3u) and at the southwestern boundary of the survey region (t1d, t2d, t3d). The central along-stream section, which had been intended to be repeated several times, was run only twice—once only halfway with CTD (init) before being cut short by rough weather and once with XCP and XCTD (ao1). Finally, a number of cross-stream sections (xo1-xo9) were run in sequence to give a synoptic picture of various quantities, from the surface to the bottom, and two sections northeast of the sill (nb1, nb2) were also occupied.

4.3 Summary of Data

Contoured sections of temperature, salinity, density and velocity perpendicular to and parallel to each line are shown in Appendix B and labeled with the section name and the station numbers included. Because of the substantial overlap and repetition within the cruise track, the description of the sections will be divided into three separate segments here designated Parts I, II and III (see Table 4.1, showing times and stations in each part). Breaking the cruise up in this way allows plotting of

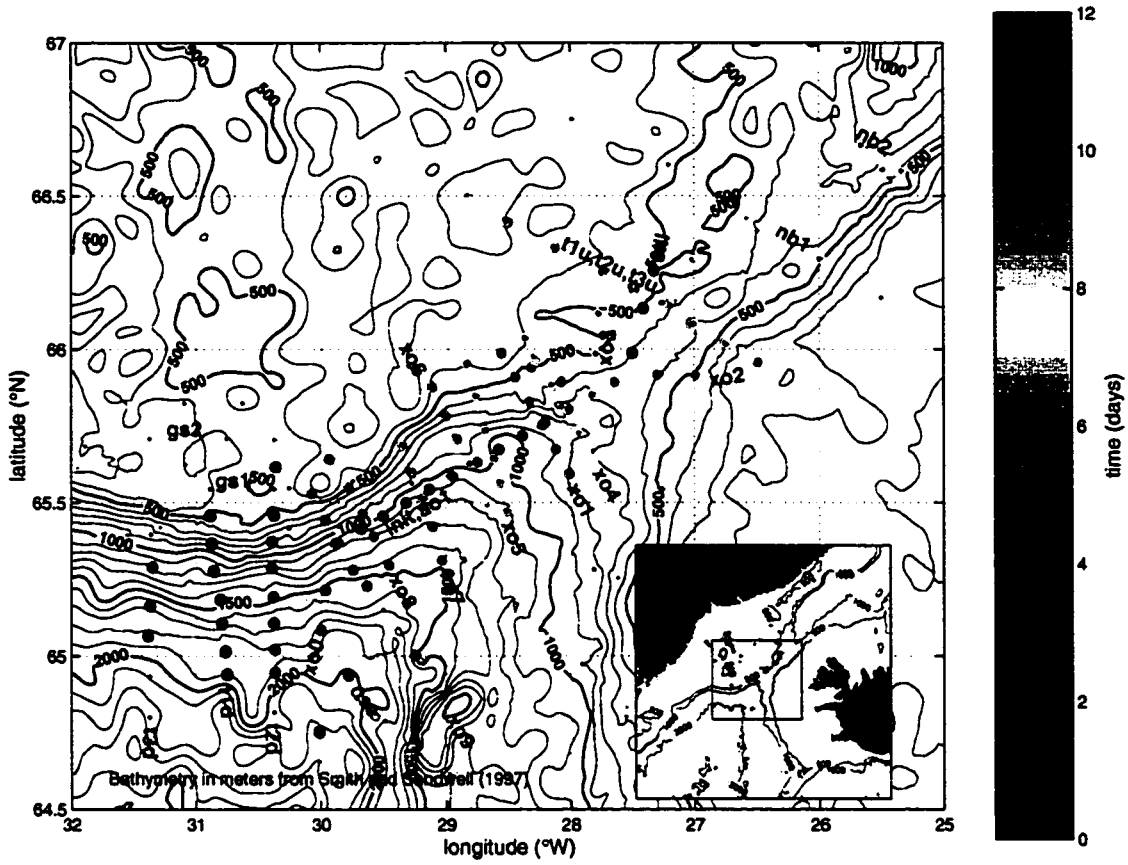


Figure 4.2: Locations of eXpendable Current Profiler (XCP) drops during *Poseidon* 244 color-coded by time elapsed after the first drop at 0558 UT on September 15, 1998. Note that the sill section and a few other stations contain overlapping symbols, which may be difficult to identify. Stations without XCPs are also shown as small dots. The inset shows the location of the survey in the Denmark Strait, between Greenland and Iceland.

data records with minimal overlap and also aids differentiation between spatial and temporal changes.

The surface temperature records for all 3 parts are shown in Figure 4.3. The most apparent feature is the varying position of the temperature front, also evident in the satellite AVHRR images of Chapter 7. This front plays an important role in the visualization of cyclonic eddies as described by *Bruce* [1995], and will be referenced in the following narrative:

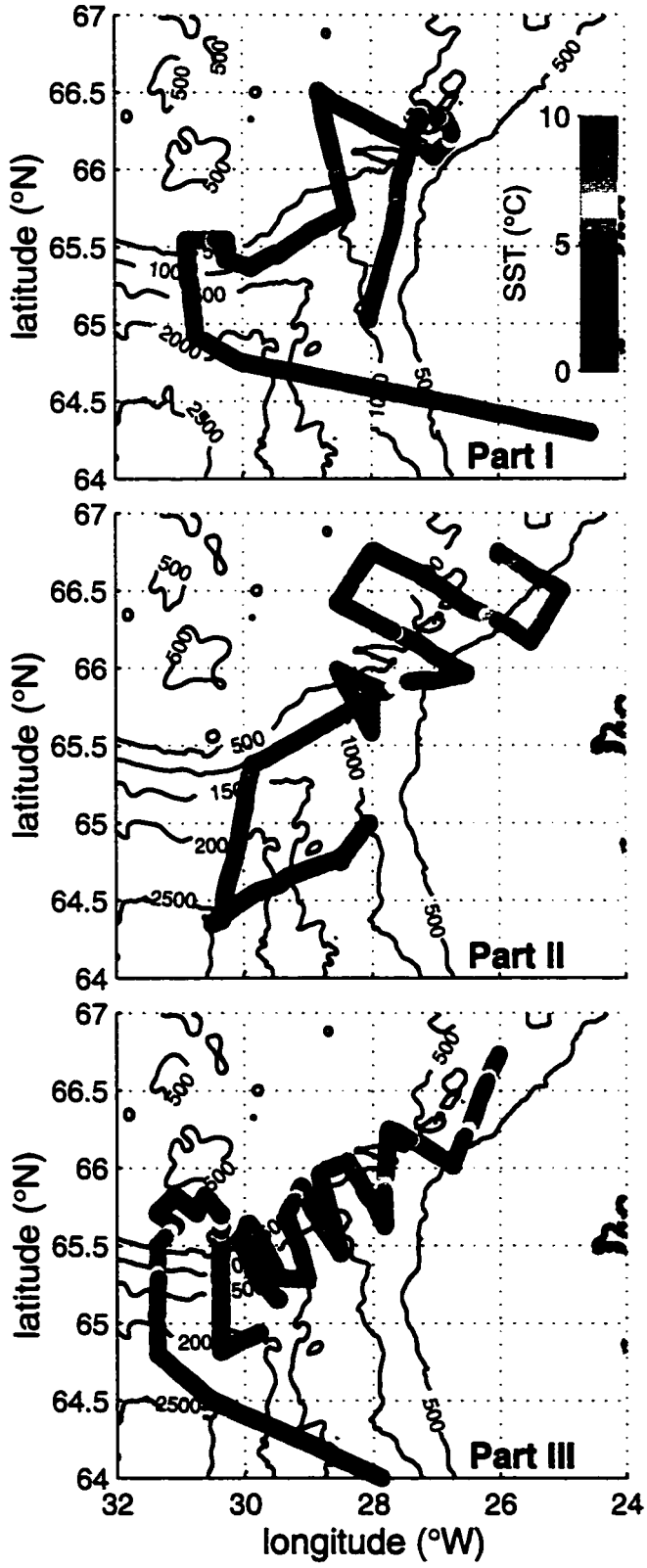


Figure 4.3: Continuously-recorded sea-surface temperature from the *Poseidon*'s thermosalinigraph (TSG). Parts I, II and III of the cruise.

Table 4.1: Station numbers and times used to divide *Poseidon* 244 cruise up into 3 parts.

	Stations	Time Interval	XCP Profiles
Part I	452–476	9/14 1200 – 9/19 0800	4101–4118
Part II	477–519	9/19 0800 – 9/22 2100	4119–4156
Part III	520–586	9/22 2100 – 9/30 0000	4157–4210

4.3.1 Part I

Sections: tld, gsl, init, tlu, sill

Near-surface and near-bottom velocities and temperatures from those stations including XCPs are shown in Figures 4.4 and 4.5.

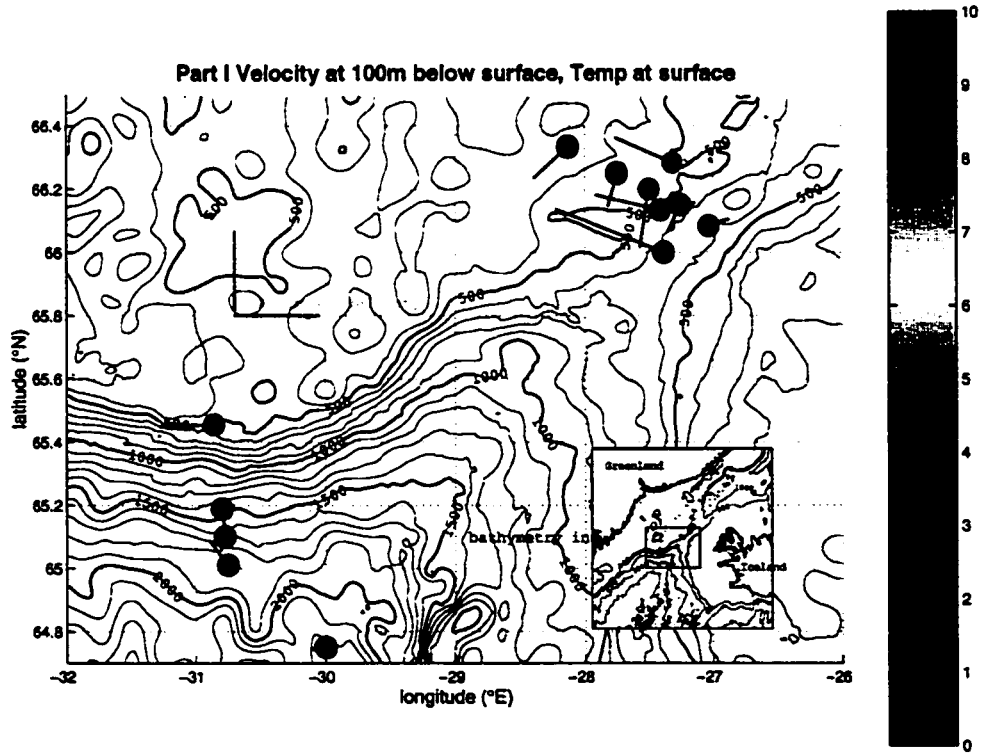


Figure 4.4: Near-surface temperature and velocity measurements from XCPs during Part I of the cruise.

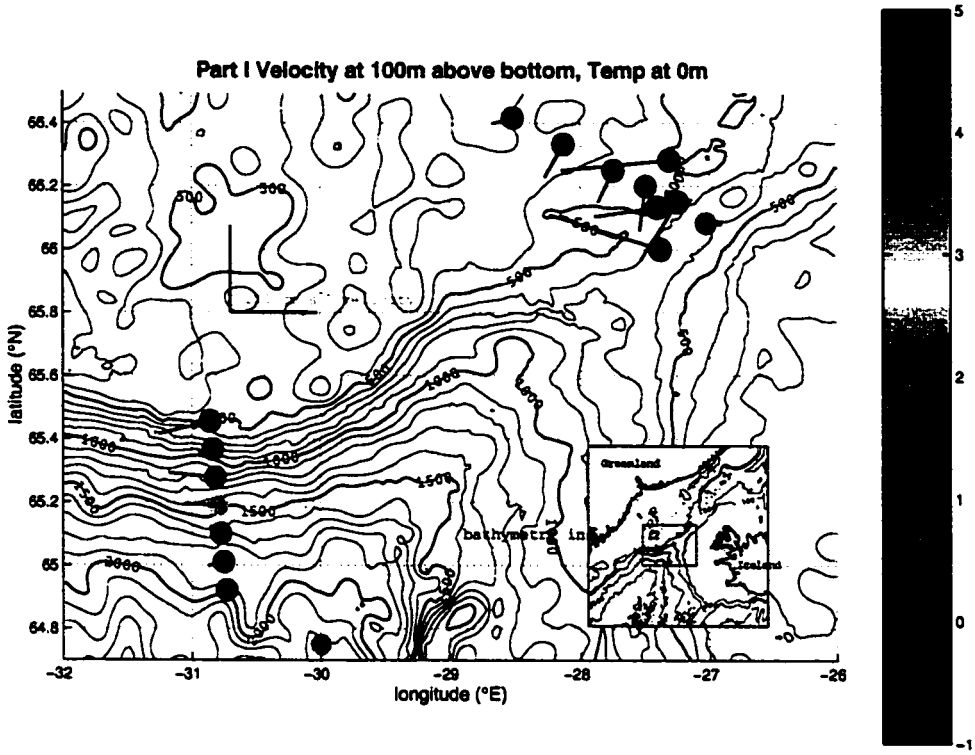


Figure 4.5: Near-bottom temperature and velocity measurements from XCPs during Part I of the cruise.

The overflow layer in section tld, the first of the cruise, was relatively thin and fast (0.5–0.7 m s^{-1} in the narrow core), as well as stratified in the cross-slope direction. At the end of the section, on the Greenland shelf, appeared a strong along-shelf barotropic flow of 0.7 m s^{-1}, but the water was all quite warm (this persisted throughout the temperature profiles of section gsl and also appears in the thermosalinigraph (TSG) record shown in Figure 4.3) indicating that the EGC must lie further on-shelf.

As we began the first along-axis section (init) with CTD stations only, the overflow layer thickened to over 400 m (including a cap of low-salinity PIW), then suddenly disappeared. The shape was very similar to the dome of overflow water observed in section J of the *Aranda* survey. Velocity information was not available for this section, and no sign of the cold water appeared in the TSG. At this point, the weather had deteriorated to the point that CTD operations had to be suspended, and the *Poseidon* moved to the Greenland shelf, hoping to find calmer seas. Once there, conditions were

suitable to begin section t1u, which showed a very thick layer of dense water but very weak outflow (only 0-0.3 m s^{-1}, and almost entirely barotropic). Near the center of the channel, the dense water ended in a steep (at our station resolution) front with very strong shear between the deep outflow and rapidly-inflowing (0.5 m s^{-1}) upper layer of Atlantic water. Unfortunately, the maximum speed of the outflow was not measured due to the breaking of the XCP wire in the excessive shear! In addition, surface weather conditions prevented the continuation of the section towards Iceland. Instead, a short perpendicular section with expendables (sill) was made across the thickest part of the dense layer, showing a puzzling alternation of thick and thin overflow layers, warm and cold surface water and strong velocity angled towards the Greenland shelf. After this, the weather shut us down entirely for almost two days and we ran before the storm, ending where Part II begins at 64.3°N, 30.5°W.

4.3.2 Part II

Sections: x00, a01, x01, x02, t2u, nb1, nb2

Near-surface and near-bottom velocities and temperatures from those stations including XCPs are shown in Figures 4.6 and 4.7.

Once the wind and waves had calmed sufficiently to allow sampling to resume, we made a section (x00) and another run at the along-axis section (a01), beginning almost immediately with a 500 m thick overflow layer, cold surface water, lots of intermediate low-S water and velocities up to 0.9 m s^{-1}! Within a few stations, this thick layer had again vanished, to be replaced with a thin (100 m), fast (>0.9 m s^{-1}) overflow, extending more than 50 km without substantial thickening. Much of this thin layer is directed strongly downslope with the overlying water sharing a similar cross-isobath component (rather than a counter flow). Near the end of section a01 the overflow thickened to about 200 m and began to show signs of a PIW layer.

To verify that the section had not simply bypassed the thick overflow, we ran a section across the slope (x01) before continuing. This showed much the same structure (thin and fast) persisting high onto the Greenland shelf, with no barotropic shelf current (and in fact, some upper-layer warm return flow at the shelf break). Not until the diagonal approach to the sill (x02) do the thick overflow and cold surface water return, increasing to both a thick dense layer and a strong, narrow barotropic outflow

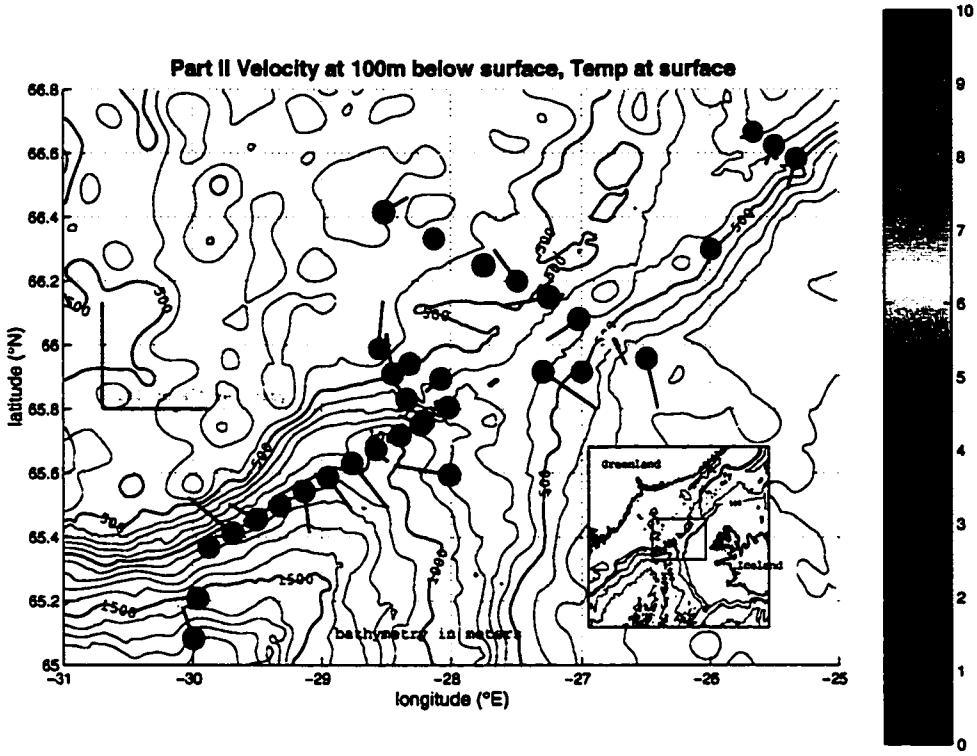


Figure 4.6: Same as Figure 4.4, Part II.

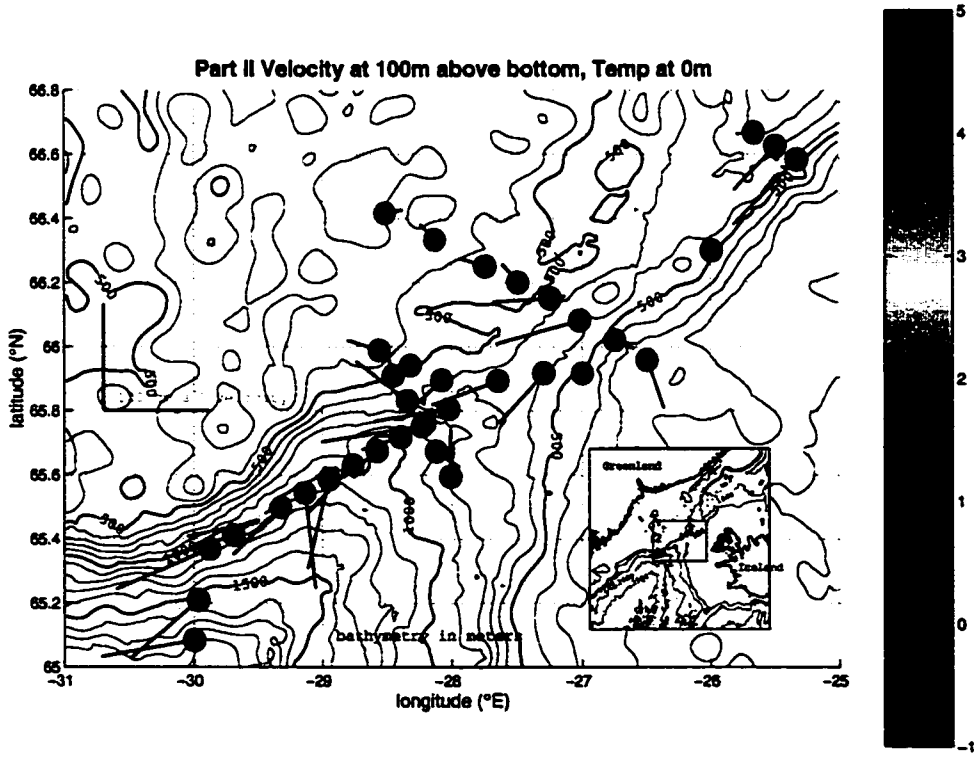


Figure 4.7: Same as Figure 4.5, Part II.

at the sill (t2u).

After this second occupation of the sill section, we moved to two sections northeast of the sill (nb1,nb2), using mostly CTD-only stations to characterize the upstream conditions for the overflow. nb1 contains a number of interleaving isopycnal layers in the water lighter than 27.8 kg m^{-3}. On nb1 the ADCP shows southwestward outflow on the Greenland shelfbreak (barotropic) and the XCPs on nb2 show bottom-intensified outflow on the Iceland slope (up to 0.9 m s^{-1}). It's likely that this bottom water continues southwestward on nb1, but below the range of the ADCP. In addition, the stronger tides in the upstream basin probably contribute to the barotropic variability.

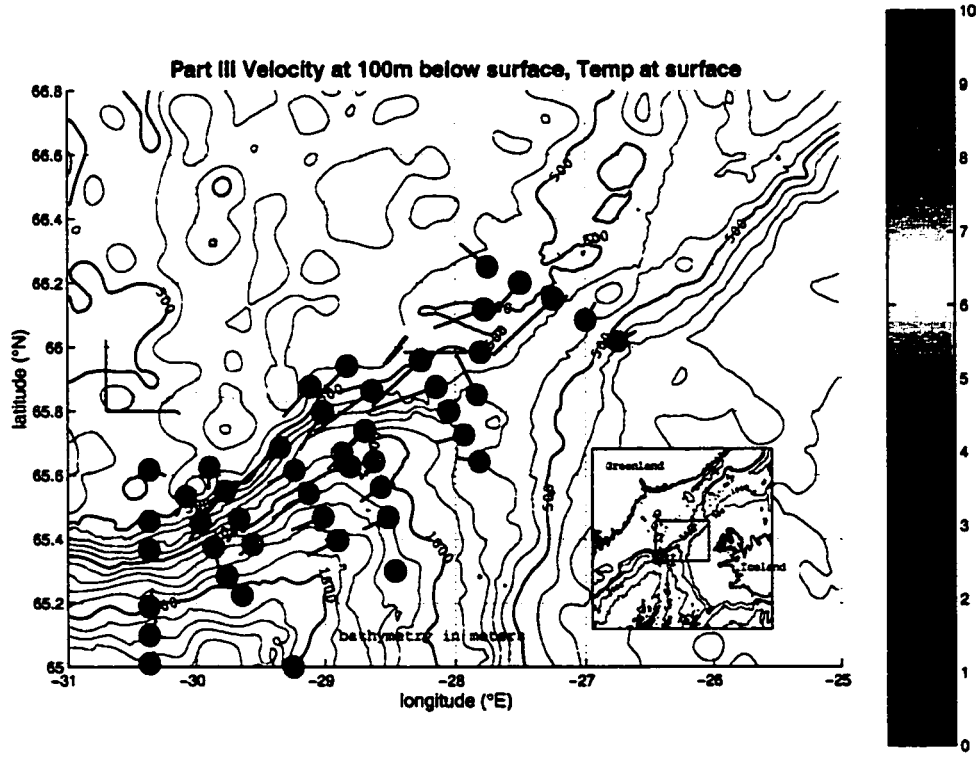


Figure 4.8: Same as Figure 4.4, Part III.

4.3.3 Part III

Sections: t3u, xo3, xo4, xo5, xo6, xo7, xo8, xo9, dse, t2d, gs2, t3d

Near-surface and near-bottom velocities and temperatures from those stations including XCPs are shown in Figures 4.8 and 4.9.

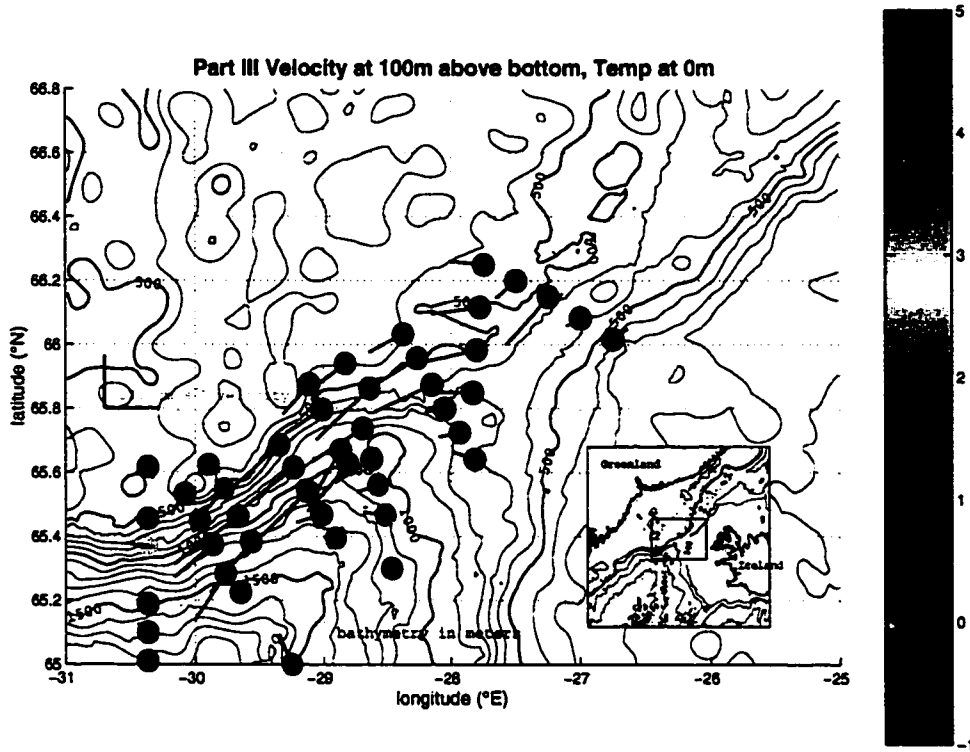


Figure 4.9: Same as Figure 4.5, Part III.

This final segment of the cruise consisted of a succession of sections across the overflow progressing downstream as quickly as weather conditions would permit. The irregular orientations of these sections came about, in large part, due to the ship's inability to proceed on certain headings. The first eight of the sections all contained thick and fast overflow layers and the first five showed the cold water front at the surface extending almost as far offshore as the 1000 m isobath. Over the course of the sequence, there was a general transition from mostly barotropic flow close to the sill to baroclinic exchange or bottom-intensified flow downstream (plus a barotropic current at or near the shelf break). In many of the sections, this produced a cyclonic circulation in the upper layer above the deep overflow. †3u had some of the strongest horizontal shear observed in the cruise, with a transition from a northeastward 0.35 m s^{-1} upper-layer inflow to a southwestward barotropic 1 m s^{-1} outflow over the 12 km between stations 521 and 522. A constant velocity gradient between the two would result in a vorticity of $0.85f$. Even larger horizontal shear of just over

f appeared in xo4 in an almost purely barotropic exchange.

The cross-isobath flow in this sequence appeared somewhat similar to that observed over the transport pulse in section J of the previous summer. Onshore (towards Greenland) flow in the upper layers of xo3 and xo4 together with offshore flow over the full water column in xo5 reinforces the impression of cyclonic circulation.

Subsequent sections (xo6, xo7, xo8, xo9) showed a greater amount of downslope component in the near-bottom velocity with less overlying flow but continued to contain thick (200 m+) and fast (0.9 m s^{-1}) overflow layers.

After a couple of stations in the interior of the Irminger Basin (dse), we returned to near the location of the first section, now t2d, only to find that the overflow layer had thinned dramatically and slowed. This was accompanied by a thickening of the layer between the 27.6 and 27.8 kg m^{-3} isopycnals. Continuing the section up onto the Greenland shelf, we encountered the cold surface front between 15 and 20 km shoreward of the shelfbreak (gs2). The last section across the slope, t3d, showed some thickening in the overflow layer, but was otherwise similar to t2d.

4.4 Interpretation

Although sampled with very different degrees of thoroughness, there do appear to have been 5 distinct transport events/pulses/eddies transected over the course of the cruise. The characteristics observed during the *Aranda* cruise are also evident here. These characteristics include thick, fast overflow layers capped by low-S water (PIW), gradual buildup on the leading edge followed by rapid cutoff on the trailing edge, a downslope velocity component in the bottom layer and an upslope velocity component in the warm water following the cutoff. Many (but not all) of the events also occur below a layer of cold surface water indicating an offshore excursion of or detachment from the cold front.

Both Part I and Part II, progressing upstream, crossed two eddies. Each leg began with thick bottom layers early in its approach (100–150 km from the sill), sudden cutoffs followed by warm upslope upper-layer flow and then large flows and cold surface water close to the sill. While the near-sill eddy in Part I is much more difficult to diagnose for certain, the multiple crossings of the cold surface front, together with the thick bottom layers adjacent to the sill in sill make it seem likely that a forming

eddy was present.

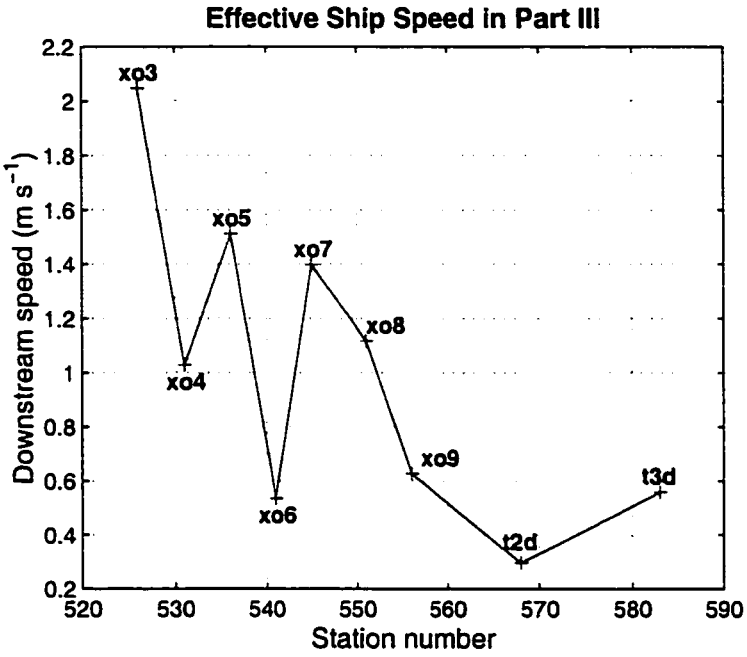


Figure 4.10: Effective downstream ship speed computed from the separation in space and time of consecutive sections in Part III.

The fifth eddy/pulse, heavily surveyed in Part III, is clearly present but somewhat difficult to piece together due to uncertainty in the relative speeds of the *Poseidon* and the propagating pulse itself. The *Poseidon*'s effective downstream speed (calculated from the separation in space and time of the center station in each consecutive section) is shown in Figure 4.10. Due to the large changes in downstream speed, the various sections across the overflow probably move alternately forward and backward relative to the progressing wavefront of the pulse. Since the rapid trailing edge cutoff occurs in section t2d, the pulse must be moving at least faster than $0.3\,\mathrm{m\,s^{-1}}$ at this point. By looking at the successive pairs of sections for which the downstream speed was greatest (*i. e.*, t2d–xo3, xo4–xo5 and xo6–xo7–xo8), it is possible to construct a sequence of snapshots of the evolving plume. From this perspective, the plume does, indeed, thin on the leading edge (and then thicken again as the subsequent longer gap in time enables it to "catch up"). If correct, this interpretation suggests that the propagation speed begins in the range $1–1.5\,\mathrm{m\,s^{-1}}$ at xo4 and slows to $0.5–1\,\mathrm{m\,s^{-1}}$ by

xo9.

When viewed in sequence, sections xo5–xo9 appear to have been occupied at very close to the downstream speed of the bottom pulse. The combination of along-section velocity and density forms a coherent picture of downslope flow and bottom layer slumping, beginning with offshore velocity in the deep layer high on the shelf followed by a thickening of the layer and downslope propagation. Even if not truly Lagrangian, this sequence does give an intriguing insight into the downstream evolution of the deep plume.

The repeated sections at and near the sill, despite large differences in layer thickness and velocity, do have a certain similarity. The presence of a barotropic jet above the dense deep layer, as well as strong lateral shear and a nearly vertical front separating the outflow from the Atlantic water on the south-eastern side of the strait, are clearly ubiquitous features of this part of the overflow. The jet, at least, has been previously observed in near-surface currents [*Fristedt et al.*, 1999].

Although not well-sampled by XCPs, the situation in the northern basin (nb1,nb2) also reinforces previous observations. The banking of dense water against the Iceland side was interpreted as a recirculating northeastward flow by *Rudels et al.* [1999a], but the few XCPs show that this water is moving southwestward, towards the sill. The Icelandic current meters in this region also indicate southward flow at all levels [*Jónsson*, 1999]. The reason for the banking is unclear, however, since it leads to a geostrophic shear that decreases the velocity approaching the bottom. Could this be a frictional affect similar to the "slippery boundary layer" of *MacCready and Rhines* [1993], pushing the deep water upslope in an Ekman layer? Or could it be a result of the approaching flow's attempt to preserve its potential vorticity?

Chapter 5

TRANSPORT AND VARIABILITY

Often, the first question asked about the flow of a current is: "What is the volume transport?" This number for the DSO is of use both as a benchmark for the comparison of results from regional numerical models and as a vital northern boundary condition for the overturning circulation in large-scale models unable to resolve the overflow dynamics. The deep boundary current transport and temperature are also crucial for estimates of the meridional heat transport in the Atlantic sector. For these reasons, the DSO transport is the subject of the first paper dealing with results from the *Poseidon* experiment [*Girton et al.*, 2001]. This chapter presents the main results from that paper, including comparisons of our measurements with historical current meter records from the OVERFLOW '73 (O73) experiment and with a regional numerical model by *Käse and Oschlies* [2000] (KO). It also discusses the issues of hydraulic control, tidal aliasing and atmospheric pressure forcing.

5.1 Near-sill Transport

The hydrodynamic environment at the Denmark Strait sill is extremely complex and variable. Nevertheless, as the deepest point on the ridge separating the Iceland Sea from the Irminger Basin, it is a logical point to study the origins of the overflow. I have used the seven *Poseidon* sections nearest the sill (see Figure 5.1) to construct estimates of the volume transport of the overflow. Three of these sections cross the saddle point (t1u, t2u, t3u), two are at approximately the O73 array location (xo1, xo4) and two are oriented diagonally in the intervening region (xo2, xo3). These seven were close enough to the sill to provide comparable estimates of overflow transport before it begins its steep descent into the North Atlantic proper. The velocity perpendicular to each section is shown in Figure 5.2, along with a snapshot for comparison from the KO numerical model.

There are a number of different methods for defining DSOW and calculating "over-

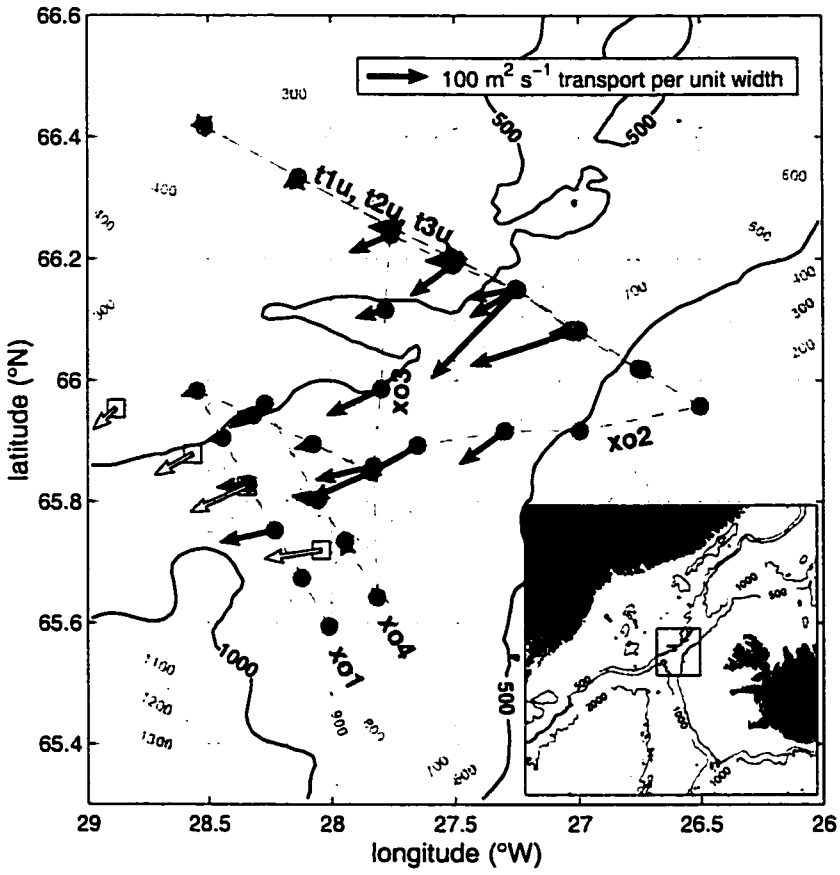


Figure 5.1: Locations of 1998 XCP/XCTD drops (dots) and 1973 current meters (squares). Open arrows are 5-week means of cold (θ < 2°C) water transport from the current meters. Solid arrows are dense (σ_θ > 27.8) water transport from single profiles. Bathymetry in meters from the *Smith and Sandwell* [1997] database is shown.

flow transport." Hydrographic surveys covering a complete set of chemical tracers have specified ranges of oxygen, CFCs and tritium in addition to temperature and salinity [*Fogelquist et al.*, 1998], while moored current meter observations have had to resort to simply including all water below a certain temperature [*Ross*, 1978]. A popular approach, given the density-driven nature of the flow has been to use density as the defining characteristic, but a single density value ignores mixing that may occur during the overflow process. Nevertheless, to provide comparison with prior and future transport estimates, I have calculated the transport values using both temperature and density definitions present in the literature.

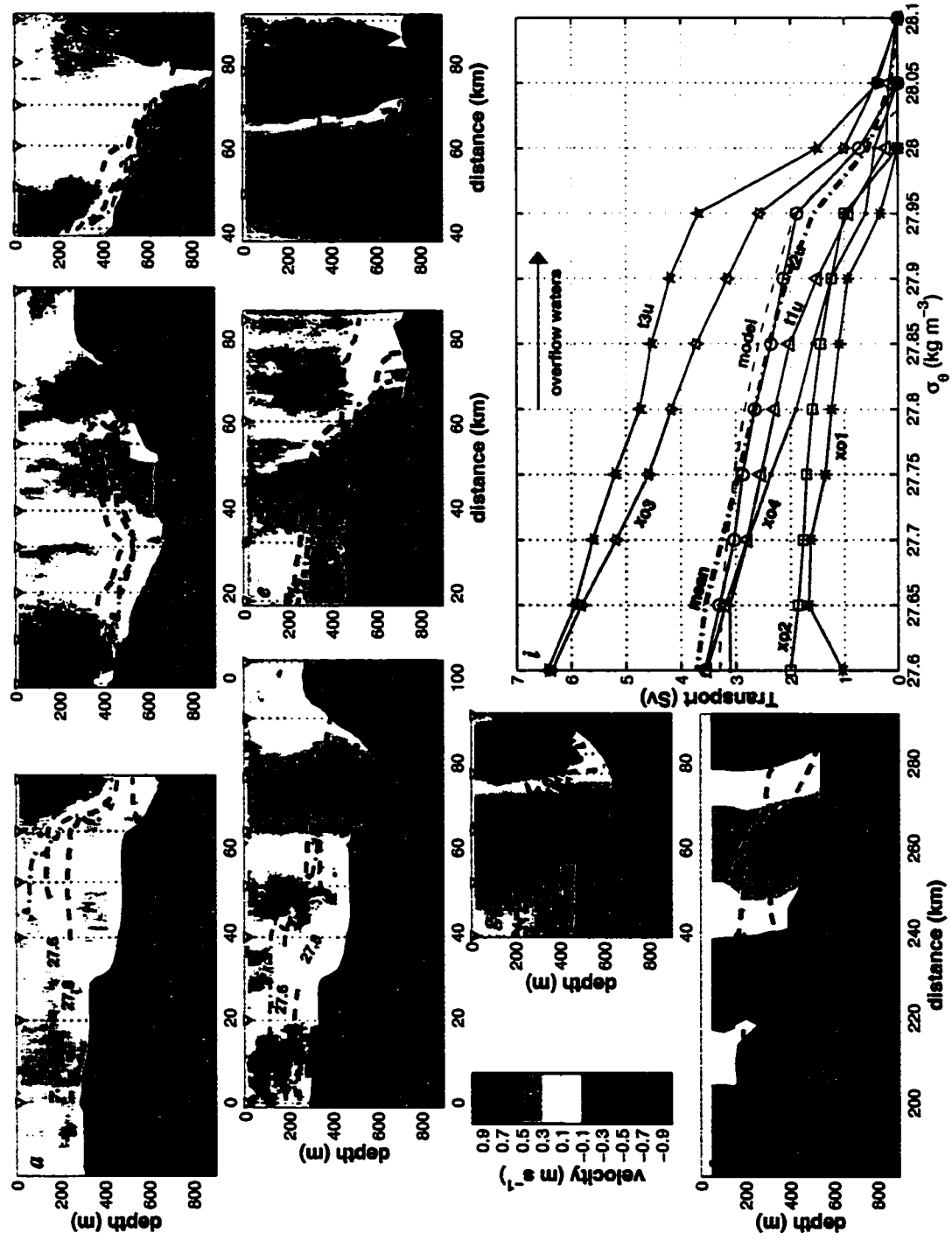


Figure 5.2: (*a–g*) Seven snapshots of XCP/ADCP velocity (component parallel to outward normal to section, shaded in color) and XCTD density (dashed contours) from sections in Figure 5.1, along with (*h*) one snapshot from a numerical model. Greenland lies to the left and Iceland to the right. Similar sections are aligned vertically for comparison. Positive velocities are directed toward the viewer, *i.e.*, southwestward. (*i*) Cumulative transports of dense water in each section, including the 7-section mean (dot-dashed) and a 22-day average from the model (dashed).

Table 5.1: Transport values from the 7 near-sill sections.

Section	$\sigma_\theta > 27.8$	$\theta < 2°C$	array-sampled
t1u	2.3 ± 0.2	4.4 ± 0.2	1.5
xo1	1.3 ± 0.2	1.4 ± 0.2	2.0
xo2	1.6 ± 0.2	1.9 ± 0.2	1.0
t2u	2.7 ± 0.1	3.1 ± 0.1	2.6
t3u	4.8 ± 0.3	5.8 ± 0.3	6.2
xo3	4.2 ± 0.2	5.4 ± 0.3	4.1
xo4	1.9 ± 0.1	4.6 ± 0.3	3.0
mean	2.7	3.8	2.9
median	2.3	4.4	2.6
$\frac{\text{st. dev.}}{\sqrt{5}}$	± 0.6	± 0.8	± 0.8

All values are in Sverdrups ($1\,\text{Sv} = 10^6\,\text{m}^3\,\text{s}^{-1}$). Error estimates include the effects of interpolation/extrapolation choices, instrumental errors and ADCP mounting angle uncertainty, representing the authors' best attempts to gauge the $\pm 1\sigma$ (67% confidence) level of each synoptic transport measurement. Array-sampled values are the effective current meter transports of $\theta < 2°C$ water estimated by subsampling the measured sections at the equivalent depths and distances of the O73 array, as described in Section 5.3.

The most commonly-used criteria have been $\sigma_\theta > 27.8$ (where $\sigma_\theta + 1000$ equals density in $\text{kg}\,\text{m}^{-3}$) [*Dickson and Brown*, 1994] and $\theta < 2°C$ [*Ross*, 1984]. Table 5.1 reports the transports through each section in Figure 5.2, computed using these two criteria. (Alternatively, using $\theta < 3°C$ [*Saunders*, 2000], the mean and median transports come out to 4.0 Sv and 4.3 Sv, respectively.) The largest contributors to the error estimates shown in Table 5.1 are uncertainty in interpolation in near-bottom regions between profiles of differing depth and extrapolation beyond the ends of sections. In only a few cases do the contributions from random instrumental (XCP, ADCP, GPS) errors make a noticeable difference in the error estimates. Uncertainty in the mean transport is clearly due more to natural variability than to either interpolation or measurement errors. I estimate this uncertainty on the last row of Table 5.1 by as-

suming a steady variability equal to the standard deviation of our measurements and an estimated 5 degrees of freedom, resulting from the close temporal spacing of some of our 7 sections relative to the integral timescale of 10 hours present in the O73 data.

Interestingly, the highly barotropic nature of the flow implies that a great deal of the overflow transport could be estimated using only measurements of near-surface velocities and a knowledge of the depth of the surface delimiting DSOW. In fact, over 80% of the full-water-column measured transport in our 7 sections can be accounted for in this way. Since a number of hydrographic surveys have been made in the sill region from ships equipped with ADCP instruments, a larger database of transport estimates could be constructed in this manner. It would not be possible, however, to do this further downstream along the Greenland slope, once the overflow has begun its rapid descent. In addition to the greater water depth and smaller fraction covered by the ADCP, the flow becomes more bottom-intensified in this region, making the barotropic component relatively less important.

5.2 Historical Variability

Since 7 samples is a small set of measurements on which to base statements about DSOW transport, I have re-examined the original 5-week current meter records from O73 (Ross, 1998, personal communication). A timeseries of hourly transport measurements, calculated in the same manner as *Ross* [1984] from the temperature and velocity records (with the exception of the tidal filtering, as I want to compare the results with our instantaneous measurements), is shown in Figure 5.3, along with the velocity records themselves. Transport values range from 0.2–8.5 Sv, with the dominant pattern being a series of high-transport episodes occurring at intervals of 2–5 days. The distribution of values shown in the upper panel of Figure 5.4 is a skewed one with the majority of values clustered near a peak between 1 and 2 Sv but also a substantial fraction of values in the high-end "tail." This results in a lower median (2.2 Sv) than mean (2.8 Sv), and a large standard deviation (1.9 Sv). De-tiding the temperature and velocity records with a 13-hour filter before calculating transport reduces the mean to 2.6 Sv, indicating a certain degree of tidal contribution through a layer velocity/thickness correlation. Tides are present in the velocity records but do not make up a large part of the variance, as will be discussed later in this chapter.

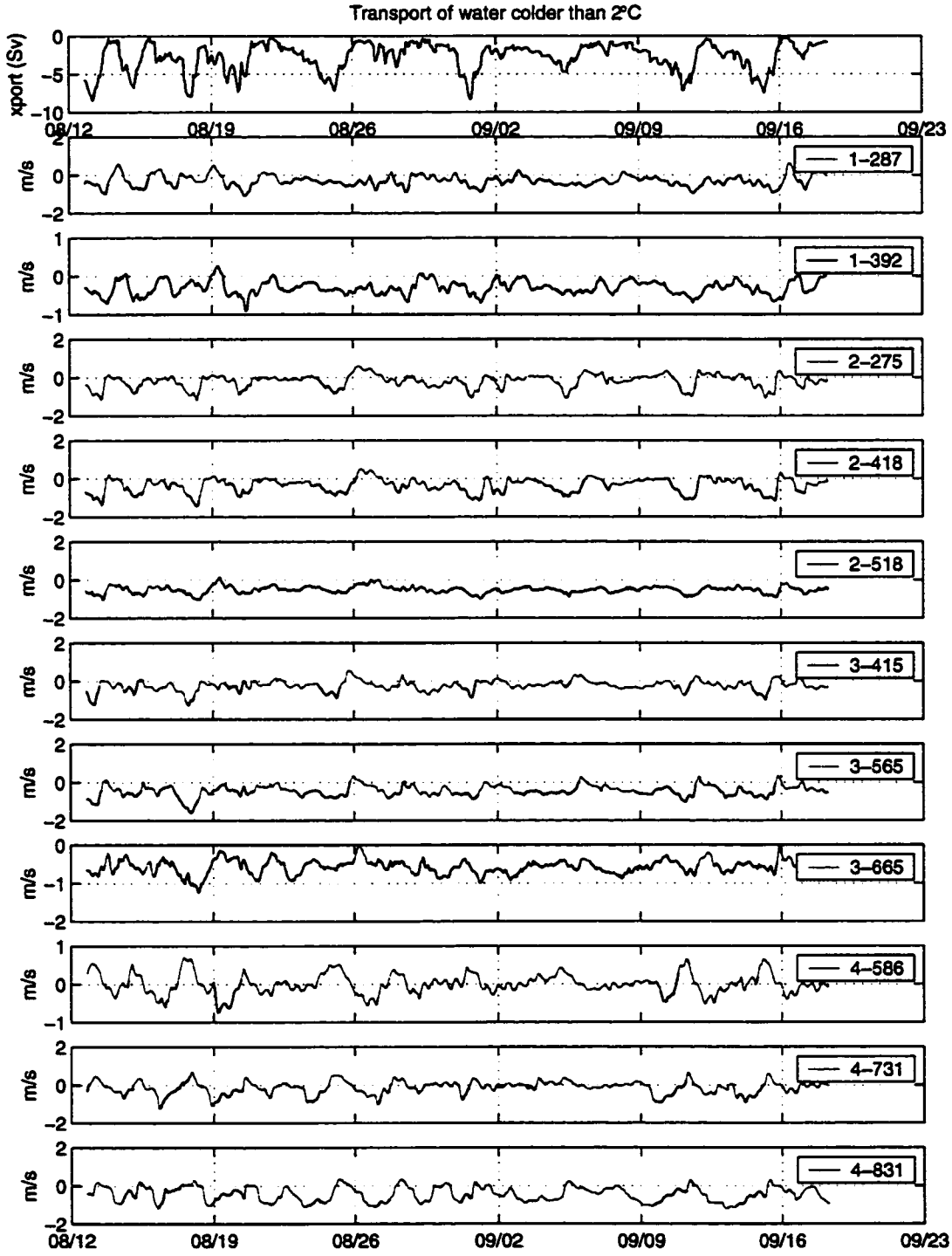


Figure 5.3: Top panel: Timeseries of transport of water colder than 2°C from O73 current meters. Negative values indicate flow to the southwest (towards 250°T). Other panels: Timeseries of velocity normal to the O73 array at each current meter. Blue indicates water colder than 2°C. Meters are labeled with the mooring number (1–4, where 1 is on the Greenland shelf) and instrument depth so that, *e.g.*, 4-831 is at 831 m depth on mooring 4.

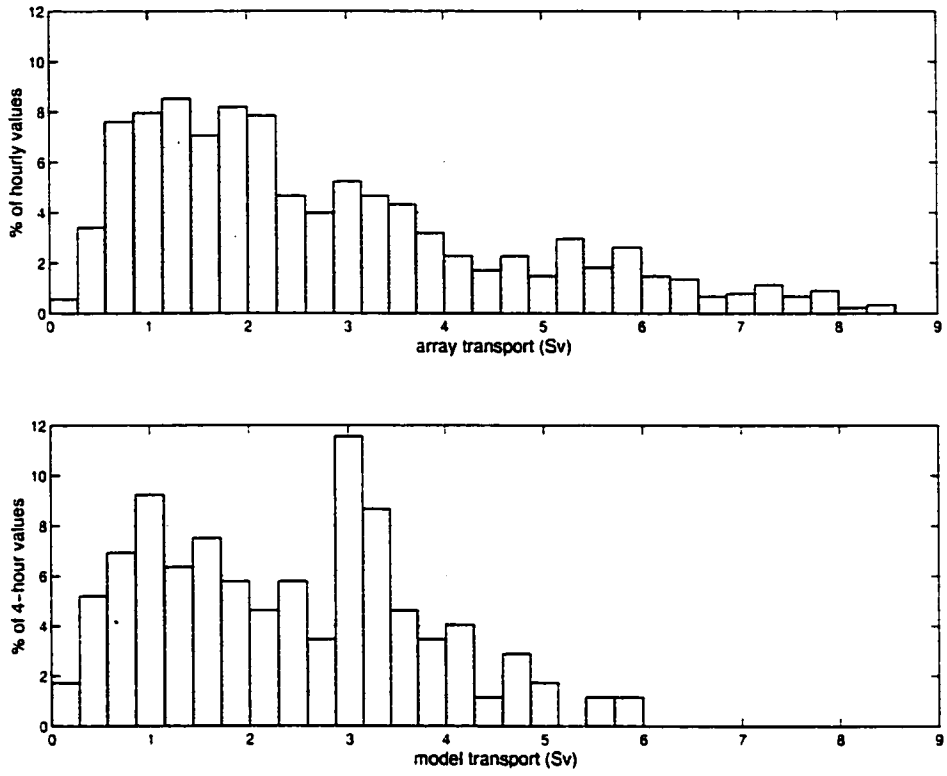


Figure 5.4: Transport distributions for $\theta < 2°C$ from a) Ross current meters and b) KO model.

5.3 Subsampling

In order to compare our measurements and O73, I performed two subsampling exercises. The first was to use observations at the same spacings and heights off the bottom as the O73 array instruments to estimate an "array-sampled" version of $\theta < 2°C$ transport in each of our velocity and temperature sections. The resulting transports are shown in the rightmost column of Table 5.1. Although some subjectivity exists in the choice of interpolation points along sections that were not congruent with the original array location, the array-sampled positions on those sections not lying close to the O73 array were chosen by projection along topography (the 400 m isobath in particular) as realistically as possible. The cumulative probability distribution of these array-sampled values (Figure 5.5) lies almost on top of that from

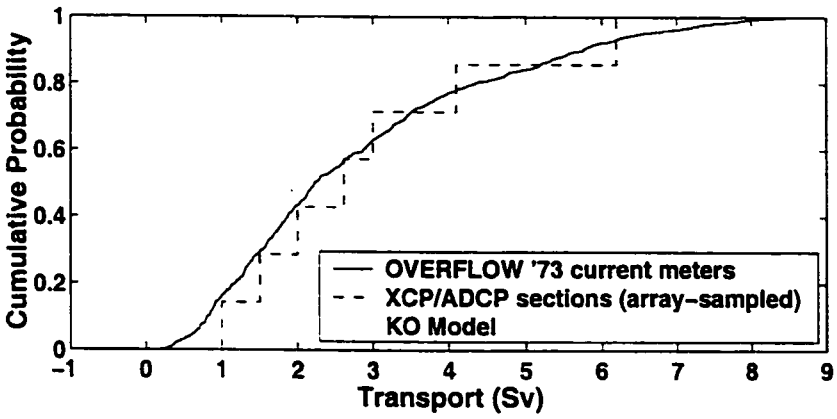


Figure 5.5: Cumulative probability distribution functions for O73 current meter transports (solid), array-sampled $\theta < 2°C$ transports from the 7 near-sill *Poseidon* sections (dashed), and numerical model transports (dotted).

the O73 array, with the Kolmogorov-Smirnov (K-S) test [*Press et al.*, 1995] finding the two distributions to be indistinguishable (null hypothesis) to the 99% confidence level. Perhaps fortuitously, the mean of the array-sampled values in Table 5.1 also falls very close to the mean of the $\sigma_\theta > 27.8$ values, indicating that the O73 array transport may, in fact, be a good proxy for the dense water.

The second exercise repeatedly picked 7 values at random from the O73 transport timeseries to construct probability distributions for the 7-sample maximum, minimum, mean, median and standard deviation. I found that each of these statistics from the array-sampled values fell within a $\pm 1\sigma$ (67%) probability range from the O73 distribution. This, along with the K-S test mentioned above, shows that our measurements are comparable in magnitude and variability to the transport observed during the O73 period.

5.4 Model Comparison

Because our observations are snapshots of a variable phenomenon, I have collaborated with Rolf Käse on a numerical process model with realistic topography and parameters appropriate to the DSO. The sigma-coordinate model described by KO is configured in both "source-driven" and "dambreak" scenarios.

In the source-driven case, described in KO, the model initially contains only warm (5°C) water everywhere. Then the source basin of the model receives a constant input of 0°C water near the bottom and an equal transport of warm water is removed from the upper layer. After about 30 days, the source basin fills with cold water to a level where cold water spills over the sill into the receiving basin. This induces an equal transport of receiving basin water into the source basin as a shallow compensating flow. More than a month after the cold water first spills over the sill and before it reaches the end of the receiving basin, the model exhibits many of the principal characteristics of the observations, including considerable variability superposed on the mean flow. The variability consists of strong barotropic eddies which occasionally interrupt the overflow. The transport histogram in the lower panel of Figure 5.4 shows a similar distribution to that in the O73 current meters, but with a more prominently bimodal character and a smaller high-end tail.

In the dambreak case, tuned to match parameters observed in the summer of 1998, light ($\sigma = 27.55\,\mathrm{kg\,m^{-3}}$) water fills the southern basin and overlies a denser ($\sigma = 28.03\,\mathrm{kg\,m^{-3}}$) layer in the northern basin. Once the model run begins, an exchange flow is set up with interface height and transport varying nearly as predicted by the steady theory. Since the reservoir is finite the exchange decreases with time as the interface height is lowered, and the northern basin is filled with lighter water at the top. The mean transport at the sill of water denser than $\sigma = 27.79\,\mathrm{kg\,m^{-3}}$is 2.9 Sv.

A snapshot of the model's flow and density structure at the sill (Figure 5.2, panel h) contains many of the features present in our observations including a sloping density interface, dominantly barotropic velocity structure with some bottom intensification, and recirculations on both sides of the outflowing jet. The model's mean cumulative transport function, shown by the dashed line in Figure 5.2 (panel i), lies very close to the mean transport from our seven sections. This agreement, despite the model's closed-basin geometry and lack of surface forcing, indicates the degree to which the overflow represents a purely source-driven flow, controlled by topography.

The model and observations indicate the significant transition from barotropic flow over the sill to predominantly baroclinic further down the slope. Also, the importance of bottom friction is captured in the model results. The model uses a Rayleigh-

type parameterization for bottom friction, $\tau/\rho = r_d U$ where U is the velocity of the bottom layer of the model and r_d is a constant equal to $4.15 \times 10^{-4}\,\mathrm{m\,s^{-1}}$. As mentioned earlier, the mean and median of this parameterization are in reasonable agreement with the observed values of τ/ρ. Note that the friction increases downstream because of two effects. The flow accelerates first as the slope increases in accordance with geostrophic influences and second as the bottom falls away.

5.5 Hydraulic Control

The geostrophic transport of a dense layer through a constriction wider than the baroclinic Rossby radius is limited by hydraulic and potential vorticity constraints to a value of $\frac{g' h_u^2}{2f}$, where f is the Coriolis parameter, g' the reduced gravity and h_u is the height above the sill of the upstream layer interface [*Whitehead*, 1998; *Killworth and MacDonald*, 1993]. Using the conditions in the northern basin during the summer of 1998 ($g' = 4.3 \times 10^{-3}\,\mathrm{m\,s^{-2}}$ and $h_u = 550\,\mathrm{m}$) gives a maximal transport of 4.9 Sv. Depending on the choice of hydrographic stations used, this estimate could be as high as 5.3 Sv, but is certainly at least 50% higher than both the observed and modeled transports.

The discrepancy is probably due to frictional or time-dependent effects, both of which are substantially present in the model and in the observed overflow. KO show that the model transport reaches the maximal value at times but is often restrained by a geostrophic front created by flow recirculation towards Greenland at the sill. In addition, estimates of near-bottom shear stress obtained from XCP profiles which reach into the turbulent boundary layer suggest that friction plays an important role in the dynamics of the overflow. Bottom stresses in the sections discussed here range from 0.04–6.7 Pa (median of 0.4 Pa), and a comparison with the velocity at a height of 50 m above the bottom yields an estimated drag coefficient of 3.1×10^{-3}. These values are comparable to those observed in the Mediterranean outflow [*Johnson et al.*, 1994], in which it has been shown that both bottom and interfacial stresses are important elements of the momentum balance in the descending plume. *Pratt's* [1986] parameter for the relevance of bottom friction in hydraulic flows, $\frac{C_d L}{H}$, (assuming an along-channel approach length, L, of 100 km and layer thickness, H, of 200 m) yields a value of 1.5, indicating that frictional forces may be significant. Interestingly, sig-

nificant differences in the KO model transports are not found between runs conducted using different values of (linear) bottom friction, but this may be because the "high" value of $r_d = 4 \times 10^{-4}\,\mathrm{m\,s^{-1}}$ (corresponding to 0.2 Pa at $0.5\,\mathrm{m\,s^{-1}}$) is still too low. The expected influence of bottom friction on transport is not clear, however, and it may still be possible to achieve maximal flow in spite of substantial friction if geostrophic constraints are more important than inertial ones.

Another possible limiting factor might be the time-dependence of the flow. In particular, *Pratt* [1991] describes the potential for "geostrophic control" to operate when the frequency of dominant variability, ω, falls within the range

$$f \gg \omega \gg \left(\frac{f\Delta\eta}{H}\right)\Delta^{-1}, \tag{5.1}$$

where f is the Coriolis parameter, $\Delta\eta$ is the change in interface height across the sill, H is the lower layer thickness, and Δ is a parameter which depends on the ratio of the strait width to Rossby radius (varying from about 1–50 as the width of the strait varies from 0.2–10.0 Rossby radii). In the DSO, using typical near-sill values of $H = \Delta\eta = 400\,\mathrm{m}$ and taking the width of the deepest channel at the sill to be 30 km, terms in (5.1) become

$$1.3 \times 10^{-4}\mathrm{s}^{-1} \gg \omega \gg 9 \times 10^{-6}\mathrm{s}^{-1}. \tag{5.2}$$

A typical DSO value of $\omega = 3 \times 10^{-5}\mathrm{s}^{-1}$, corresponding to a period of 2.5 days, falls within this range. Hydraulic control may become valid for frequencies below the rightmost term in (5.2), but this is difficult to define reliably because the strait width could be as large as the broad 300–400 m-deep shelf between Greenland and Iceland, *i. e.*, more than 200 km. This means that geostrophic control could operate to periods as long as 60 days.

Finally, the Denmark Strait contains neither a true 1.5-layer flow nor a 2-layer exchange but has elements of each, in addition to a barotropic component. The slowly-inflowing upper layer partially balances the outflow but does not provide a constraint to the volume flux since most of the inflow occurs to the southwest of Iceland. Where baroclinic shear is substantial, the constraints of geostrophic control may cause the inflow to further restrict the outflow.

In fact, considering the drastic differences between the real flow observed in the Denmark Strait and the idealized flow described by hydraulic theory, it seems re-

markable how close the hydraulic prediction does come. Is this pure coincidence or are the hydraulic constraints able to operate on the larger scale of the overflow despite seeming violations in the local dynamics? A more detailed accounting for the piecewise energy and vorticity budget of the flow may help to answer this question.

5.6 Tides

According to both current meter measurements and a finite-element model [*LeProvost et al.*, 1994], tides are substantially smaller than the measured velocity fluctuations, although not insignificant. Due to the correlation between lower layer thickness and velocity, the removal of tidal currents from our measurements is probably not desirable, even if it is possible.

5.6.1 OVERFLOW '73

Tides are evident in the O73 current meters but only a small part of the velocity variability in the overflow itself can be attributed to tides. Figure 5.6 shows the M2 tidal ellipses computed from fitting 8 constituents to the 5-week mooring record. In the northern basin, the tides are substantial, reaching $0.25\,\mathrm{m\,s^{-1}}$ and making up by far the majority of the signal, while in the array of primary interest for this study (50 km southwest of the sill) tidal currents are less than half that, and only account for 2–10% of the total variance in these records.

5.6.2 FES94

I have compared the tidal constituents derived from the O73 current meters with the barotropic currents from the FES94 tide model *LeProvost et al.* [1994] interpolated to the mooring positions. While the amplitudes of the model tides are similar to the tides in the mooring data, the phases of the constituents are substantially different. These differences make it unlikely that a meaningful detiding could be performed using the model results.

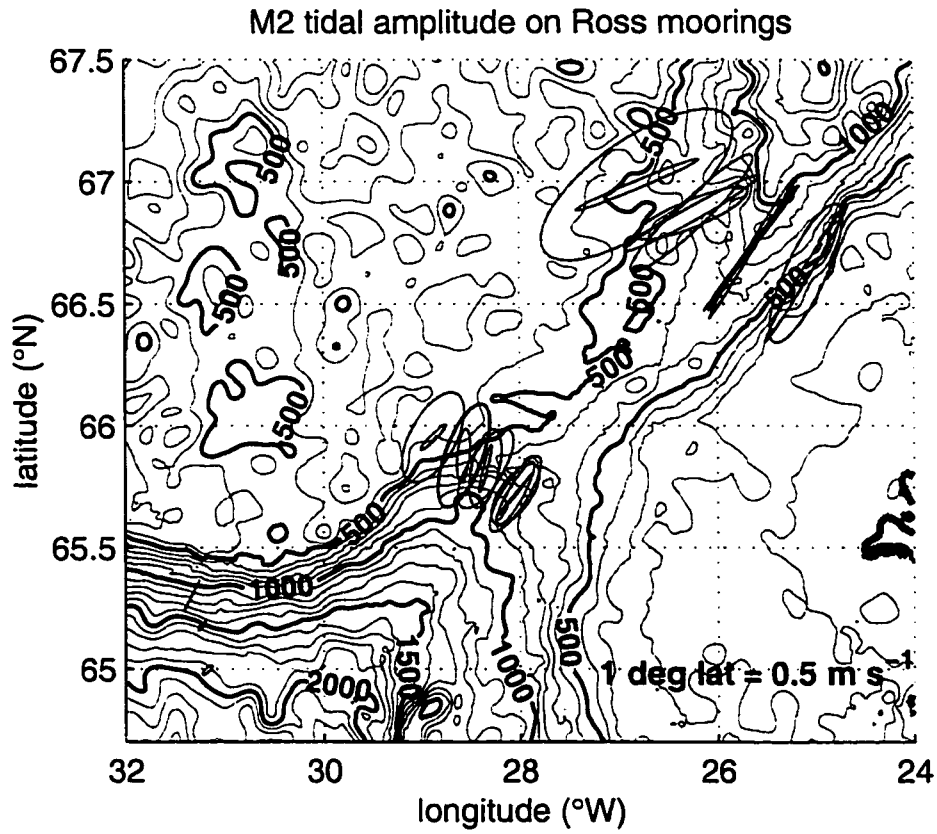


Figure 5.6: Amplitude of the M2 tide determined from the O73 mooring data. The largest signals are in the northern basin with currents reaching 0.2–0.3 m s^{-1} while in the central overflow array they drop to 0.1 m s^{-1} or less.

5.7 Atmospheric Pressure

I have also looked into an additional possible source of velocity variance through atmospheric forcing. *Ross* [1976] saw a hint of this in his data but was not able to make sense of the analysis. From an initial look at NCEP reanalysis fields for the period of the *Poseidon* survey, neither a direct atmospheric pressure (inverted barometer) driving nor a direct correlation with wind seems likely. The synoptic atmospheric variability occurs on much longer periods than the velocity fluctuations in the strait.

5.8 Conclusions

My estimate of the mean transport of 2.7 ± 0.6 Sv of dense water through the Denmark Strait, made over a 1-week period, is essentially identical to the 2.9 Sv of cold water measured in 1973 [*Ross*, 1984]. In fact, while our measurements show that the $\theta < 2°C$ criterion encompasses a substantial amount of non-overflow water, the positioning of the O73 array was able to give a reasonable measurement of overflow transport. Although both the O73 program and our new measurements took place in late summer and neither was of particularly long duration, the equivalent results do add more evidence to support the view of the DSO as an unchanging, hydraulically-controlled flow on timescales longer than a few days. This view is supported by current meter studies in the DSO to date, both upstream and downstream of the sill, which have been unable to identify significant seasonal or interannual variability [*Aagaard and Malmberg*, 1978; *Dickson and Brown*, 1994].

Recent hydrographic studies of the dense water downstream have brought the steady-state into question [*Bacon*, 1998; *McCartney et al.*, 1998] but are vulnerable to errors due to assumptions about geostrophic reference levels. In addition, the multi-year changes in atmospheric forcing and convective activity of the Nordic Seas discussed by *Dickson et al.* [1996] are likely to have some effect on the DSO, and it is surprising that this has not yet been seen. Perhaps the answer lies in the substantial variety of source waters available to supply the overflow (generated by processes in the Arctic Ocean, Greenland Sea, Iceland Sea and East Greenland Current, see *Rudels et al.* [1999a]), combined with the restraint imposed on the flow by the shoaling and constriction in the Strait.

Chapter 6

OVERFLOW PATH, MOMENTUM BUDGET AND ENERGETICS

In this chapter a number of bulk properties of the DSO will be investigated using the entire ensemble of sections from both the *Poseidon* and *Aranda* cruises. This ensemble includes 18 cross-sections of overflow velocity and density (described individually in Chapters 3 and 4) extending between the sill and 250 km downstream. The hope is that by including data from two separate years and a number of distinct passes through the region, a consistent picture can be constructed of both the mean properties of the overflow plume and the envelope of variability of these properties. In fact, the number, timing and positioning of sections appears to be just sufficient to characterize both the high and low-transport overflow regimes and give a reasonable picture of downstream trends and envelope variability of certain properties, while the detection of other trends is clearly swamped by the large variability.

6.1 Streamtube Theory

In it's most basic description, the DSO can be thought of simply as a slab of dense water sliding down the continental slope through a stratified background (Figure 6.1). The flow trades the potential energy it possesses through its density anomaly and height on the slope for downstream kinetic energy, which is in turn a) used to accelerate ambient fluid entrained into the flow and b) extracted by turbulent stresses in the bottom boundary layer.

Cross-isobath transport and release of available potential energy (APE) are firmly linked to the overflow's ability to overcome the constraints of geostrophic balance, which tends to prevent APE release. One way for geophysical fluids to release APE is through friction, which reduces velocities and resulting Coriolis accelerations. Figure 6.2 illustrates how the resulting balance between downslope gravitational force, Coriolis force and retarding friction produces an angled path, with the flow's downward angle decreasing as slope and density anomaly decrease through entrainment

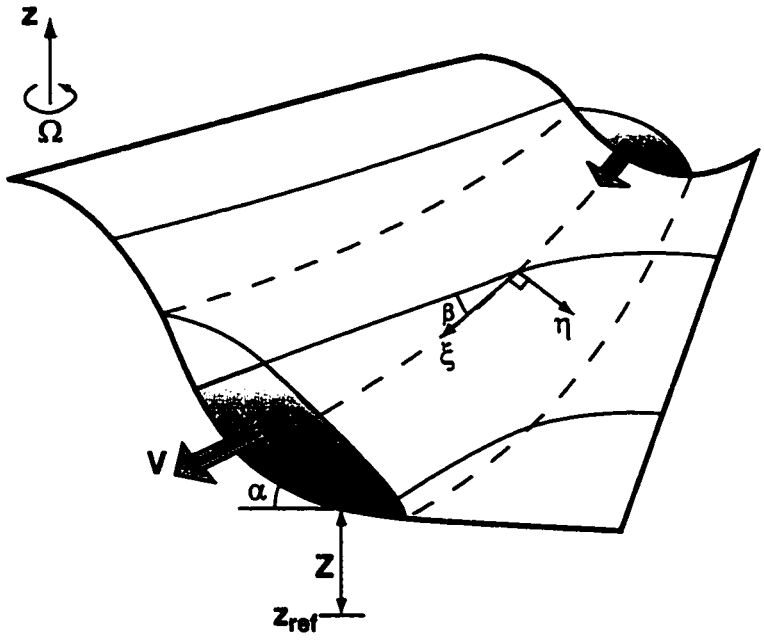


Figure 6.1: Schematic illustration of the streamtube concept, intended to capture the dominant physics of bottom density currents and overflows.

or flow into denser background water or less-steep topography. This simple force balance allows the calculation of the rate of plume descent as simply

$$\frac{dZ}{d\xi} = -\sin\alpha \sin\beta = \frac{\tau \cos\gamma}{\rho' g h}, \tag{6.1}$$

where τ is the magnitude of the combined bottom and interfacial stresses and γ is the angle between the stress and velocity vectors. This is the idealized situation studied with simplified analytical and numerical "streamtube" models [*Smith*, 1975; *Killworth*, 1977; *Price and Baringer*, 1994] and, to a large extent, it is a valid description of the DSO. Applications to date for the DSO have not looked in any detail at the entrainment region that is the focus of this study, but have focused on the steadier regions further downstream, where the streamtube assumptions are arguably more valid.

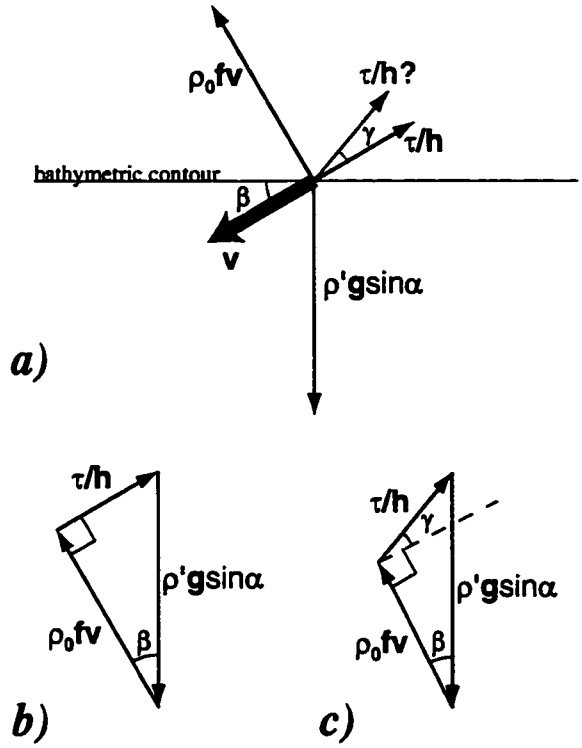


Figure 6.2: Dominant balance of forces on a 1-D slab-like overflow, illustrating how friction allows descent across bathymetric contours. Panel *c* shows how if the stress (τ) is applied not in the reverse direction to the velocity but at some angle (γ), the downslope angle (β) can be diminished (see Eq. 6.1).

6.2 Observed Quantities

In order to investigate a streamtube description of overflow dynamics from real observations and sampling patterns, it is necessary to make some compromises. The true structure of flow and hydrography involves far more complex patterns than the simple one-dimensional properties of the streamtube, so choices in how to average or transform the observations into the desired integral quantities for comparison may have an impact on the credibility of the model. Figure 6.3 illustrates some of the choices and defines the variables used in the following descriptions.

First of all, I have chosen to define the overflow in terms of density, including

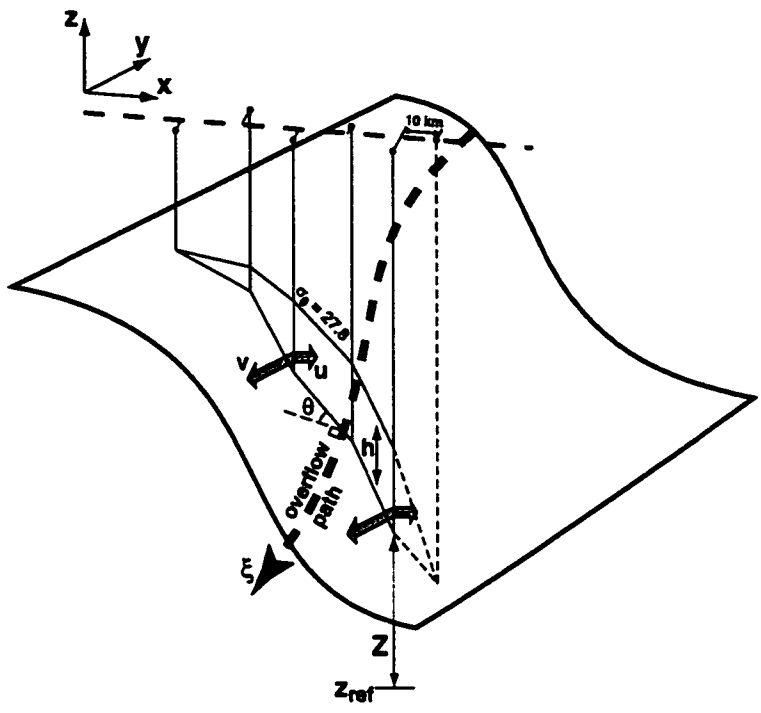


Figure 6.3: Use of a velocity and water properties section to determine streamtube quantities.

all water with σ_θ>27.8 kg m^{-3}, following *Dickson and Brown* [1994].[1] Fortunately, the $\tilde{\rho}$ profile constructed from stations in the interior of the Irminger Basin does not reach 27.8 kg m^{-3} until 2000 m depth (essentially the maximum depth reached by the overflow in the survey area), so this appears to be an adequate way to define the overflow for determining general characteristics.

The sections making up our survey were not always perfectly straight lines and were not always perpendicular to the overflow's path. In order to estimate along-section distance, then, the station positions have all been projected onto a best-fit line for the section. When cross-sectional area is important, the approximate angle, θ, of this line to the flow path normal has been estimated and used as a scaling factor

[1]In the discussions which follow, density (ρ) will always refer to potential density referenced to the surface, and $\sigma_\theta = \rho - 1000$. At times it will be convenient to decompose density into a constant mean (ρ_0), stratified background ($\tilde{\rho}$) and anomaly (ρ'), as shown in Figure 6.4.

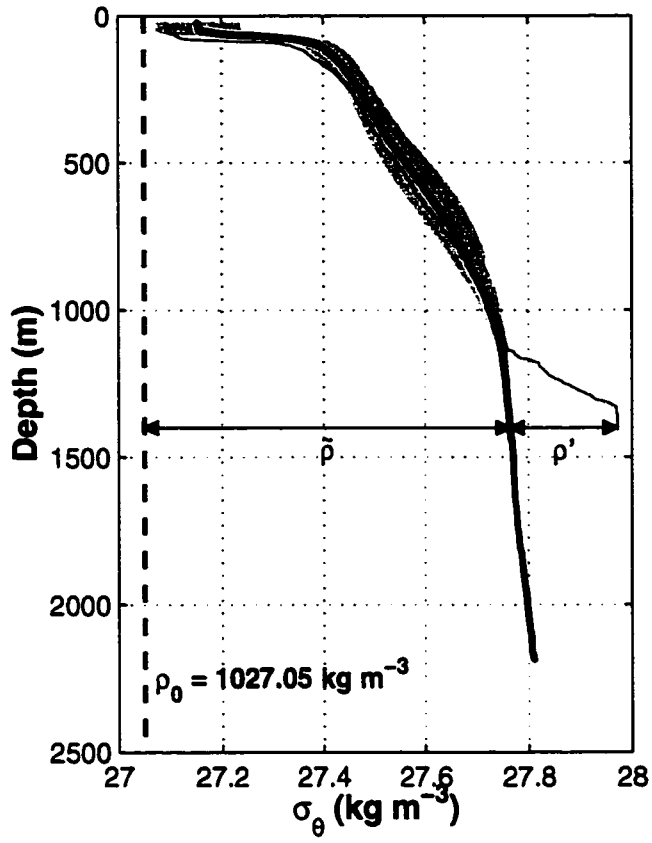


Figure 6.4: Decomposition of density into mean, background and anomaly contributions. The thin red line is a typical overflow density profile. The thick black line is the mean background ($\tilde{\rho}$) density profile from several profiles in deep water either above or beyond the boundaries of the overflow water. Gray shading covers the region within 1 standard deviation of the mean.

for integrated values. For example, the cross-sectional area of the overflow is

$$A = \cos\theta \iint_A dz dx = \cos\theta \int_W h dx \tag{6.2}$$

where h is then the thickness of the overflow layer, $\int_W$ denotes integration across the width of the overflow water and $\iint_A$ specifies an integration over the cross-sectional area of the overflow water. In general, most such areal integrations are constructed by deriving averages for the overflow water in each profile, along with thickness h, and then integrating along the section ($\int_W dx$) using the trapezoidal method.

The scaling factor θ is not used when through-section property fluxes are calculated, since the integrated velocity perpendicular to the section is independent of

angle. For example, the volume transport of overflow water is

$$Q = \int\int_A v dz dx = \int_W \bar{v} h dx, \tag{6.3}$$

where v is the component of velocity perpendicular to the best-fit section line and $\bar{v}$ is the layer mean for a single profile.

Certain mean quantities for streamtube comparison can be equivalently derived from others, such as an overall velocity

$$V = \frac{\int\int_A v dz dx}{A} = \frac{Q}{A}. \tag{6.4}$$

Many of the results presented in this chapter deal with density-anomaly-weighted averages of various properties, which are compared to the constant properties assumed by the streamtube concept. This approach has been employed using data from a survey of the Mediterranean outflow [*Baringer and Price*, 1997] with considerable success. Two of the simplest such quantities to define are the position of the center of mass anomaly,

$$X = \frac{\int\int \rho' x dz dx}{\int\int \rho' dz dx}, \tag{6.5}$$

and the anomaly-weighted bottom-depth,

$$\overline{Z} = \frac{\int\int \rho' Z dz dx}{\int\int \rho' dz dx}. \tag{6.6}$$

Some uncertainty arises when the stations did not span both edges of the overflow water. In these cases, I have chosen to extrapolate the overflow water to zero thickness at a distance 10 km beyond the end of each section but have also generated "error bars" whose lower limit derives from a lack of extrapolation beyond the section and whose upper limit would result from a constant-value extrapolation to 10 km. Large error bars, then, are an attempt to convey the lack of certain knowledge of overflow extent, although in most cases the 10 km extrapolation to zero does appear to be a reasonable guess, with the error bars generally producing (in my opinion) over-estimates of the probable error.

The calculation of mean quantities presents special problems for those values which could tend to disproportionately weight the overflow edges, such as a mean thickness. Even more difficult is an estimate of overflow width, since many sections did not reach the limit of the overflow water at both ends, while most sections did

cover the vast majority of overflow volume. One way around this is through the use of a plume "half-width," $W_{0.5}$, defined such that

$$\int_{X-\frac{W_{0.5}}{2}}^{X+\frac{W_{0.5}}{2}} \int \rho' dz dx = \frac{1}{2} \iint_A \rho' dz dx \tag{6.7}$$

(*i. e.*, the middle 50% of the mass anomaly is contained within a width $W_{0.5}$). A reasonable estimate of the mean thickness is then given by

$$H = \frac{A}{2 \times W_{0.5}}. \tag{6.8}$$

6.3 Pathway and Descent

The geographical distribution of X from all 18 sections is shown in Figure 6.6 (asterisks), along with estimates of $W_{0.5}$. Despite the great deal of temporal variability in overflow transport, thickness and velocity described in Chapter 5, the mean path appears quite stable. Cross-stream variability in X decreases from only 15 km or so within the first 50 km of the sill (the region primarily discussed on Ch. 5) to less than 5 km at the western edge of the domain, just over 220 km from the sill.

As shown in Figure 6.5, the plume descends relatively slowly at first (during the first 50 km from the sill) and then at a more-or-less constant rate of 6 m km^{-1}.

The angled lines in Figure 6.5 show the slope in plume depth *vs.* distance expected from Equation 6.1, using mean quantities determined at each section (assuming bottom stress to be the primary contributor to τ and applying the measured magnitude of τ_b in the direction exactly opposite to $\mathbf{v}$—*i. e.*, $\gamma = 0$). If τ_b is permitted to act at an angle to $\mathbf{v}$, the resulting rate of descent will be diminished somewhat due to the Ekman veering near the bottom of the velocity profile (Figure 6.2).

While the bottom stresses, and, hence, the expected rates of descent, do vary considerably from section to section, the plume depth shown in Figure 6.5 is the result of the integrated history of descent that the flow has undergone since the sill, and so is expected to be substantially smoother than other in-situ properties. This might not be the case, however, if the inhomogeneities in τ were linked to individual water parcels (say, propagating boluses or pulses which carry anomalous water and isolate it from its surroundings). The relative variance in τ and depth, then, holds important implications for the phenomenology of the overflow pulses and sets a limit on the

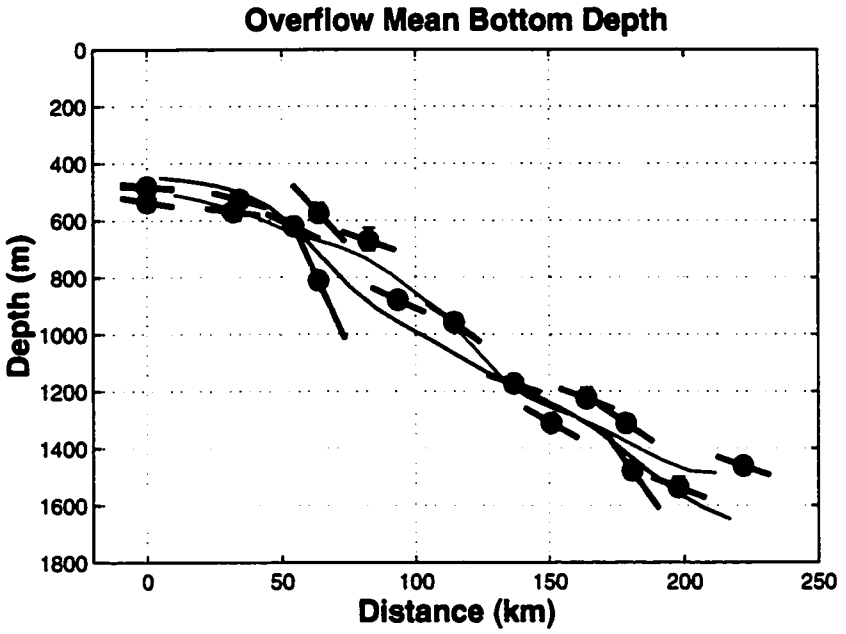


Figure 6.5: The descent of the overflow with distance from the sill (including sections E and D from the *Aranda* cruise). The red dots show Z, the mass-anomaly-weighted bottom depth of the plume (Eq. 6.6) for each section. The thick blue angled lines indicate the rate of descent, $\frac{dZ}{d\xi}$, expected from a simple balance between buoyancy, Coriolis force and bottom stress (Eq. 6.1). The continuous red and blue lines compare the smoothed Z values and a smoothed integration of $\frac{dZ}{d\xi}$, respectively.

internal isolation of features.

6.3.1 Drag Coefficient

The log-fit determined values of bottom stress can be compared to the absolute speed of the water (at 50 m or some other height above the bottom) to estimate a drag coefficient. In aggregate (Figure 6.7), bottom stress estimates yield $C_D = 3 \times 10^{-3}$, in good agreement with other studies of oceanographic flows. The chosen height of 50 m was intended to be above the boundary layer but still within the overflow water. In fact, due to the frequently large barotropic component of velocity, the mean value of C_D does not depend strongly on the depth chosen.

Experiments with a numerical model described in *Käse and Oschlies* [2000] (hereafter KO), as well as earlier results from simpler models [*Price and Baringer*, 1994],

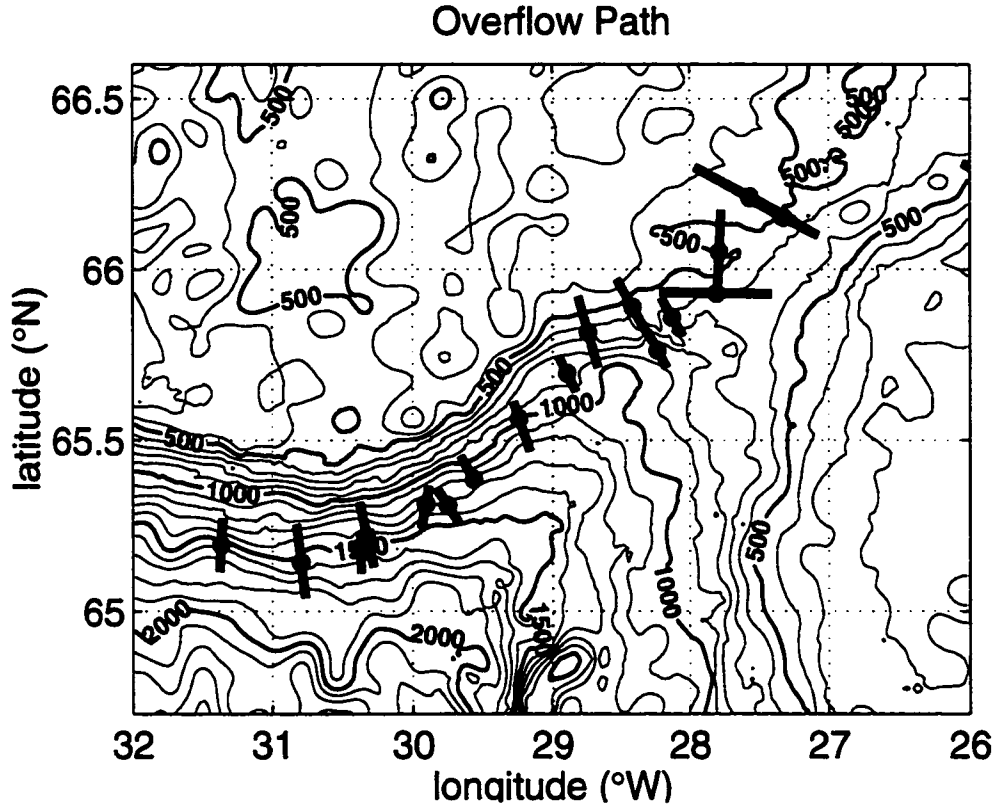


Figure 6.6: Position of overflow center of mass (X) and half-width ($W_{0.5}$) on each of 18 cross-sections. Apart from some variability at the sill and early in the descent, the flow follows a well-defined path with remarkably little cross-stream scatter.

have shown that the pathway of the overflow plume depends strongly on the amount of bottom friction used. The model's (linear) drag coefficient that appears to give the best agreement with the measured pathway, though, yields a substantially lower bottom stress value than the median obtained from our observations.

6.3.2 Slippery Boundary Layers

Bottom shear stress is often a dominant process retarding deep currents, but its importance may be reduced in cases where the near-bottom stratification and topographic slope are substantial. As *MacCready and Rhines* [1993] point out, buoyancy transport by the bottom Ekman layer can lead to both a shut-down of the Ekman flow

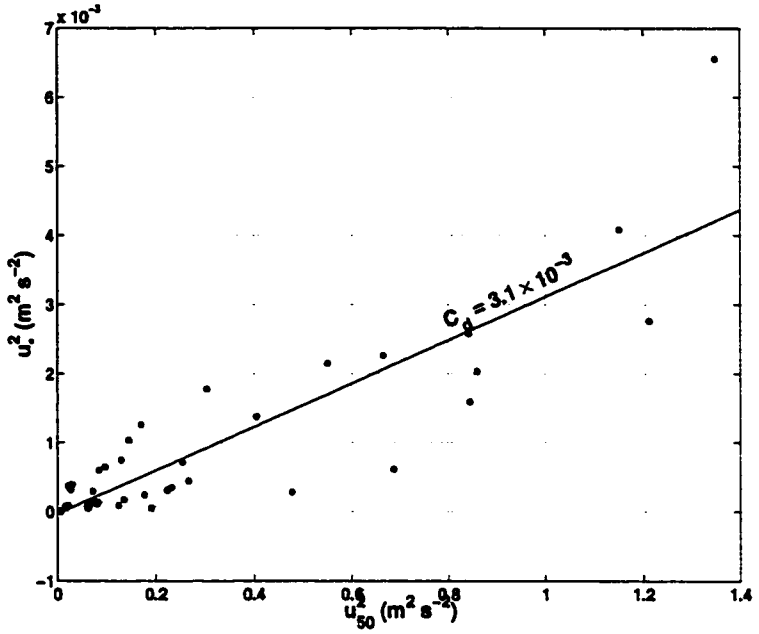


Figure 6.7: Best guess at C_D from linear fit of u_*^2 *vs.* u_{50}^2, where u_{50} is the speed 50 m above the bottom.

and a reduction in near-bottom velocities through thermal wind shear. This process has the potential to greatly reduce the energy lost to turbulent stresses but may be difficult to detect in the DSO.

For one thing, the interior of the overflow does not appear to be noticeably stratified in the cross-stream direction, making any interior Ekman flow ineffective in producing buoyancy forces. This same difficulty was noted in a survey of the Deep Western Boundary Current at the Blake Outer Ridge (some 6000 km downstream of the Denmark Strait) [*Stahr and Sanford*, 1999]. This appears to point toward a substantial difference between the type of boundary layer beneath a plume of anomalous fluid entering (under its own power) a stratified ocean and the general case of a boundary layer beneath a stratified current (driven by external forces).

It may still be possible, however, for the stratification at the upslope edge of the plume to contribute to thermal wind shear, reducing stress and further downslope flow at that edge but not at the lower edge. This would contribute to the spreading of the plume, and would also tend to reduce the the entrainment of ambient fluid from

the upslope edge. For a given topographic slope α and buoyancy frequency N, the Ekman transport process can induce a thermal wind shear of, at most [*MacCready and Rhines*, 1993],

$$\frac{\partial v}{\partial z}_{\max} = \frac{\alpha N^2}{f} \tag{6.9}$$

which is set up on a timescale,

$$t = \frac{f}{(N\alpha)^2}. \tag{6.10}$$

Using values observed near the upper edge of the plume of $N^2 = 2 \times 10^{-5}\,\mathrm{s}^{-2}$ and $\alpha = 0.04$ gives a shear of $0.6\,\mathrm{m\,s}^{-1}$ over a 100 m layer and a timescale of just over an hour. In many cases, the observed shears in the near-bottom region are considerably larger than this (see Appendix B), particularly in the presence of the strong barotropic currents which tend to dominate the upslope edge of the overflow in the survey region. The short timescale does imply, though, that once the shear reduces to a supportable magnitude, the adjustment could be quite rapid.

6.3.3 Other mechanisms for cross-isobath transport

Another process which can break the geostrophic constraint and allow APE release and descent across topography is baroclinic instability. However, the potential for linear instability of the DSO in the region of steep plume descent is limited by the magnitude of the slope there [*Swaters*, 1991]. It may be possible that flow instability occurs earlier, over the gradual topography of the sill region. In this case, the inhomogeneities produced near or before the sill could become amplified during the descent of the slope. This topic will be addressed further in Chapter 7.

6.4 Mixing and Momentum

Compounding the loss of potential energy due to its descent, the plume's density anomaly also undergoes substantial dilution with distance from the sill. This dilution is clearly due to mixing with the surrounding waters, but whether this is through a vertical (diapycnal) process at the interface or more through horizontal (isopycnal) stirring by eddies is not yet entirely certain. In either case, the addition of non-moving ambient fluid acts to reduce the kinetic energy of the flow while conserving momentum. This slowing is termed "entrainment stress."

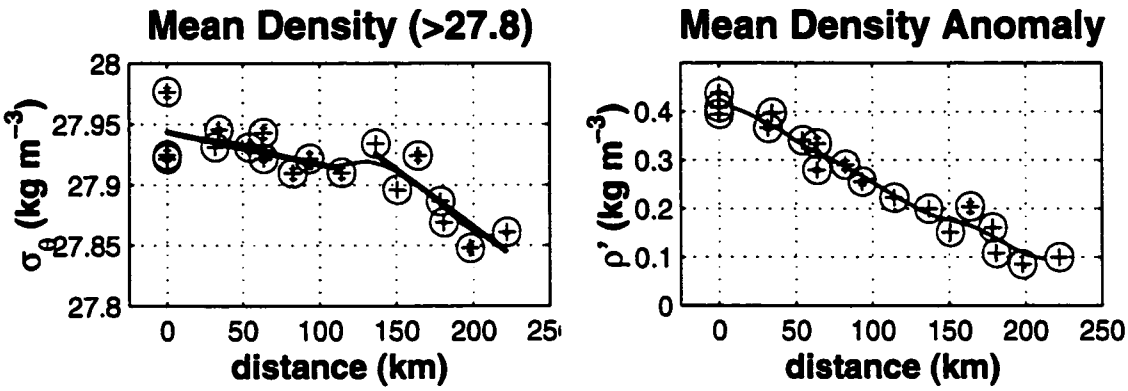


Figure 6.8: Evolution of plume density ($\overline{\sigma_\theta}$) and density anomaly ($\overline{\rho'}$) with distance from the sill. The solid red line is from a smoothing of the points with a 20 km Gaussian window. The two green lines in the left-hand panel are from linear fits to the regions before and after 125 km, and seem to show a significant change in slope.

If the entrainment process is purely diapycnal, as it must be when the plume boundary intersects the bottom, it can be parameterized as an entrainment velocity (w_e), representing a net volume influx into the plume through a combination of vertical flow across the boundary (in this case, the $\sigma_\theta = 27.8$ isopycnal) and vertical motion of the boundary itself due to turbulent mixing and redistribution of isopycnals.[2]

6.4.1 Density Changes

Both average density,

$$\overline{\sigma_\theta} = \frac{\iint_A (\rho - 1000) dz dx}{\iint_A dz dx}, \tag{6.11}$$

and density anomaly from the background,

$$\overline{\rho'} = \frac{\iint_A (\rho - \rho_0 - \bar{\rho}) dz dx}{\iint_A dz dx}, \tag{6.12}$$

decrease with distance from the sill (Figure 6.8), with the $\overline{\rho'}$ decrease being, of course, larger due to the increasing background density as the plume descends. The fact that $\overline{\sigma_\theta}$ itself does decrease, however, points to the additional importance of the entrainment of ambient fluid. Although the background stratification ($\frac{\partial \bar{\rho}}{\partial z}$) decreases

[2]In fact, due to the isopycnal definition of the boundary, this interpretation could cause problems if there is substantial mixing between the boundary fluid itself and the background, producing anomalous fluid "outside" the plume.

from $4 \times 10^{-4}\,\mathrm{kg\,m^{-4}}$ to $6 \times 10^{-5}\,\mathrm{kg\,m^{-4}}$ (N drops from $2 \times 10^{-3}\,\mathrm{s^{-1}}$ to $8 \times 10^{-4}\,\mathrm{s^{-1}}$) fairly abruptly at around 1000 m, neither the overflow descent nor the rate of ρ' decrease appear to change at this point, while the rate of σ_θ decrease appears to become steeper. A simplistic estimate of average entrainment velocity is:

$$w_e = \frac{VH}{\overline{\rho'}} \frac{d\overline{\sigma_\theta}}{d\xi}, \tag{6.13}$$

where ξ indicates the downstream coordinate, as shown in Figure 6.1. Using the slopes shown in Figure 6.8 to estimate $\frac{d\overline{\sigma_\theta}}{d\xi}$ for the two regions above and below 1000 m (~125 km from the sill), combined with mean values of V, H and $\overline{\rho'}$ in each region, indicates more than an order of magnitude increase in w_e from $6 \times 10^{-5}\,\mathrm{m\,s^{-1}}$ before 125 km to $8 \times 10^{-4}\,\mathrm{m\,s^{-1}}$ after 125 km. This increase could be the result of a decrease in bulk Richardson number,

$$\mathrm{Ri_b} = \frac{\overline{\rho'} g H}{\rho_0 V^2}, \tag{6.14}$$

as the plume anomaly decreases (average $\overline{\rho'}$ goes from $0.34\,\mathrm{kg\,m^{-3}}$ to $0.14\,\mathrm{kg\,m^{-3}}$) and thickness increases (average H goes from 150 m to 240 m). However, the large variability in thickness and velocity make the significance of this decrease difficult to determine. Estimates from section-averaged quantities do show a larger fraction of $\mathrm{Ri_b}<1$ values beyond 125 km from the sill and the mean $\mathrm{Ri_b}$ over the regions before and after 125 km are 1.8 and 1.2, respectively. Another possibility is that it is the decrease in background stratification itself which is responsible for this increase in entrainment. While the large stratification at the layer interface has been the focus of most investigations, the weaker stratification above the interface might have an influence on the shape and penetration of the eddies which drive the entrainment.

Even the lower estimates of w_e above are an order of magnitude higher than values estimated from the few existing microstructure measurements in the Denmark Strait [Oakey and Elliott, 1980]. Although these measurements were far from comprehensive in coverage, they did estimate vertical diffusivities (K_z) resulting from temperature microstructure and determine that microscale turbulent processes alone are insufficient to account for the bulk w_e estimates of *Smith* [1975] (which are on the order of $10^{-4}\,\mathrm{m\,s^{-1}}$—smaller than the downstream region of this study).

In addition to its consequences for overflow mean density, w_e should have a profound effect on transport changes resulting from the inclusion of new water. Fig-

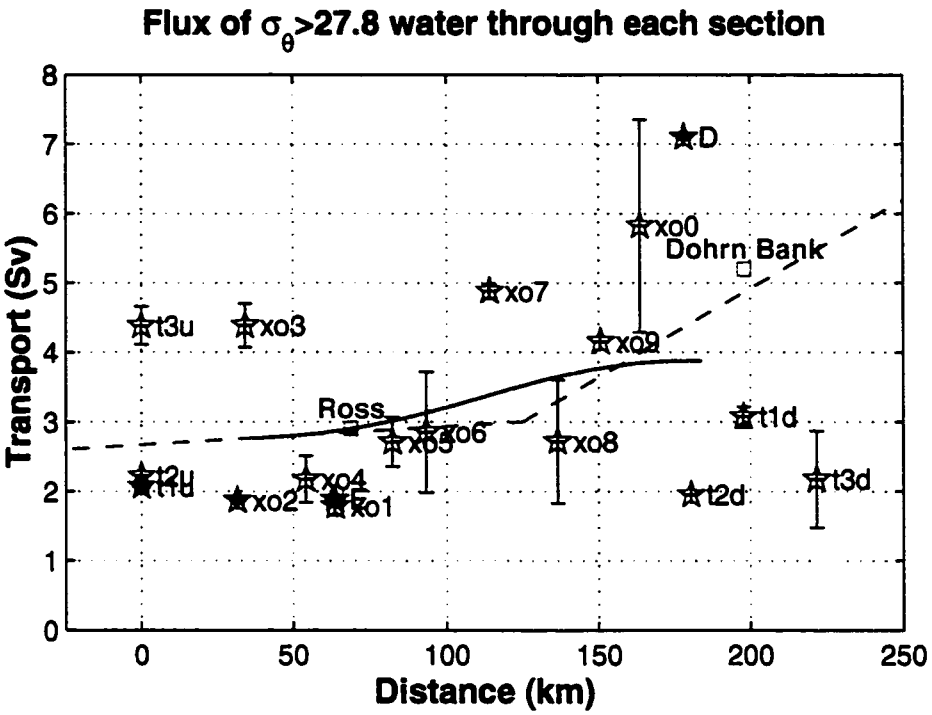


Figure 6.9: Dense water transport (Q) *vs.* distance from the sill, as measured by all 18 sections with XCPs (including two from the *Aranda*) as well as two current meter arrays (labeled as "Ross" and "Dohrn Bank"). Green dashed lines show rates of transport increase expected from constant w_e values of 6×10^{-5} m s^{-1} and 8×10^{-4} m s^{-1} (estimated from Eq. 6.13 and Fig. 6.8 lines) over widths of 44 km and 32 km (average values of $2 \times H_{0.5}$ in the regions before and after 125 km, respectively). The red curve is from a smoothing of the Q values with a 75 km Gaussian filter.

ure 6.9 shows the through-section transport (Q) of σ_θ>27.8 kg m^{-3} water on all sections, demonstrating that the effect of entrainment may be particularly difficult to pick out of the short-term variability present in the measurements. Although the integrating effect mentioned above in Section 6.3 should apply to total transport as well, the constituent measurements of velocity (V) and cross-sectional area (A) are themselves highly variable (see Figure 6.10). In fact, a substantial fraction of total transport may be due to the co-variability of these quantities, casting further doubt on the simplified streamtube model.

Immediately, complications come to mind due to the fact that the overflow does not, in fact, have only a single velocity and density, and the overlying water is neither

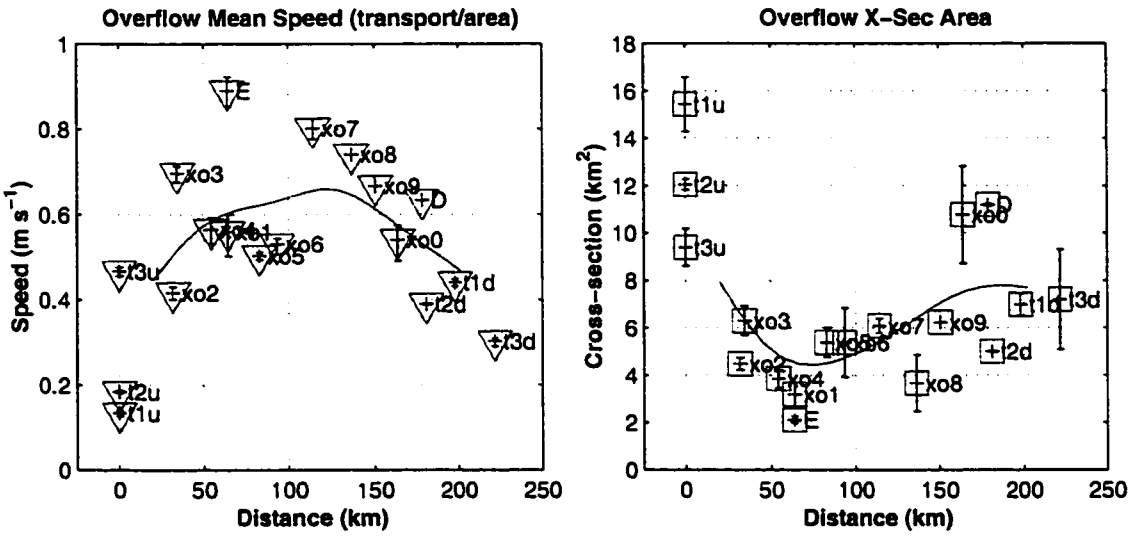


Figure 6.10: Variability of plume velocity (V) and cross-sectional area (A) over distance from the sill. See Equations 6.4 and 6.2 for definitions of these section-averaged quantities. Curves show smoothed versions using a 40 km Gaussian window.

motionless nor uniform in structure from station to station. However, it is important to know how close the reality comes to following these idealized models and whether the dominant force balances are as they describe.

6.4.2 Energy Changes

As mentioned previously, the energy source for the overflow is the potential energy (PE) of the density anomaly due its thickness (internal potential energy—iPE) and height on the slope (external potential energy—ePE). Energy terms are calculated as follows:

$$\text{KE} = \frac{1}{2}\int_W \rho_0 |\mathbf{u}|^2 h dx \tag{6.15}$$

$$\text{iPE} = \frac{1}{2} g \int_W \rho' h^2 dx \tag{6.16}$$

$$\text{ePE} = g \int_W \rho' h Z dx \tag{6.17}$$

Previous studies of oceanic outflows—particularly from the Mediterranean [*Johnson et al.*, 1994; *Baringer and Price*, 1997]—have suggested that the loss of potential energy is primarily due to frictional stresses at the ocean bottom and plume interface.

The expected streamtube momentum balance gives

$$\frac{d}{d\xi}(\mathrm{KE} + \mathrm{iPE} + \mathrm{ePE}) = -\int_W (\tau_b + \tau_i) d\eta. \tag{6.18}$$

In terms of their contribution to the along-stream momentum budget, frictional forces applied over the surface of the plume should produce changes in total energy with downstream distance. Figure 6.11 shows the total energy (TE = KE + iPE + ePE) measured at each section as well as the expected slope ($\frac{d}{d\xi}$(TE)) from bottom stress measurements alone. While the section-to-section variability makes a definitive statement difficult, there does appear to be a decrease in TE with distance, primarily due to the descent of the plume and subsequent loss of ePE. While the magnitudes of kinetic energy (KE) and iPE terms are substantially smaller than that of ePE, there is a hint of an exchange between KE and iPE occurring separately from ePE changes. The major sink of ePE appears to be frictional losses. The exception to this pattern is clearly the high ePE of the sill sections (†1u, †2u, †3u) which does not appear to carry over into the downstream sections. In fact, the sill sections do not release all of their APE into the downslope overflow, in part, due to the presence of a cross-strait geostrophic flow which holds the dense water back. This same effect has been seen in the KO model, with the cross-strait current contributing to both recirculating flow in the northern basin and to the southwestward-flowing East Greenland Current on the shelf. It appears that the intermittency of this front is responsible for (or a consequence of) the majority of the variability in the downstream flow.

Clearly, the streamtube approach is not an appropriate way to connect observations at the sill with those in the overflow downstream. Instead, the less restrictive assumptions of an energy *flux* approach will be considered in Section 6.5.

6.4.3 Entrainment Stress

The overflow undergoes substantial modification during the first 100 km of its path from the sill. At this stage it is passing through the intermediate depth Labrador Sea Water which fills the Irminger Basin between 500 and 1500 m depth, and the influx of this water through turbulent entrainment forms an important part of the intermediate depth thermohaline circulation. The tendency for turbulent mixing can be quantified by measurements of gradient Richardson number ($\mathrm{Ri_g}$), which indicates the ten-

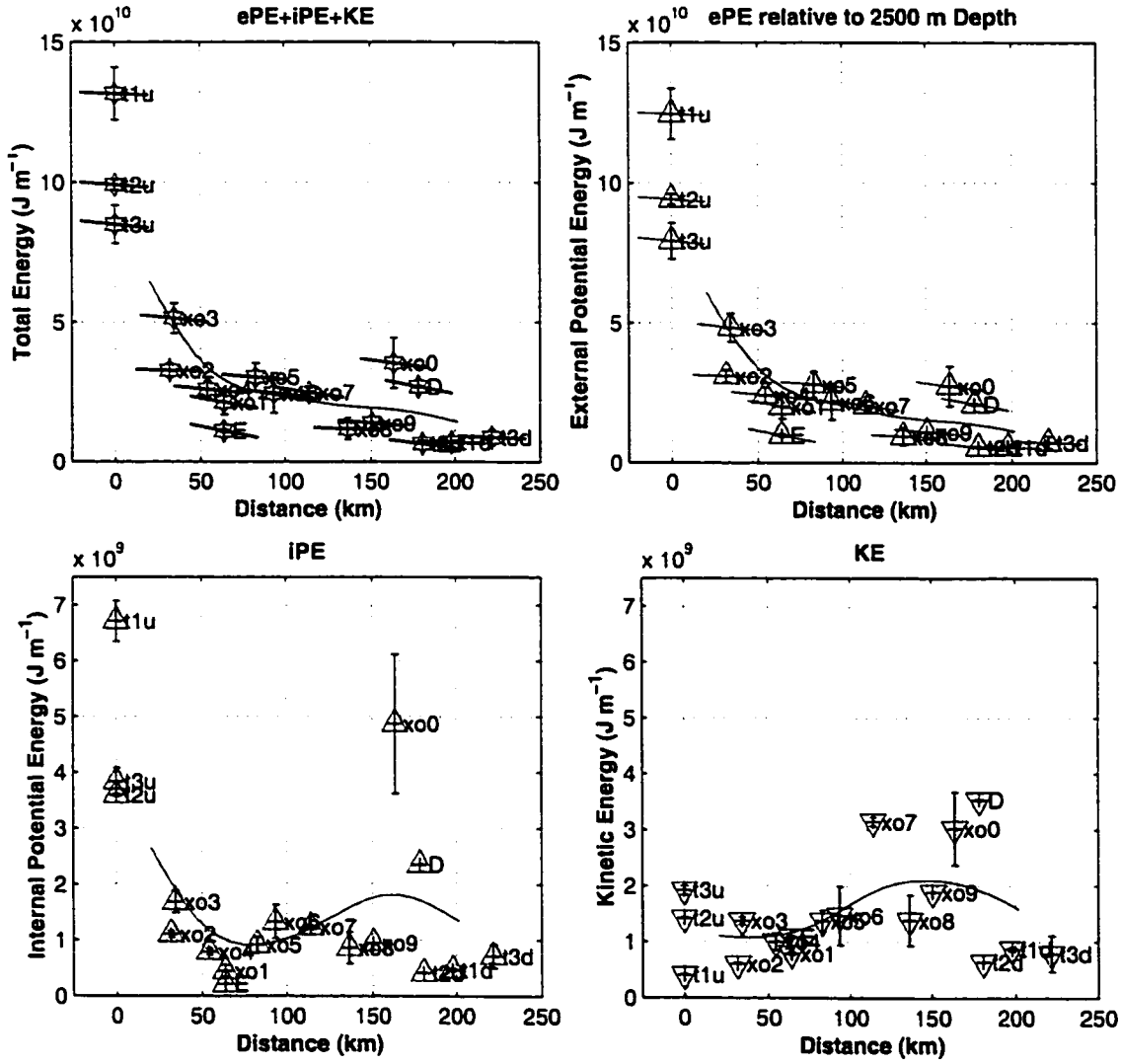


Figure 6.11: Evolution of energy terms with distance from the sill. Note the exponent in the y-axis, with the energy range of the upper two panels a factor of 20 greater than the lower two. The sloping lines on upper-left panel indicate rate of energy loss expected from bottom friction measurements at each section, as determined from Eq. 6.18 (and neglecting τ_i). Solid curves are the values smoothed with a 40 km Gaussian window.

dency for shear instability to occur at values less than 1/4. In their one-dimensional model of oceanic outflows, *Price and Baringer* [1994] use a bulk Richardson number to parameterize entrainment, achieving realistic overflow behaviors. However, it is exactly in the high-entrainment region of the current study that the model is least certain in its predictions.

The stress exerted on the plume itself by the entrainment of slower water may be an important term in the momentum balance. Assuming a steady and continuous flow, *Johnson et al.* [1994] used XCP and hydrographic sections across the plume to compute a bulk estimate of the vertical turbulent buoyancy flux, calculated from the residual of mass and volume fluxes, combined with assumptions about the relative magnitudes of buoyancy flux and dissipation. Another attempt to estimate interfacial stress was developed by *Pedersen* [1990] from a compilation of laboratory and field measurements. This method relates stress (τ_i) to an interfacial friction factor (f_i), which can be derived from the Reynolds number (Re_i) through an empirical relation. While Pedersen's method, designed for steady two-layer flow, may not fully apply in the case of the DSO, it could be compared with bulk estimates.

Using the rough estimates of w_e from Section 6.4.1 it is possible to estimate the effective mean entrainment stress as $\tau_i = \rho_0 V w_e$, where V is the streamtube velocity [*Price and Baringer*, 1994]. Taking $0.6\,\mathrm{m\,s^{-1}}$ as a reasonable mean velocity over the entire region (from Figure 6.10), the τ_i values estimated in the low-entrainment and high-entrainment regions are 0.04 Pa and 0.8 Pa, respectively. These can be compared to the overall mean section-averaged bottom stress (τ_b) of 1.7 Pa (where section-averages range from 0.5 Pa to 4 Pa on individual sections). If the high-entrainment region diagnosed from σ_θ changes is, in fact, a real feature of the DSO, then it is clear that entrainment stress could play a significant role in the momentum balance of this region.

6.5 Energy Flux

In order to examine the effects of bottom friction and entrainment stress on the overflow without having to resort completely to the assumptions of a streamtube model, it may be helpful to examine the energy flux carried by the flow. I will still proceed by assuming that there is a more-or-less continuous flow from the sill along the Greenland

slope. I will then attempt to relate along-stream changes in total flux to processes occurring within and at the boundaries of the overflow. Energy partition changes will also be examined. The nature of residuals will not be known exactly, but can be related to bottom friction and entrainment stress as estimated by previously-mentioned means.

The advantages of a flux-based approach are that the flux through a section is made up of the areal integral of the perpendicular component of the flux vector and so should not depend very strongly on the angle of the section to the flow. In addition, cross-sectional variations in thickness, density and velocity can be included in the total flux to give a more accurate representation. A major disadvantage to interpreting energy flux is the additional variability produced by an extra factor of velocity included in most of the terms.

Following Gill, the kinetic energy equation is derived from the dot-product of $\mathbf{u}$ with the momentum equation, giving:

$$\frac{\partial}{\partial t}(\frac{1}{2}\rho|\mathbf{u}|^2) + \nabla \cdot \mathbf{F} = -wg\rho - \rho\epsilon, \tag{6.19}$$

where $\mathbf{F} = (p + \frac{1}{2}\rho|\mathbf{u}|^2)\mathbf{u} - \mu\nabla(\frac{1}{2}|\mathbf{u}|^2)$ is the mechanical energy flux density. Note that the KE flux includes not only the advective flux of KE but also a viscous flux and a pressure flux. While molecular viscosity can probably be neglected, the effects of bottom and interfacial stresses can be included by substituting an eddy viscosity for μ (rather than trying to include turbulent fluctuations in u and p). Adding in the potential energy equation,

$$\frac{\partial}{\partial t}(\rho\Phi) + \nabla\cdot(\rho\Phi\mathbf{u}) = wg\rho \tag{6.20}$$

(where Φ, the geopotential, is defined by $\nabla\Phi = g\hat{\mathbf{k}}$ and so contains an arbitrary reference height), removes the vertical velocity term, giving the total energy equation:

$$\frac{\partial}{\partial t}(\rho(\Phi + \frac{1}{2}|\mathbf{u}|^2)) + \nabla \cdot \mathbf{F^{tot}} = -\rho\epsilon, \tag{6.21}$$

where $\mathbf{F^{tot}} = \rho\mathbf{u}(\Phi + \frac{1}{2}|\mathbf{u}|^2 + \frac{p}{\rho}) - \mu\nabla(\frac{1}{2}|\mathbf{u}|^2)$ is the total energy flux density.

The conservation of total energy within a volume then comes from the volume integral of 6.21, giving:

$$\frac{\partial}{\partial t}(K + P) + \int\int_S \mathbf{F^{tot}} \cdot \hat{\mathbf{n}} dS = \int\int\int_V (-\rho\epsilon) dV, \tag{6.22}$$

where $K = \iiint_V \frac{1}{2}\rho|\mathbf{u}|^2 dV$, $P = \iiint_V \rho\Phi dV$, and $\iint_S()dS$ and $\iiint_V()dV$ indicate surface and volume integrals, respectively.

The volume in question is bounded by the σ_θ=27.8 isopycnal surface and the ocean floor, and we expect that $\frac{\partial}{\partial t}(K + P) = 0$ over an interval of a few days or longer (as supported by the stable means of long-term current meter records *Dickson and Brown* [1994]; *Ross* [1984]). If we assume that the dissipation rate (ϵ) is much smaller than the throughput of energy flux, we are left with a balance between downstream changes in flux through vertical cross-sections and fluxes through the top and bottom of the volume. As pictured in Figures 6.1 and 6.3, the coordinates parallel to and perpendicular to each section are x and y (unit vectors $\hat{i}$ and $\hat{j}$), while the idealized along-stream coordinate (often plotted as "distance from the sill") is ξ.

Since a steady state is only expected to hold in the mean, it is likely that fluctuating components do contribute to the time-mean flux. Any such fluctuating flux in the cross-stream direction (due, for example, to the radiation of internal waves) will only appear as part of the residual of along-stream flux changes.

The energy lost to bottom friction can be evaluated from the integral over the bottom surface of the overflow of the turbulent form of the $-\mu\nabla(\frac{1}{2}|\mathbf{u}|^2)$ term in $\mathbf{F^{tot}}$. Noting that the turbulent stress $|\tau_b|$ takes the place of the viscous stress $\mu\frac{\partial|\mathbf{u}|}{\partial z}$ and neglecting horizontal derivatives and vertical velocities gives:

$$-\mu\nabla(\frac{1}{2}|\mathbf{u}|^2) \approx -\mu\frac{\partial}{\partial z}(\frac{1}{2}|\mathbf{u}|^2) \tag{6.23}$$

$$\approx -\mu|\mathbf{u}|\frac{\partial|\mathbf{u}|}{\partial z} \tag{6.24}$$

$$\approx -|\tau_b||\mathbf{u}|. \tag{6.25}$$

Over a distance $\Delta\xi$ along the overflow, bottom friction will contribute an amount $-\Delta\xi\int_W |\tau_b||\mathbf{u}|dx$ to the surface integral of $\mathbf{F^{tot}}\cdot\hat{\mathbf{n}}$. Alternatively, loss to bottom friction alone should result in a balance of

$$\frac{d}{d\xi}\iint_A(\mathbf{F^{tot}}\cdot\hat{\mathbf{j}})dzdx = \int_W |\tau_b||\mathbf{u}|dx. \tag{6.26}$$

This rate of change is shown by the slopes of the lines in Figure 6.13. A similar term resulting from entrainment stress could also be added.

The total energy flux through an overflow cross-section, $\hat{n} = \hat{j}$, is made up of the

sum of 6 terms:

$$\begin{aligned}
\iint_A (\mathbf{F}^{\mathbf{tot}} \cdot \hat{\mathbf{j}}) dz dx &= [\#1]\ \frac{1}{2}\int_W \rho_0 v|\mathbf{u}|^2 h dx \ \text{(KE)} \\
&+ [\#2]\ g\int_W \rho' v h^2 dx \ \text{(iPE} \times 2\text{, includes } p'\mathbf{u} \text{ term)} \\
&+ [\#3]\ g\int_W \rho' v h Z dx \ \text{(ePE)} \\
&+ [\#4]\ \frac{1}{2} g\int_W \tilde{\rho} v h^2 dx \ \text{(iPE} - \text{like)} \\
&+ [\#5]\ g\int_W \tilde{\rho} v h Z dx \ \text{(ePE} - \text{like)} \\
&+ [\#6]\ g\int_W [v\int_H (\int_z^0 \tilde{\rho} dz) dz] dx \ (\tilde{\rho}\mathbf{u} \text{ term})
\end{aligned}$$

where v is the velocity component normal to the section, h is the overflow layer thickness, Z is the bottom height relative to a reference depth of 2500 m, $\int_W$ and $\int_H$ indicate integrals over the width and thickness of the overflow, respectively, and ρ has been decomposed into a constant mean ($\rho_0 = 1027.2\,\mathrm{kg\,m^{-3}}$), stratified background ($\tilde{\rho}(z)$) and plume anomaly (ρ').

The first three terms are simply the through-section flux of the quantities plotted in Figure 6.11, with the exception that the iPE term (#2) is doubled due to the addition of an identical pressure term from the KE equation (6.19). The last three terms are contributions of the stratified background and represent both the downslope flow of background density from one region into another and the increase of internal energy due to the increasing pressure of the stratified background. The six terms are shown separately in Figure 6.12, and the total through-section flux is shown in Figure 6.13, along with the downstream decrease rate expected from τ_b measurements.

Trends are difficult to pick out of the substantial scatter in the energy flux terms. Any change in total energy flux (Figure 6.13) is, if anything, less significant than the change in overflow volume transport (Figure 6.9) which is already clearly undersampled. The dominant energy flux terms include ePE (#3) and two of the background terms (#5 and #6), indicating that the bulk of the ePE flux decrease is taken up by the work against the background stratification. Despite flux divergence due to bottom friction (shown in Figure 6.13) as well as additional loss to entrainment stress and possibly wave radiation, the total energy flux appears to *increase*. This is difficult to say with certainty, but could indicate the influence of an external pressure

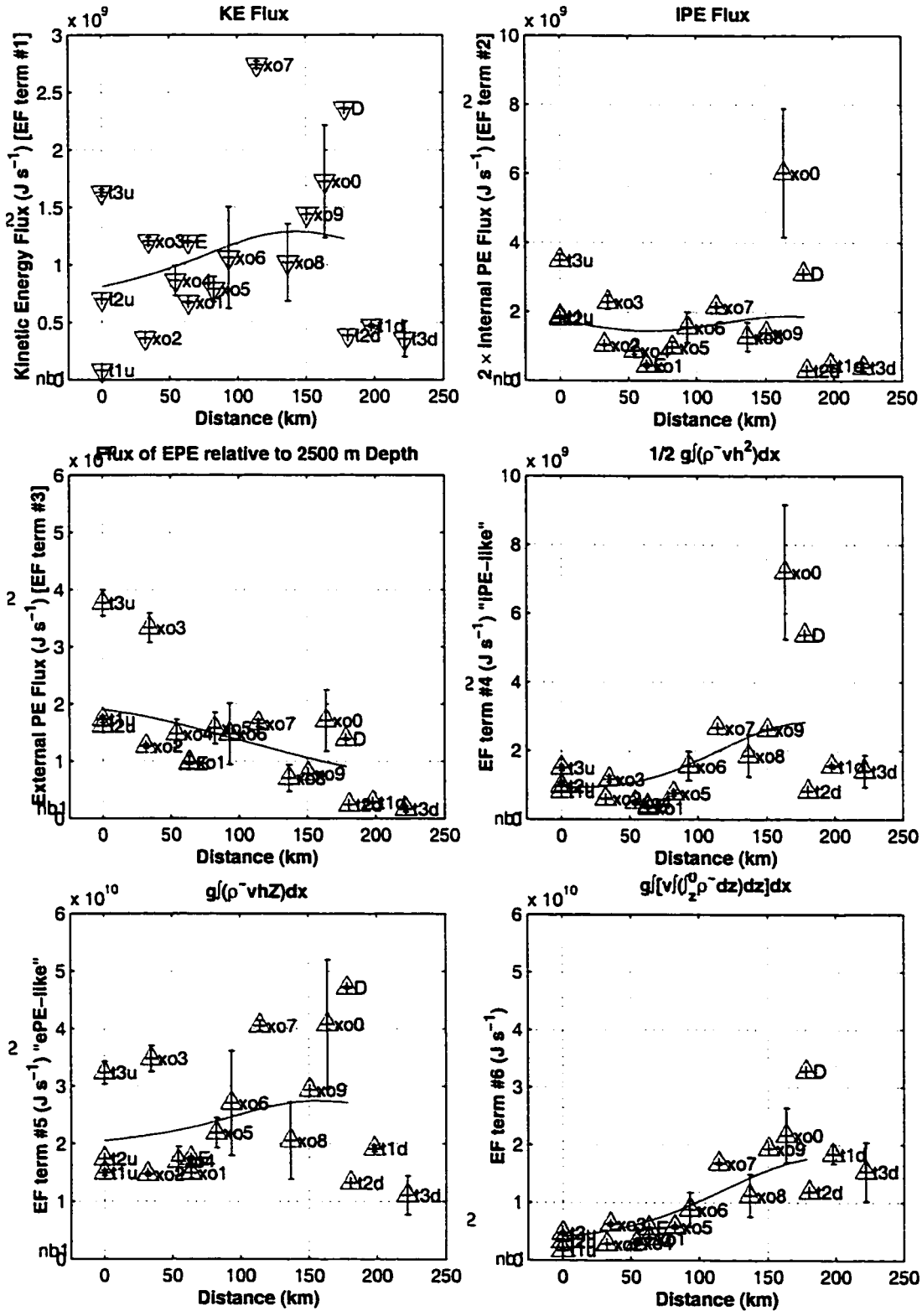


Figure 6.12: Through-section energy flux *vs.* downstream distance. Each panel shows one of the six terms in $\int\int_A (\mathbf{F^{tot}} \cdot \hat{\mathbf{j}}) dz dx$. Curves were smoothed with a 75 km Gaussian window.

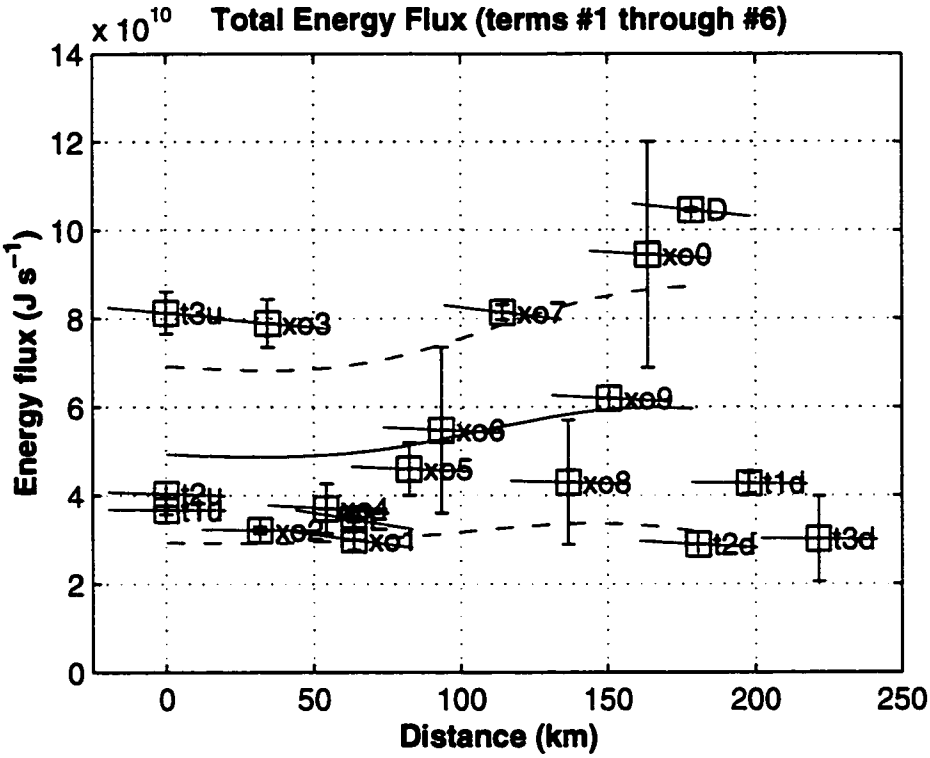


Figure 6.13: Total energy flux ($\iint_A (\mathbf{F}^{\mathbf{tot}} \cdot \hat{\mathbf{j}}) dz dx$) observed at each of 18 sections across the overflow. Values plotted are the sum of all six panels in Fig. 6.12. Slanted lines at each section indicate the rate of decrease expected from bottom stress measurements (Eq. 6.26). The solid curve is a smoothing of the energy flux values using a 75 km Gaussian window, with the dashed curves indicating the envelope of 1σ variance (weighted with the same filter).

gradient (either due to surface slope or variations in the water above the overflow) that is tending to accelerate the flow. One clue to the existence of such a gradient is the cross-strait flow at the sill. Although such an external gradient has been explicitly ignored in the streamtube model, it may be a direct consequence of the hydraulic control and barotropic dynamics at the sill, and would provide a source of increasing energy flux.

Another feature of the total energy flux apparent in Figure 6.13 is a downstream increase in the envelope of variability. This increase may indicate a steepening of the flux-carrying features in the overflow as they propagate downstream. This argues in favor of an instability or nonlinear process affecting the evolution of the flow through

internal flux convergences. Some of this increase in variability envelope is also apparent in the smaller individual terms #1 and #2, indicating that at least part of the process includes both a conversion of potential to kinetic energy and a steepening in overflow interface excursions as might be expected from a soliton-type wave.

6.5.1 Inertial Wave Drag

In rotating laboratory experiments, much of the energy lost during the descent and geostrophic adjustment of a dense turbulent plume on a slope is through the radiation of inertial waves [*Griffiths*, 1983]. This effect has not been observed in the field (*e.g.* the Mediterranean outflow) but may still be an important effect controlling the rates of adjustment and decay. Before this can be determined, a survey of inertial wave energy must be included in the overflow energy budget.

6.6 Conclusions

The primary results of this chapter can be summarized as follows:

- In aggregate, the set of velocity and hydrography sections collected on the *Poseidon* and *Aranda* cruises considered in the context of a streamtube description do capture a "zeroth-order" picture of certain properties and dominant balances of the overflow. In particular, the pathway and descent of the plume are relatively constant over the first 250 km from the sill, and appear to be dominated by topography and bottom stress.

- The mean plume density steadily decreases throughout the descent, with an apparent break in slope at ~125 km. This points to increased entrainment in the latter half of the survey area. The increase could be due to the larger topographic slopes in this region (see Figure 6.14), in combination with the loss of density anomaly as the plume enters deeper water. Average Richardson numbers in these two regions do indicate less stability (and, hence, the likelihood of greater entrainment) in the latter region, but the difference is small.

- Other properties, such as V, A and Q have much higher levels of variability, and

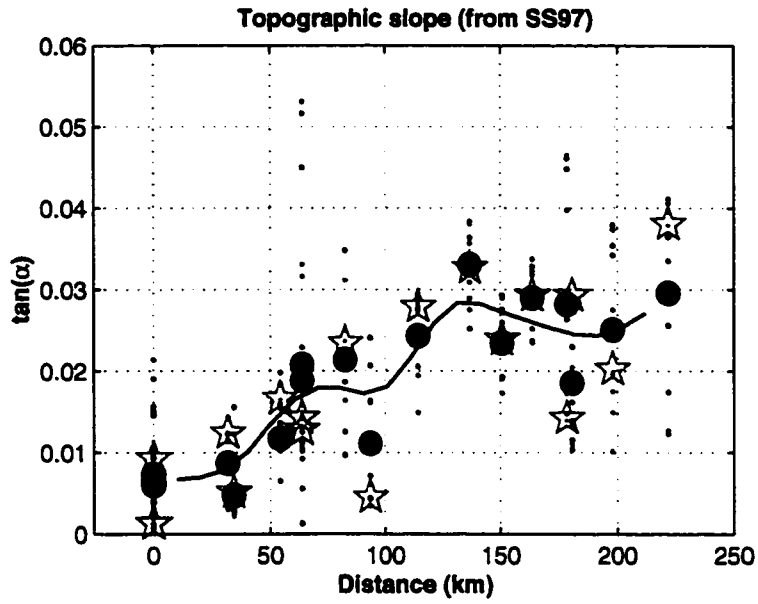


Figure 6.14: Topographic slopes at each section computed from SS97 bathymetry. Large dots show the average slope across the width of each section. Stars indicate the slope under the center of overflow mass anomaly. Small dots are the slope at each station, indicating the range of slopes over each section. The solid curve is a smoothing of the average slopes using a 20 km Gaussian window.

are not quite so readily interpreted. The eddies responsible for this variability will be discussed in Ch. 7.

- The energy partitioning of the plume is dominated by "external potential energy" (ePE) due to the position of the density anomaly on the slope, which decreases in the downstream direction due to friction. However, the sections at the sill have a much higher ePE than those on the slope, implying that not all PE at the sill is released into the overflow.

- Energy *flux* through the sill sections is consistent with the flux downstream, demonstrating the continuity of the overflow, even if not all potential energy present at the sill is released into the plume.

- The energy flux is also dominated by ePE as well as by the pressure resulting

from the descent into a stratified background.

- Although there there is substantial variability, the total energy flux appears to increase or at least steepen with distance from the sill (as shown by the increasing envelope of Figure 6.13). An increase in the mean flux could imply additional forcing by, for example, a surface pressure gradient. The increasing envelope is likely related to the evolution of the eddies in their transit through the survey region.

Chapter 7

EDDIES

The persistent chain of cyclonic eddies on the continental slope off southeastern Greenland is one of the most fascinating aspects of the DSO region. Observation by satellite imagery [*Bruce*, 1995] and surface drifters [*Krauss*, 1996] has shown the eddies to be approximately 20–30 km across, with spacings of 50 km or more between eddy centers There has been much speculation as to their origin, including a number of modeling studies [*Spall and Price*, 1998; *Krauss and Käse*, 1998; *Jungclaus et al.*, 2000], with the bulk of evidence (including laboratory experiments [*Whitehead et al.*, 1990; *Griffiths*, 1983]) pointing toward a connection with the deep overflow. The exact nature of this connection, along with the influence of the eddies in stirring or transporting overflow water or draining its energy, has not yet been firmly established. In this chapter, the presence of eddies in the *Poseidon* and *Aranda* datasets is discussed, along with the implications for generation and enhancement mechanisms.

7.1 Surface Eddies in Satellite IR

Immediately prior to the *Poseidon* cruise, high-resolution infrared data from the Advanced Very High-Resolution Radiometer (AVHRR) sensor on the NOAA-12 polar orbiting satellite showed cloud-free conditions over the Denmark Strait. Figures 7.1–7.3 from September 13–15 give an impressive view of eddy structures in the surface temperature front of the region. The LAC format (1 km resolution) data were obtained and processed with the TeraScan software package.

7.1.1 Form and Evolution

The surface imagery is valuable in that it gives a detailed picture of the situation in the Denmark Strait immediately prior to our measurements. Unfortunately, weather conditions did not permit further satellite images during the cruise, making a direct

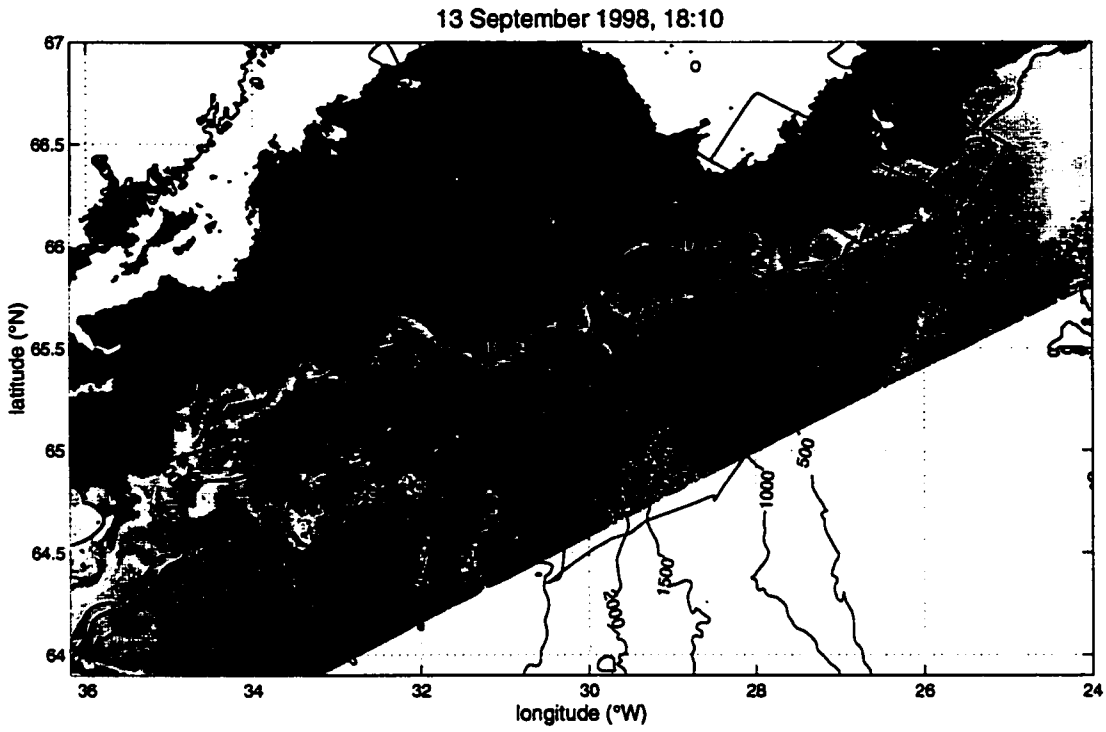


Figure 7.1: Satellite infrared image (NOAA-12 AVHRR) on the first of three clear days before the *Poseidon* 244 cruise, showing the structure of the surface temperature front in the Denmark Strait. Warmer water is orange; colder water is blue. Some cloud contamination is evident as white regions, as well as speckling in some adjacent colored regions. Contours of bathymetry in meters from *Smith and Sandwell* [1997] are overlaid in black. The cruise track is shown in green. Five eddies are labeled A–E for tracking in subsequent images.

correspondence between AVHRR-observed eddies and profile measurements difficult to establish.

Nevertheless, in the three days that are available, a number of salient features are evident. The frontal structures for which rotation can be determined are predominantly cyclones, and the shapes and sizes give some clue of what to look for in the in-situ data. Of particular interest are the two jet-like structures observed in approximately the same location on Sep 13 and Sep 14 (but certainly different features, as indicated by the labels C and D attached to them in Figures 7.1 and 7.2). These jets appear to signal the birth of new cyclones, and will be discussed further in the following section. Of final note is the extension of the temperature front upstream of the

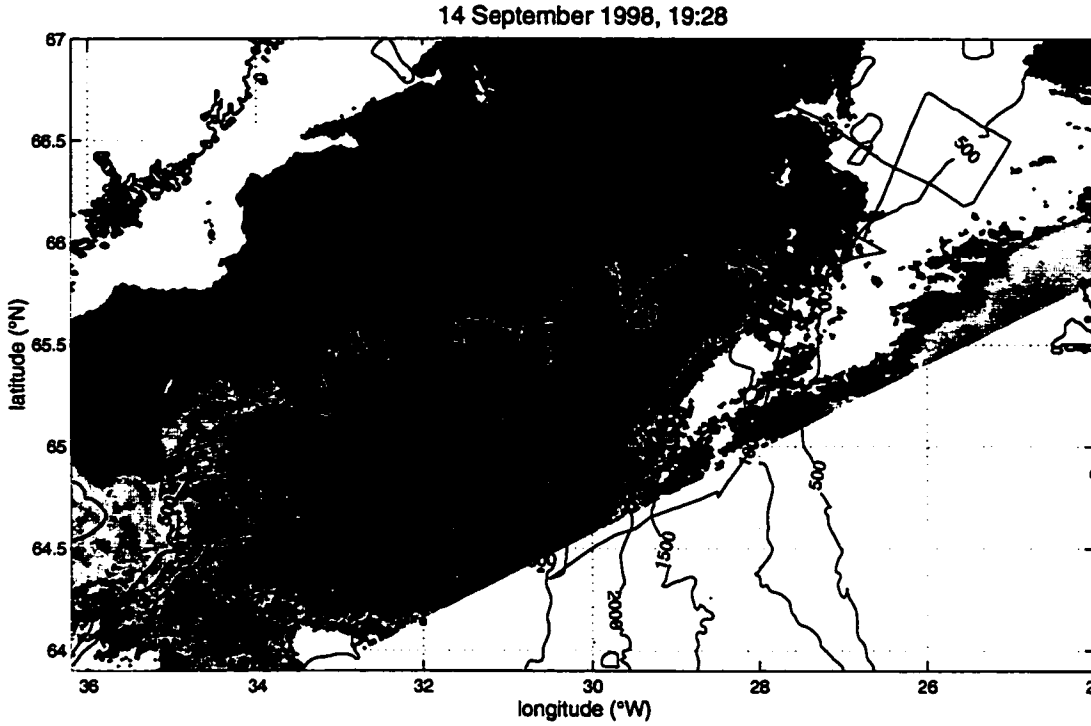


Figure 7.2: Same as Fig. 7.1 on the second of the three clear days.

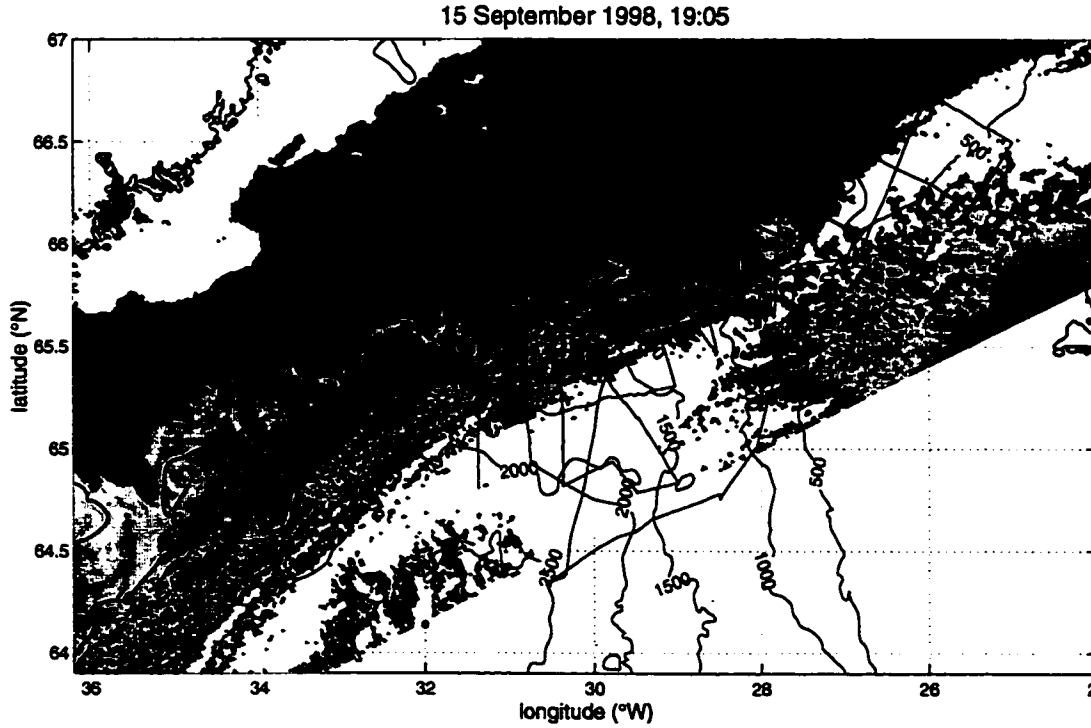


Figure 7.3: Same as Fig. 7.1 on the third of the three clear days.

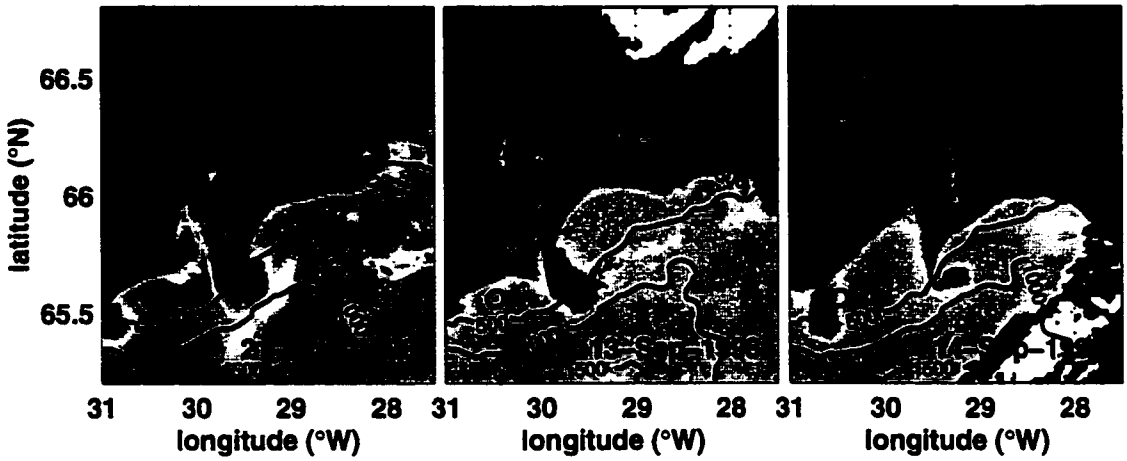


Figure 7.4: Three images of SST from satellite IR showing the jet-like birth of new eddies directly over the initial descent of the overflow. The date of each image is printed in the lower right-hand corner. Note that in panel c the eddy born the previous day (panel b) is still visible at approximately 30.7°W, while a new jet is already forming.

sill along the Icelandic slope, supporting the hydraulic prediction of a flow entering on the left-hand side of the Strait and exiting on the right after a transition at the sill. Eddy-like features are apparent in this upstream region but seem to have a less direct connection to the downstream cyclones.

7.1.2 Eddy Birth

The jet-like influx of cold frontal water seen in the Sep 13 and Sep 14 images also appears in an image from Aug 21, almost a month earlier (one of the few cloud and ice-free days found in a search of the months of August and September, 1998). It would thus appear that this jet is a common feature of the region. Enlargements of the three jets are shown in Figure 7.4, showing their positions relative to topography and each other. In the sequential images of Figures 7.1–7.3, it is these new eddies (C and D), and not upstream features (E), which then translate to the southwest. The jet, therefore, seems to be the birthplace of all of the cyclones observed by *Bruce* [1995], *Krauss* [1996] and others. The location of this jet is just downstream (west) of the OVERFLOW '73 current meter array, and quite close to the point (~125 km from the sill) where the overflow's entrainment undergoes a dramatic increase (as discussed

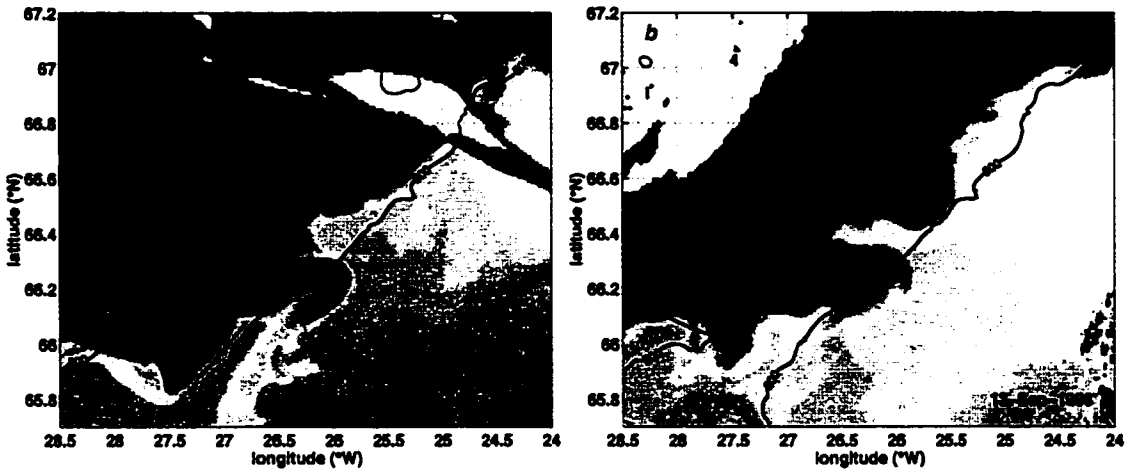


Figure 7.5: Two images of SST from satellite IR showing the character of the temperature front at the Denmark Strait sill.

in Chapter 6). While it is not really possible to diagnose the internal motions from SST images, it does appear that these jets are the result of internal sinking motions which draw in new surface waters and induce cyclonic vorticity, as might be expected from the stretching of the overlying water column.

7.1.3 Sill and Upstream Features

If the strong cyclones are born 100 km after the sill, then what is the origin of the features seen upstream from that location? Figure 7.5 shows enlargements of the sill region, as seen on Sep 13 and Aug 24, including the existence of eddy-like features with a somewhat different character from the cyclones downstream. Two eddies at 66.6°N, 25.8°W and 66.25°N, 26.3°W on Sep 13 (panel b) form a closely-packed train and appear to consist of almost equal portions of water from the two sides of the front. These sill eddies are also more-or-less symmetrical, rather than clear displacements from the mean frontal position. In this respect, they are suggestive of the "cat-eye" patterns familiar from Kelvin-Helmholtz instabilities.

Aug 24 (panel a) shows a single spiral of intermediate-temperature water (66.5°N, 26.4°W) and a hook-like feature (66.2°N, 26.1°W), both of which appear to indicate cross-frontal exchange. These features are not positioned so cleanly on the frontal

axis but indicate complex patterns of currents rather than the clear jet-like structures of Figure 7.4.

By picking out individual eddies and tracking their movements over the three days of AVHRR measurements, it is possible to make a rough determination of eddy propagation speeds. Although I have not found sequential images with clear weather at the sill, the feature labeled E in Figures 7.1–7.3 is marginally visible during the 3 days and appears to move much slower than the features downstream. It is also evident that none of the other sill features from Sep 13 have crossed the sill by Sep 15, indicating that they are either stationary or quite slow-moving.

7.2 Surface Eddies in In-situ Survey

The ubiquitous nature of eddies in the DSO region made it inevitable that we would cross several during our survey, although a deliberate effort to hunt for eddies was not made due to time and weather constraints.

7.2.1 Appearance in Thermosalinigraph

The shipboard measurement most comparable to the satellite SST imagery is that of the continuously-recorded thermosalinigraph (TSG). While the TSG doesn't measure *exactly* the same quantity as the satellite (the TSG intake is several meters below the surface while the satellite measures only the top few millimeters) the two measurements are of similar accuracy (*i. e.*, not great but certainly good enough to resolve the 5–10°C differences across the surface front in the Denmark Strait) and should be useful in trying to compare features observed in the survey with the type seen in satellite imagery.

The TSG record for Part III of the *Poseidon* cruise (in Figure 7.6, along with ADCP vectors) clearly shows the location of the surface temperature front where it intersects the ship's track, generally agreeing with the position in the satellite images. It is not possible to identify the positions of eddies from the along-track TSG alone. However, some clues do exist, for example in southward extent of the front in Figure 7.6—reaching as far as the 1000 m isobath at one point—or in the presence of a warm patch on the Greenland side of the front, indicating some cross-frontal exchange.

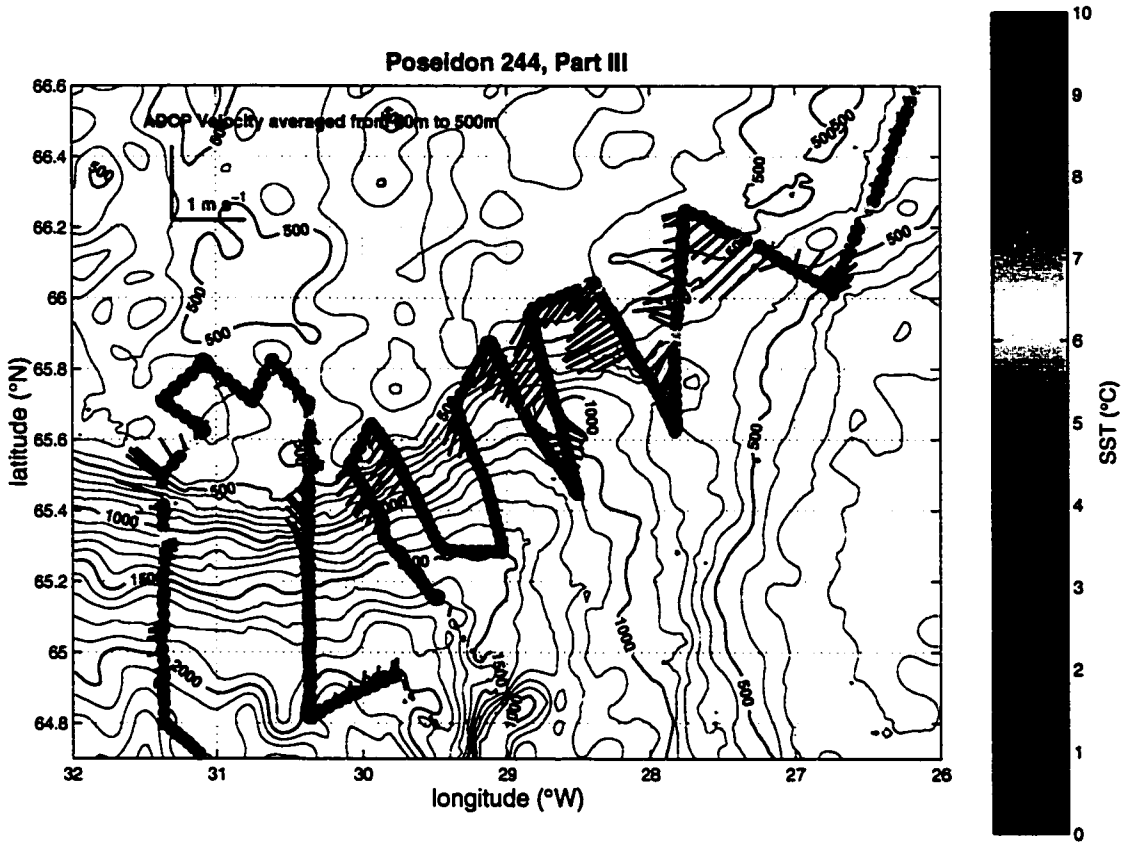


Figure 7.6: Continuously-recorded sea-surface temperature from the *Poseidon's* thermosalinigraph (TSG) and upper-layer velocity from the ADCP during Part III. The ADCP vectors are averages over the full range of the ADCP, which varied with conditions but at times extended as deep as 500 m.

7.2.2 Appearance in ADCP

A complementary picture to the TSG is provided by the near-surface currents of the shipboard ADCP. Although the ADCP measures a profile of water velocity to as deep as 500 m, the variations over this depth are substantially less than the mean (at least partly due to the relatively low stratification in the region). For the purposes of identifying eddies, then, and to minimize the effects of ADCP noise, I have chosen to use only the mean of the ADCP over its entire range below 50 m. Interestingly, the velocity structure derived from using only the first (12–20 m) or second (20–28 m) ADCP bin is not substantially different from this mean, justifying the choice.

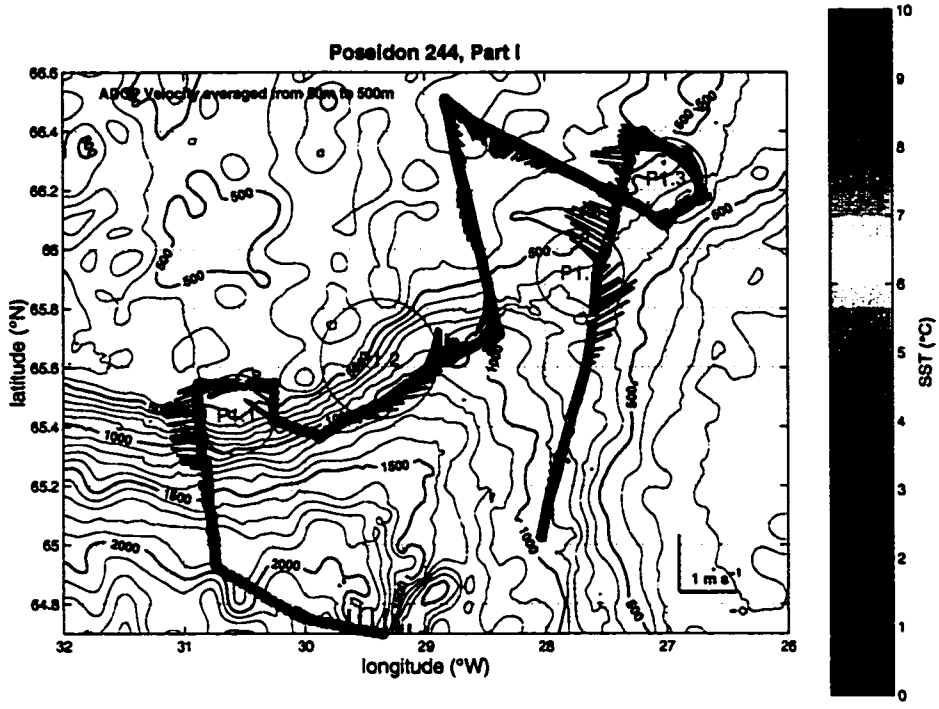


Figure 7.7: Examples of subjective eddy fits to ADCP data in Part I of *Poseidon* track. The TSG record is also shown. Eddies identified in the *Poseidon* survey have been labeled according to which of the three survey parts (see Ch. 4) they appeared. For example, "P1.4" is the fourth eddy in Part I. This is partly to distinguish these eddies from those observed in the satellite images, labeled alphabetically (*i. e.*, A–E).

The ADCP velocities reveal a number of instances of cyclonic circulation, some associated with a temperature front (generally at the center of the vortex) and some without. The patterns are fairly complex, though, and it is difficult to imagine a simple vortex structure which will fit the various velocity patterns with much reliability. Instead, I have adopted a subjective procedure of fitting "cyclonic-looking" features to a circular velocity to determine the position of each vortex center at the time that the cruise track passed by. Four examples of these subjective fits, using ADCP vectors from Part I of the cruise, are shown in Figure 7.7. Interestingly, it appears that sections tld, gsl and inlt perfectly circumnavigated the northern side of eddy D from the satellite images without encountering a surface signature (although there is a moderately-thick overflow layer in tld, symptomatic of the leading edge.)

7.3 Deep Eddy Signature

The relationship of the overflow layer velocity, temperature and thickness to the upper-layer eddy features has already been discussed somewhat in Chapters 3 and 4. In particular, the surface cyclones are generally connected with a thickening of the dense bottom layer, as well as often with enhanced near-bottom downslope velocities. Eddies observed in both the *Aranda* and *Poseidon* surveys show a similar pattern of gradually increasing bottom-layer thickness on the leading edge followed by high overflow transport in a thick layer (often accompanied by the presence of low-salinity Polar Intermediate Water) and, finally, a sudden overflow decrease in conjunction with warm on-slope flow.

This pattern is perhaps clearest in the *Aranda* data, which lacked surface temperature measurements but did include high-quality CTD information close to the surface. Section J, in particular, reveals the cold surface tongues associated with two of the eddies transected by the survey, as well as strong near-bottom velocities almost in opposition to the surface velocity. As the bottom plume descends with a large downslope angle, the near-surface flow sweeps in to replace it. Both layers display cyclonic curvature but with the centers of rotation in different locations (offshore for the deep flow and onshore for the surface).

7.4 Eddy Positions and Speeds

In all, eddies were sampled by a total of 11 segments of cruise track in the *Poseidon* survey (four in Part I, two in Part II and five in Part III). Combining these with the labeled features in the satellite images, it is possible to construct a full set of eddy positions, shown in Figure 7.8. There is a hint of a separation resulting from the different definitions of the in-situ *vs.* satellite eddies (one using velocity, the other SST), with the satellite-observed eddies consequently appearing higher on the slope than the velocity signatures. This is consistent with some of the TSG records showing the cold front extending only as far as the vortex center and may indicate a slight misinterpretation of the eddy positions in the satellite images. In the mean, the path described by all of these eddy positions essentially coincides with the mean overflow path from Chapter 6 (Figure 6.6) in the initial region but then diverges somewhat

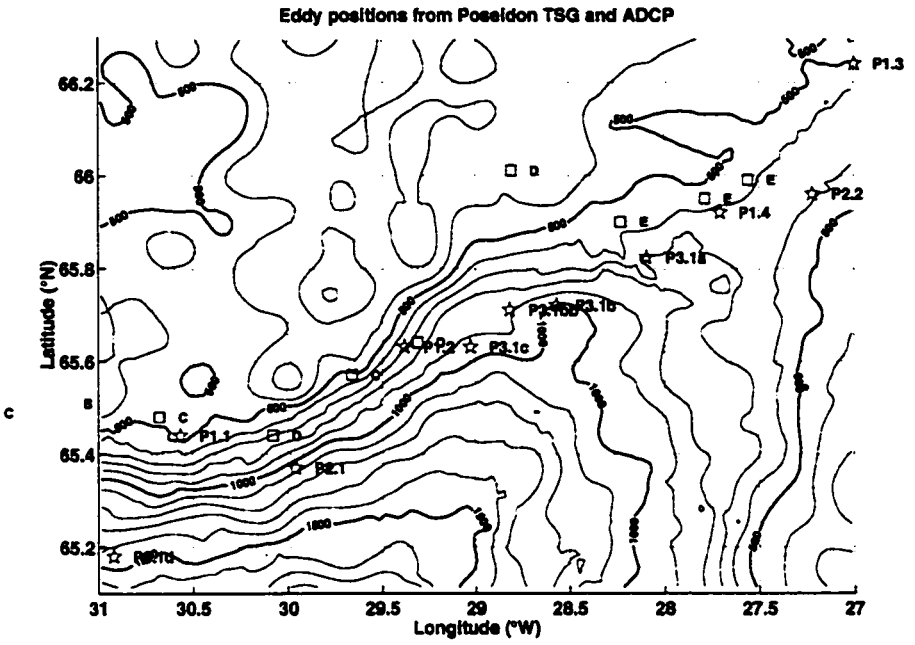


Figure 7.8: Positions of all eddies picked out in satellite imagery and ADCP velocities from *Poseidon* in-situ survey.

after the overflow descends, with the eddies moving offshore more slowly than the overflow mass anomaly.

The evolution of the eddies makes more sense when these positions are plotted as distance from the sill *vs.* time of observation (Figure 7.9). In this presentation, it becomes clear that the eddies observed in the *Poseidon* survey are, in fact, being generated at a more-or-less constant rate and propagating downstream with a speed that is initially slow, picks up at around 100–125 km from the sill and then gradually decreases further downstream. There also appears to be a continuity between the features observed close to the sill and those further down (after the "birth" region apparent in the satellite images). It seems likely, then, that the initiation of variability occurs prior to the dramatic vortex stretching which gives rise to the surface eddies. Since the speed of features during their transit of the sill is relatively slow, it is possible that one of the proposed instability mechanisms will have time to operate during this initial phase, while the rapid descent, entrainment and vortex stretching suggested by the laboratory experiments of *Whitehead et al.* [1990] characterize the

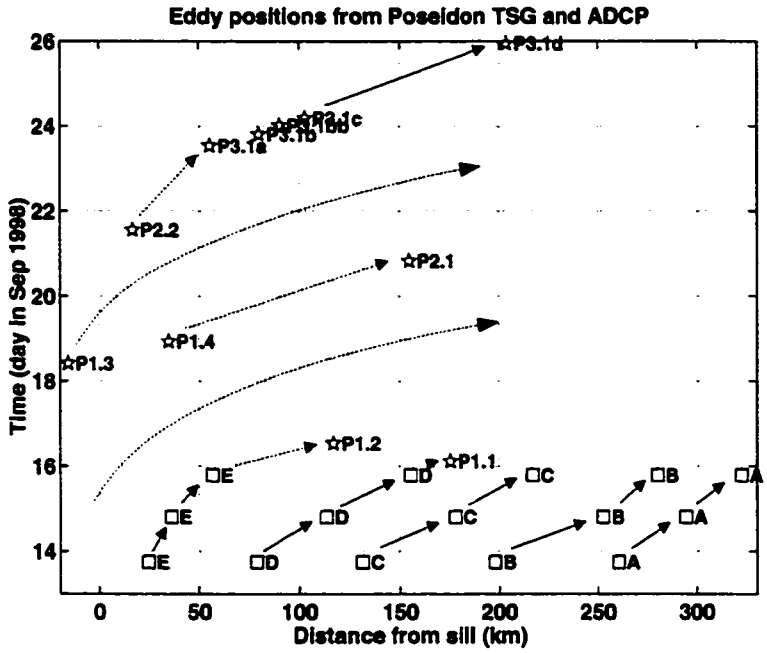


Figure 7.9: Downstream motion of eddies in satellite imagery and in-situ survey, indicating connections not previously noted. Solid arrows indicate eddies that I am reasonably certain were observed at successive times, while dashed lines are more speculative trajectories, based in part comparison to other eddies at approximately the same distance regime.

second phase. Although there is some uncertainty to this interpretation, made up, as it is, of isolated observations which appear to connect, it does fit in well with the evolving picture of the overflow and suggests answers to a few questions.

To test some of the hypothesized connections suggested by Figure 7.9, I have computed speeds from sequential pairs of positions for each eddy. Plotted *vs.* distance (Figure 7.10) these speeds are highly variable, but still fit the general description of low values in the region nearest to the sill, maximum speeds around 100 km and subsequent downstream decrease. In fact, this pattern is remarkably similar to the distribution of mean overflow velocity V shown in Chapter 6 (Figure 6.10). This similarity, along with the critical region of ~100–125 km for both surface eddy birth and increased entrainment, makes the connection between the eddies and overflow virtually certain.

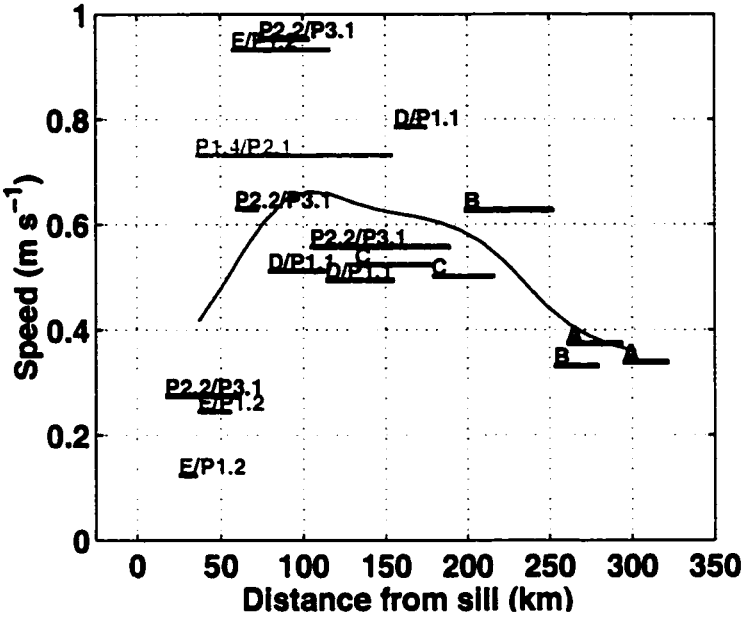


Figure 7.10: Estimated speeds of eddies picked out in satellite imagery and ADCP velocities from in-situ survey. Each speed estimate is obtained from a simple differencing of positions (shown in Fig. 7.8) at two different observation times. Horizontal lines extend between the two positions used in each difference. The solid curve is from a smoothing of the speeds with a 40 km Gaussian window. Compare with overflow speeds in Fig. 6.10

7.5 A Composite Eddy

The best-sampled eddy by far is the one caught by multiple sections during the second week of the *Poseidon* cruise (Part III). This set of sections clearly shows a cyclonic upper-layer circulation in connection with cold surface water, as expected from the satellite images. The mean upper-layer velocity of $0.5\,\mathrm{m\,s^{-1}}$ is in agreement with observed eddy propagation speeds, while the lower-layer water velocities are up to three times greater. A total of 8 cross-stream sections reveal a combination of barotropic and baroclinic situations at different water depths.

In order to compile a composite picture of this eddy's structure and evolution, I have taken the center positions shown in Figure 7.8 (eddy P2.2/P3.1) and linearly interpolated between them in time and space to model the eddy's motion. This allows all points on the ship's track to be referenced to the eddy center, resulting in the cov-

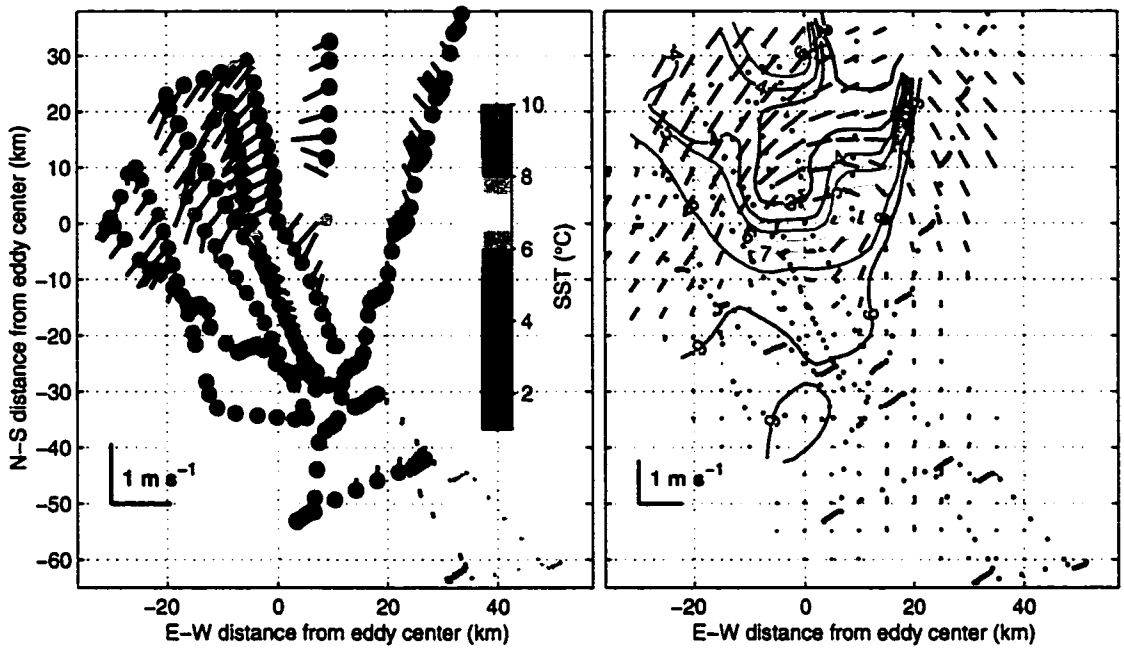


Figure 7.11: Composite picture of the eddy observed in Part III of the *Poseidon* cruise. Measurement positions relative to the eddy were determined by interpolating the eddy's motion in time from the positions in Fig. 7.8. The left-hand panel shows 15-minute averages of full-range ADCP velocity and TSG temperature. The right-hand panel shows the same fields smoothed with a 5 km gaussian window.

erage of a region approximately 150 km in diameter. Of course, the eddy is certainly undergoing a substantial evolution during this period, and all results of this composite must be interpreted in light of that evolution. Still, there are some interesting features that appear which cannot be investigated in any other way.

7.5.1 Upper-Layer Composite

The left-hand panel of Figure 7.11 shows 15-min averages of TSG temperatures and ADCP velocities referenced to the eddy's moving center. The cyclonic circulation is now plainly apparent, but there is also a substantial asymmetry to the velocities, with a stronger and broader flow on the northwest (upslope) side of the eddy. This is not simply the result of an additive mean advection velocity over the entire domain (since the center of the eddy is, in fact, already motionless) but may be considered the additional contribution of the East Greenland Current over the shelf-break. It is not

entirely clear that this is a fair interpretation, since not all of the *Poseidon*'s forays onto the Greenland shelf observed this level of velocity. Instead, it seems more likely that the enhanced shelf velocity is somehow linked to the eddy's acceleration at this location.

Another feature of note is the fact that the cold surface water only extends as far as the center of the velocity signature and does not wrap around the eddy. This is likely due to the relatively recent entrance of the surface front into the vortex, but may also indicate either that the velocity signature of the eddy propagates at a different rate from the advected temperature front or that the thin, cold surface layer is able to mix with warmer water below before it has a chance to extend further.

A smoothed version of the upper-layer velocity and surface temperature using a 5 km Gaussian filter (Figure 7.11, right-hand panel) clarifies the intrusion of surface water from the north but also seems to indicate an inward-spiraling component to the velocity. Likewise, a decomposition of the velocity into radial and azimuthal components (Figure 7.12) indicates a mean negative (inward) radial component. The combined effects of time-variability and the uncertainty in the eddy-tracking algorithm make this inflow difficult to interpret with much confidence (in fact, a straightforward computation of influx using the velocities in Figure 7.12 yields total sinking values on the order of several 10s of Sv, which is unreasonable). The azimuthal velocity curve may be a bit more reliable, indicating a central region of near-solid body rotation within a region of velocity decay with distance, not unlike the curve constructed by *Krauss* [1996] from drifter paths. The radius of the core region appears to increase with time as its velocity decreases. The velocity decrease is not proportional to $1/r$, however, implying that the *total* vorticity of the eddy is, in fact, increasing over time. This increase could be driven by the vortex stretching resulting from overflow entrainment and surface inflow.

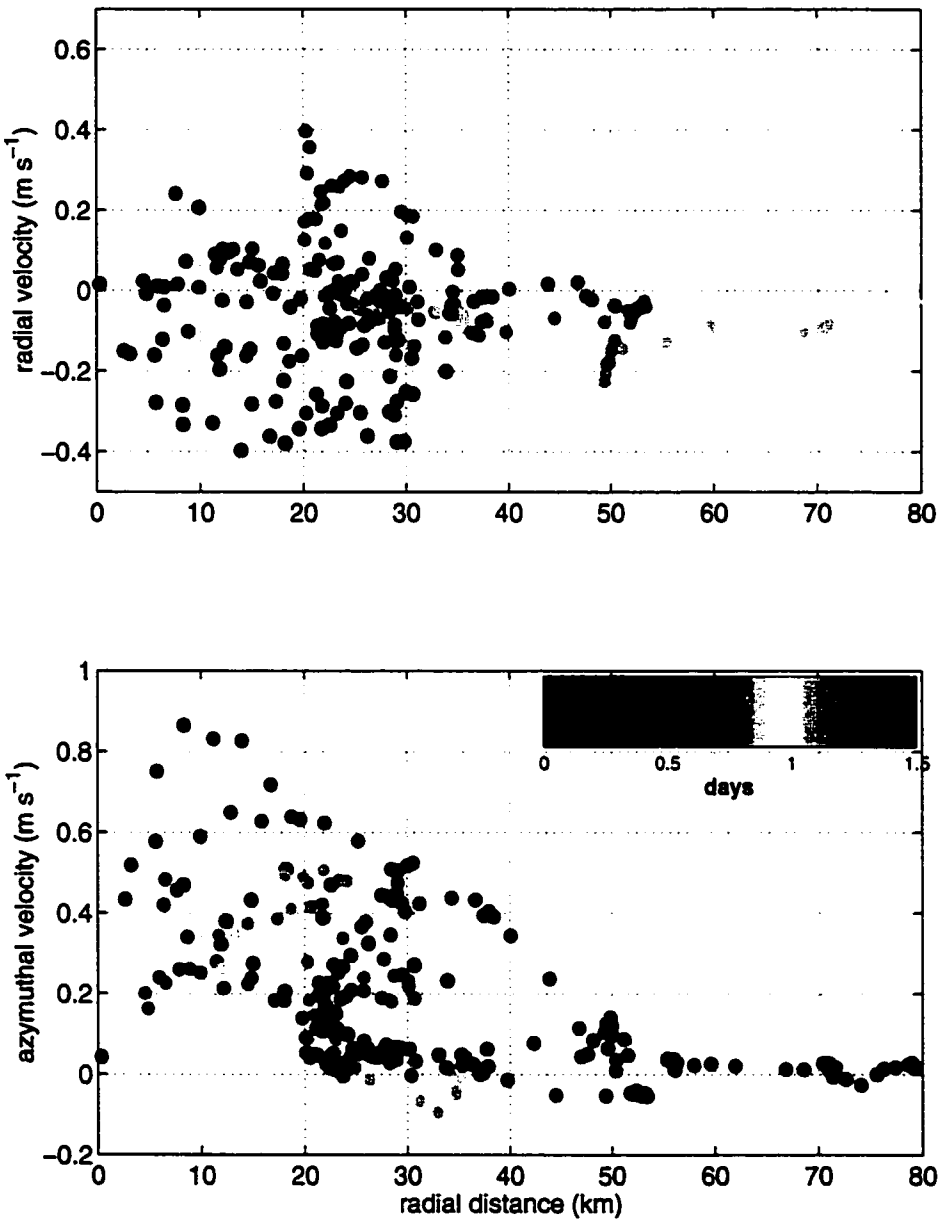


Figure 7.12: Decomposition of eddy velocities into radial and azimuthal components. Colored dots indicate the progression of time from the first encounter with the eddy on September 23, 1998.

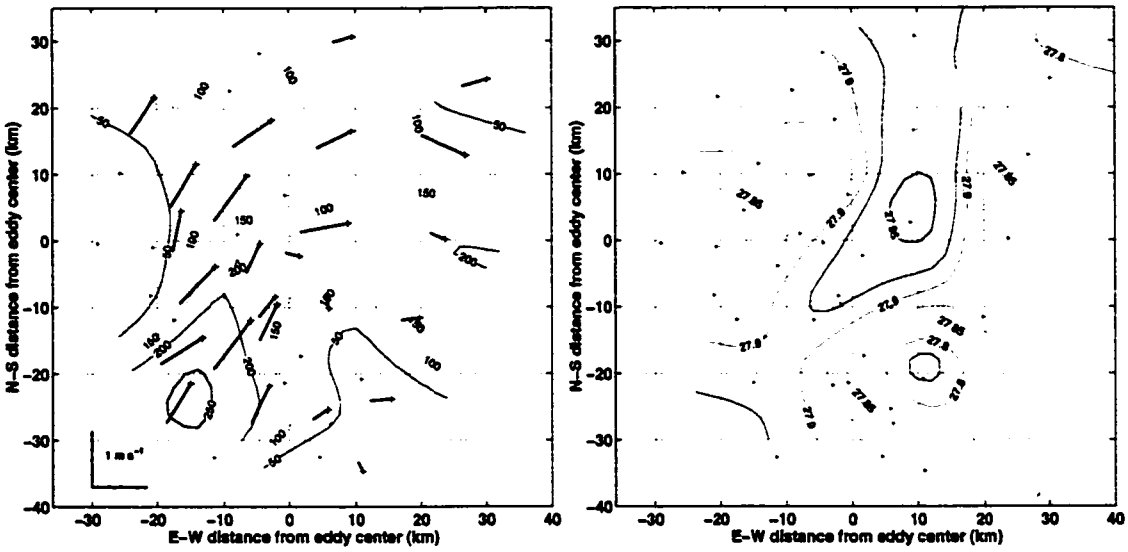


Figure 7.13: Properties of the deep layer in the composite of Fig. 7.11. The left-hand panel shows the average velocity over the σ_θ>27.8 layer, along with a smoothed field of the thickness of the layer in meters. Pluses indicate the position of simultaneous XCP/XCTD drops and form the base of each velocity vector while dots indicate station locations for which either the XCP or the XCTD is unavailable. The right-hand panel shows the mean density within the σ_θ>27.8 layer, highlighting the path of the densest overflow water.

7.5.2 Deep-Layer Composite

The thickness and velocity of the deep overflow layer (σ_θ>27.8) underneath the eddy composite is shown in Figure 7.13 (generated by referencing the locations of velocity profiles to the eddy center, as described above). In this picture, the eddy is almost completely gone, replaced with a descending plume of dense water, crossing only slightly to the upslope side of the surface eddy. If a cyclonic circulation is evident, its center is some 30 km to the southwest of the surface vortex, and there may even be a hint of the anticyclonic circulation seen by *Krauss and Käse* [1998] on the upslope side of the plume. As noted in the Chapter 4 discussion of velocity sections, the combination of the bottom plume and surface vortex leads to a barotropic velocity profile over the slope and baroclinic profile offshore. The fact that both surface and bottom features appear to move at the same rate argues against a simple superposition, however, and it seems rather that the barotropic reach of the deep flow provides the impulse to move the surface layer over the shelf and slope. While being contin-

uously pushed in this way, the upper layer develops its own propagation speed as a half-dipole, with the other half made unnecessary (or, rather, reduced to a virtual image) by the presence of the steep slope (R. Käse, personal communication).

7.6 Conclusions

Through the ensemble of many observations of eddies during both the *Poseidon* and *Aranda* cruises, a number of repeatable characteristics have become apparent:

- Cyclonic features observed in the near-surface flow at the sill propagate approximately along the mean overflow path with a speed that increases to ~125 km from the sill, then gradually decreases with distance. This pattern matches the speed of the overflow plume itself nearly identically.

- Eddies observed in satellite imagery do not seem to propagate from the sill region but are spontaneously created in offshore jets of cold surface waters approximately 125 km southwest of the sill.

- The composite structure of an eddy observed in Part III of the *Poseidon* survey appears as a half-dipole with a strong impulsive jet parallel to a boundary (the Greenland slope) and a slower offshore recirculation, all moving at approximately the speed of the wall jet itself. The lower-layer dense water seems to be flowing continuously downslope with a similar velocity to the upper-layer jet but diverging somewhat in direction.

Clearly, the point at 125 km from the sill is a critical one for both eddies and the overflow. The combination of surface eddy birth (or enhancement) with increased entrainment in the deep plume argues for the existence of strong downward velocities in the overlying layer, and this may even be supported by convergences in the observed upper-layer currents. The root cause of the enhanced entrainment is, itself, less certain but may be related to the increased topographic slope in this region.

Chapter 8

CONCLUSIONS

The strong flow, intense entrainment and energetic variability in the Denmark Strait have made this choke point in the global thermohaline circulation a puzzle to oceanographers for almost 50 years. The combination of ice-covered conditions much of the year and the likelihood of fierce weather that can strike at any time have made this a difficult region to study. Nevertheless, a number of research cruises have been made to the Denmark Strait and have documented the rapidly-changing properties of its water masses. The hydrographic complexity, combined with mooring records showing fluctuations as large as the mean current, has made the hope of deciphering the overflow's dynamics with conventional ship-lowered instrumentation seem exceedingly faint.

Now, with the combination of two rapid in-situ surveys with expendable profilers, along with the analysis of satellite imagery and past current meter records, I have undertaken to study the development of overflow variability and to achieve a new understanding of the processes at work. The significance of this work is mostly in its unique ability to quantify the velocities in a synoptic sense, establishing both the magnitude and pattern of the steady-state flow and the structure and magnitude of the variations on the steady state. While the results will not give a definitive answer to all of the outstanding questions about the Denmark Strait Overflow, they will provide a new basis for the testing of hypotheses and a context for future observations.

8.1 Velocity Structure

Knowledge of the structure of the velocity through the Denmark Strait has been, until now, fairly slim. The full water column sections described here illustrate the persistence of a barotropic jet in the near-sill flow, often including a recirculation on the Greenland shelf in addition to the counter-flow on the Iceland slope. The mechanism underlying this barotropic flow in a situation in which the primary forcing

is by internal density gradients has still to be explained.

As the overflow descends, the bottom-trapped velocity structure of a density current becomes apparent, but even then a barotropic flow persists near the Greenland shelf-break. This shelf-break flow gradually diverges from the dense current with distance downstream. At least during the initial descent, however, the two are directly connected, and a substantial fraction of the dense water flux is contributed by the barotropic current. While the presence of both surface and deep flows in the region has been known by investigators since the first studies there, the extent of the relationship between the two could not be known without direct velocity measurements.

8.2 Transport

One of the significant results of this work is the impressive agreement between the transport and variability in these short-term surveys and that in historical records. After a careful comparison between the different geographical coverages and temporal distributions of the current meter measurements from OVERFLOW '73 and the velocity profiles from the *Poseidon* cruise, it appears that not only was the *mean* overflow transport during the two periods statistically identical (to an accuracy of about 0.6 Sv), but also the *distribution* of variability was statistically indistinguishable. In fact the measured mean transport values only differed by 0.2 Sv, suggesting that a relatively brief survey, as long as it spans the extent of the outflowing waters and includes direct velocity measurements, is sufficient to quantify the overflow flux with equivalent accuracy to a current meter array of substantially longer duration. This could be due to the ability of the greater areal coverage and resolution of the *Poseidon* survey to give additional effective degrees of freedom, thereby reducing the true error in the mean transport. The direct velocity measurements are certainly a key element in the ability to survey DSO transport, since the steep topographic slope, narrow and often barotropic nature of the currents and rapid variability make an estimate of transport from the density field alone almost useless.

8.3 Energetics

Once the agreement between the 1973 and 1998 observations is established, it becomes more plausible that significant features observed in the new surveys can be considered universal characteristics of the DSO. In particular, the evolution of streamtube-averaged properties is important for diagnosing the forcing and modification the overflow undergoes in its path to becoming North Atlantic Deep Water.

Some of the important points resulting from the bulk overflow (streamtube) analysis include:

- The path of the dense water as it descends the Greenland continental slope has surprisingly little variability, following a path of essentially constant rate of descent over topography consistent with a balance between buoyancy, Coriolis acceleration and stress at the bottom of the dense plume.

- Also, at 125 km from the sill a number of changes occur in the behavior of the dense overflow:

    1. The plume-averaged mean velocity reaches a maximum;
    2. the plume encounters an abrupt reduction in background stratification at approximately 1000 m depth; and
    3. the rate of density change with distance in the plume increases, suggesting an increase in entrainment velocity (w_e) from $6 \times 10^{-5}\,\mathrm{m\,s^{-1}}$ to $8 \times 10^{-4}\,\mathrm{m\,s^{-1}}$.

8.4 Eddies

With the combination of two days of clear weather and an in-situ survey that made multiple passes through the DSO region, it is now finally possible to make a direct connection between specific eddies observed in the satellite SST images and their velocity and hydrographic structure. Unfortunately, since the clear weather occurred *before* the survey started, these two elements still have not been linked simultaneously, but from an analysis of the propagation speeds of the observed surface and

subsurface eddies I am confident that at least one and possibly two eddies were observed by both satellite and in-situ methods.

When taken together, the ensemble of remote and in-situ eddy measurements paint a consistent picture of the generation and intensification of the DSO variability. While the persistent chain of cyclones described by *Bruce* [1995] originates in jet-like events approximately 125 km to the southwest of the sill, these events occur almost instantaneously and are not consistent with the day-long or longer growth periods predicted by most instability models [*Smith*, 1976; *Fristedt et al.*, 1999]. However, there is ample evidence for flow variability and instability (propagating at a much slower speed) in the immediate approach to the sill itself, as well as at least one instance of a subsurface cyclonic feature being tracked from the sill into the region of surface intensification. The most likely explanation, then, is that two distinct and geographically-separated processes are at work:

1. First an instability of the relatively slow-moving flow at the broad sill generates small-amplitude eddies.

2. Then, as the deep overflow descends, the resulting entrainment and upper-layer sinking causes a horizontal convergence and vortex stretching which dramatically intensifies only the cyclonic eddies present at that point (due to the sign of the potential vorticity given by f).

These two processes are illustrated schematically in Figure 8.1.

In fact, far from being merely noise on top of the transport measurements, the high degree of variability in the form of eddies appears to be a major mechanism facilitating the transport and modification of waters in the overflow and East Greenland Current. The velocity structure of the developing eddies, even before they receive the surface frontal water that makes them appear in satellite images, is very similar to the cyclonic half of a propagating dipole which moves with the same speed as the underlying overflow plume (even reaching a maximum at 125 km from the sill, just as in the dense water).

At this point, questions remain as to what triggers the increased entrainment during the plume's descent and what process generates the initial instability at the sill.

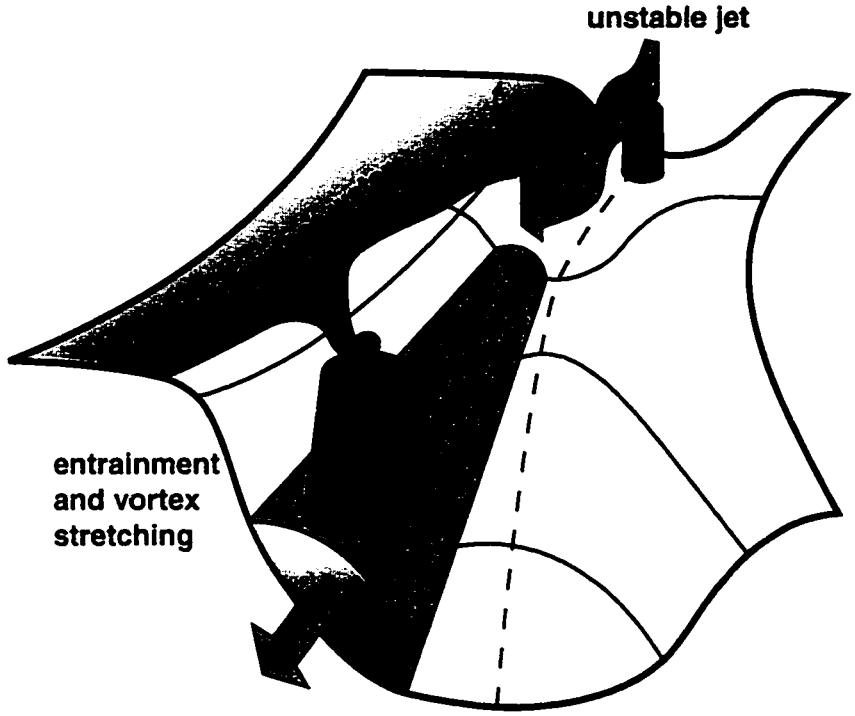


Figure 8.1: Cartoon illustrating the separate processes at work in generating the surface eddies observed in the DSO satellite imagery.

Clues to the entrainment process have already been given by examination of the topographic slopes in the region, which tend to increase the plume speeds, and, along with decreasing overflow density anomaly, lead to lower Richardson numbers and greater likelihood of shear instability. The sill instability process remains less certain (and possibly even more complex). Given the strongly barotropic nature of the flow there and the dipole (or half-dipole)-like nature of the disturbances, a barotropic instability mechanism is probably the most-likely candidate for a dominant role in that process. In any case, some form of barotropic development must occur in, or prior to, the sill region as a way to transform the density gradient forcing into the barotropic flow observed. The restrictive assumptions of the classic baroclinic instability models don't really suit this process, but it might be possible to modify them appropriately. I would suggest that future theoretical attention to instability processes should be focused on the sill and approach regions rather than the downstream slope flow, as many studies have done.

GLOSSARY

ADCP: Acoustic Doppler Current Profiler—An instrument that uses the Doppler shift of sound scattered from suspended particles in the water to compute a profile of velocity. ADCPs in use on the *Poseidon* and *Aranda* were both narrowband units manufactured by RD Instruments.

ADU: Attitude Determination Unit—A 4-antenna GPS heading sensor manufactured by Ashtech. Uses phase interferometry to precisely determine the relative positions of the antennas in its array, allowing the computation of very accurate headings.

AIW: Arctic Intermediate Water

AVHRR: Advanced Very High Resolution Radiometer—An instrument that measures sea-surface temperature from the NASA polar-orbiting satellites.

AW: Atlantic Water

CTD: Conductivity, Temperature and Depth—The workhorse of oceanography, generally used in a profiling instrument package lowered from a ship. The CTD actually measures pressure, rather than depth, but there is a direct correspondence between the two. Conductivity and temperature allow for the calculation of salinity and density, which are useful for estimating geostrophic currents as well as to track watermasses.

DGPS: Differential GPS—A method for correcting errors in positions determined from the GPS satellites by comparing with a receiver at a fixed location. Can be done in real-time using signals from established beacons or as a post-processing step using data from a broad region (sometimes called wide-area differential GPS, or WADGPS).

DSO: Denmark Strait Overflow

DSOW: Denmark Strait Overflow Water

EGC: East Greenland Current

ES: Echo Sounder—An instrument that uses the round-trip travel time of an acoustic pulse to infer water depth.

FIMR: Finnish Institute for Marine Research

GIN SEAS: Greenland, Iceland and Norwegian seas. Also called the "Nordic Seas."

GPS: Global Positioning System—A constellation of satellites used for precise navigation, often in conjunction with a shore-based differential station to correct for atmospheric effects and the deliberately degraded signal.

KO: *Käse and Oschlies* [2000]

LADCP: Lowered ADCP—A self-contained ADCP Mounted on a CTD package to get full water column velocity.

MRI: Marine Research Institute of Iceland

NAO: North Atlantic Oscillation

NASA: National Aeronautics and Space Administration

NOAA: National Oceanic and Atmospheric Administration

NSW: Norwegian Sea Deep Water

O73: The ICES OVERFLOW '73 experiment

PIW: Polar Intermediate Water

SA: Selective Availability—Deliberate degradation of the GPS signal by the Department of Defense as a national security measure. As of spring 2000, SA has been turned off, but it was in effect during the measurement programs discussed in this dissertation. One way to circumvent SA is through the use of DGPS stations.

SS97: *Smith and Sandwell* [1997]

SST: Sea-Surface Temperature

TSG: ThermoSaliniGraph

VEINS: Variability of Exchanges in the Nordic Seas—A program run by the EC to monitor all inflows and outflows to the GIN seas.

$\bar{v}^*$: "Vee-bar-star"—The conductivity-weighted depth-averaged velocity determined by measuring the oceanic electric field from a fixed platform.

WOCE: World Ocean Circulation Experiment

XBT: eXpendable BathyThermograph—An expendable probe (manufactured primarily by Sippican) to measure temperature only.

XCP: eXpendable Current Profiler—An instrument manufactured by Sippican that uses the principles of geomagnetic induction to obtain a profile of relative velocity to a depth of up to 2000 meters [*Sanford et al.*, 1993].

XCTD: eXpendable CTD—An expendable version of the ship-lowered CTD. Provides a profile of temperature and electrical conductivity to a depth of up to 1800 m. (Sippican)

BIBLIOGRAPHY

Aagaard, K., and S.-A. Malmberg, Low-frequency characteristics of the Denmark Strait Overflow, in *ICES CM 1978/C:47*, Int. Counc. for the Explor. of the Sea, Copenhagen, 1978.

Alberola, C., C. Millot, U. Send, C. Mertens, and J. L. Fuda, Comparison of XCTD/CTD data, *Deep-Sea Res.*, *43*, 859–876, 1996.

Ashtech, *ADU-II Operator Manual*, P/N 630061, Rev. II, 1996.

Bacon, S., Decadal variability in the outflow from the Nordic Seas to the deep Atlantic Ocean, *Nature*, *394*, 871–874, 1998.

Baringer, M. O., and J. F. Price, Momentum and energy balance of the Mediterranean outflow, *J. Phys. Oceanogr.*, *27*, 1678–1692, 1997.

Beckmann, A., and R. Döscher, A method for improved representation of dense water spreading over topography in geopotential-coordinate models, *J. Phys. Oceanogr.*, *27*, 581–591, 1997.

Bond, G., W. Broecker, S. Johnsen, J. McManus, L. Labeyrie, J. Jouzel, and G. Bonani, Correlations between climate records from North Atlantic sediments and Greenland ice, *Nature*, *365*, 143–147, 1993.

Borenäs, K. M., and J. A. Whitehead, Upstream separation in a rotating channel flow, *J. Geophys. Res.*, *103*, 7567–7578, 1998.

Broecker, W. S., The great ocean conveyor, *Oceanography*, *4*, 79–89, 1991.

Bruce, J. G., Eddies southwest of the Denmark Strait, *Deep-Sea Res.*, *42*, 13–29, 1995.

Cooper, L. H. N., Deep water movements in the North Atlantic as a link between climatic changes around Iceland and biological productivity of the English Channel and Celtic Sea, *J. Mar. Res.*, *14*, 347–362, 1955.

Dansgaard, W., et al., Evidence for general instability of past climate from a 250-kyr ice-core record, *Nature*, *364*, 218–220, 1993.

Dickson, B., J. Meincke, I. Vassie, J. Jungclaus, and S. Østerhus, Possible predictability in overflow from the Denmark Strait, *Nature*, *397*, 243–246, 1999.

Dickson, R., J. Lazier, J. Meincke, P. Rhines, and J. Swift, Long-term coordinated changes in the convective activity of the North Atlantic, *Progr. Oceanogr.*, *38*, 241–295, 1996.

Dickson, R. R., and J. Brown, The production of North Atlantic Deep Water: Sources, rates, and pathways, *J. Geophys. Res.*, *99*, 12,319–12,341, 1994.

Dietrich, G., Some thoughts on the working-up of the observations made during the "polar front survey" in the I.G.Y. 1958, *Rapp. P.-v. Réun. Cons. int. Explor. Mer.*, *149*, 103–110, 1961.

Doney, S. C., and W. J. Jenkins, Ventilation of the deep western boundary current and abyssal western North Atlantic: estimates from tritium and ^{3}He distributions, *J. Phys. Oceanogr.*, *24*, 638–659, 1994.

DYNAMO Group, Dynamics of North Atlantic models: Final scientific report, *Tech. rep.*, Institut für Meereskunde an der Universität Kiel, Germany, 1997.

Fanning, A. F., and A. J. Weaver, Temporal-geographical meltwater influences on the North Atlantic conveyor: implications for the Younger Dryas, *Paleoceanogr.*, *12*, 307–320, 1997.

Fogelquist, E., J. Blindheim, T. Tanhua, E. Buch, and S. Østerhus, Greenland–Scotland overflow studied by hydro-chemical multivariate analysis, 1998, deep-sea Research, in press.

Fristedt, T., R. Hietala, and P. Lundberg, Stability properties of a barotropic surface-water jet observed in the Denmark Strait, *Tellus*, *51*, 979, 1999.

Girton, J. B., and T. B. Sanford, Velocity profile measurements of the Denmark Strait Overflow, 1998, poster presented at AGU Ocean Sciences meeting, San Diego.

Girton, J. B., and T. B. Sanford, Velocity profile measurements of the Denmark Strait Overflow, *Int. WOCE Newslett.*, *37*, 28–30, 1999.

Girton, J. B., T. B. Sanford, J. H. Dunlap, R. H. Käse, and J. Hauser, Velocity surveying of the Denmark Strait overflow and eddies, in *WOCE North Atlantic Workshop, 23–27 August 1999*, Report No. 169/2000, p. 93, Kiel, Germany, 2000, poster (available from `http://ohm.apl.washington.edu/~girton/`).

Girton, J. B., T. B. Sanford, and R. H. Käse, Synoptic sections of the Denmark Strait overflow, *Geophys. Res. Lett.*, *28*, 1619–1622, 2001.

Griffiths, R. W., Inertial wave drag and the production of intense vortices by turbulent gravity currents, *Ocean Modeling*, *50*, 9–12, 1983.

Jiang, L., and R. W. Garwood, Jr., Three-dimensional simulations of overflows on continental slopes, *J. Phys. Oceanogr.*, *26*, 1214–1233, 1996.

Johnson, G. C., and D. R. Ohlsen, Frictionally modified rotating hydraulic channel exchange and ocean outflows, *J. Phys. Oceanogr.*, *24*, 66–78, 1994.

Johnson, G. C., and T. B. Sanford, Secondary circulation in the Faroe Bank Channel outflow, *J. Phys. Oceanogr.*, *22*, 927–933, 1992.

Johnson, G. C., T. B. Sanford, and M. O'Neil-Baringer, Stress on the Mediterranean outflow plume I: Velocity and water property measurements, *J. Phys. Oceanogr.*, *24*, 2072–2083, 1994.

Jónsson, S., The circulation in the northern part of the Denmark Strait and its variability, in *ICES CM 1999/L:06*, Int. Counc. for the Explor. of the Sea, Copenhagen, 1999.

Joyce, T. M., On in situ "calibration" of shipboard ADCPs, *J. Atmos. Ocean. Tech.*, *6*, 169–172, 1989.

Jungclaus, J. H., and J. O. Backhaus, Application of a transient reduced gravity plume model to the Denmark Strait Overflow, *J. Geophys. Res.*, *99*, 12,375–12,396, 1994.

Jungclaus, J. H., J. Hauser, and R. H. Käse, Cyclogenesis in the Denmark Strait overflow, *J. Phys. Oceanogr.*, 2000, in press.

Käse, R. H., and A. Oschlies, Flow through Denmark Strait, *J. Geophys. Res.*, *105*, 28,527–28,546, 2000.

Killworth, P. D., Mixing on the Weddell Sea continental slope, *Deep-Sea Res.*, *24*, 427–448, 1977.

Killworth, P. D., and N. R. Edwards, A turbulent bottom boundary layer code for use in numerical ocean models, *J. Phys. Oceanogr.*, *29*, 1221–1238, 1999.

Killworth, P. D., and N. R. MacDonald, Maximal reduced-gravity flux in rotating hydraulics, *Geophys. Astrophys. Fluid Dyn.*, *70*, 31–40, 1993.

King, B. A., and E. B. Cooper, Comparison of ship's heading determined from an array of GPS antennas with heading from conventional gyrocompass measurements, *Deep-Sea Res. I*, *40*, 2207–2216, 1993.

Krauss, W., A note on overflow eddies, *Deep-Sea Res. II*, *43*, 1661–7, 1996.

Krauss, W., and R. H. Käse, Eddy formation in the Denmark Strait overflow, *J. Geophys. Res.*, *103*, 15,525–15,538, 1998.

Lee, A., and D. Ellett, On the contribution of overflow water from the Norwegian Sea to the hydrographic structure of the North Atlantic Ocean, *Deep-Sea Res.*, *12*, 129–142, 1965.

LeProvost, C., M. L. Genco, F. Lyard, P. Vincent, and P. Canceil, Spectroscopy of the world ocean tides from a finite element hydrodynamic model, *J. Geophys. Res.*, *99*, 24,777–24,797, 1994.

Livingston, H. D., J. H. Swift, and H. G. Ostlund, Artificial radionuclide tracer supply to the Denmark Strait overflow between 1972 and 1981, *J. Geophys. Res.*, *90*, 6971–6982, 1985.

MacCready, P., and P. B. Rhines, Slippery bottom boundary layers on a slope, *J. Phys. Oceanogr.*, *23*, 5–22, 1993.

Manabe, S., and R. J. Stouffer, Two stable equilibria of a coupled ocean-atmosphere model, *Journal of Climate*, *1*, 841–866, 1988.

Mann, C. R., Temperature and salinity characteristics of the Denmark Strait overflow, *Deep-Sea Res., 16 (Suppl.)*, 125–137, 1969.

Marotzke, J., and J. Willebrand, The North Atlantic mean circulation: Combining data and dynamics, in *The Warmwatersphere of the North Atlantic*, edited by W. Krauss, chap. 20, pp. 55–90, Berlin, Stuttgart: Borntraeger, 1996.

Mauritzen, C., Production of dense overflow waters feeding the North Atlantic across the Greenland–Scotland Ridge. part 1: Evidence for a revised circulation scheme, *Deep-Sea Res. I, 43*, 769–806, 1996a.

Mauritzen, C., Production of dense overflow waters feeding the North Atlantic across the Greenland–Scotland Ridge. part 2: An inverse model, *Deep-Sea Res. I, 43*, 807–835, 1996b.

McCartney, M., K. Donohue, R. Curry, C. Mauritzen, and S. Bacon, Did the overflow from the Nordic Seas intensify in 1996–1997?, *Int. WOCE Newslett., 31*, 3–7, 1998.

Mooney, C. J., and G. E. Swaters, Finite-amplitude baroclinic instability of a mesoscale gravity current in a channel, *Geophys. Astrophys. Fluid Dyn., 82*, 173–205, 1996.

Pedersen, F. B., Friction in a shallow two-layer flow in a rotating ocean, in *The physical oceanography of sea straits*, edited by L. Pratt, pp. 545–557, Kluwer Academic, The Netherlands, 1990.

Pierce, S. D., J. A. Barth, and R. L. Smith, Improving acoustic Doppler current profiler accuracy with wide-area differential GPS and adaptive smoothing of ship velocity, *J. Atmos. Ocean. Tech., 16*, 591–596, 1999.

Pollard, R., and J. Read, A method for calibrating shipmounted acoustic Doppler profilers and the limitations of gyro compasses, *J. Atmos. Ocean. Tech., 6*, 859–865, 1989.

Prater, M. D., A method for depth and temperature correction of expendable probes, *J. Atmos. Ocean. Tech., 8*, 888–894, 1991.

Pratt, L. J., Hydraulic control of sill flow with bottom friction, *J. Phys. Oceanogr.*, *16*, 1970–1980, 1986.

Pratt, L. J., Geostrophic versus critical control in straits, *J. Phys. Oceanogr.*, *21*, 728–732, 1991.

Press, W. H., S. A. Teukolsky, W. T. Vetterling, and B. P. Flannery, *Numerical Recipes in C: The Art of Scientific Computing*, second ed., Cambridge University Press, 1995.

Price, J. F., and M. O. Baringer, Outflows and deep water production by marginal seas, *Progr. Oceanogr.*, *33*, 161–200, 1994.

Ross, C. K., Overflow '73—transport of overflow water through Denmark Strait, in *ICES CM 1976/C:16*, Int. Counc. for the Explor. of the Sea, Copenhagen, 1976.

Ross, C. K., Overflow variability in Denmark Strait, in *ICES CM 1978/C:21*, no. 38 in Overflow '73, International Council for the Exploration of the Sea, Copenhagen, 1978, ICES Overflow Contribution No. 38.

Ross, C. K., Temperature–salinity characteristics of the "overflow" water in Denmark Strait during "OVERFLOW '73", *Rapp. P.-v. Réun. Cons. int. Explor. Mer.*, *185*, 111–119, 1984.

Rudels, B., P. Eriksson, H. Grönvall, R. Hietala, and J. Launiainen, Hydrographic observations in Denmark Strait in fall 1997, and their implications for the entrainment into the overflow plume, *Geophys. Res. Lett.*, *26*, 1325–1328, 1999a.

Rudels, B., H. J. Friedrich, and D. Quadfasel, The arctic circumpolar boundary current, *Deep-Sea Res. II*, *46*, 1023–62, 1999b.

Sanford, T. B., Motionally induced electric and magnetic fields in the sea, *J. Geophys. Res.*, *76*, 3467–3492, 1971.

Sanford, T. B., and R.-C. Lien, Turbulent properties in a homogeneous tidal bottom boundary layer, *J. Geophys. Res.*, *104*, 1245–1257, 1999.

Sanford, T. B., R. G. Drever, and J. H. Dunlap, A velocity profiler based on the principles of geomagnetic induction, *Deep-Sea Res.*, *25*, 183–210, 1978.

Sanford, T. B., R. G. Drever, J. H. Dunlap, and E. A. D'Asaro, Design, operation and performance of an expendable temperature and velocity profiler (XTVP), *Tech. Rep. APL/UW 8110*, Applied Physics Laboratory, University of Washington, Seattle, WA, 1982.

Sanford, T. B., E. A. D'Asaro, E. L. Kunze, J. H. Dunlap, R. G. Drever, M. A. Kennelly, M. D. Prater, and M. S. Horgan, An XCP user's guide and reference manual, *Tech. Rep. APL/UW 9309*, Applied Physics Laboratory, University of Washington, Seattle, WA, 1993.

Saunders, P., The dense northern overflows, in *Ocean Circulation and Climate*, edited by G. Siedler, J. Church,, and J. Gould, Academic Press, 2000, in press.

Schiller, A., U. Mikolajewicz, and R. Voss, The stability of the North Atlantic thermohaline circulation in a coupled ocean-atmosphere general circulation model, *Clim. Dyn.*, *13*, 325–347, 1997.

Smethie, W. M., Jr., and R. A. Fine, Rates of North Atlantic Deep Water formation calculated from chlorofluorocarbon inventories, *dsr1*, *48*, 189, 2001.

Smethie, W. M., Jr., and J. H. Swift, The tritium:krypton-85 age of Denmark Strait overflow water and Gibbs Fracture Zone water just south of Denmark Strait, *J. Geophys. Res.*, *94*, 8265–8275, 1989.

Smith, P. C., A streamtube model for bottom boundary currents in the ocean, *Deep-Sea Res.*, *22*, 853–873, 1975.

Smith, P. C., Baroclinic instability in the Denmark Strait Overflow, *J. Phys. Oceanogr.*, *6*, 355–371, 1976.

Smith, W. H. F., and D. T. Sandwell, Global sea floor topography from satellite altimetry and ship depth soundings, *Science*, *277*, 1956–1962, 1997.

Song, Y. T., and Y. Chao, An embedded bottom boundary layer formulation for z-coordinate ocean models, *J. Atmos. Ocean. Tech.*, *17*, 546–560, 2000.

Spall, M. A., and J. F. Price, Mesoscale variability in Denmark Strait: The PV outflow hypotheses, *J. Phys. Oceanogr.*, *28*, 1598–1623, 1998.

Stahr, F. R., and T. B. Sanford, Transport and bottom boundary layer observations of the North Atlantic Deep Western Boundary Current at the Blake Outer Ridge, *Deep-Sea Res. II*, *46*, 205–243, 1999.

Stein, M., Observations on the variability of the outflow of the Greenland Sea through the Denmark Strait, *Ber. dt. wiss. Kommn. Meeresforsch.*, *23*, 337–351, 1974.

Strass, V. H., E. Fahrbach, U. Schauer, and L. Sellmann, Formation of Denmark Strait Overflow Water by mixing in the East Greenland Current, *J. Geophys. Res.*, *98*, 6907–6919, 1993.

Swaters, G. E., On the baroclinic instability of cold-core coupled density fronts on a sloping continental shelf, *J. Fluid Mech.*, *224*, 361–382, 1991.

Swift, J. H., The circulation of the Denmark Strait and Iceland–Scotland overflow waters in the North Atlantic, *Deep-Sea Res.*, *31*, 1339–1355, 1984.

Swift, J. H., Ventilation of Denmark Strait Overflow Water, 1999, poster presented at WOCE North Atlantic Workshop, Kiel, Germany.

Swift, J. H., K. Aagaard, and S.-A. Malmberg, The contribution of the Denmark Strait overflow to the deep North Atlantic, *Deep-Sea Res.*, *27A*, 29–42, 1980.

Whitehead, J. A., Internal hydraulic control in rotating fluids—applications to oceans, *Geophys. Astrophys. Fluid Dyn.*, *48*, 169–192, 1989.

Whitehead, J. A., Topographic control of oceanic flows in deep passages and straits, *Rev. Geophys.*, *36*, 423–440, 1998.

Whitehead, J. A., and J. Salzig, Rotating channel flow: control and upstream currents, 1999, unpublished.

Whitehead, J. A., M. E. Stern, G. R. Flierl, and B. A. Klinger, Experimental observations of baroclinic eddies on a sloping bottom, *J. Geophys. Res.*, *95*, 9585–9610, 1990.

Willebrand, J., et al., Circulation characteristics in three eddy-permitting models of the North Atlantic, *Progr. Oceanogr.*, 1999, submitted.

Winton, M., R. Hallberg, and A. Gnanadesikan, Simulation of density-driven frictional downslope flow in z-coordinate ocean models, *J. Phys. Oceanogr.*, *28*, 2163–2174, 1998.

Worthington, L. V., An attempt to measure the volume transport of Norwegian Sea overflow water through the Denmark Strait, *Deep-Sea Res.*, *16*, 421–432, 1969.

Yang, J., and J. G. Price, Water-mass formation and potential vorticity balance in an abyssal ocean circulation, *J. Mar. Res.*, *58*, 2000.

Appendix A

MAGNETOTELLURIC CONTAMINATION

Since the XCP measures velocity using motionally-induced electrical currents in the ocean, it is vulnerable to external processes which may also generate electrical currents. These may come from a variety of atmospheric, ionospheric or geophysical sources having nothing to do with the water velocity, yet appearing as velocity signals in the XCP measurement.

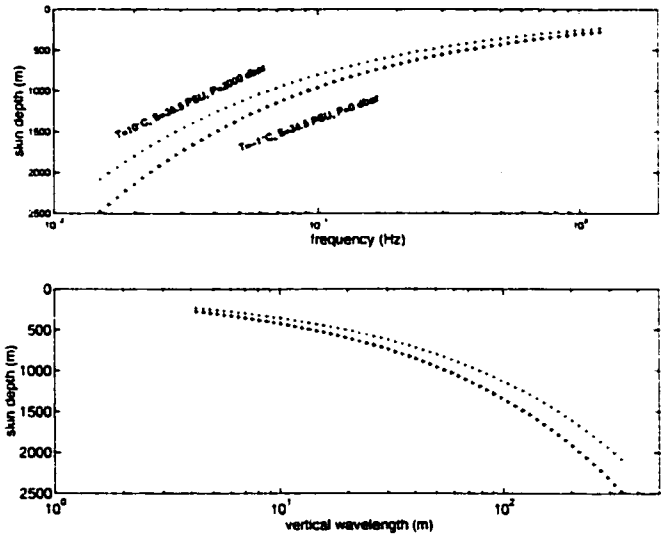


Figure A.1: An estimate of the skin depth of electromagnetic (EM) wave penetration into the ocean for a likely range of oceanographic parameters. Skin depth is plotted versus incoming frequency (upper panel) and apparent vertical wavelength, as measured by an XCP falling at $5\,\mathrm{m\,s^{-1}}$ (lower panel).

A.1 Electromagnetic Frequency Window

Fortunately, the conductivity of seawater shields the deep ocean from high-frequency electromagnetic signals (see Figure A.1) while slowly-varying external electrical currents only show up as a depth-independent XCP offset, which is removed by ADCP

referencing. There is a window of frequencies, however, from approximately 8×10^{-4} Hz to 0.4 Hz (periods of 2.5 s to 20 min) which could have an effect by producing apparent shears in the XCP profile.

At the high-frequency end, a signal with a period of 2.5 s could reach to about 500 m depth, appearing in the velocity profile as a feature with a vertical wavelength of 12 m. Most of the velocity profiles presented in this thesis have been smoothed by a Savitsky-Golay (polynomial) filter which effectively removes features smaller than about 50 m, corresponding to a 10 s period, or 0.1 Hz. At this new upper end frequency limit, the skin depth is about 900 m. The high-frequency shielding of the ocean at typical conductivities, then, is not really sufficient to limit spurious XCP signals.

At the low-frequency end, a 20-min period would appear as a more-or-less linear trend over 1000 m (about 1 radian). Slower oscillations will contribute primarily to the mean offset of the velocity profile (see Section A.3) and will not change the shear profile, except in the case of particularly large signals.

A.2 Sources—aurora!

Magnetic records from nearby observatories in Leirvogur, Iceland (LRV), and Narsarsuaq, Greenland (NAQ), show periods of substantial magnetic activity during the course of our cruise. Since the cruise location was right in the center of the latitude band of strongest *aurora borealis* activity, and, in fact, the aurora was visually apparent during the few clear nights of the cruise, it is likely that the aurora played a role in generating these magnetic storms. Images from the Ultraviolet Imager (UVI) on the Polar satellite at around the time of several XCP drops support this view (Figure A.2). Two of the most likely candidates for auroral contamination (XCP 4197 and 4210) show large bursts of UV emission over the Denmark Strait in conjunction with rapid, large-amplitude variability in accompanying magnetogram records. Drops during periods of quieter magnetogram activity (*e.g.*, XCP 4108 and 4152) show little UV emission and little evidence of contamination in the velocity profile (though this is not always obvious).

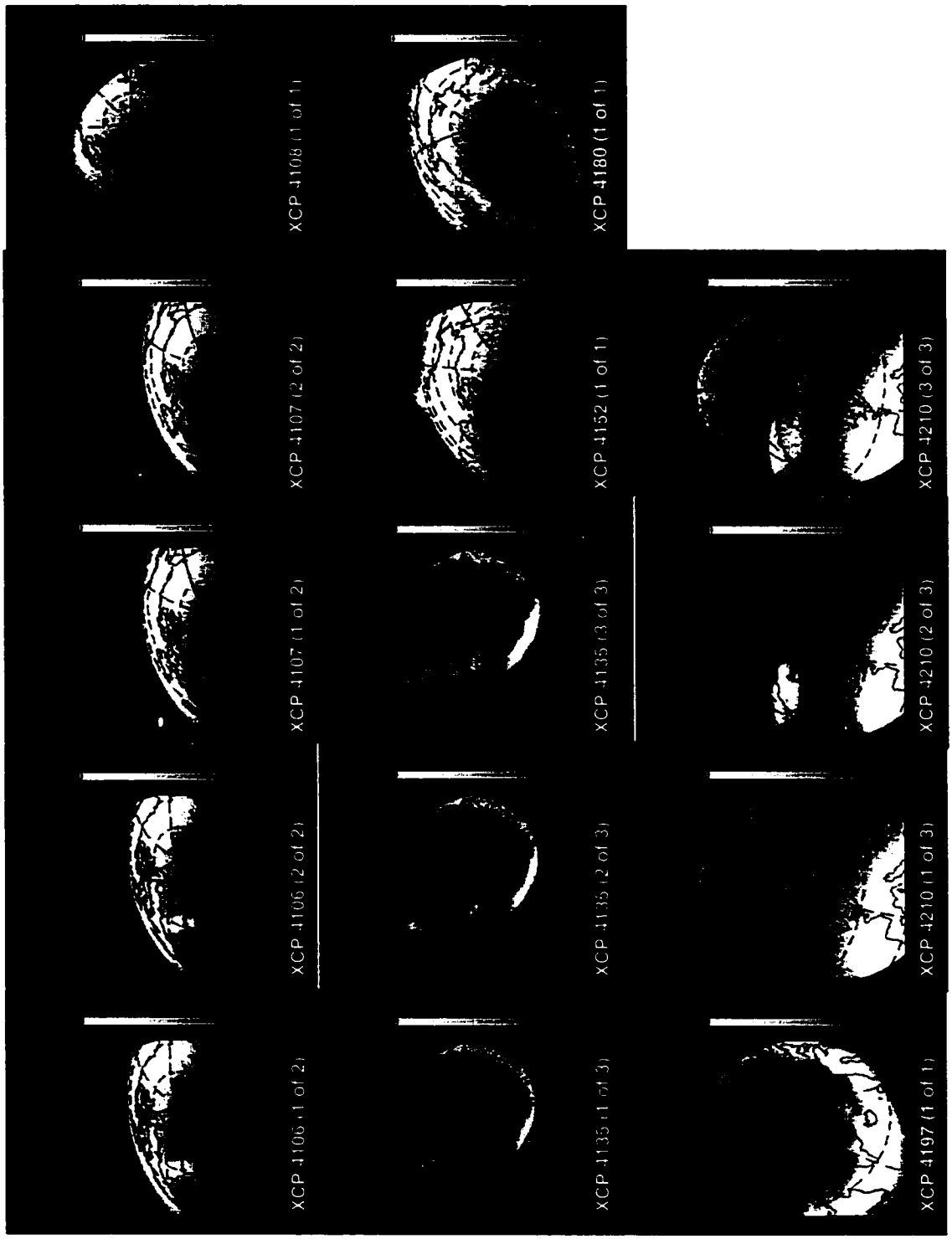


Figure A.2: Images of ultraviolet emissions from the *aurora borealis* near the times of selected XCP drops as observed by the Ultraviolet Imager (UVI) on the Polar satellite. XCP profile number and number of consecutive images for each drop are labeled on the figure, as are the date and time of each image. Consecutive images are approximately 5 minutes apart.

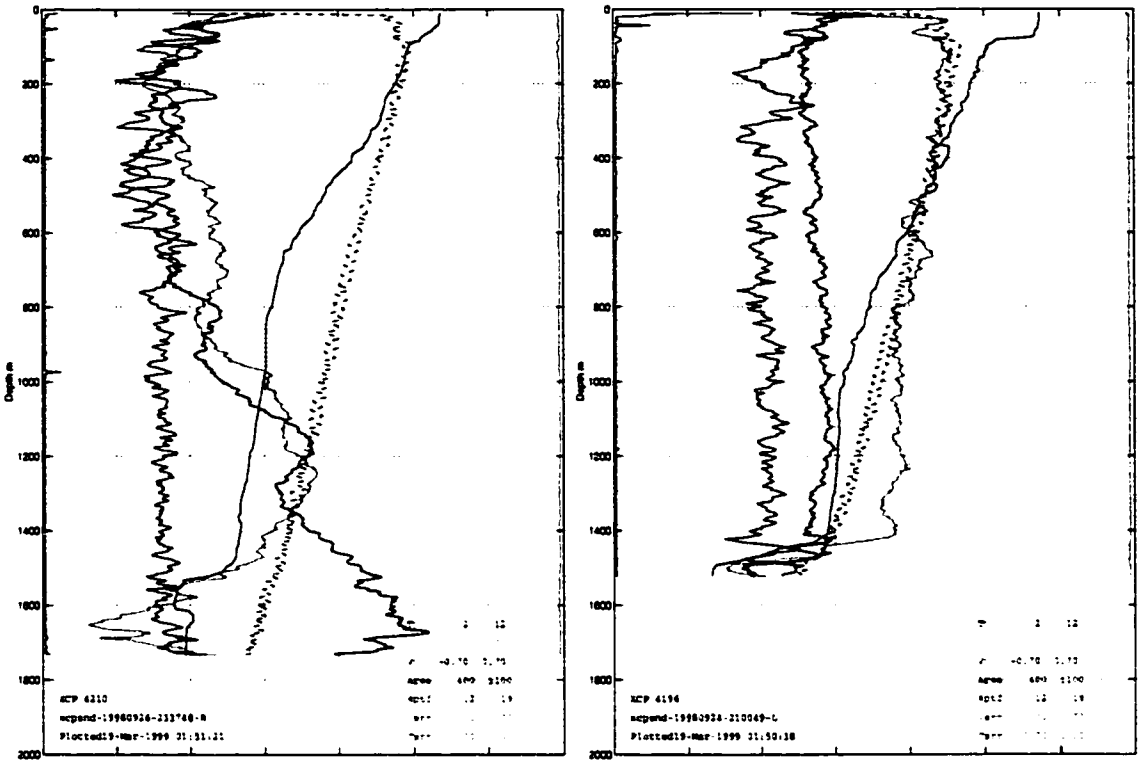


Figure A.3: Profiles of velocity (east-west and north-south in red and blue, respectively), temperature (in black) and probe diagnostics (in green and cyan) from XCP 4210 and XCP 4196.

A.3 XCP Offsets and magnetogram rate of change

It is difficult to determine exactly how much contamination of this sort is occurring with our measurements. One indicator might be the presence of shear over a substantial depth-range, as seen in XCP 4210 (Figure A.3), which is not expected from oceanic conditions. (On the other hand, localized shear near the top and/or bottom *is* expected and seen in, for example, XCP 4196.) A non-oceanic shear of this kind might be detectable via differences between the velocity profiles measured by the XCP and ADCP in the upper water column. However, diagnosing this difference is difficult because of the many other factors that can contribute to ADCP/XCP differences, including oceanic variability, ADCP noise and differing vertical resolutions.

Another diagnostic of external electrical currents is from the depth-averaged XCP velocity offset which, according to EM induction theory, should be small, or, at most,

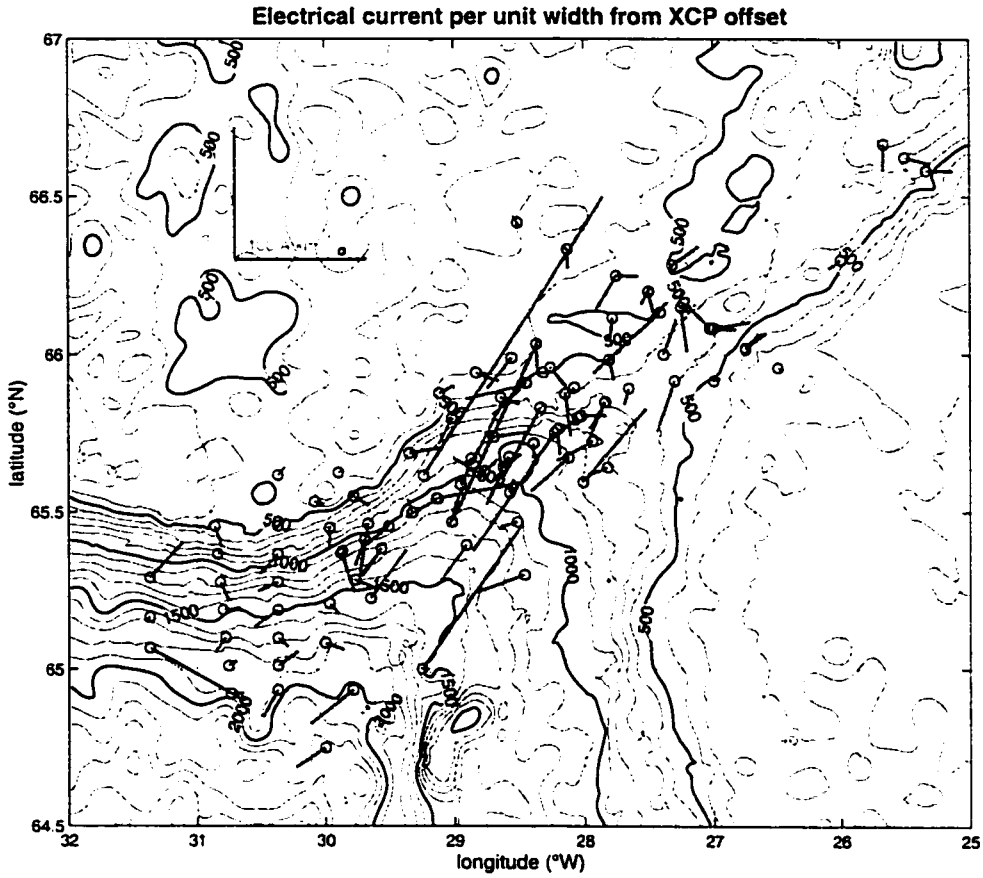


Figure A.4: Electric current required to produce the observed XCP offset at each drop location. Vectors plotted are essentially the velocity offsets rotated clockwise by 90° and multiplied by local depth, vertical geomagnetic field and conductivity to give electrical current integrated over the water column.

weakly proportional to the true depth-averaged water velocity. As the ADCP-referenced data show, however, the XCP offsets exhibit a $\pm 0.15\,\mathrm{m\,s^{-1}}$ scatter around this predicted range, with several outliers to 0.5 or $1.0\,\mathrm{m\,s^{-1}}$, probably indicating external contamination. (It should be noted that these offsets in themselves do not affect the validity of the XCP profile, since they are removed by ADCP referencing, but they may be symptomatic of external activity.) The orientation and geographic distribution of XCP velocity offsets is shown in Figure A.4, rotated by 90°and scaled by water depth into units of electrical current, indicating the effective current required to produce such an offset. The vectors in Figure A.4 do show a preferred orientation, roughly aligned with topography, possibly indicating the presence of large-scale electrical currents channeled by topographic features such as the Denmark Strait.

When taken all together, the mean of the XCP offsets indicates a current per unit width of about $8\,\mathrm{A\,km^{-1}}$, directed out of the Nordic Seas. If not simply a residual of large random fluctuations, this could be related to the "global electric circuit" of the troposphere/ionosphere system, although the magnitude seems quite large.

Although initial visual inspection of the magnetogram records at the times of questionable XCP drops generally does turn up enhanced magnetic activity, a quantititative match has so far eluded detection. One might expect that magnetogram variations such as a change over time (single difference) or a trend over time (linear fit) would produce an induced electrical current in the perpendicular direction. Since the observed electrical currents from XCP offsets appear to be mostly aligned with the strait (35°T), I have attempted to correlate these with the perpendicular magnetogram component (towards 125°T), but this has not produced any obviously positive results (Figure A.5). Neither has an attempt to correlate magnetogram activity with XCP/ADCP fit RMS difference, which might be expected to respond to higher frequency electrical signals than the mean offset. The lack of correlation either implies that too many other factors are responsible for producing either the magnetogram variability or the XCP signals to allow the connections to be easily detected, or that the sources of the XCP and magnetogram signals are, in fact, not directly related.

A.4 1-D transfer function estimates of apparent shear

The next step in the attempt to determine the cause of XCP offsets (and, by extension, the likely source of less-obvious XCP contamination) is to use some sort of model of the earth's conductivity structure to construct a timeseries of predicted electrical currents that would be induced by the observed magnetogram records. This method, known as a magnetotelluric (MT) transfer function, involves assumptions about the nature of incoming EM radiation (generally taken to be plane waves), and can rapidly become quite complicated if 2-D and 3-D effects are to be included, but has the potential to produce a timeseries that can be directly compared to XCP profiles, or possibly even used to correct them. The first attempt at a model of this kind would be to use a 3-layered (earth, water, air) system, followed by some sort of continuous 1-D profile of sediment and rock conductivity.

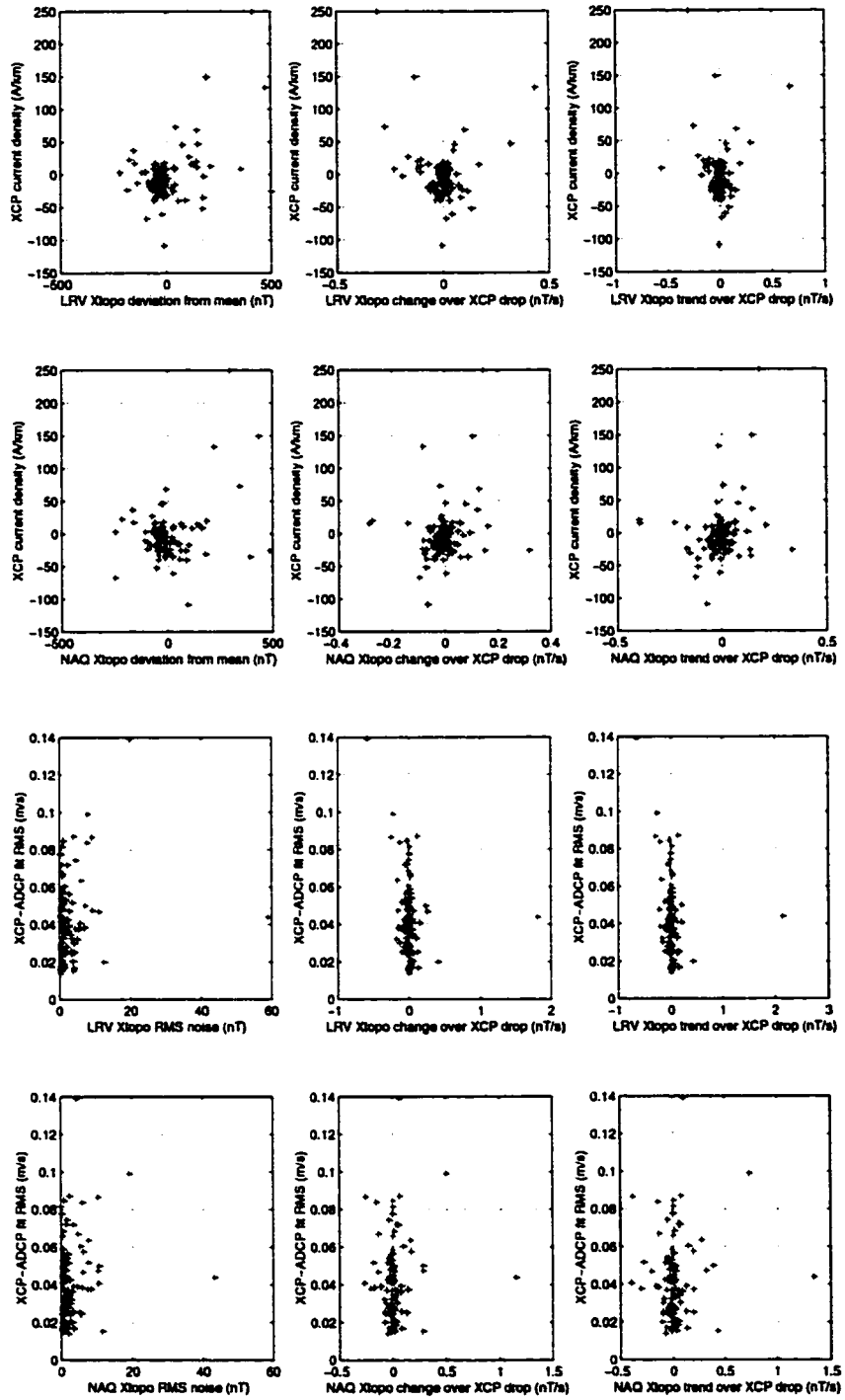


Figure A.5: Correlation between various parameters from *Poseidon* XCPs and nearby magnetograms in Iceland (LRV) and Greenland (NAQ). The top two rows show the XCP velocity offset component in the direction of maximum variability (55°W—corresponds to electrical currents towards 35°E) *versus* the magnetogram activity in the same direction (across topography, or "Xtopo"). The three comparisons are (from left to right) the deviation of the magnetogram record at the time of the drop from the 2-week mean, the magnetogram change over the time (~5 min) that the XCP was falling, and the slope of the magnetogram's linear trend over the same time period. The bottom two rows show the RMS differences between the XCP and ADCP velocities in the region of overlap *versus* magnetogram activity.

Appendix B

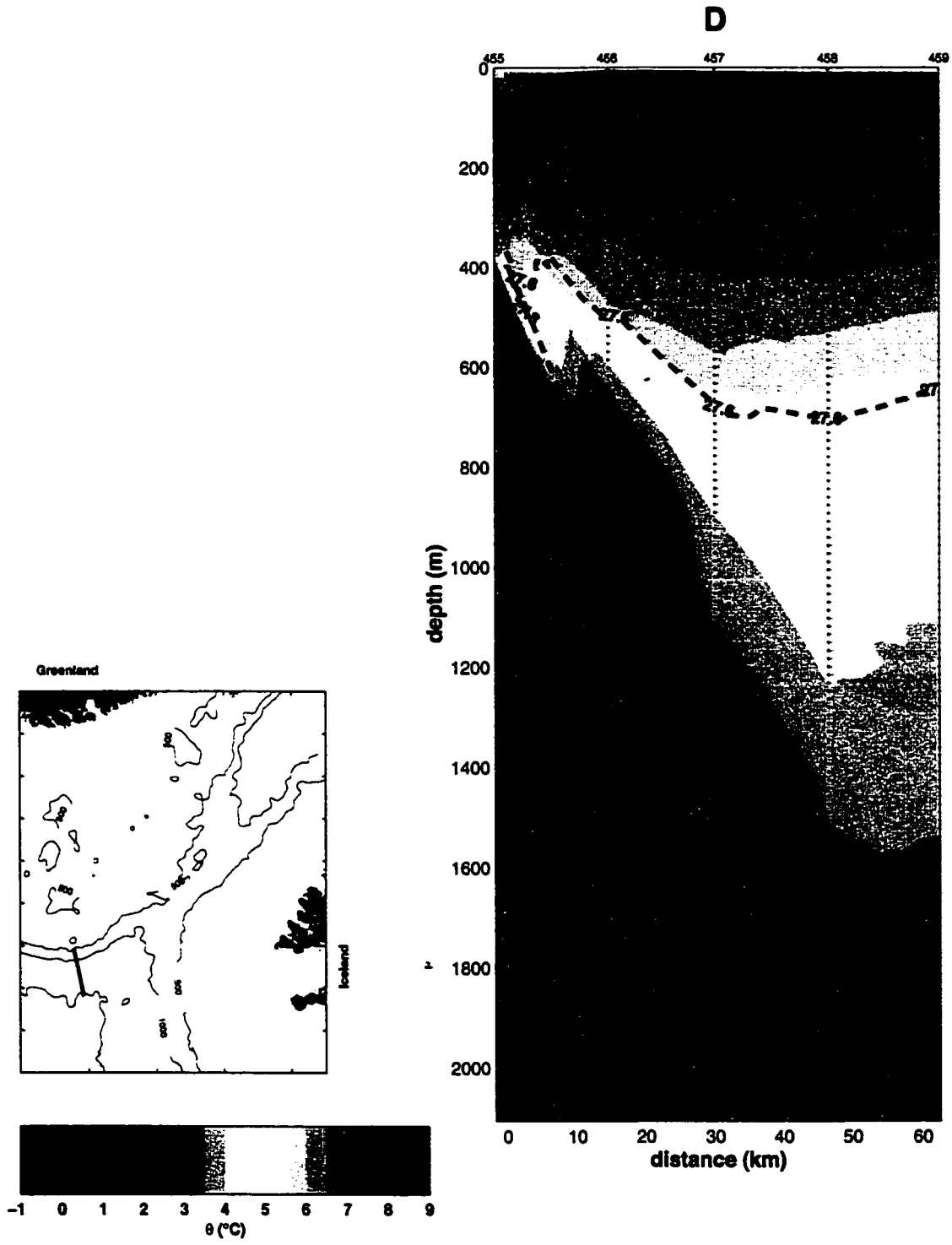
ATLAS OF SECTIONS

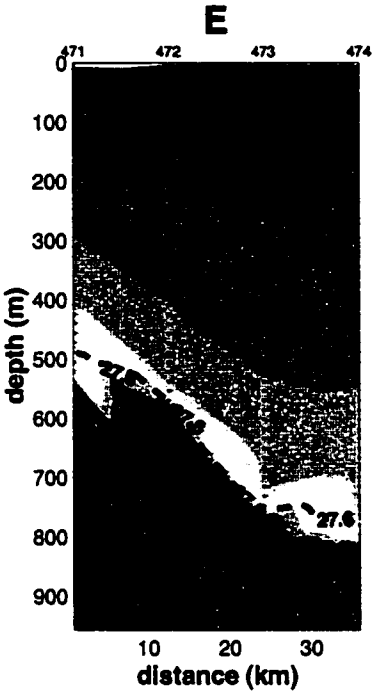
This appendix contains the complete set of contoured sections used for the analyses presented in this dissertation. Data are from CTD, XCP and XCTD profiles taken on the *Aranda* and *Poseidon* cruises described in Chapters 3 and 4, respectively. Descriptions of the locations and circumstances of these sections can also be found in those chapters.

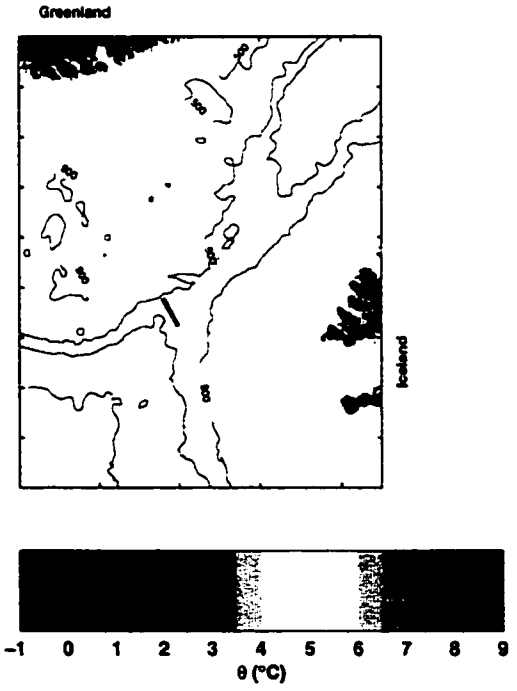
Each variable uses a distinct color scale, except for the two components of velocity, and the depth and length coordinates have been kept consistent throughout all sections for ease of comparison. The order of presentation is:

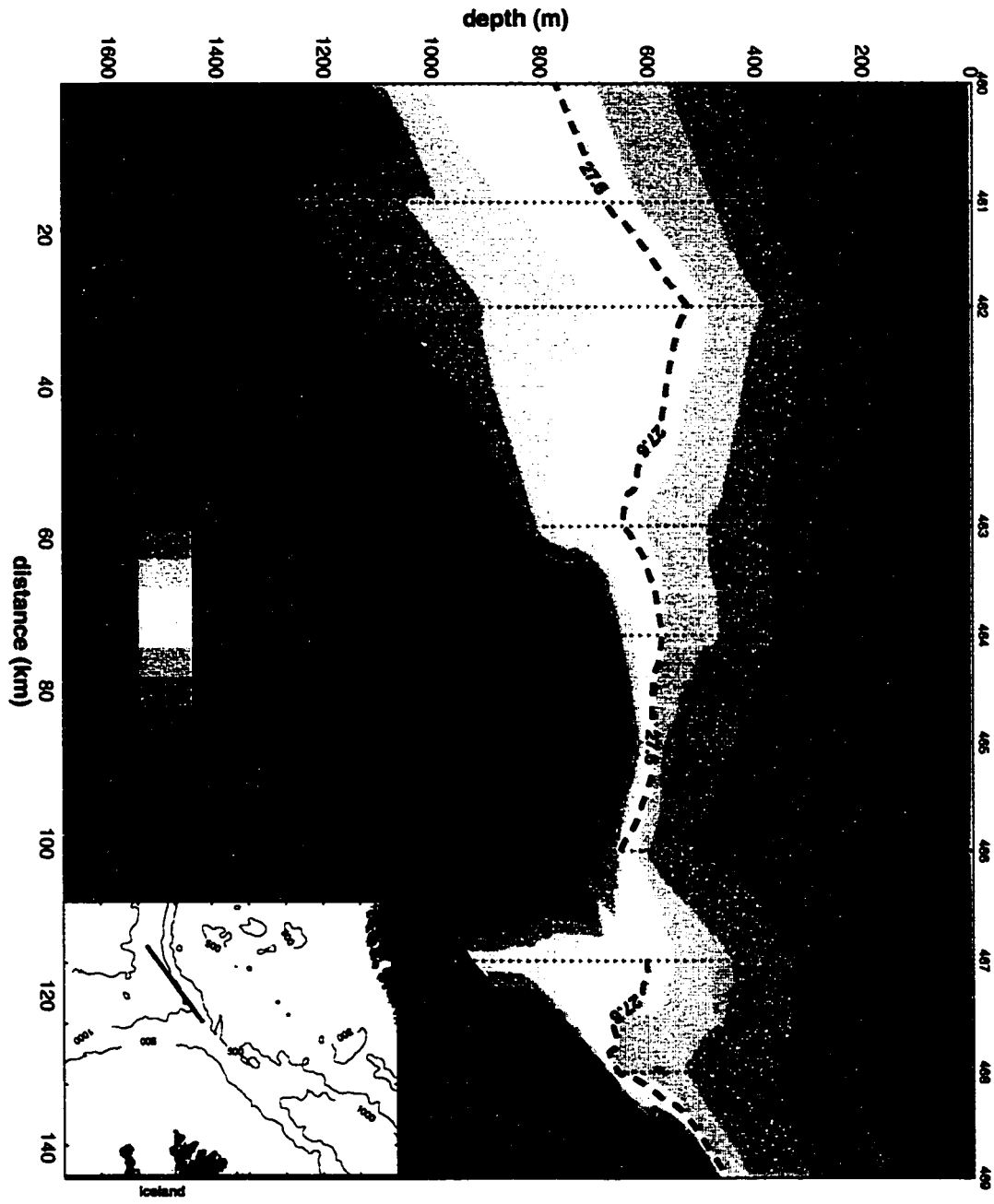
1. temperature (θ),
2. salinity (S),
3. potential density (σ_θ),
4. velocity component perpendicular to each section and
5. velocity component parallel to each section.

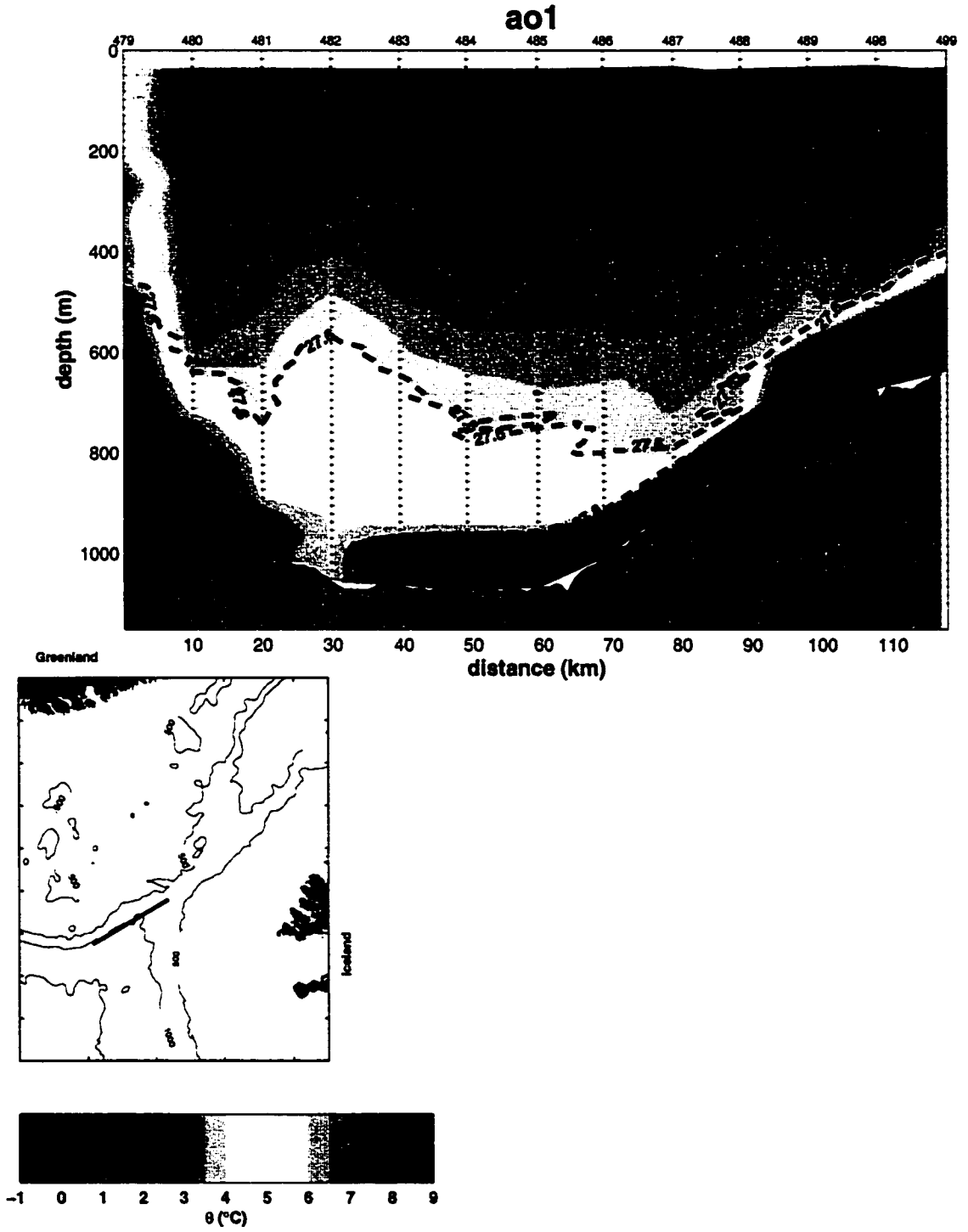
Within each grouping by variable, the *Aranda* sections are presented first and *Poseidon* second, ordered alphabetically using the names assigned in Figures 3.1 and 4.2. Note that sections dse, gs1, gs2, init and nb1 did not include XCP drops so no velocity data are available for these.

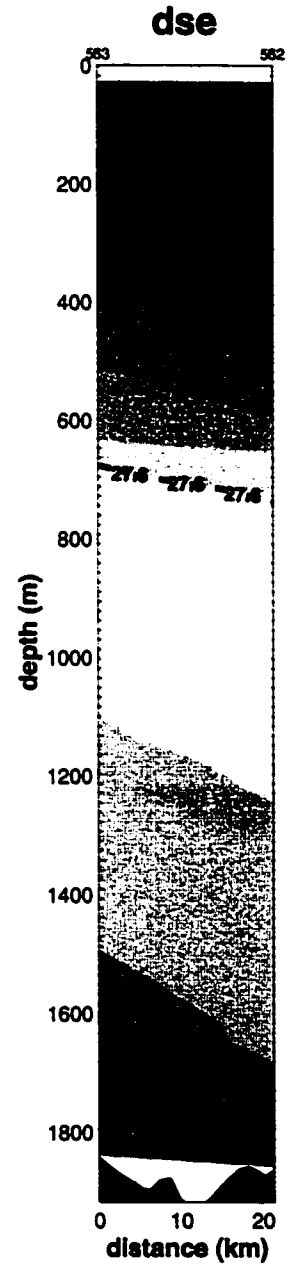

D
455
456
457
458
459
0
200
400
600
800
1000
1200
1400
1600
1800
2000
depth (m)
27
27.6
27.8
0
10
20
30
40
50
60
distance (km)
Greenland
Iceland
−1
0
1
2
3
4
5
6
7
8
9
θ (°C)

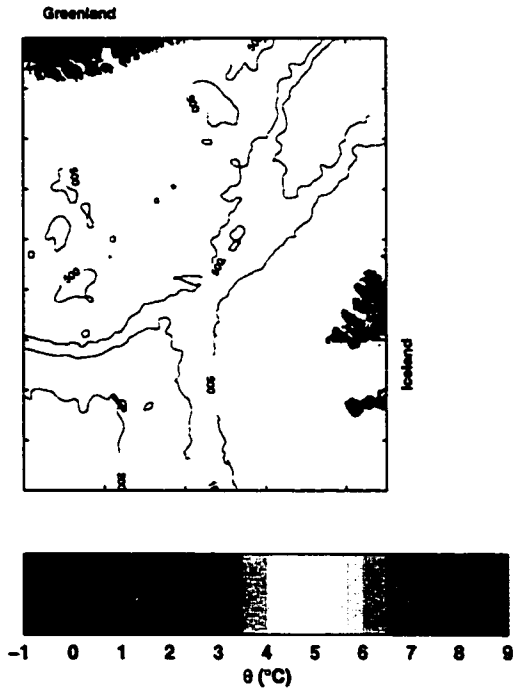

E
471
472
473
474
0
100
200
300
400
500
600
700
800
900
depth (m)
27.6
10
20
30
distance (km)

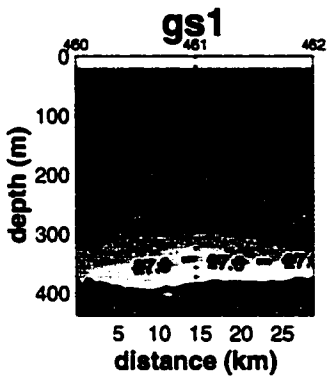

Greenland
Iceland
−1
0
1
2
3
4
5
6
7
8
9
θ (°C)

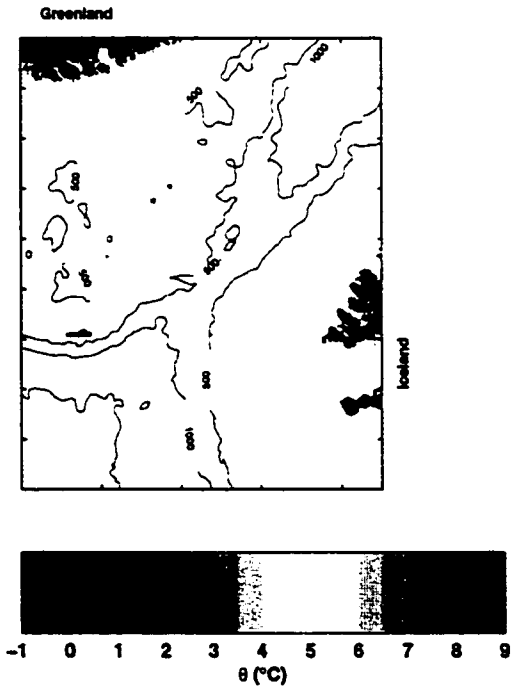

depth (m)
0
200
400
600
800
1000
1200
1400
1600
distance (km)
20
40
60
80
100
120
140
27.6
27.8
27.8
27.8
J
Iceland

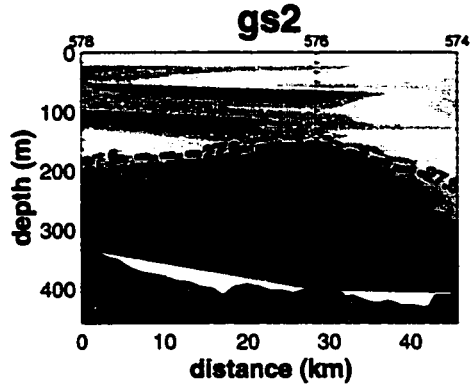

ao1
depth (m)
distance (km)
Greenland
Iceland
θ (°C)

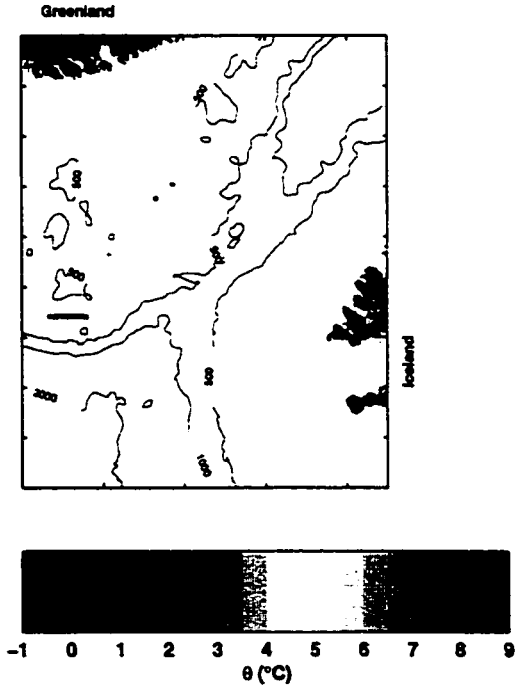

dse
563
562
0
200
400
600
800
1000
1200
1400
1600
1800
depth (m)
27.6
27.6
27.6
0
10
20
distance (km)

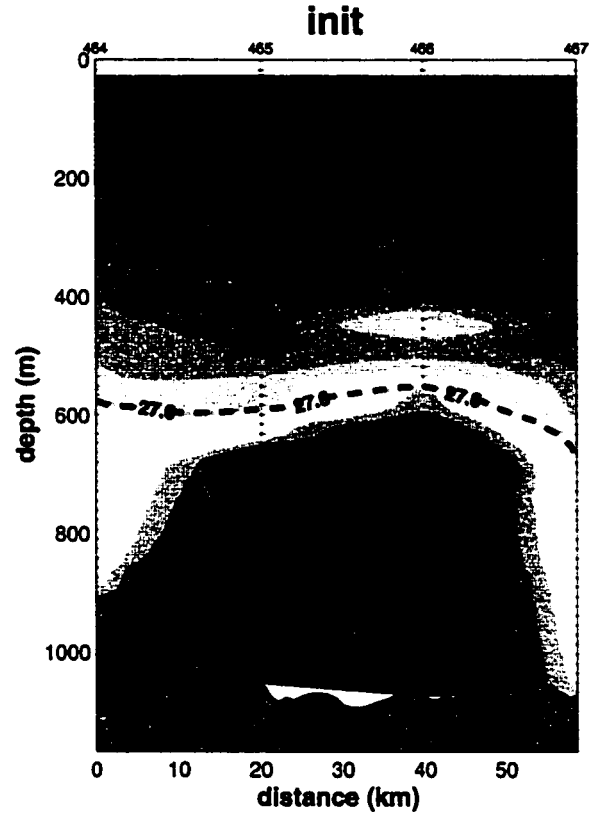

Greenland
Iceland
−1
0
1
2
3
4
5
6
7
8
9
θ (°C)

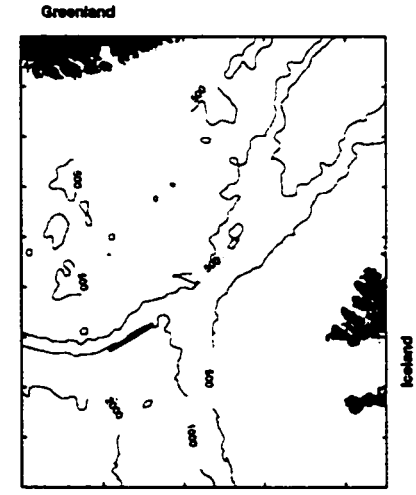

gs1
460
461
462
0
100
200
300
400
depth (m)
5 10 15 20 25
distance (km)

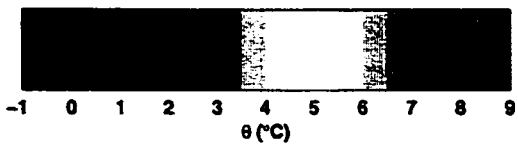

Greenland
Iceland
−1 0 1 2 3 4 5 6 7 8 9
θ (°C)

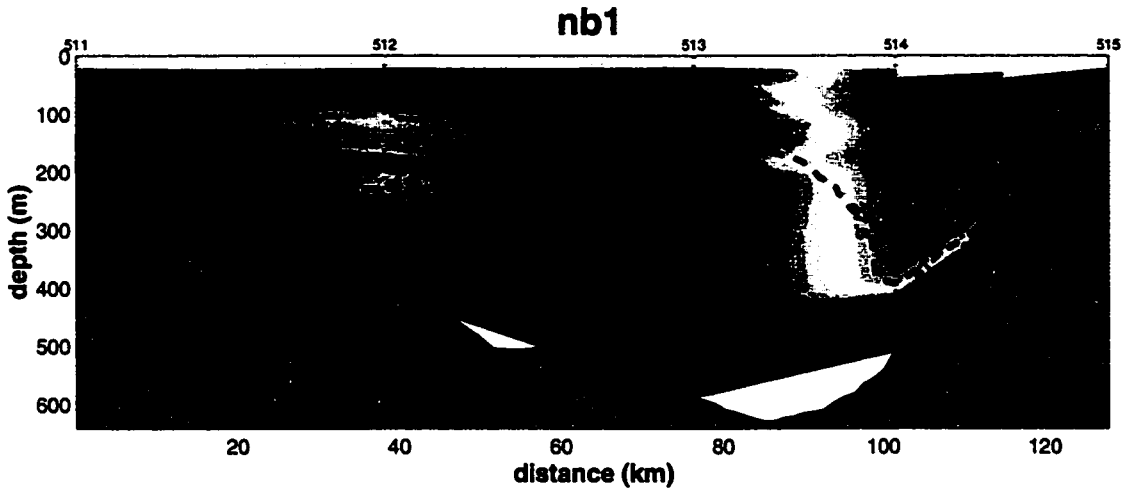

gs2
578
576
574
0
100
200
300
400
depth (m)
0
10
20
30
40
distance (km)

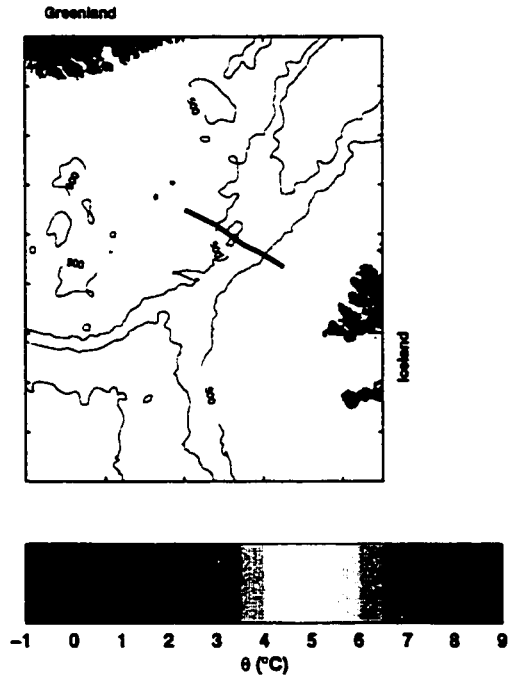

Greenland
Iceland
−1
0
1
2
3
4
5
6
7
8
9
θ (°C)

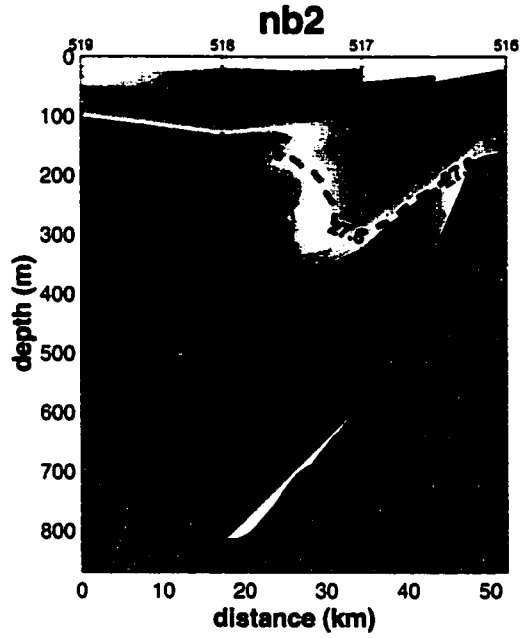

init
464
465
466
467
0
200
400
600
800
1000
depth (m)
27.6
27.8
27.6
0
10
20
30
40
50
distance (km)

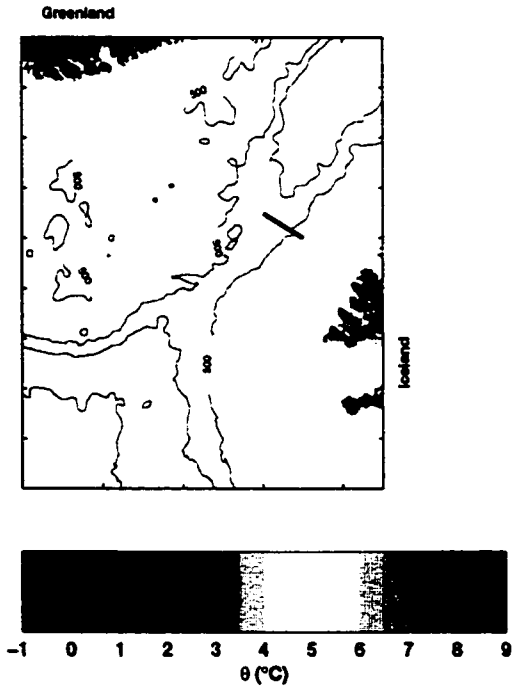

Greenland
Iceland

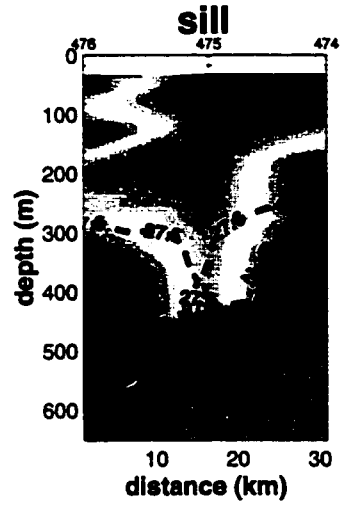

−1
0
1
2
3
4
5
6
7
8
9
θ (°C)

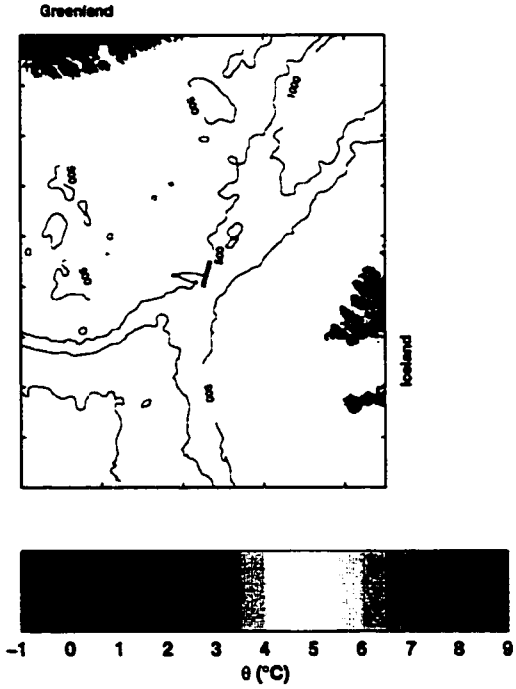

nb1
511
512
513
514
515
0
100
200
300
400
500
600
depth (m)
20
40
60
80
100
120
distance (km)

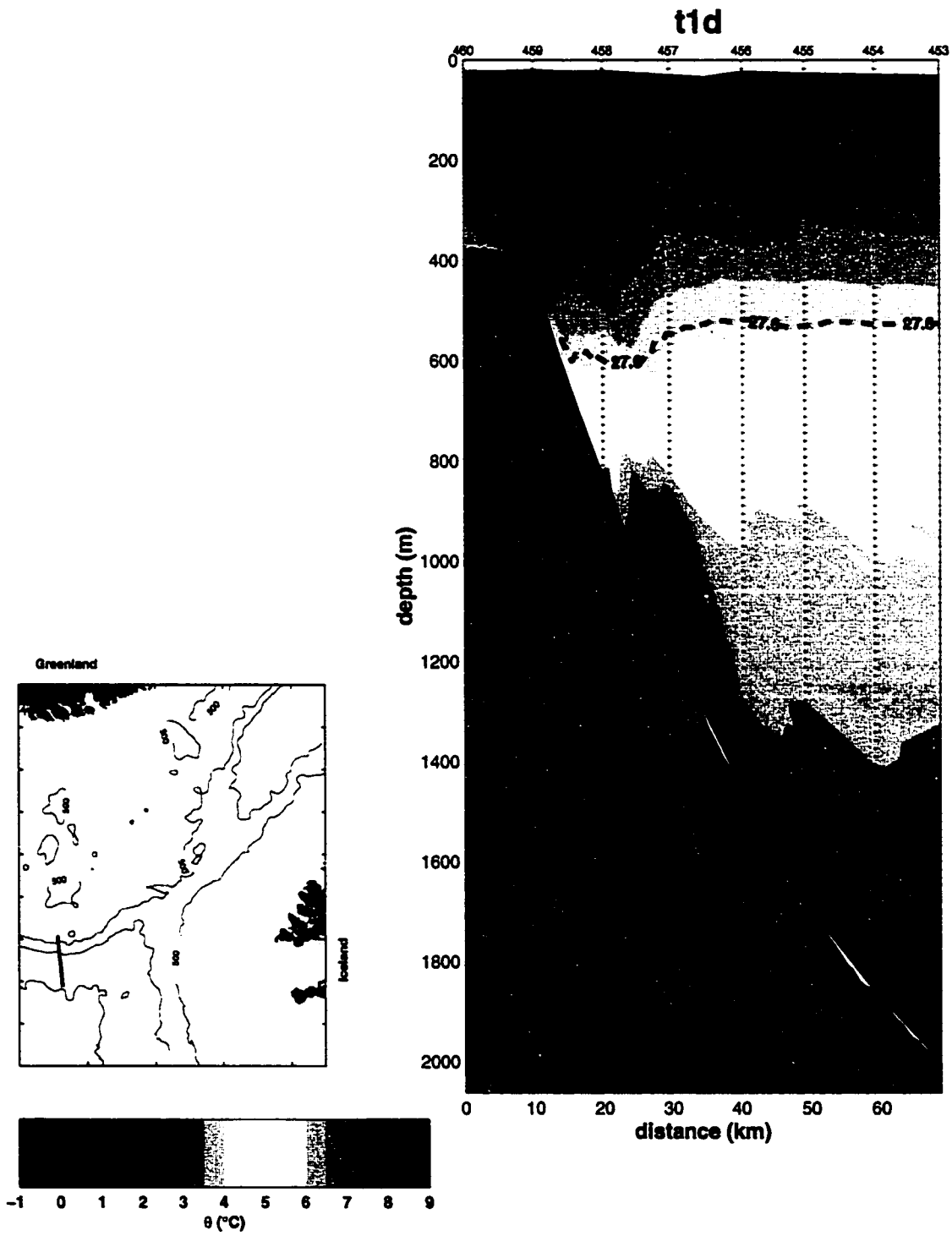

Greenland
Iceland
−1
0
1
2
3
4
5
6
7
8
9
θ (°C)

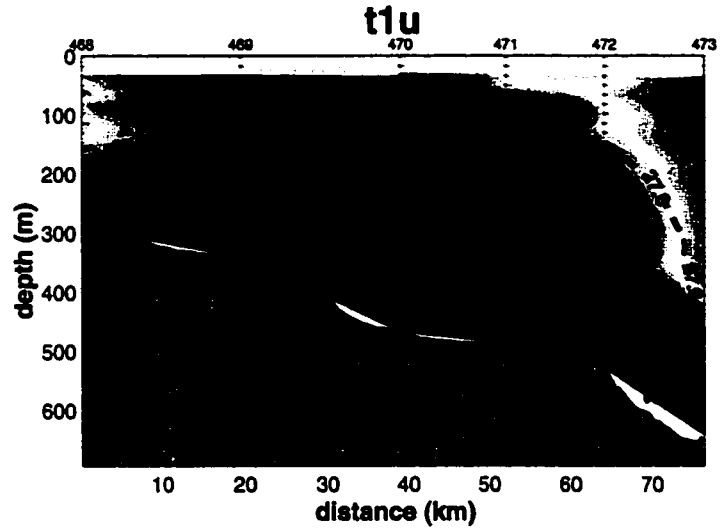

nb2
519
518
517
516
0
100
200
300
400
500
600
700
800
depth (m)
0
10
20
30
40
50
distance (km)

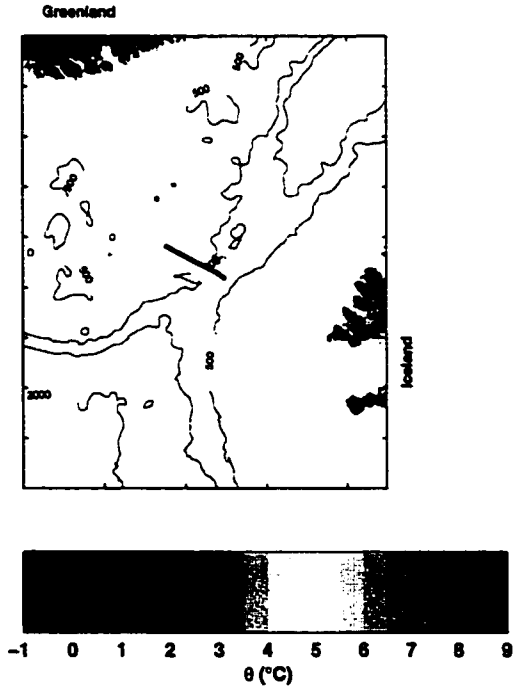

Greenland
Iceland
−1
0
1
2
3
4
5
6
7
8
9
θ (°C)

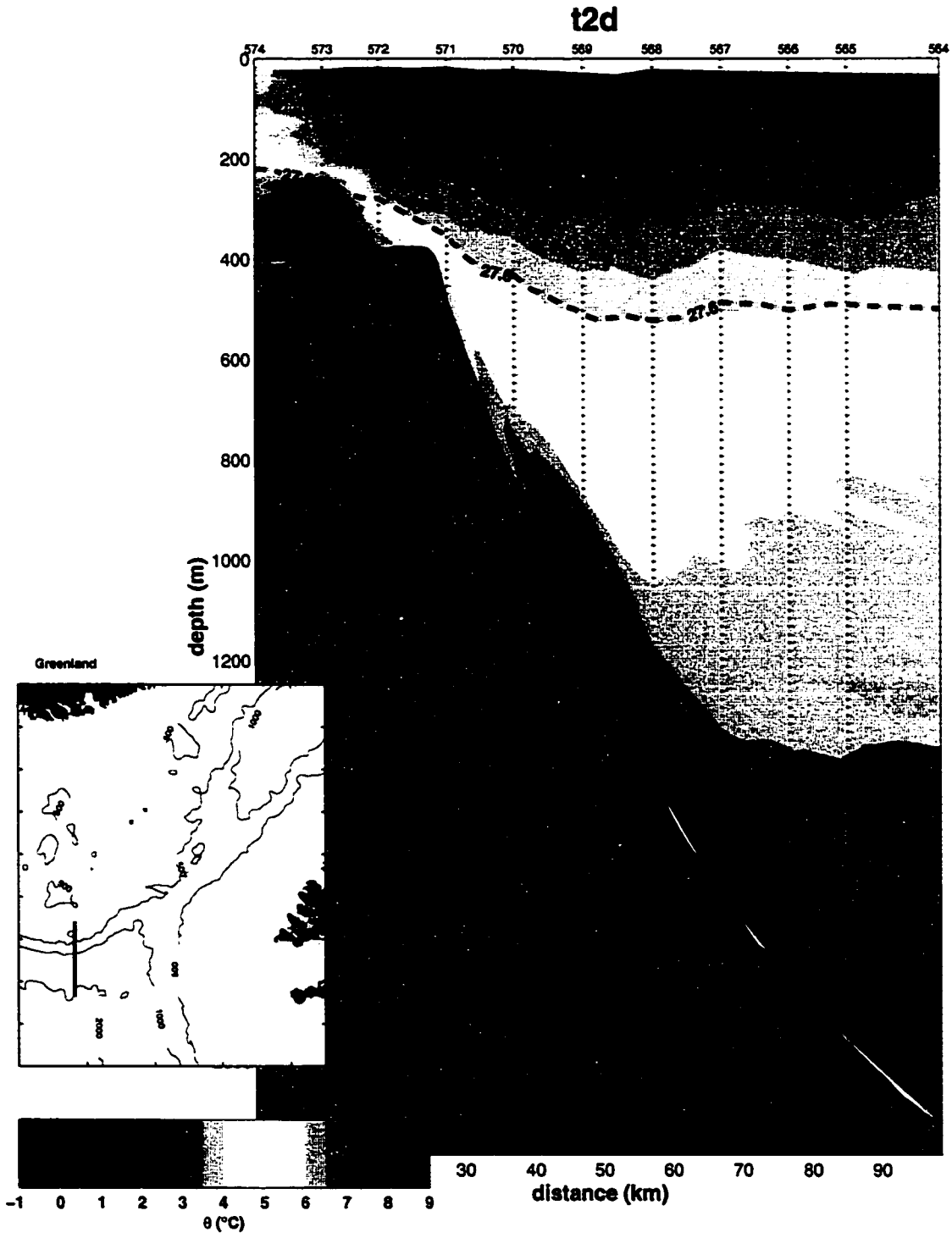

sill
476
475
474
0
100
200
300
400
500
600
depth (m)
10
20
30
distance (km)

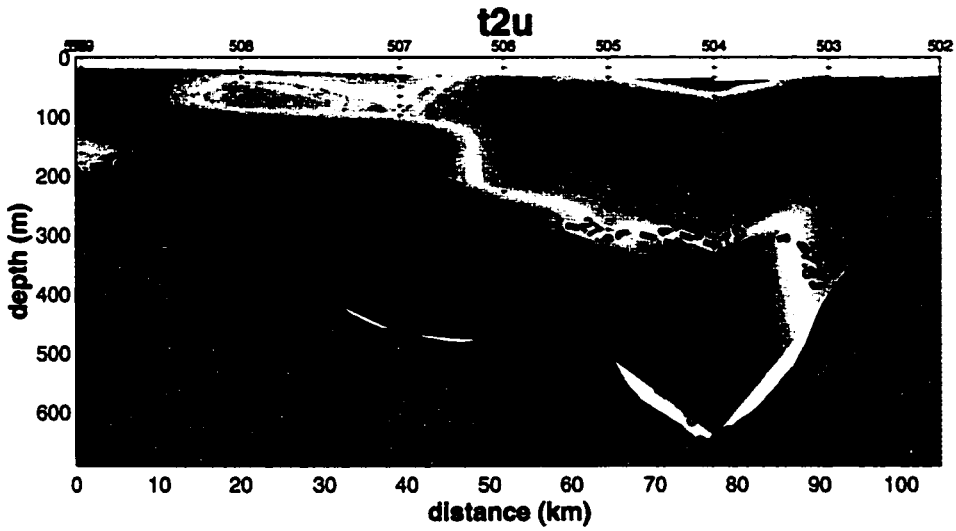

Greenland
Iceland
−1
0
1
2
3
4
5
6
7
8
9
θ (°C)

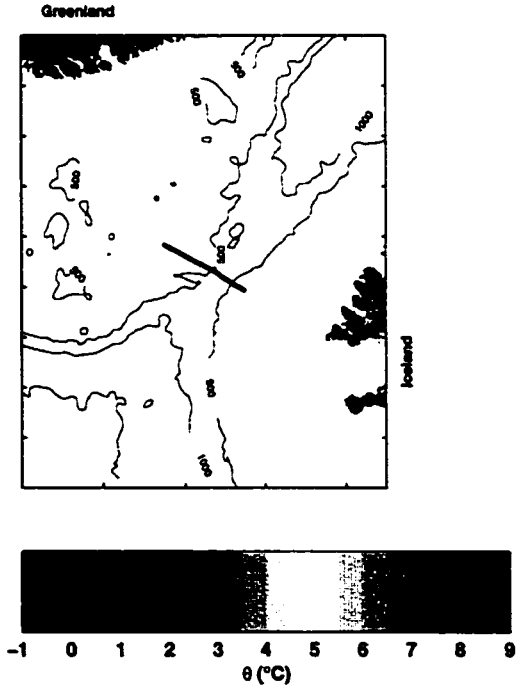

t1d
460
459
458
457
456
455
454
453
0
200
400
600
800
1000
1200
1400
1600
1800
2000
depth (m)
27.6
27.6
27.8
0
10
20
30
40
50
60
distance (km)
Greenland
Iceland
−1
0
1
2
3
4
5
6
7
8
9
θ (°C)


t1u
468
469
470
471
472
473
0
100
200
300
400
500
600
depth (m)
10
20
30
40
50
60
70
distance (km)

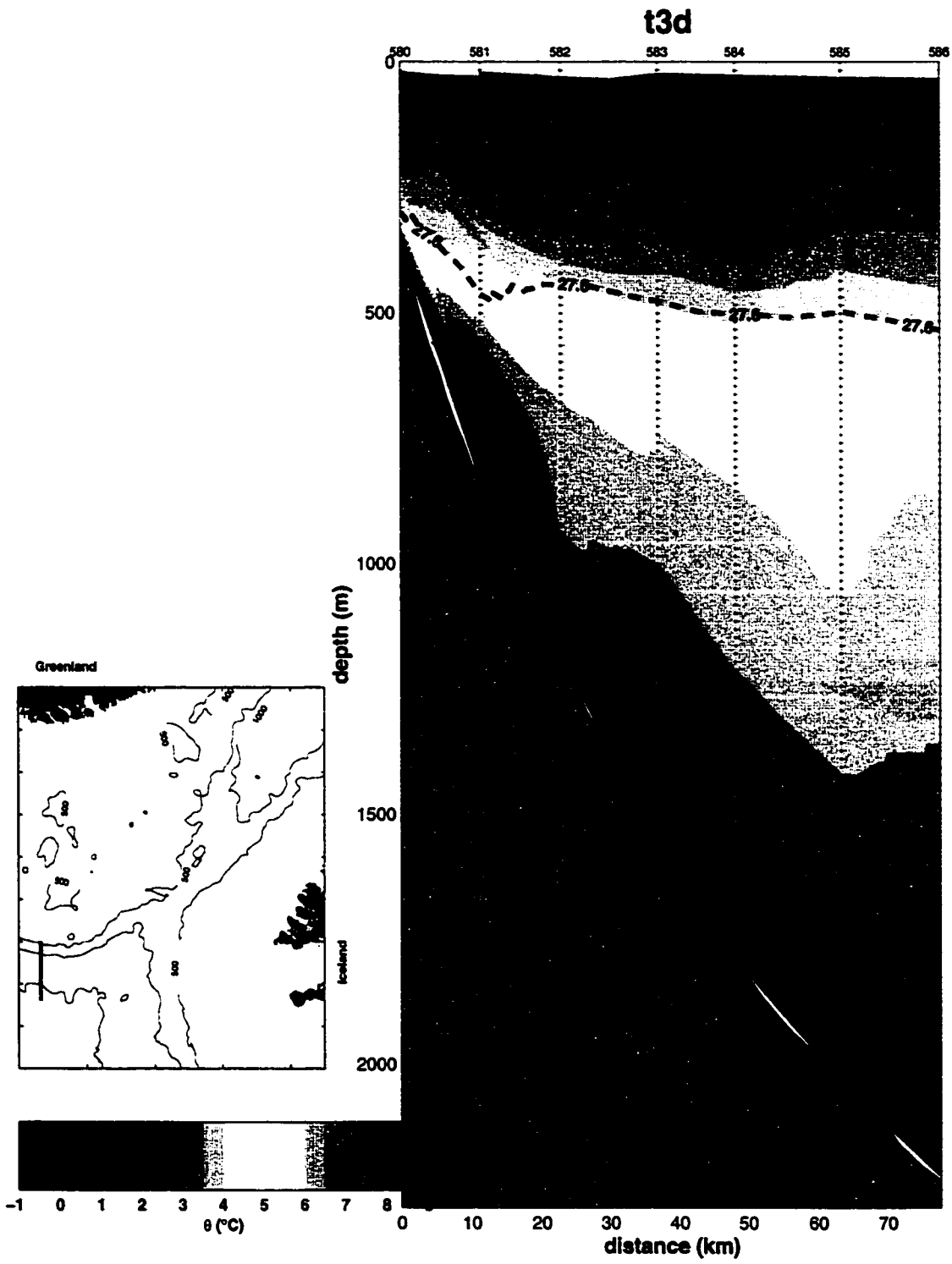

Greenland
Iceland
−1
0
1
2
3
4
5
6
7
8
9
θ (°C)

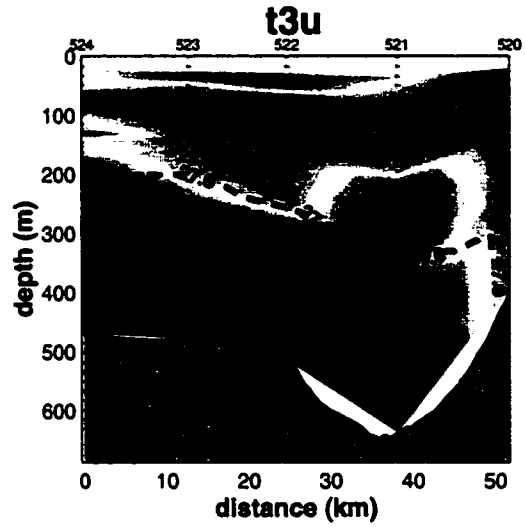

t2d
574
573
572
571
570
569
568
567
566
565
564
0
200
400
600
800
1000
1200
depth (m)
27.6
27.8
Greenland
30
40
50
60
70
80
90
distance (km)
−1
0
1
2
3
4
5
6
7
8
9
θ (°C)

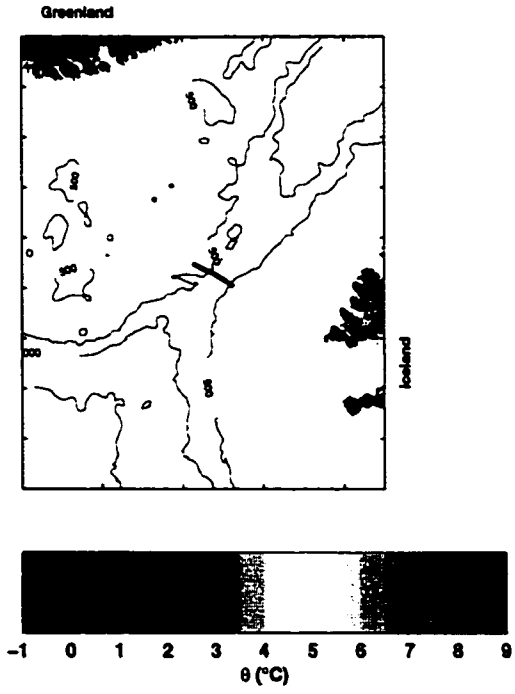

t2u
509
508
507
506
505
504
503
502
0
100
200
300
400
500
600
depth (m)
0
10
20
30
40
50
60
70
80
90
100
distance (km)

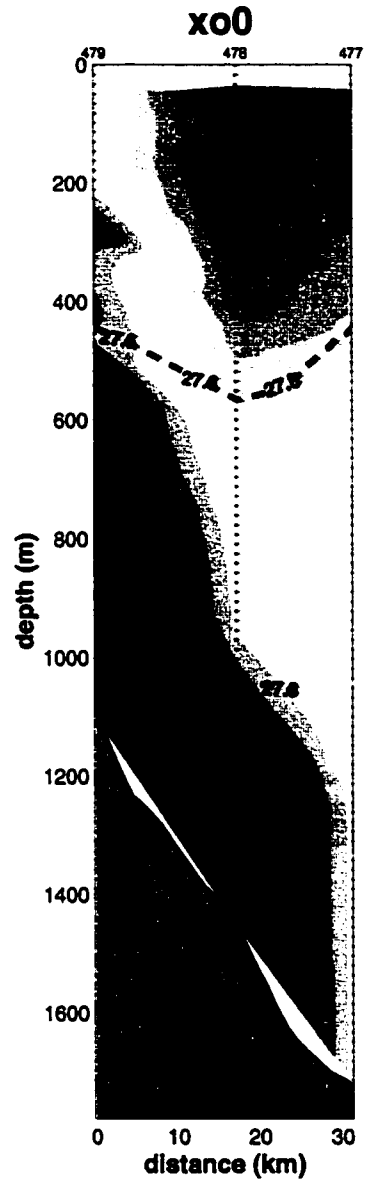

Greenland
Iceland

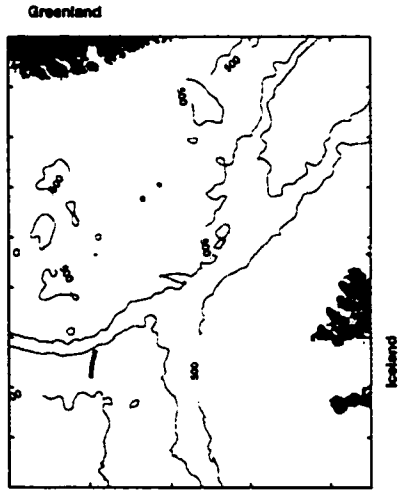
-1
0
1
2
3
4
5
6
7
8
9
θ (°C)

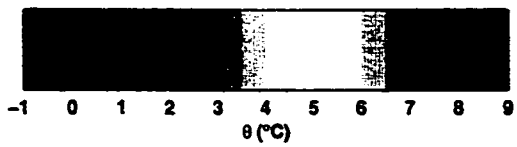

t3d
580
581
582
583
584
585
586
0
500
1000
1500
2000
27.5
27.6
27.6
27.6
depth (m)
Greenland
Iceland
−1
0
1
2
3
4
5
6
7
8
θ (°C)
0
10
20
30
40
50
60
70
distance (km)

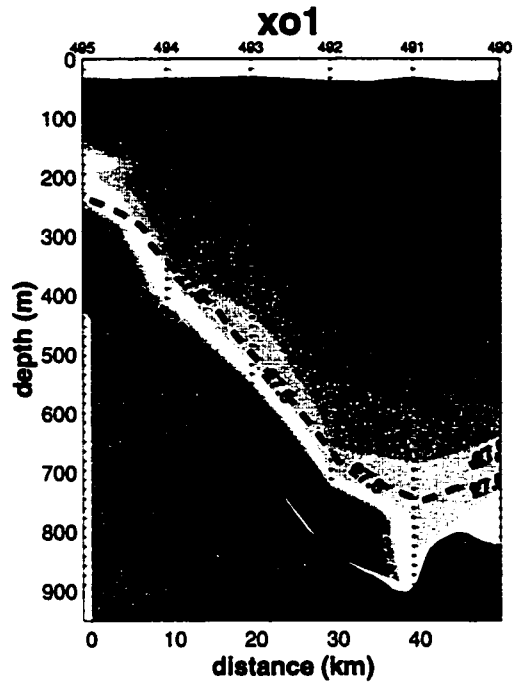

t3u
524
523
522
521
520
0
100
200
300
400
500
600
depth (m)
0
10
20
30
40
50
distance (km)

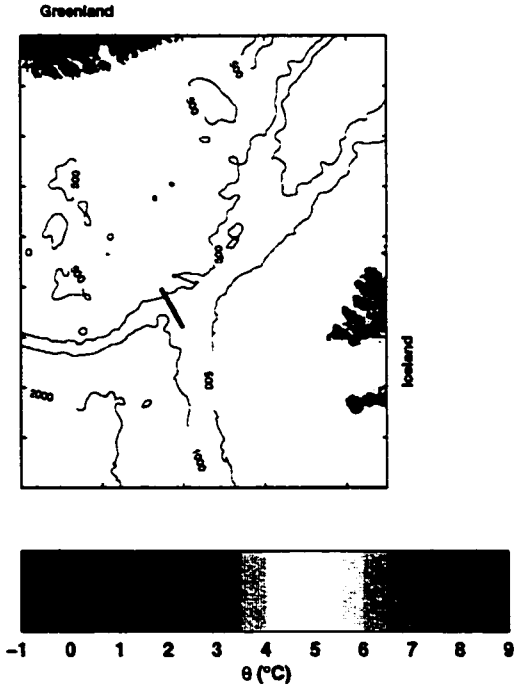

Greenland
Iceland
-1
0
1
2
3
4
5
6
7
8
9
θ (°C)

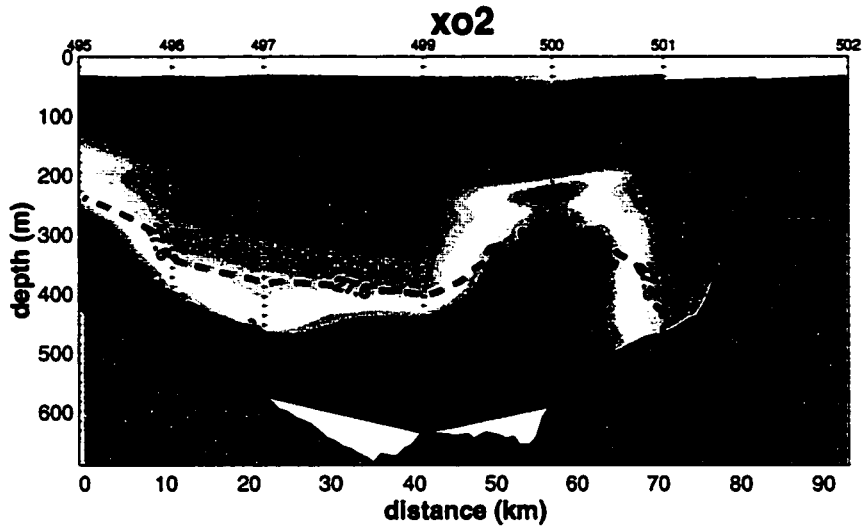

xo0
479
478
477
0
200
400
600
800
1000
1200
1400
1600
depth (m)
27.6
27.65
27.7
27.8
0
10
20
30
distance (km)

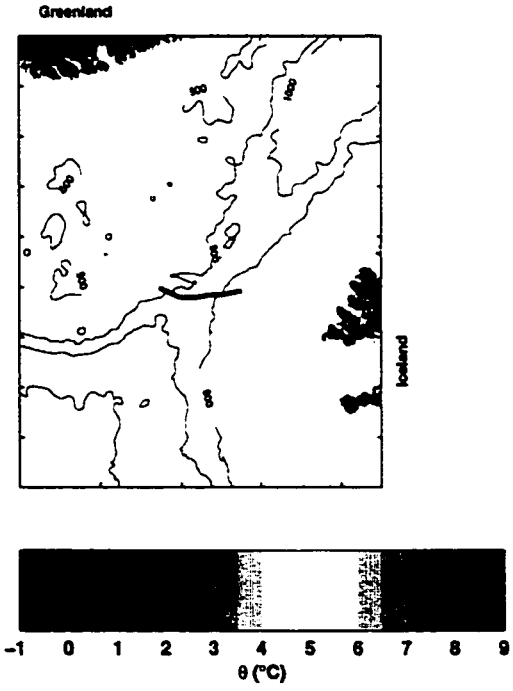

Greenland
Iceland

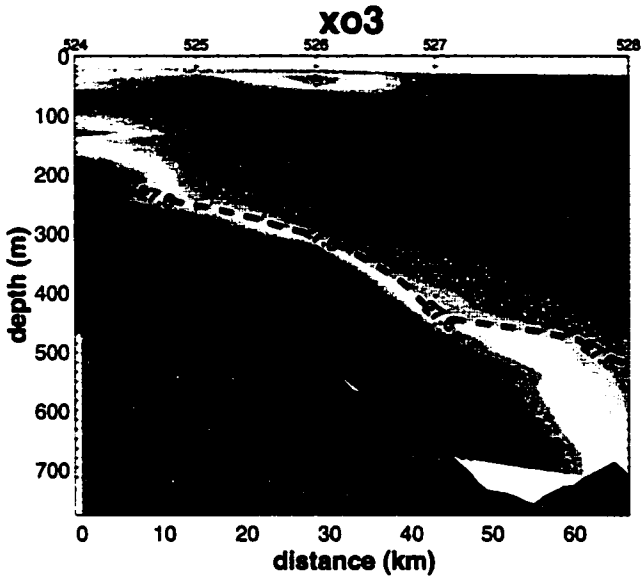

−1
0
1
2
3
4
5
6
7
8
9
θ (°C)

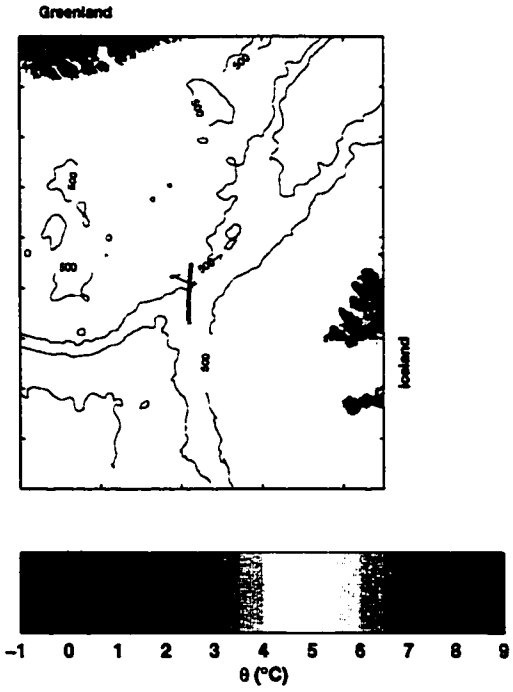

xo1
495
494
493
492
491
490
0
100
200
300
400
500
600
700
800
900
depth (m)
0
10
20
30
40
distance (km)

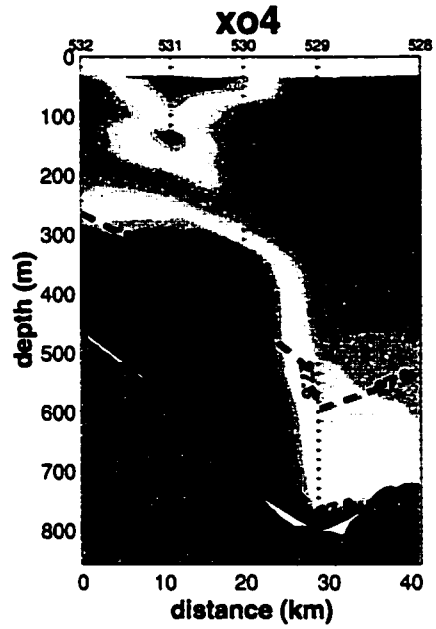

Greenland
Iceland
−1
0
1
2
3
4
5
6
7
8
9
θ (°C)

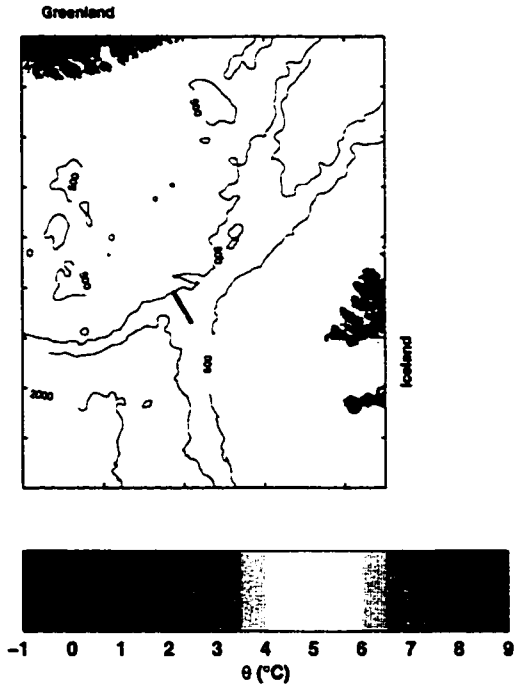

xo2
495
496
497
499
500
501
502
0
100
200
300
400
500
600
depth (m)
0
10
20
30
40
50
60
70
80
90
distance (km)

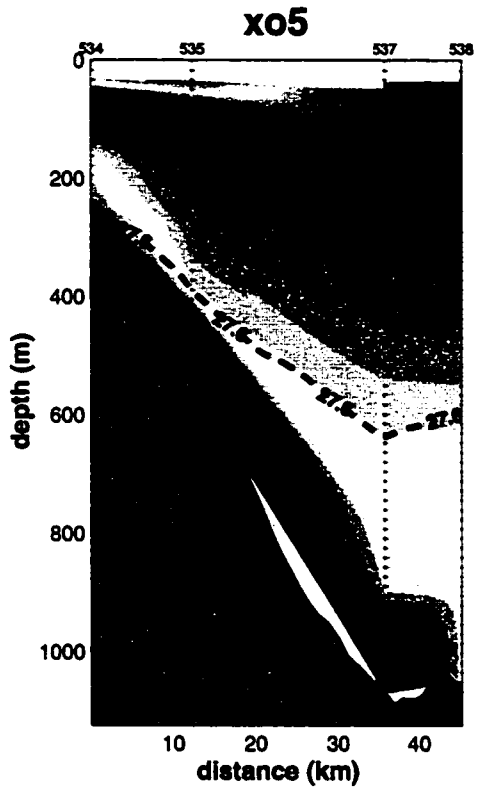

Greenland
Iceland
-1
0
1
2
3
4
5
6
7
8
9
θ (°C)

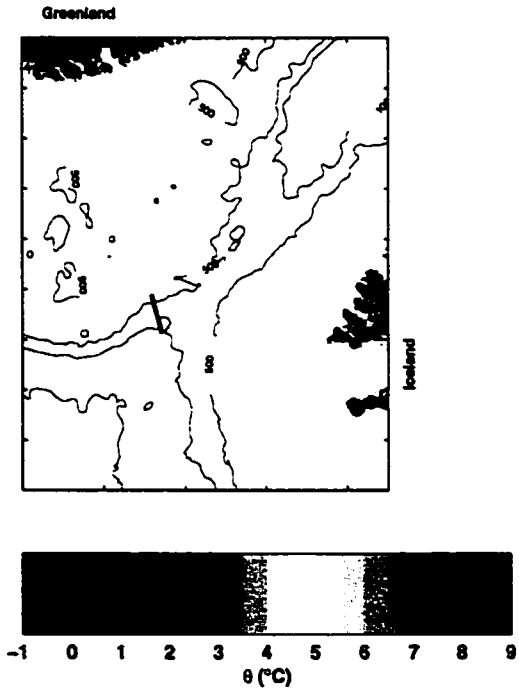

xo3
524
525
526
527
528
0
100
200
300
400
500
600
700
depth (m)
0
10
20
30
40
50
60
distance (km)

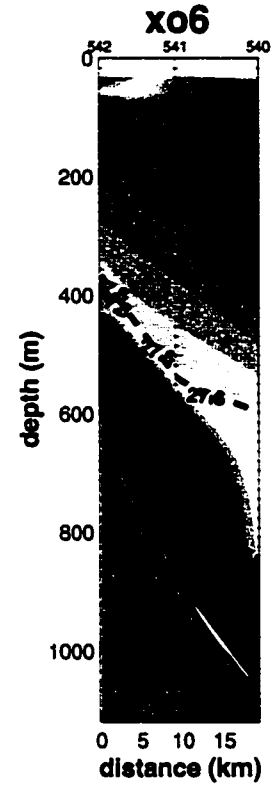

Greenland
Iceland
−1
0
1
2
3
4
5
6
7
8
9
θ (°C)

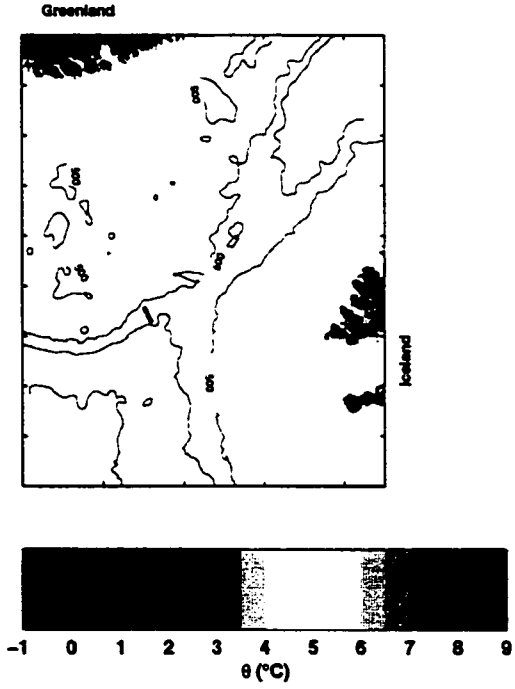

XO4
532
531
530
529
528
0
100
200
300
400
500
600
700
800
depth (m)
0
10
20
30
40
distance (km)

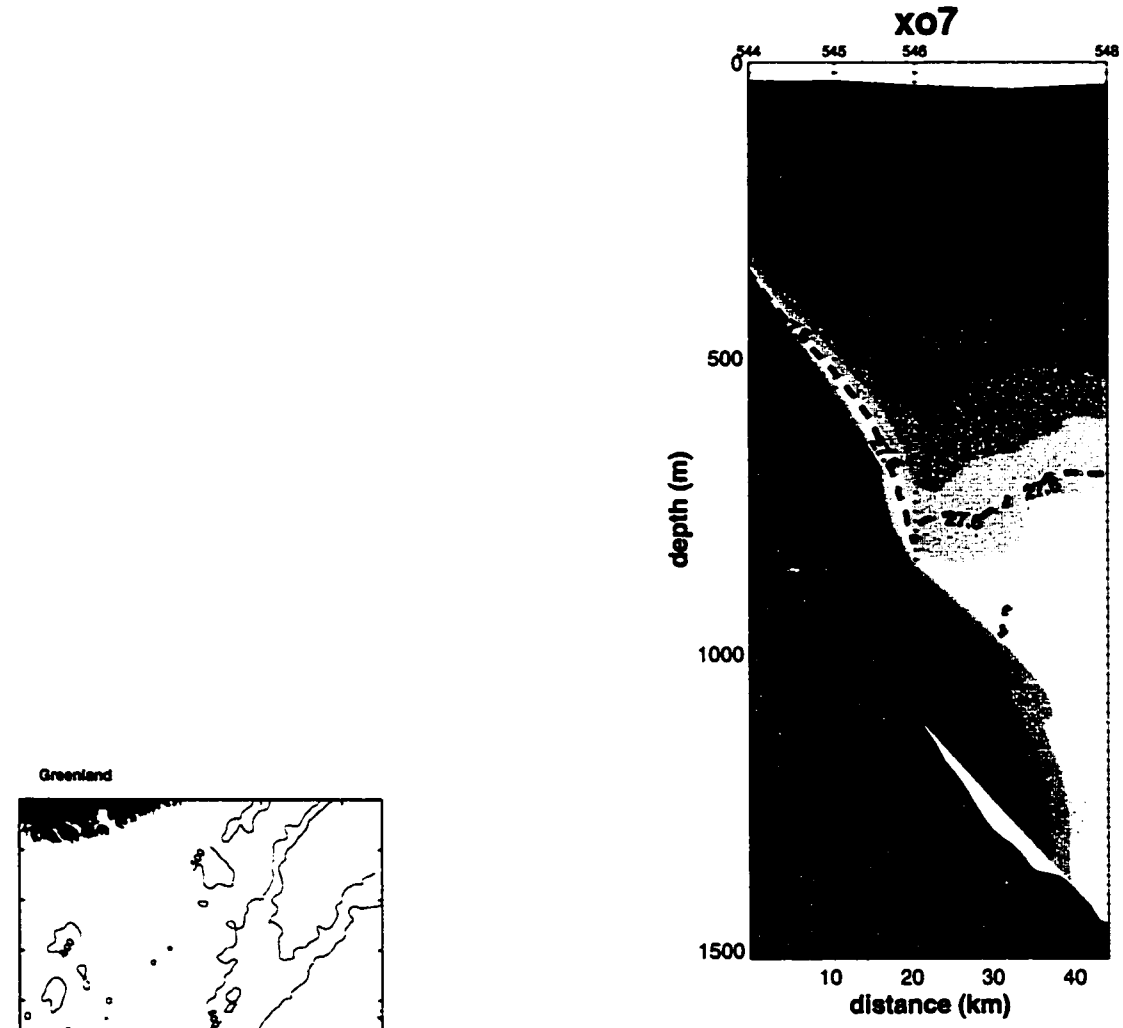

Greenland
Iceland
θ (°C)
−1
0
1
2
3
4
5
6
7
8
9

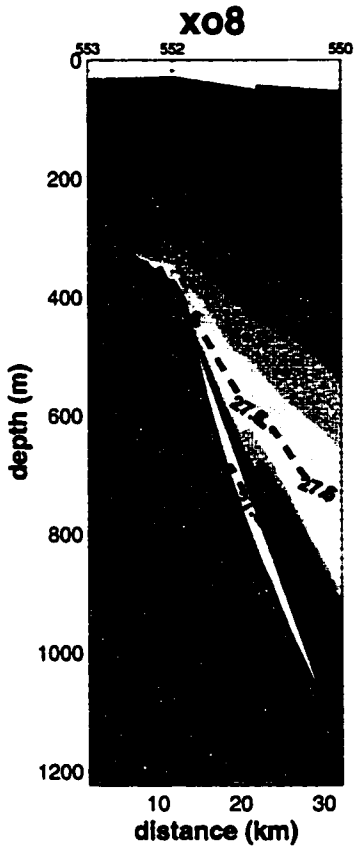

xo5
534
535
537
538
0
200
400
600
800
1000
depth (m)
10
20
30
40
distance (km)

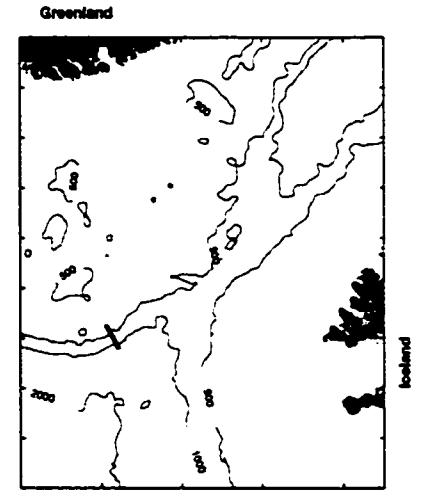

Greenland
Iceland
−1
0
1
2
3
4
5
6
7
8
9
θ (°C)

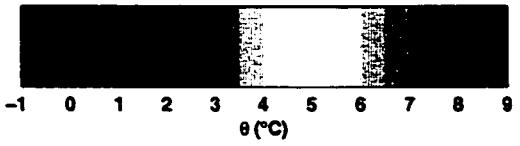

xo6
542
541
540
0
200
400
600
800
1000
depth (m)
27.6
0 5 10 15
distance (km)

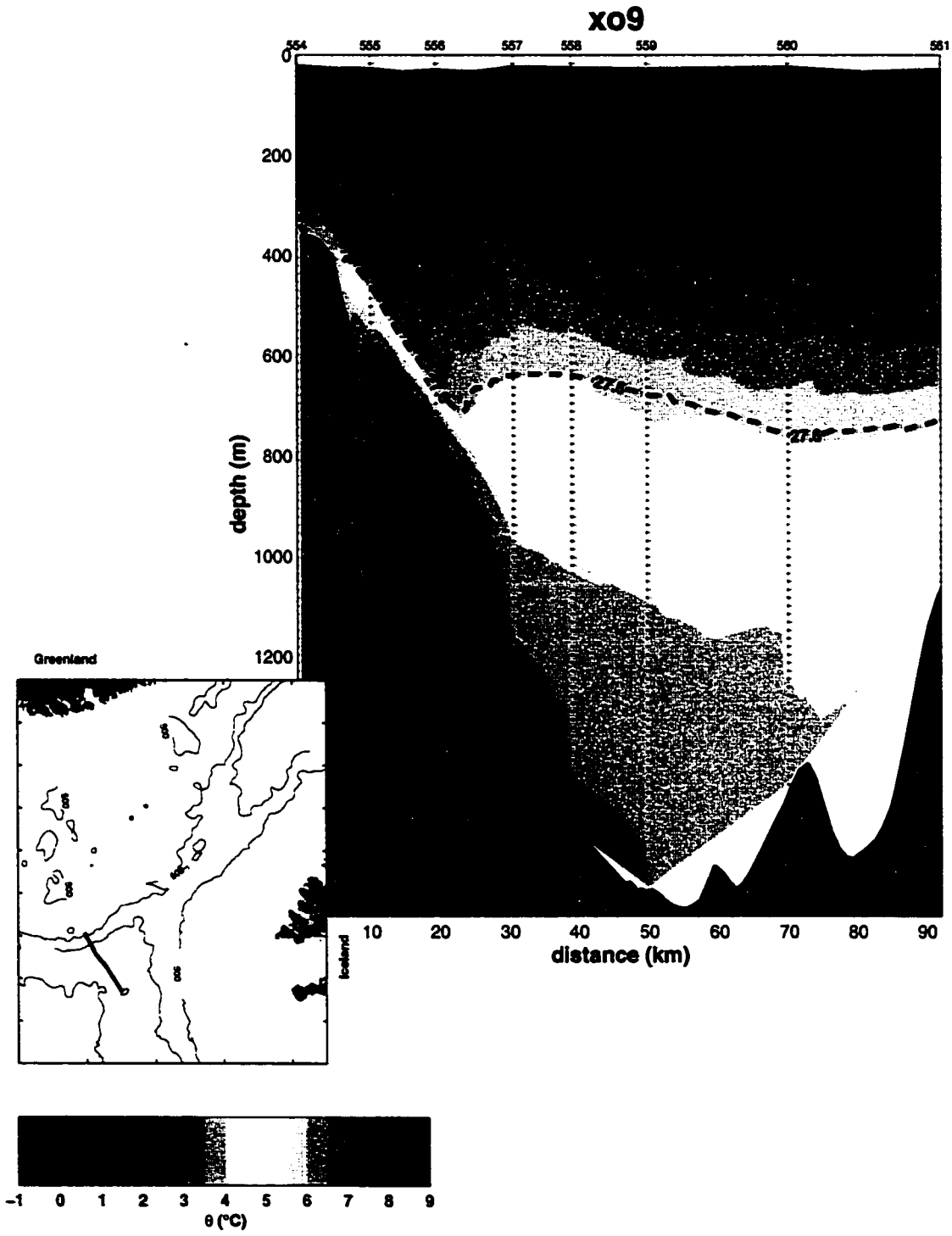

Greenland
Iceland
-1 0 1 2 3 4 5 6 7 8 9
θ (°C)

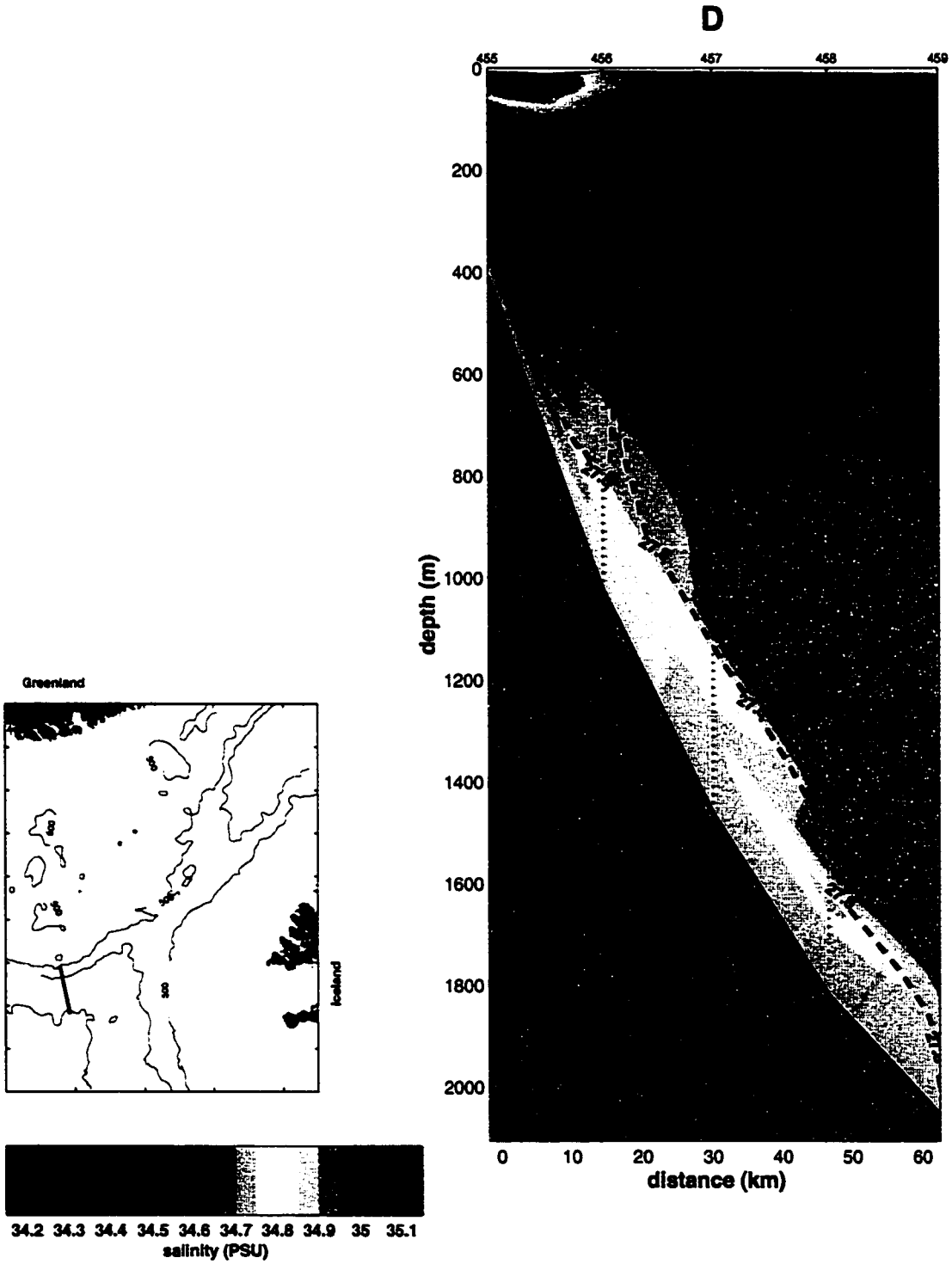

XO7
544
545
546
548
0
500
1000
1500
depth (m)
10
20
30
40
distance (km)
Greenland
Iceland
−1
0
1
2
3
4
5
6
7
8
9
θ (°C)

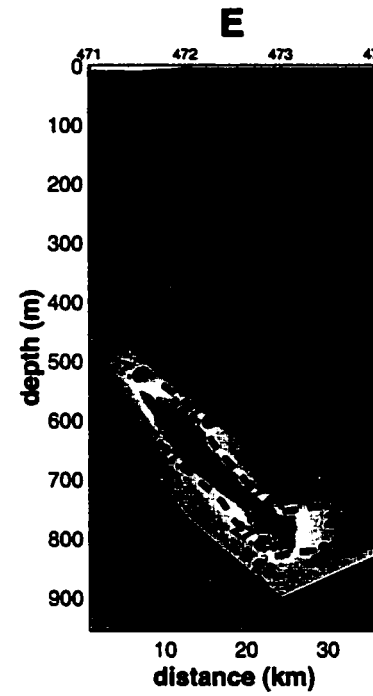

xo8
553
552
550
0
200
400
600
800
1000
1200
depth (m)
10
20
30
distance (km)

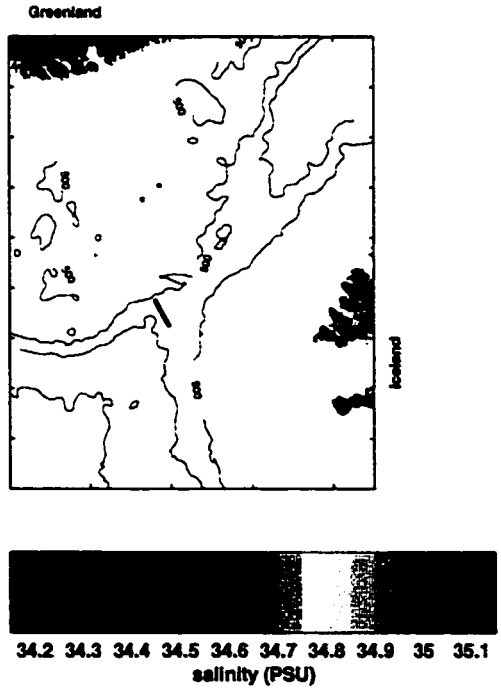

Greenland
Iceland
400
600
800
1000
2000


−1 0 1 2 3 4 5 6 7 8 9
θ (°C)

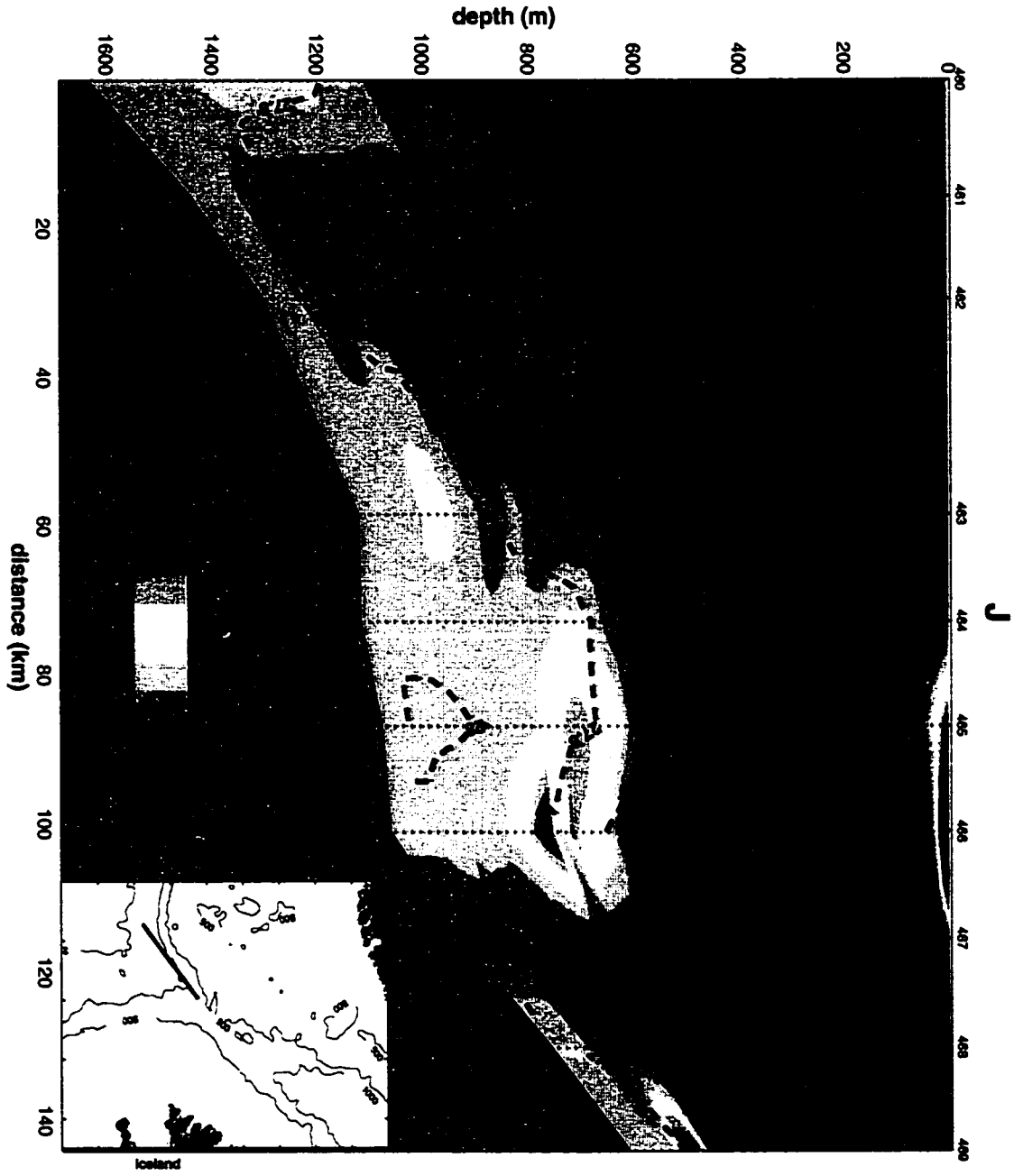

xo9
554
555
556
557
558
559
560
561
0
200
400
600
800
1000
1200
depth (m)
27.6
27.8
10
20
30
40
50
60
70
80
90
distance (km)
Greenland
Iceland
−1
0
1
2
3
4
5
6
7
8
9
θ (°C)

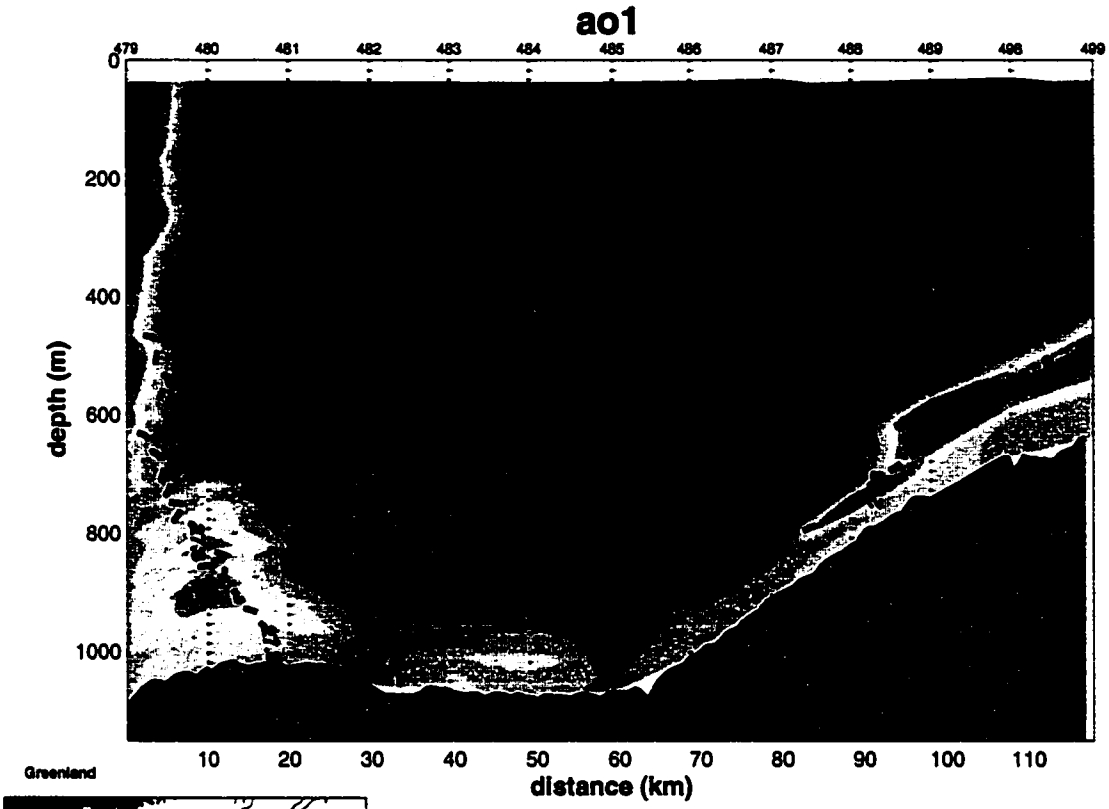

D
455
456
457
458
459
0
200
400
600
800
1000
1200
1400
1600
1800
2000
depth (m)
0
10
20
30
40
50
60
distance (km)
Greenland
Iceland
34.2 34.3 34.4 34.5 34.6 34.7 34.8 34.9 35 35.1
salinity (PSU)

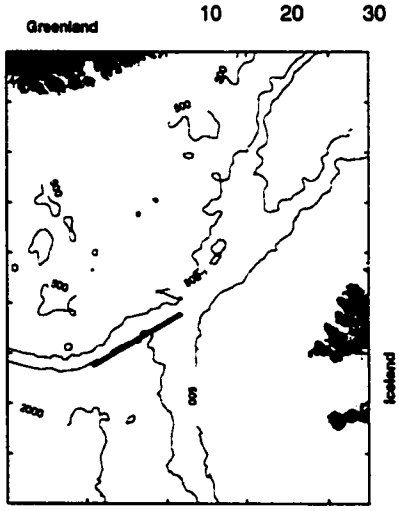

E
471
472
473
474
0
100
200
300
400
500
600
700
800
900
depth (m)
10
20
30
distance (km)

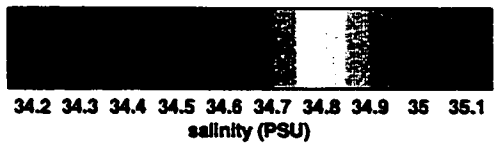

Greenland
Iceland

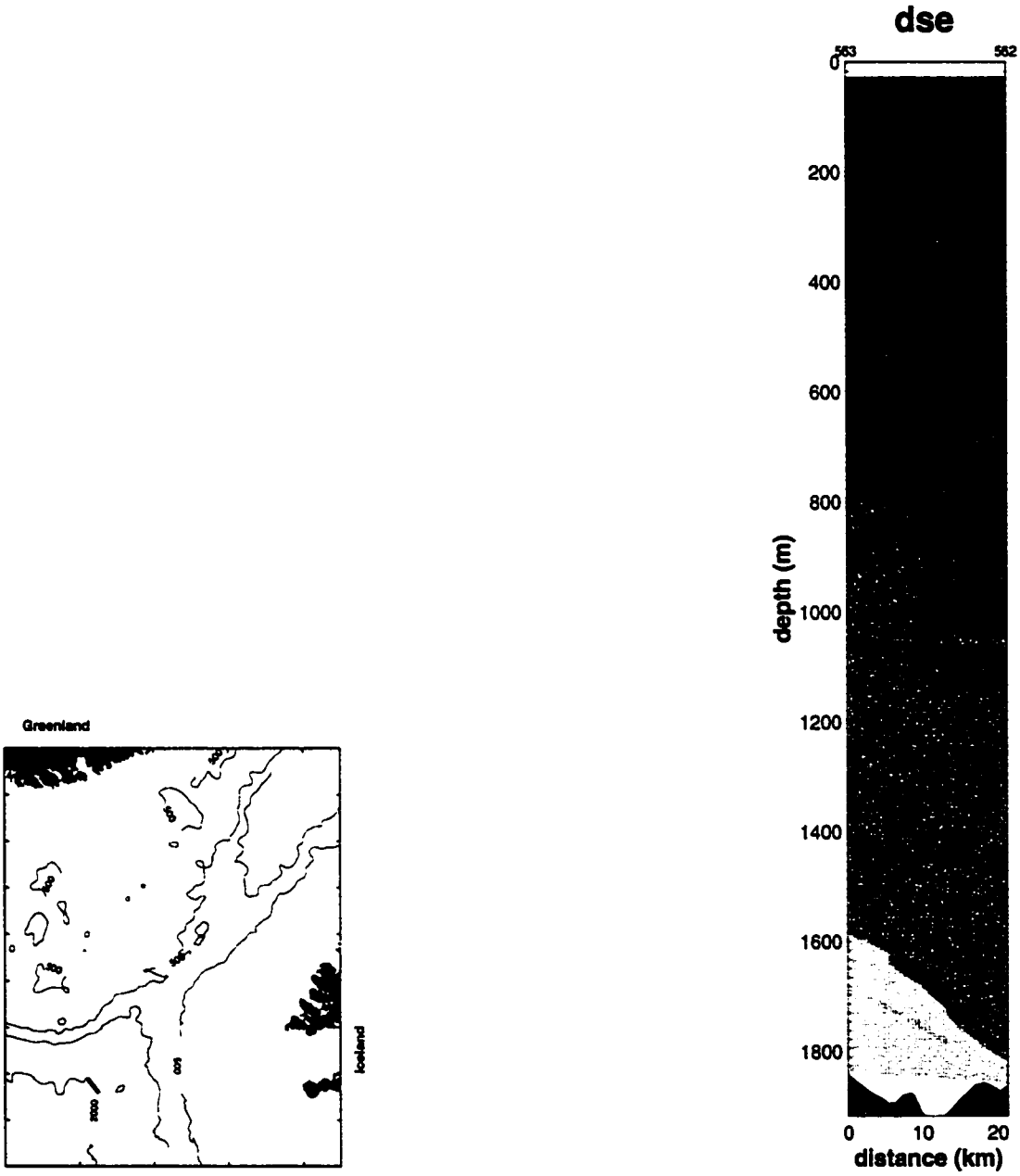
34.2 34.3 34.4 34.5 34.6 34.7 34.8 34.9 35 35.1
salinity (PSU)

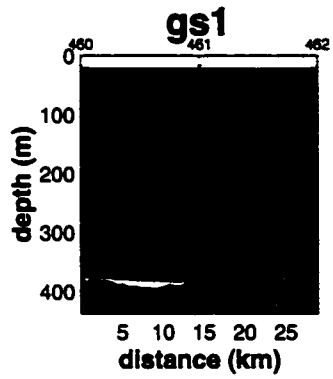

depth (m)
1600
1400
1200
1000
800
600
400
200
0
distance (km)
20
40
60
80
100
120
140
Iceland
460
461
462
463
464
465
466
467
468
469
J

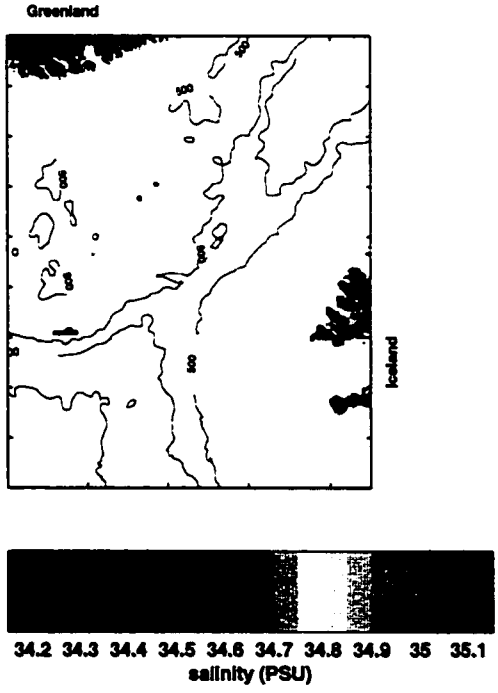

ao1
479
480
481
482
483
484
485
486
487
488
489
498
499
0
200
400
600
800
1000
depth (m)
10
20
30
40
50
60
70
80
90
100
110
distance (km)

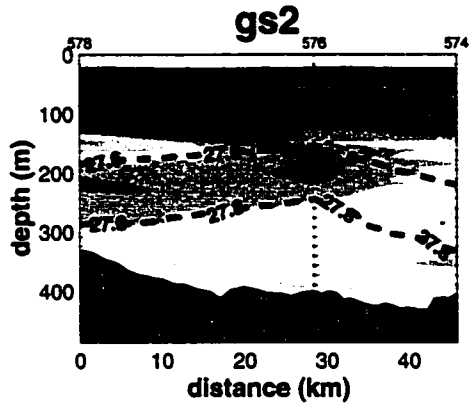

Greenland
Iceland

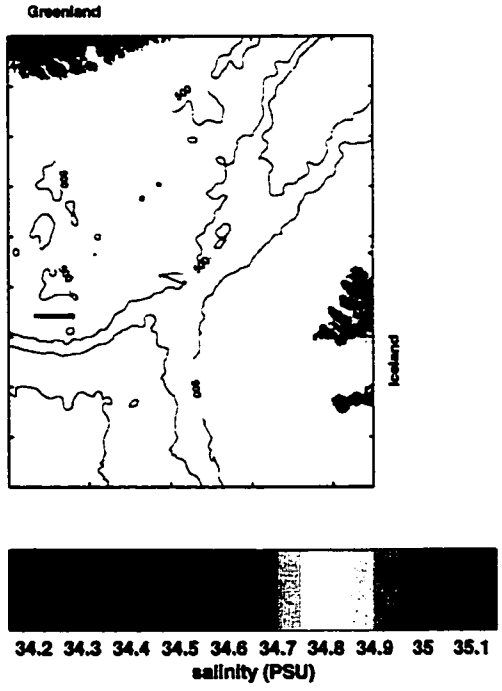

34.2 34.3 34.4 34.5 34.6 34.7 34.8 34.9 35 35.1
salinity (PSU)

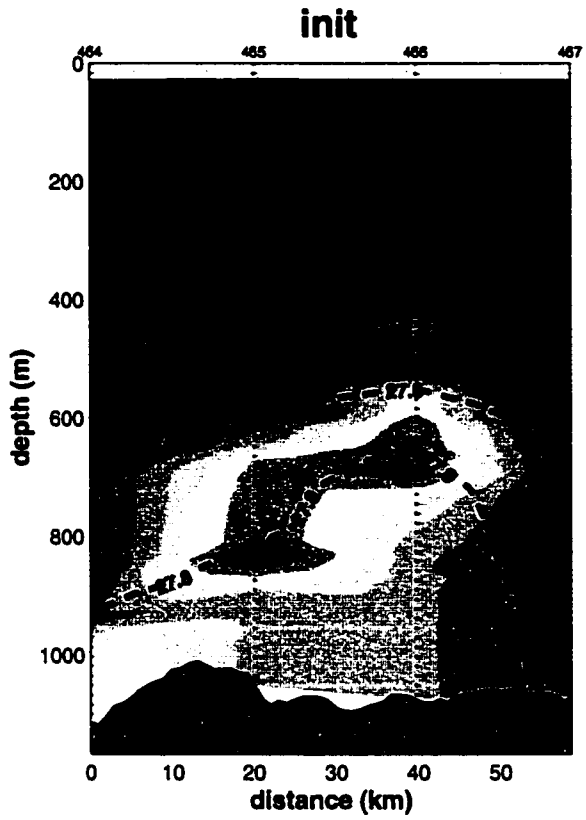

dse
563
562
0
200
400
600
800
1000
1200
1400
1600
1800
depth (m)
0
10
20
distance (km)
Greenland
Iceland
34.2 34.3 34.4 34.5 34.6 34.7 34.8 34.9 35 35.1
salinity (PSU)

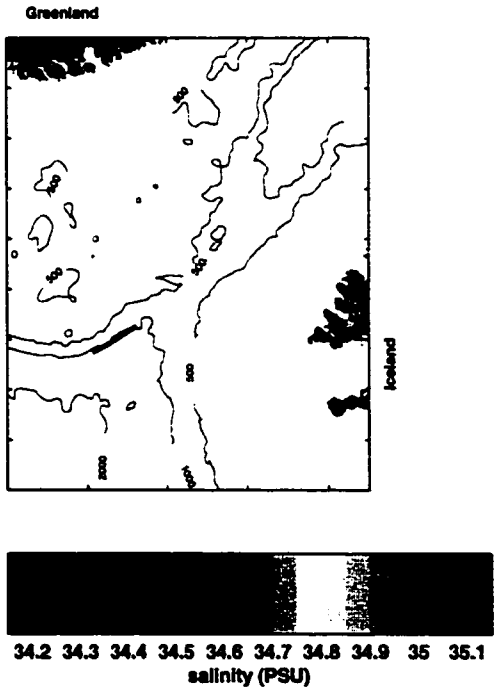

gs1
460
461
462
0
100
200
300
400
depth (m)
5 10 15 20 25
distance (km)

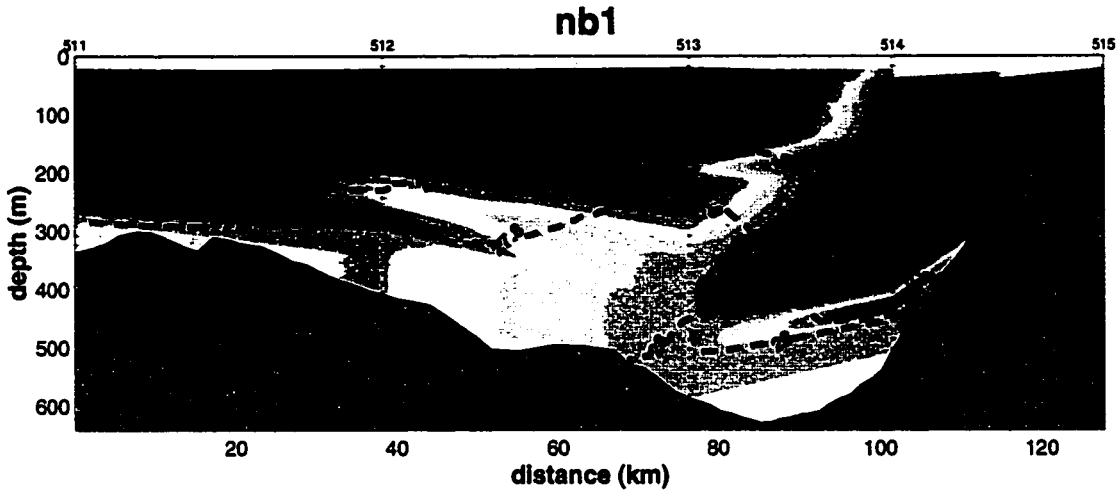

Greenland
Iceland
34.2 34.3 34.4 34.5 34.6 34.7 34.8 34.9 35 35.1
salinity (PSU)

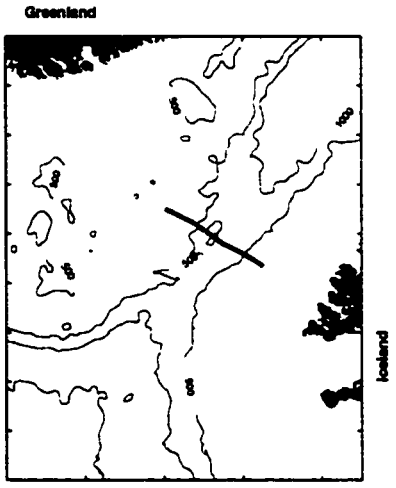

gs2
578
576
574
0
100
200
300
400
depth (m)
0
10
20
30
40
distance (km)

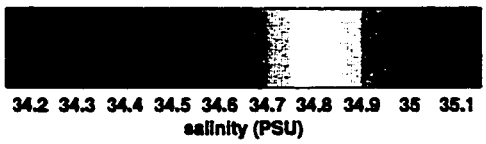

Greenland
Iceland
34.2 34.3 34.4 34.5 34.6 34.7 34.8 34.9 35 35.1
salinity (PSU)

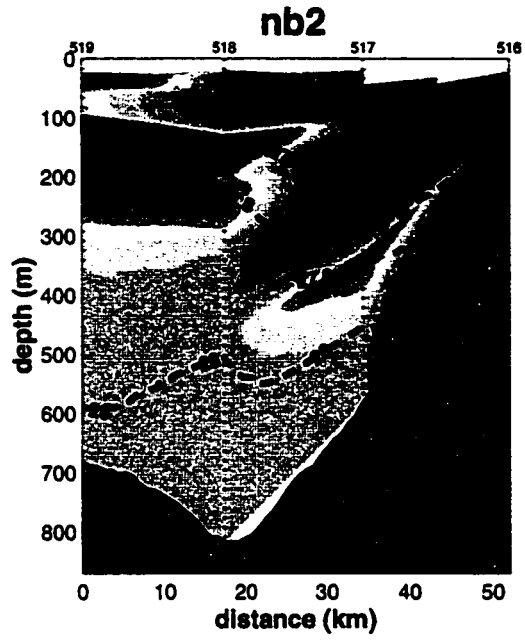

init
464
465
466
467
0
200
400
600
800
1000
depth (m)
0
10
20
30
40
50
distance (km)

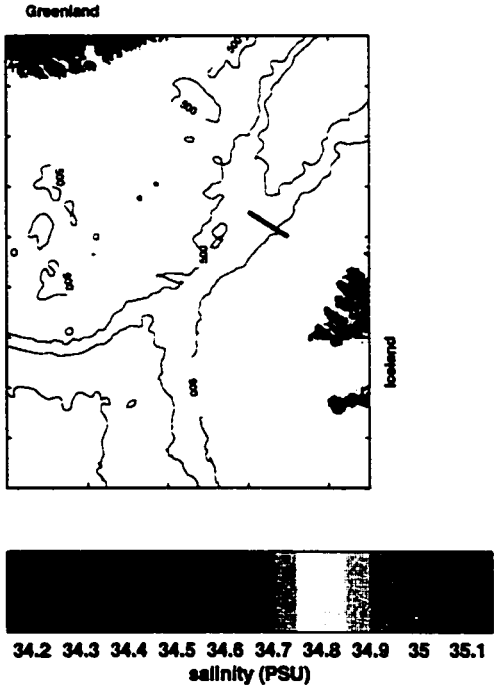

Greenland
Iceland
34.2 34.3 34.4 34.5 34.6 34.7 34.8 34.9 35 35.1
salinity (PSU)

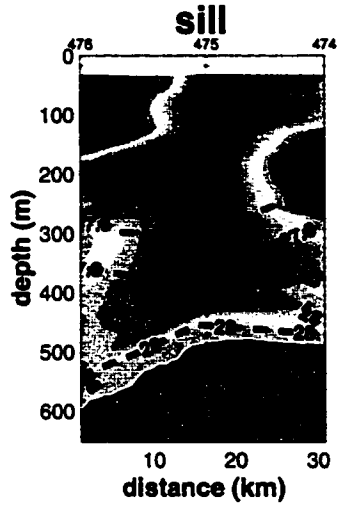

nb1
511
512
513
514
515
0
100
200
300
400
500
600
depth (m)
20
40
60
80
100
120
distance (km)

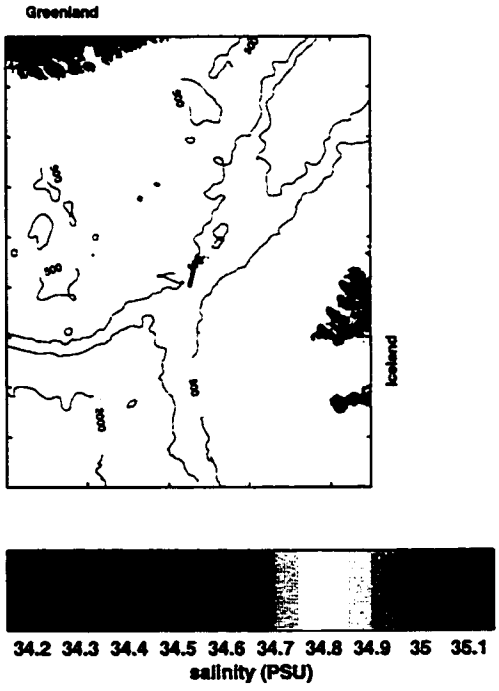

Greenland
Iceland

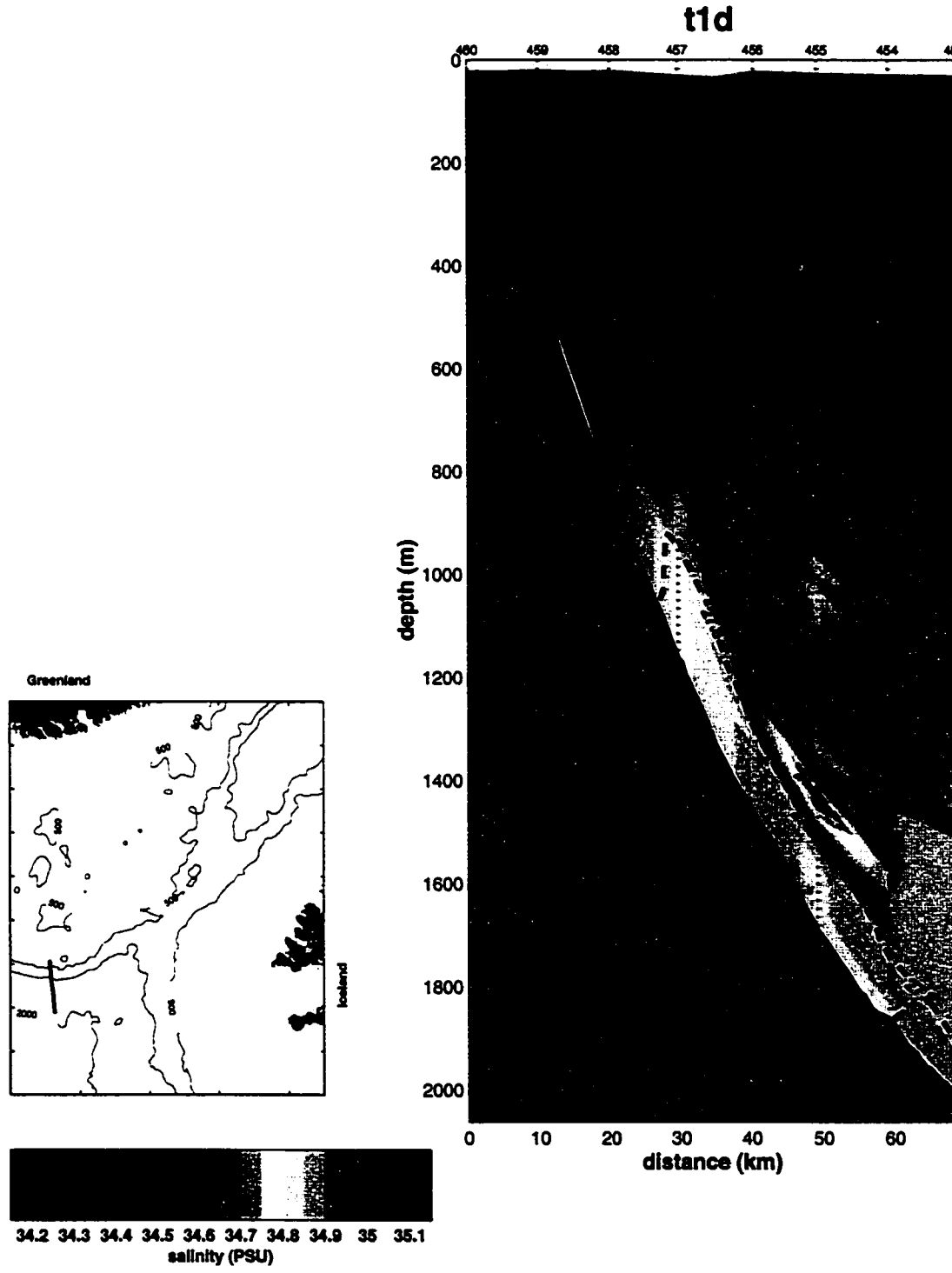

34.2 34.3 34.4 34.5 34.6 34.7 34.8 34.9 35 35.1
salinity (PSU)

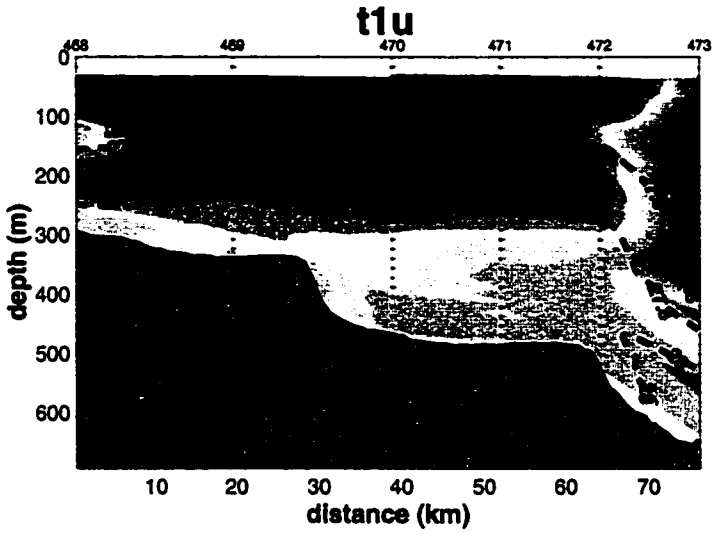

nb2
519
518
517
516
0
100
200
300
400
500
600
700
800
depth (m)
0
10
20
30
40
50
distance (km)

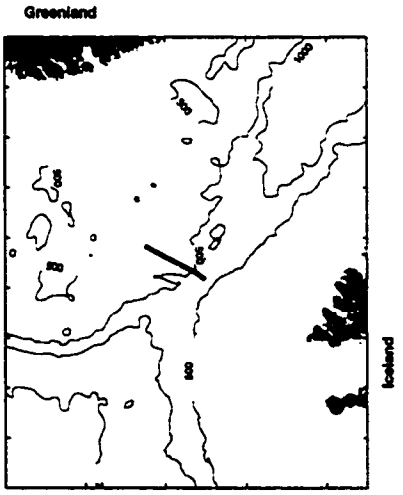

Greenland
Iceland
34.2 34.3 34.4 34.5 34.6 34.7 34.8 34.9 35 35.1
salinity (PSU)

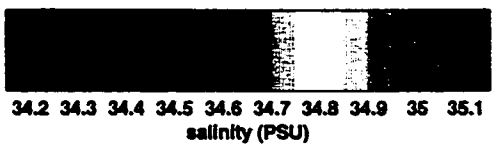

sill
476
475
474
0
100
200
300
400
500
600
depth (m)
10
20
30
distance (km)

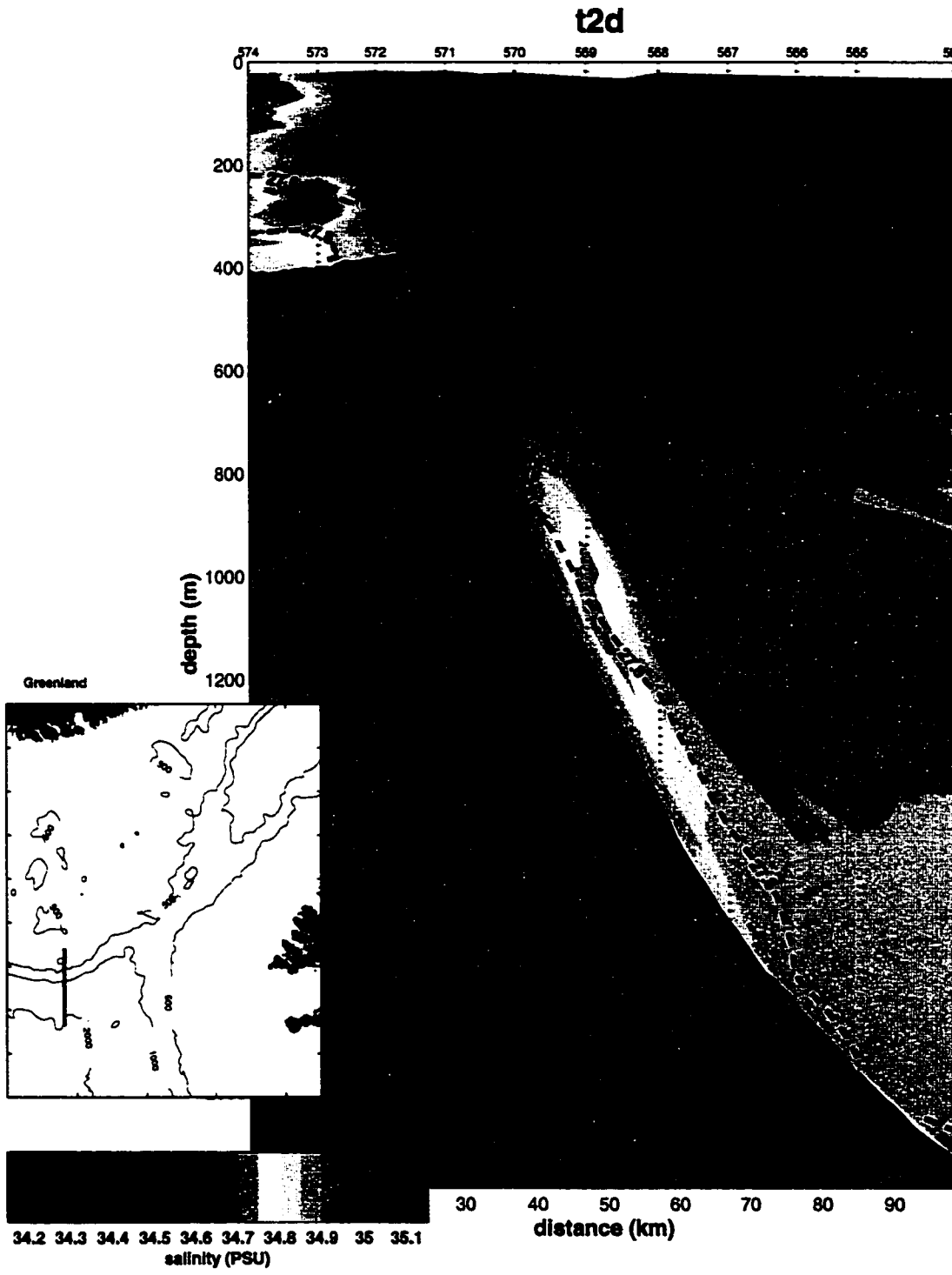

Greenland
Iceland
34.2 34.3 34.4 34.5 34.6 34.7 34.8 34.9 35 35.1
salinity (PSU)

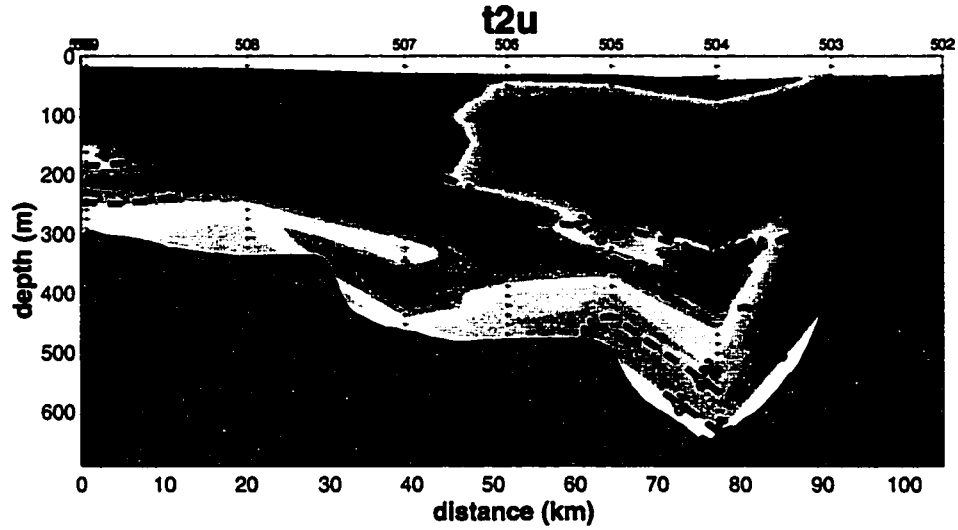

t1d
460
459
458
457
456
455
454
453
0
200
400
600
800
1000
1200
1400
1600
1800
2000
depth (m)
0
10
20
30
40
50
60
distance (km)
Greenland
Iceland
34.2 34.3 34.4 34.5 34.6 34.7 34.8 34.9 35 35.1
salinity (PSU)

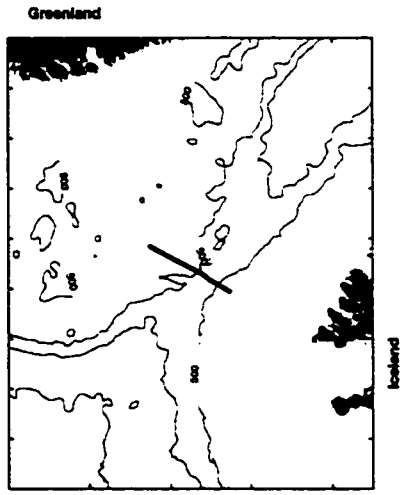

t1u
468
469
470
471
472
473
0
100
200
300
400
500
600
depth (m)
10
20
30
40
50
60
70
distance (km)

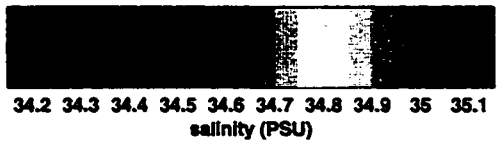

Greenland
Iceland

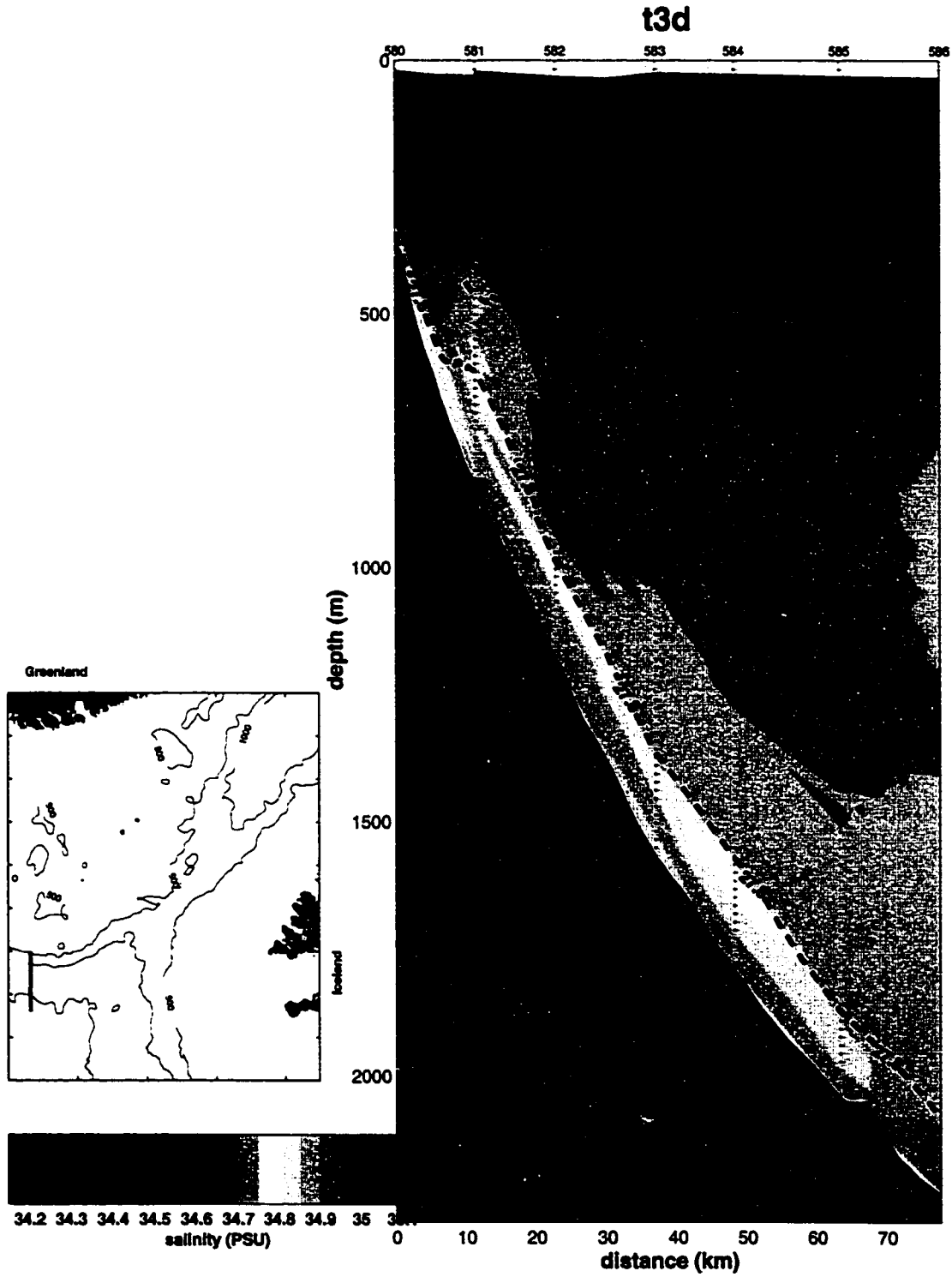

34.2 34.3 34.4 34.5 34.6 34.7 34.8 34.9 35 35.1
salinity (PSU)

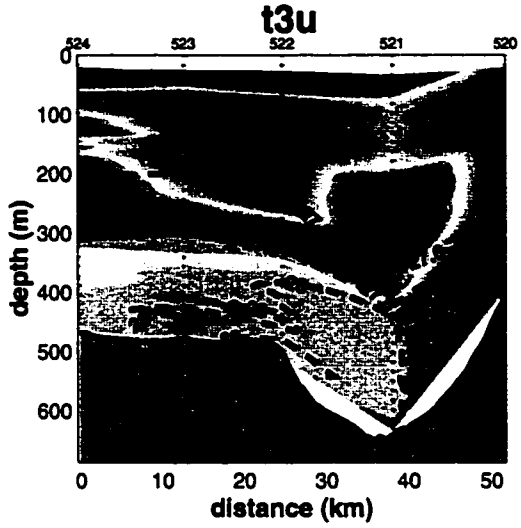

t2d
574 573 572 571 570 569 568 567 566 565 564
0
200
400
600
800
1000
1200
depth (m)
Greenland
30 40 50 60 70 80 90
distance (km)
34.2 34.3 34.4 34.5 34.6 34.7 34.8 34.9 35 35.1
salinity (PSU)

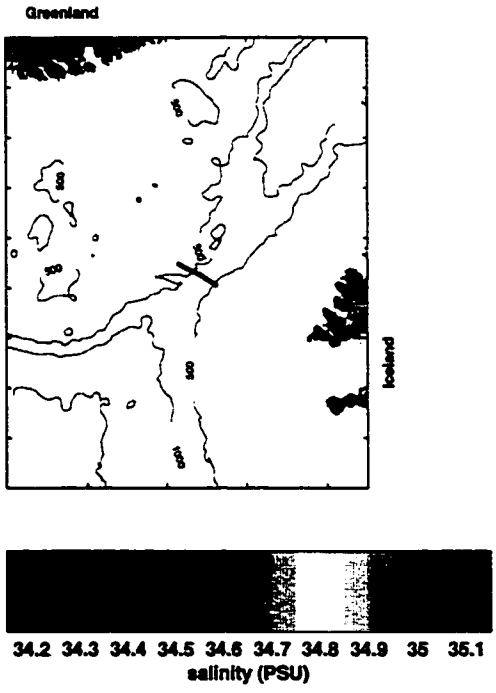

t2u
508
507
506
505
504
503
502
0
100
200
300
400
500
600
depth (m)
0
10
20
30
40
50
60
70
80
90
100
distance (km)

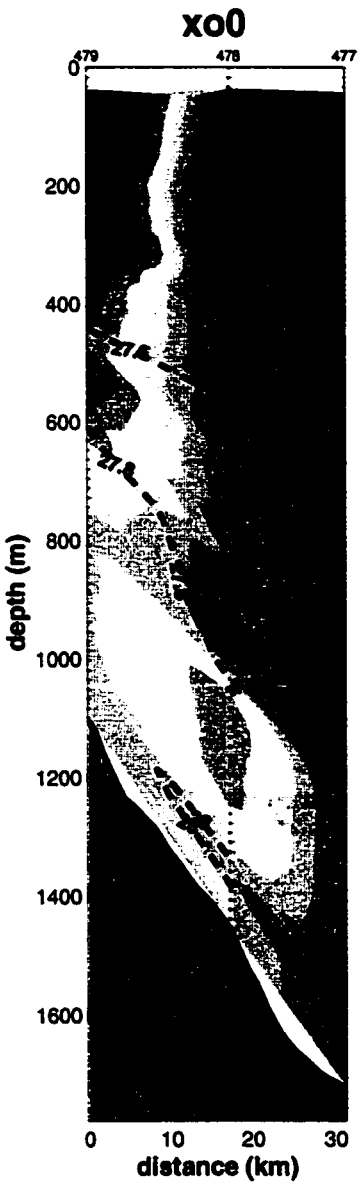

Greenland
Iceland

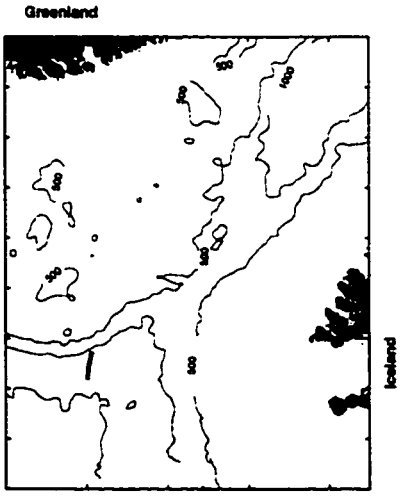

34.2 34.3 34.4 34.5 34.6 34.7 34.8 34.9 35 35.1
salinity (PSU)

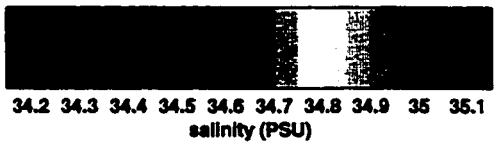

t3d
580
581
582
583
584
585
586
0
500
1000
1500
2000
depth (m)
Greenland
Iceland
34.2 34.3 34.4 34.5 34.6 34.7 34.8 34.9 35
salinity (PSU)
0 10 20 30 40 50 60 70
distance (km)

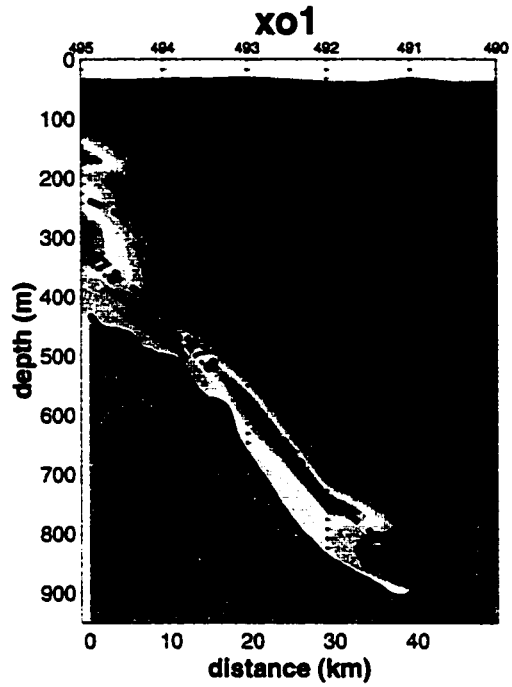

t3u
524
523
522
521
520
0
100
200
300
400
500
600
depth (m)
0
10
20
30
40
50
distance (km)

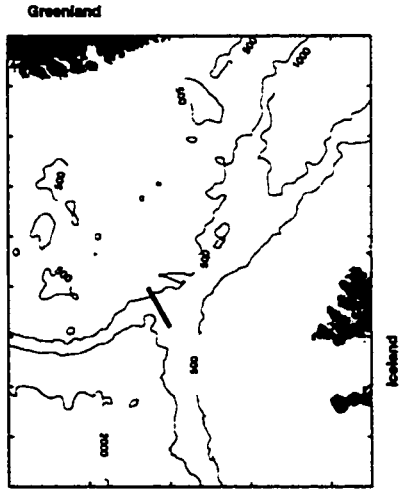

Greenland
Iceland
34.2 34.3 34.4 34.5 34.6 34.7 34.8 34.9 35 35.1
salinity (PSU)

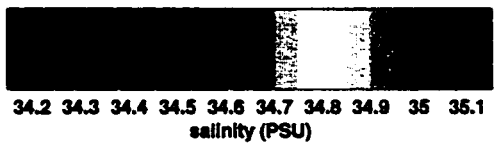

xo0
479
478
477
0
200
400
600
800
1000
1200
1400
1600
depth (m)
0
10
20
30
distance (km)

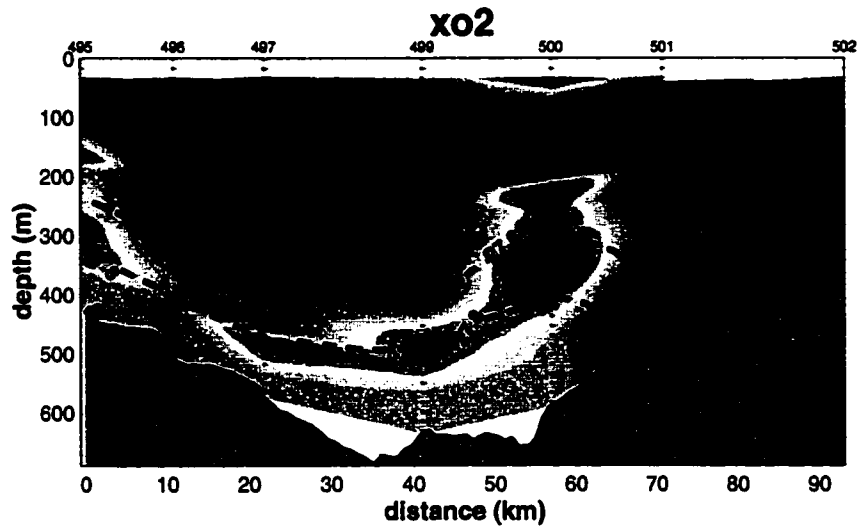

Greenland
Iceland

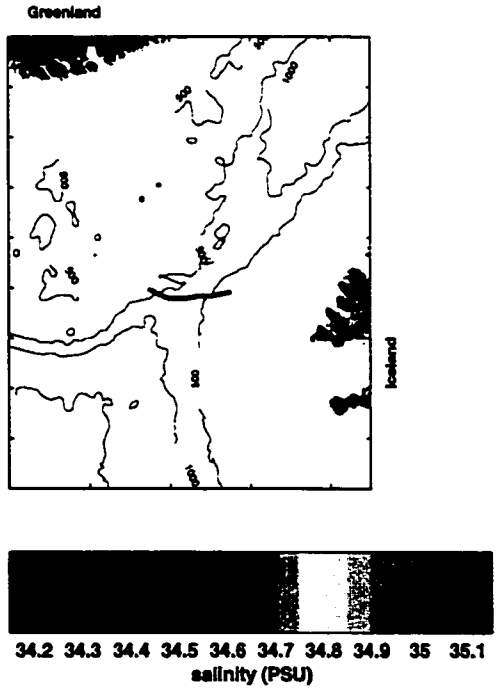

34.2 34.3 34.4 34.5 34.6 34.7 34.8 34.9 35 35.1
salinity (PSU)

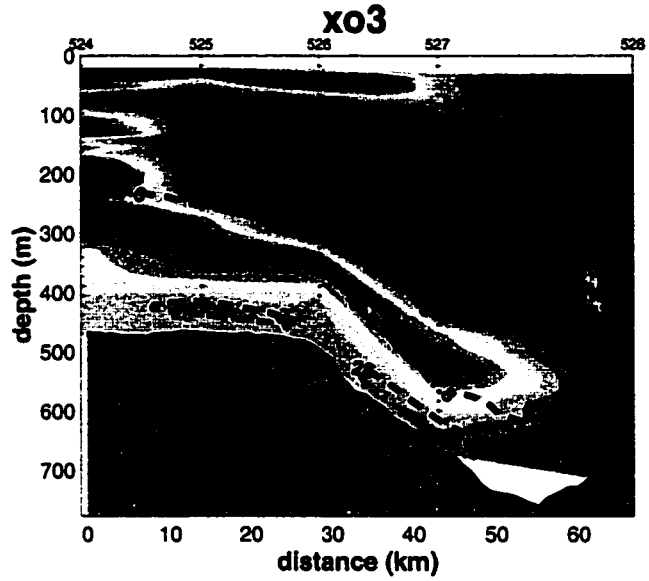

xo1
495
494
493
492
491
490
0
100
200
300
400
500
600
700
800
900
depth (m)
0
10
20
30
40
distance (km)

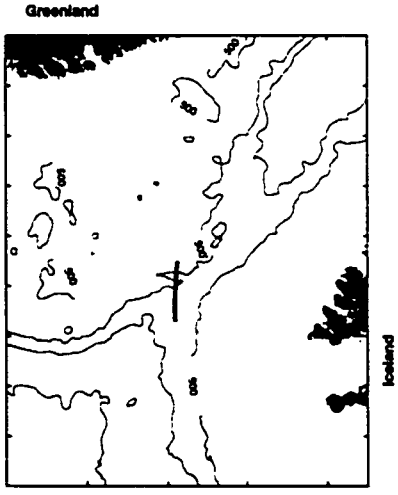

Greenland
Iceland

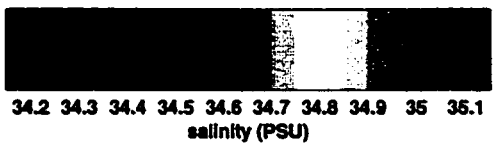

34.2 34.3 34.4 34.5 34.6 34.7 34.8 34.9 35 35.1
salinity (PSU)

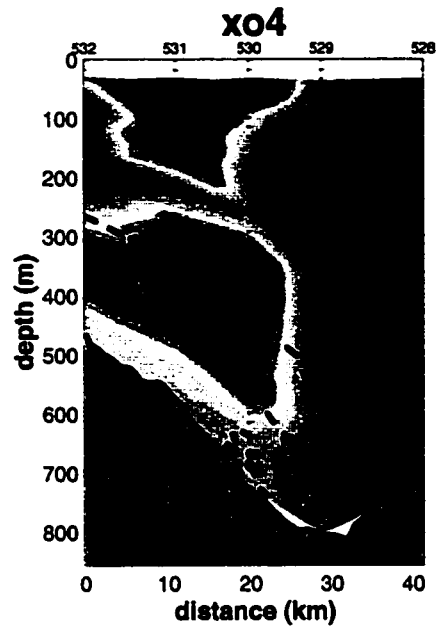

xo2
495
496
497
499
500
501
502
0
100
200
300
400
500
600
depth (m)
0
10
20
30
40
50
60
70
80
90
distance (km)

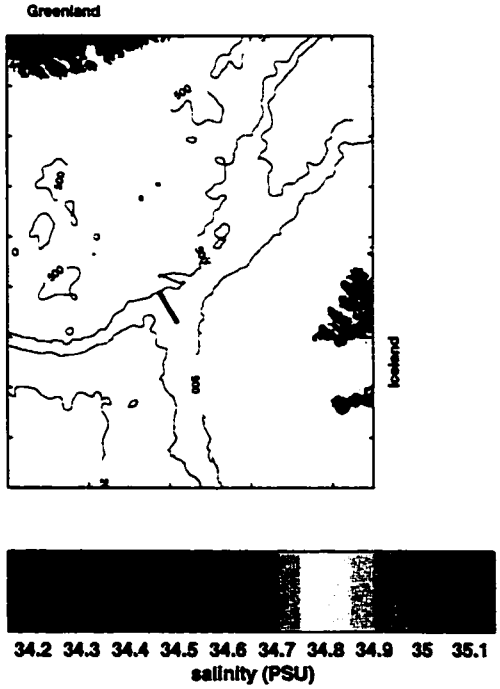

Greenland
Iceland
34.2 34.3 34.4 34.5 34.6 34.7 34.8 34.9 35 35.1
salinity (PSU)

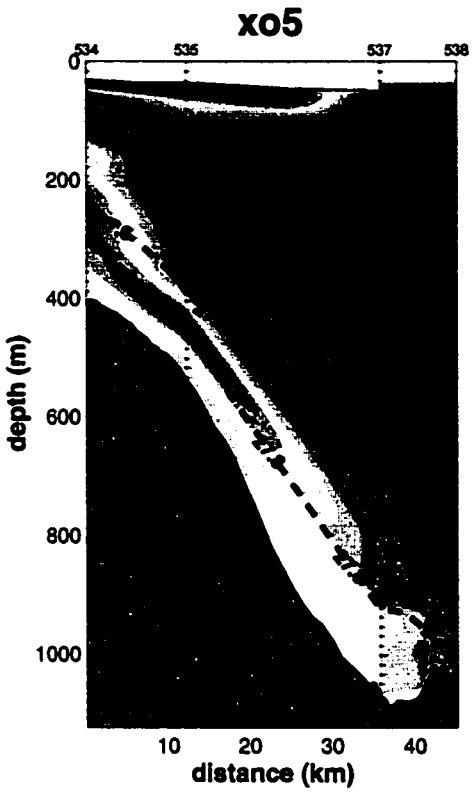

xo3
524
525
526
527
528
0
100
200
300
400
500
600
700
depth (m)
0
10
20
30
40
50
60
distance (km)

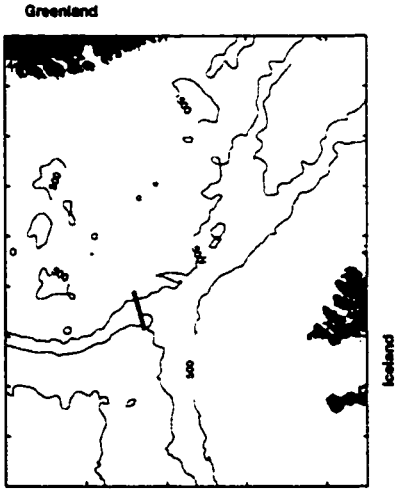

Greenland
Iceland

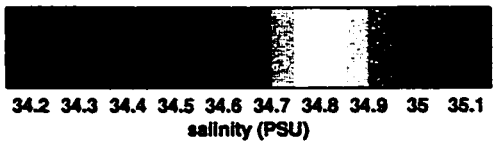

34.2 34.3 34.4 34.5 34.6 34.7 34.8 34.9 35 35.1
salinity (PSU)

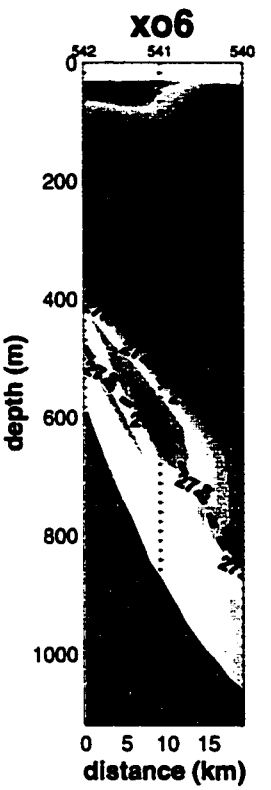

xo4
532
531
530
529
528
0
100
200
300
400
500
600
700
800
depth (m)
0
10
20
30
40
distance (km)

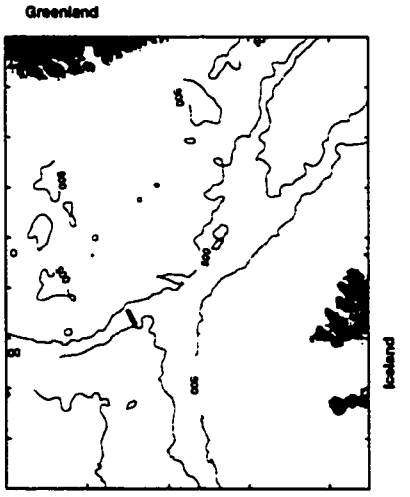

Greenland
Iceland
34.2 34.3 34.4 34.5 34.6 34.7 34.8 34.9 35 35.1
salinity (PSU)

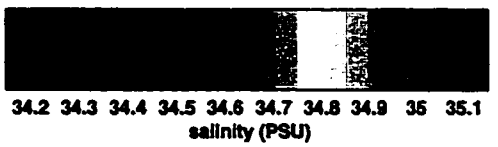

xo5
534
535
537
538
0
200
400
600
800
1000
depth (m)
10
20
30
40
distance (km)

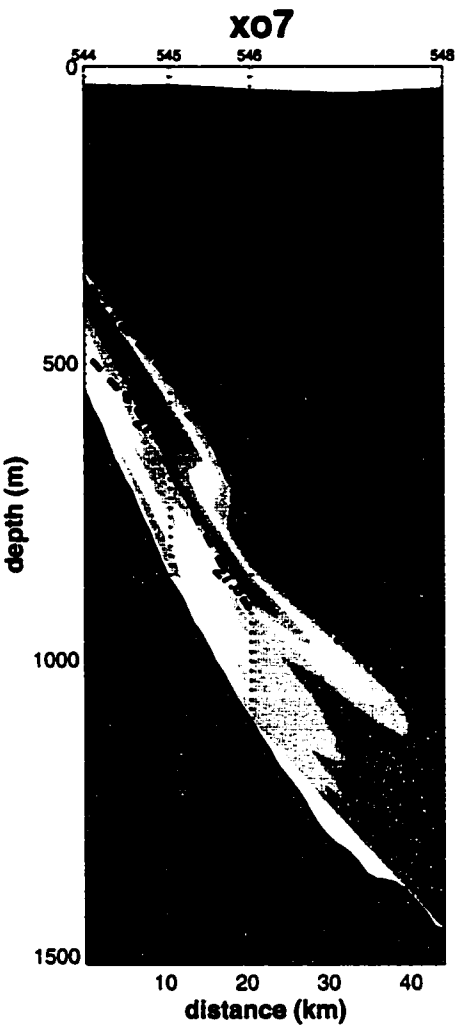

Greenland
Iceland

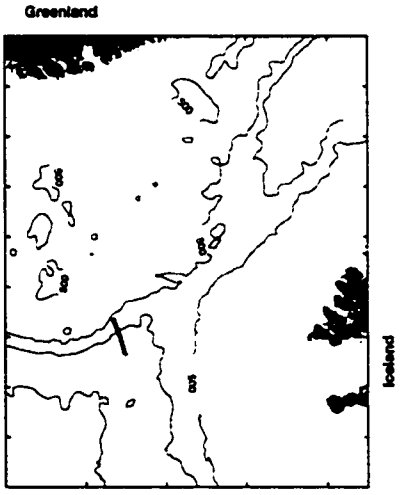

34.2 34.3 34.4 34.5 34.6 34.7 34.8 34.9 35 35.1
salinity (PSU)

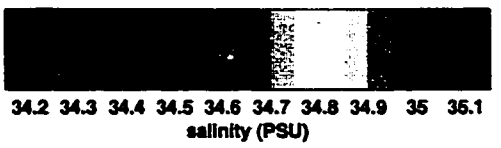

XO6
542
541
540
0
200
400
600
800
1000
depth (m)
0 5 10 15
distance (km)

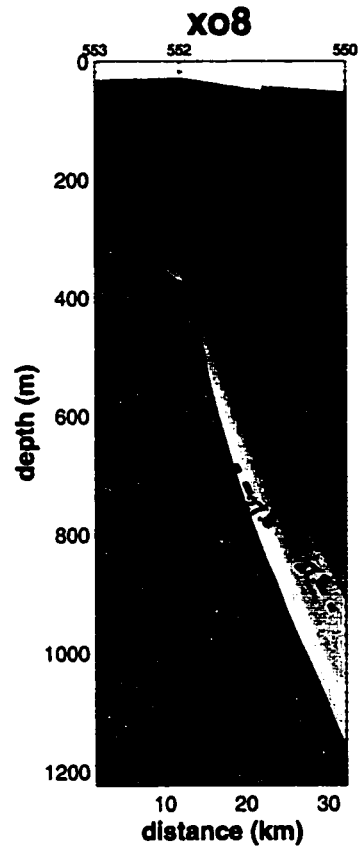

Greenland
Iceland

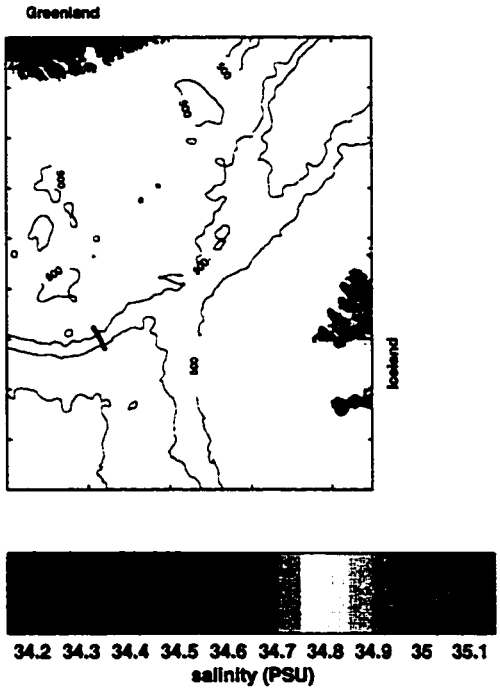

34.2 34.3 34.4 34.5 34.6 34.7 34.8 34.9 35 35.1
salinity (PSU)

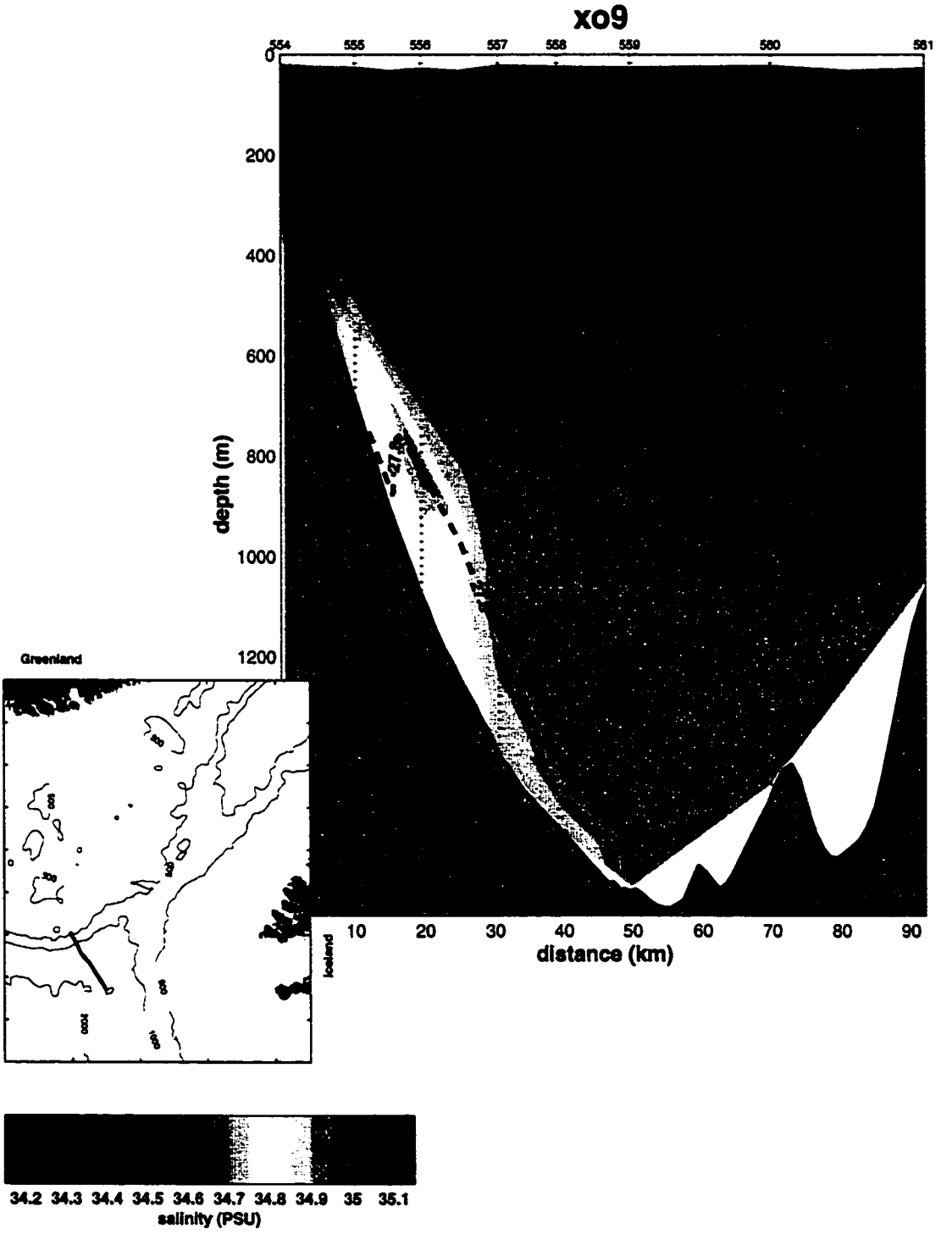

xo7
544
545
546
548
0
500
1000
1500
depth (m)
10
20
30
40
distance (km)

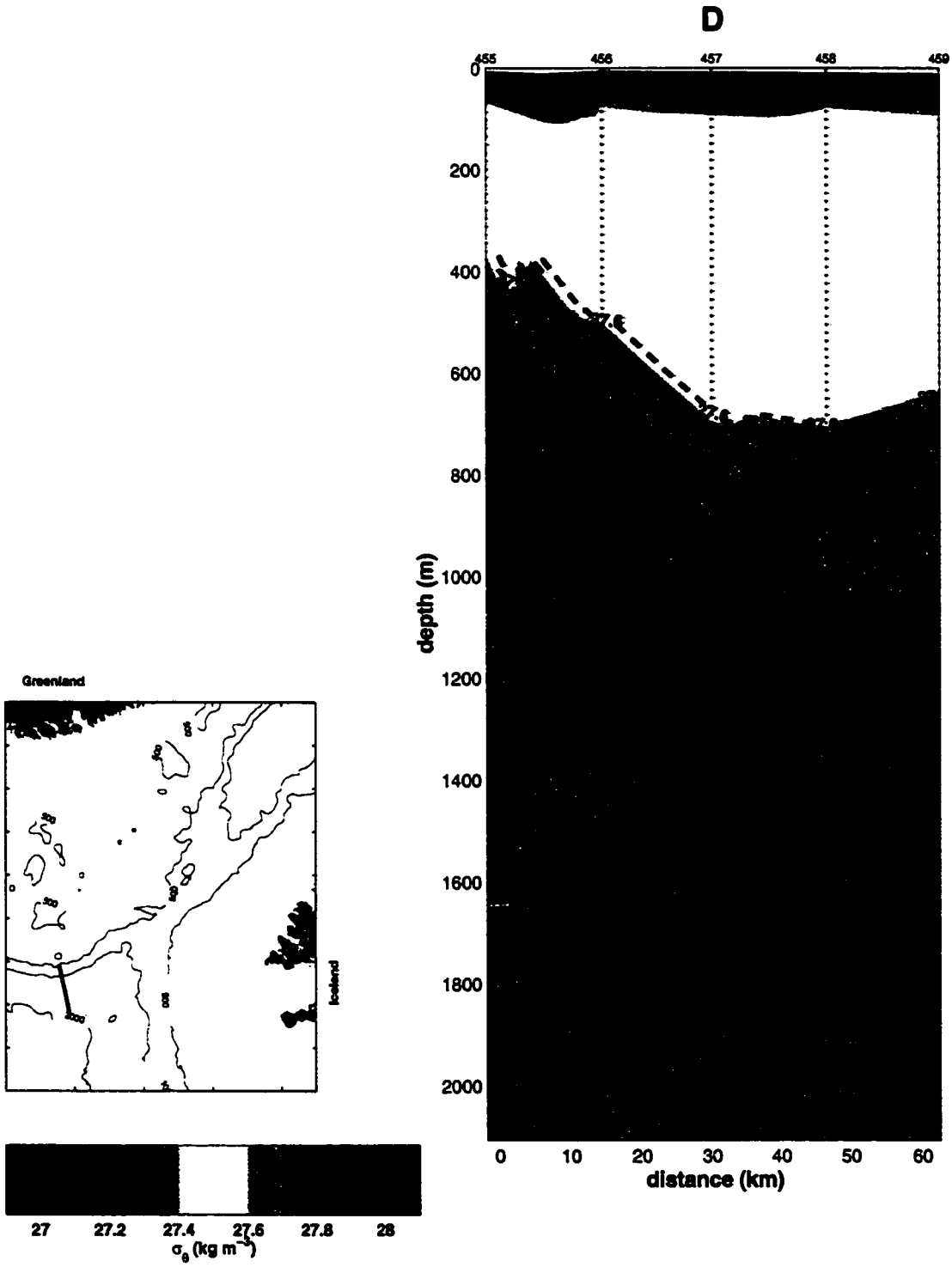

Greenland
Iceland

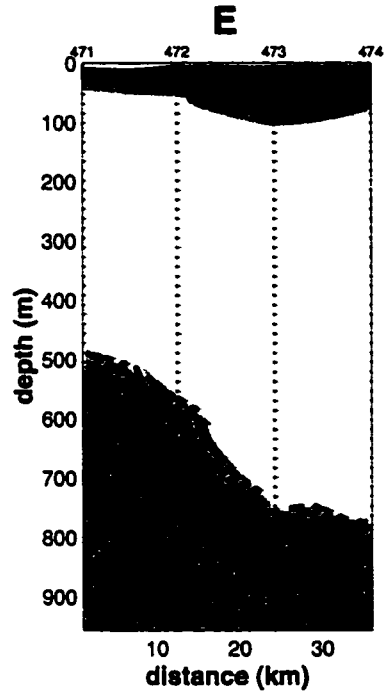

34.2 34.3 34.4 34.5 34.6 34.7 34.8 34.9 35 35.1
salinity (PSU)

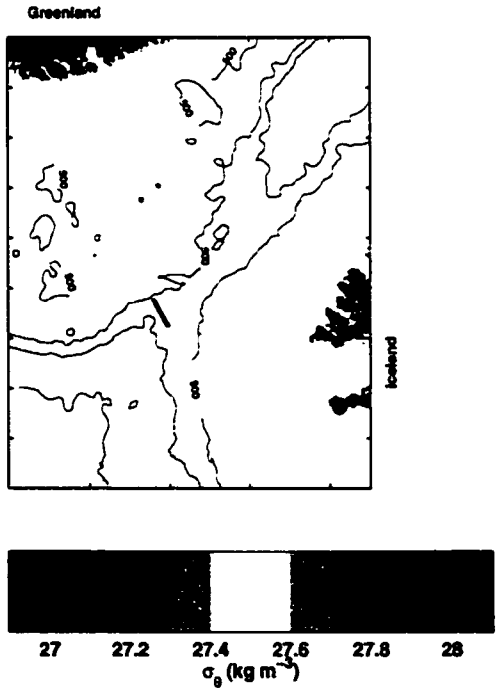

xo8
553
552
550
0
200
400
600
800
1000
1200
depth (m)
10
20
30
distance (km)


Greenland
Iceland
34.2 34.3 34.4 34.5 34.6 34.7 34.8 34.9 35 35.1
salinity (PSU)

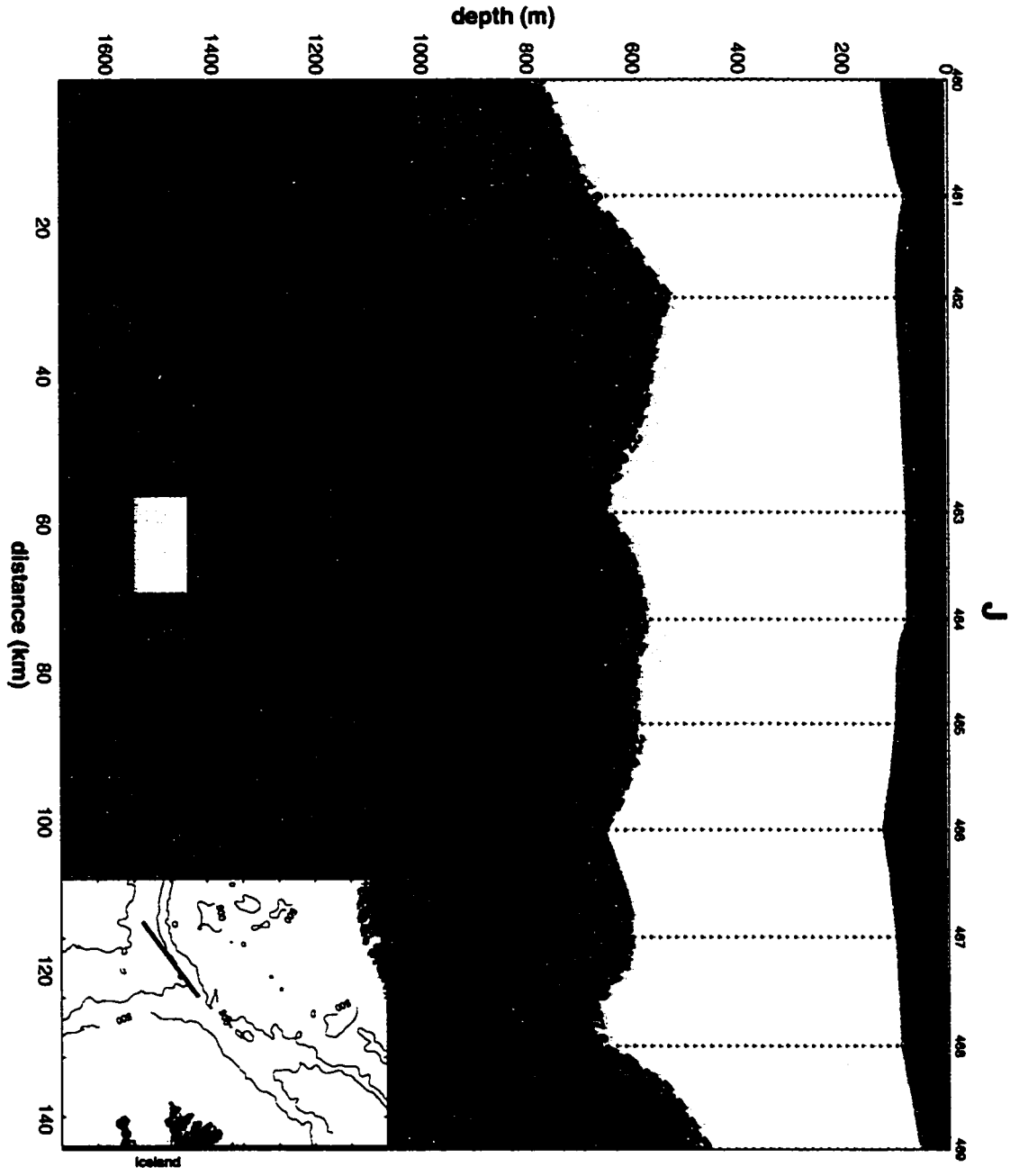

xo9
554
555
556
557
558
559
560
561
0
200
400
600
800
1000
1200
depth (m)
10
20
30
40
50
60
70
80
90
distance (km)
Greenland
Iceland
34.2 34.3 34.4 34.5 34.6 34.7 34.8 34.9 35 35.1
salinity (PSU)

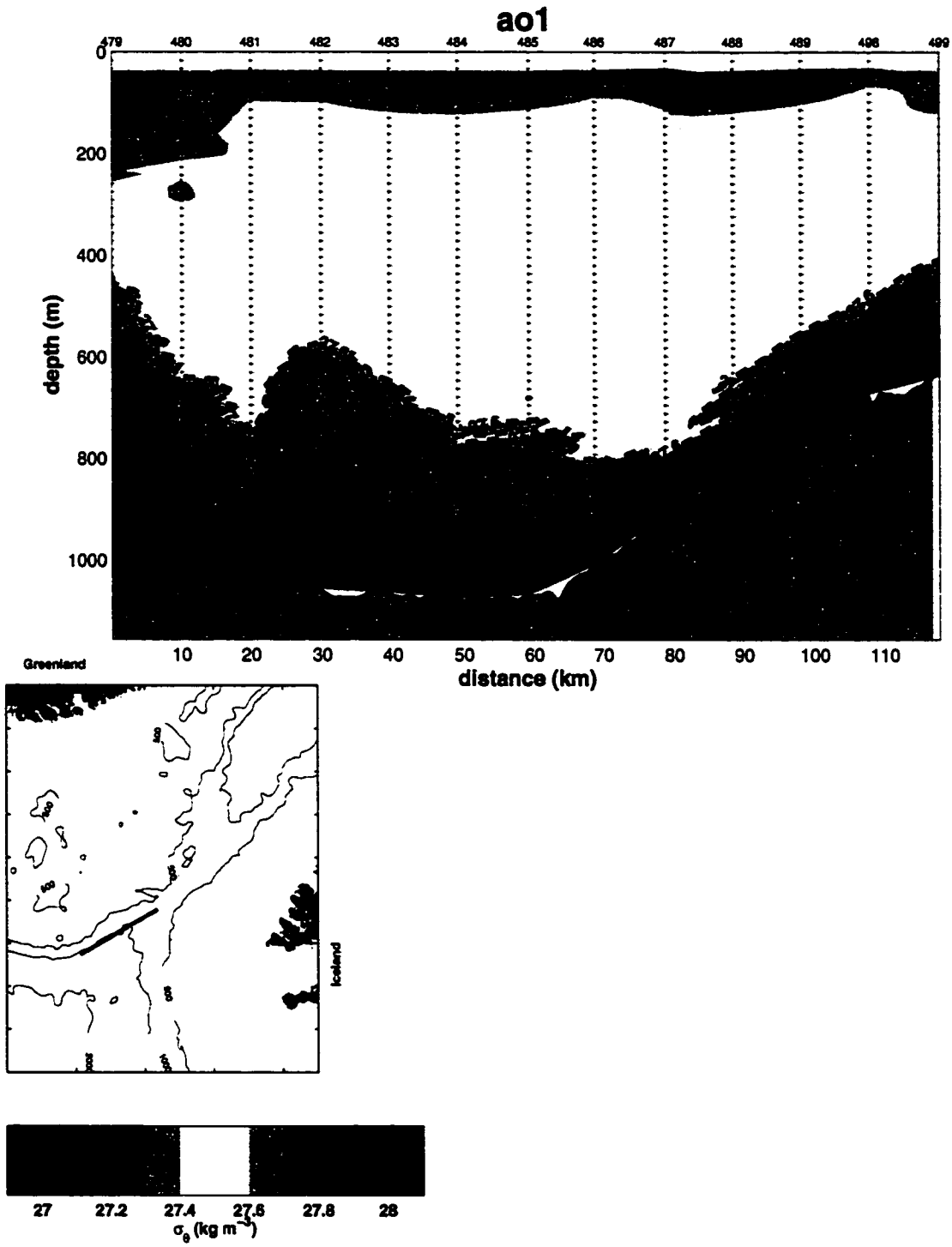

D
455
456
457
458
459
0
200
400
600
800
1000
1200
1400
1600
1800
2000
depth (m)
0
10
20
30
40
50
60
distance (km)
Greenland
Iceland
27
27.2
27.4
27.6
27.8
28
σ_θ (kg m^{-3})

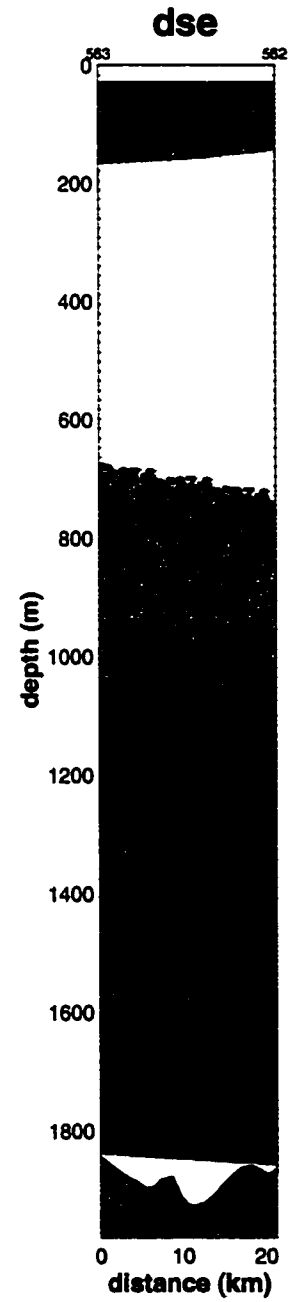

E
471
472
473
474
0
100
200
300
400
500
600
700
800
900
depth (m)
10
20
30
distance (km)

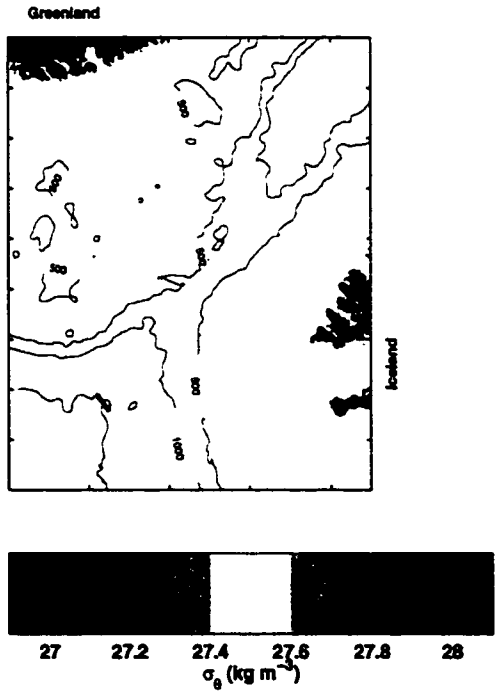

Greenland
Iceland

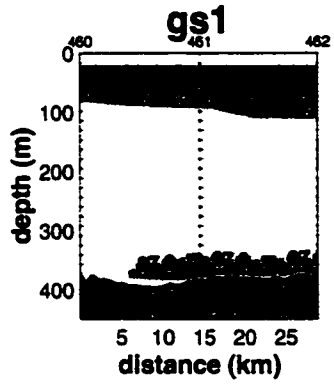
27
27.2
27.4
27.6
27.8
28
σθ (kg m⁻³)

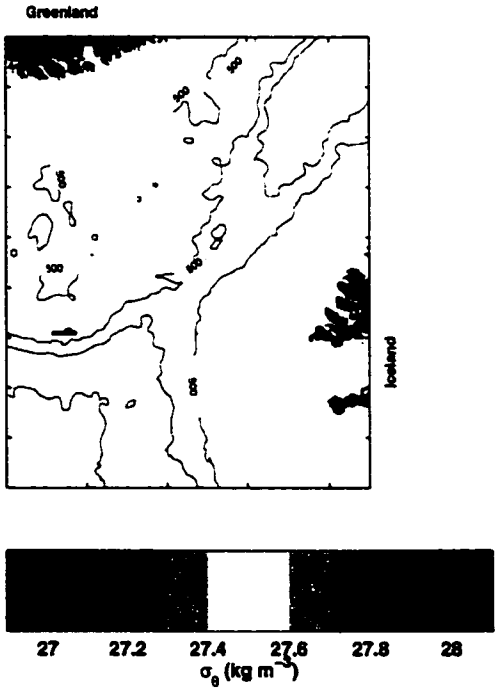

depth (m)
0
200
400
600
800
1000
1200
1400
1600
distance (km)
20
40
60
80
100
120
140
J
490
491
492
493
494
495
496
497
498
499
Iceland

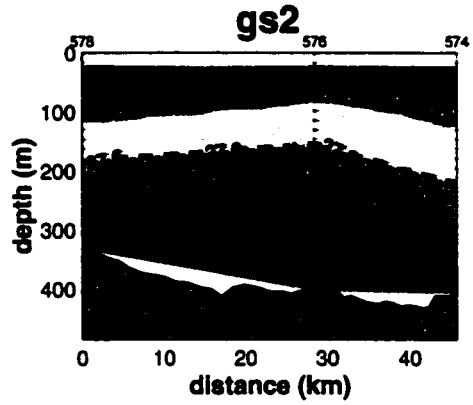

ao1
479
480
481
482
483
484
485
486
487
488
489
498
499
0
200
400
600
800
1000
depth (m)
10
20
30
40
50
60
70
80
90
100
110
distance (km)
Greenland
Iceland
27
27.2
27.4
27.6
27.8
28
σθ (kg m-3)

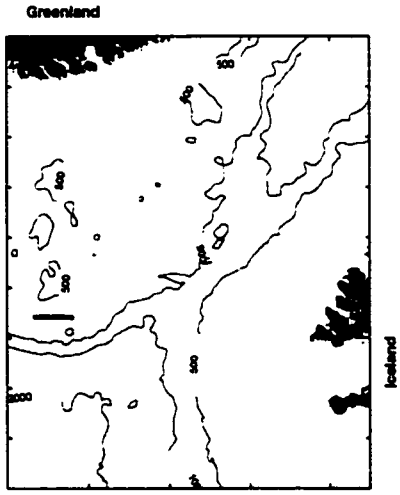

dse
563
562
0
200
400
600
800
1000
1200
1400
1600
1800
depth (m)
0
10
20
distance (km)

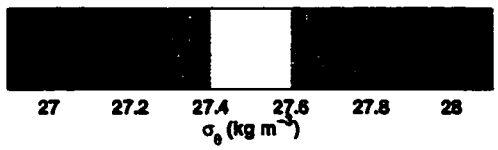

Greenland
Iceland
27
27.2
27.4
27.6
27.8
28
σ_θ (kg m^{-3})

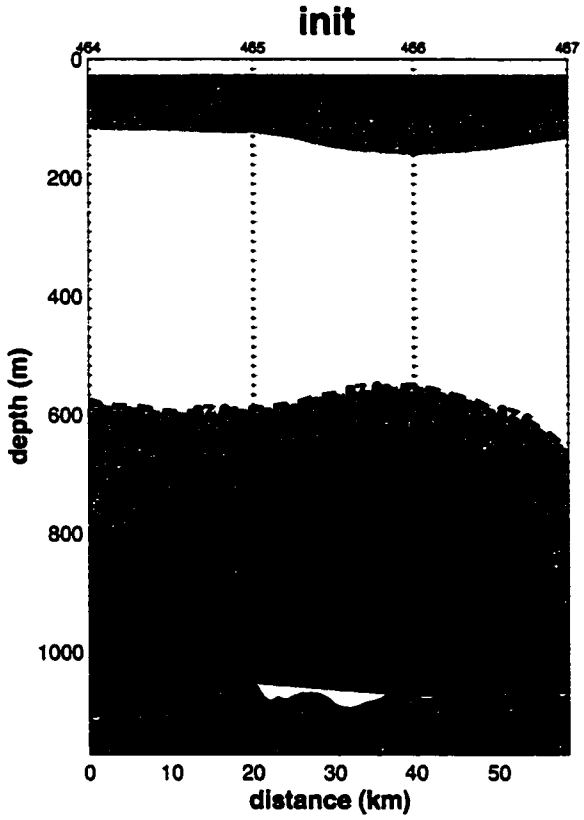

gs1
460
461
462
0
100
200
300
400
depth (m)
5 10 15 20 25
distance (km)

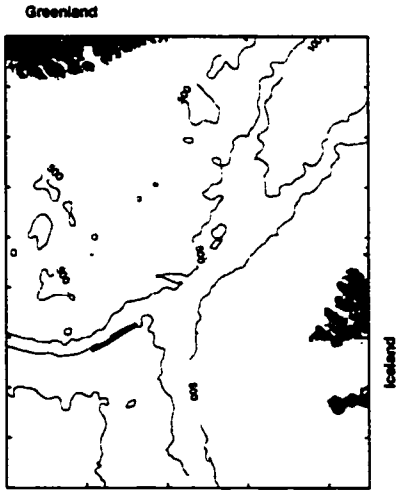

Greenland
Iceland
27
27.2
27.4
27.6
27.8
28
σθ (kg m-3)

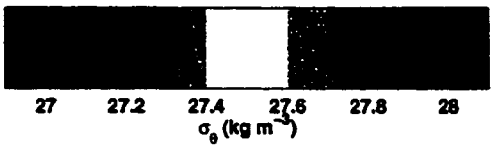

gs2
578
576
574
0
100
200
300
400
depth (m)
0
10
20
30
40
distance (km)

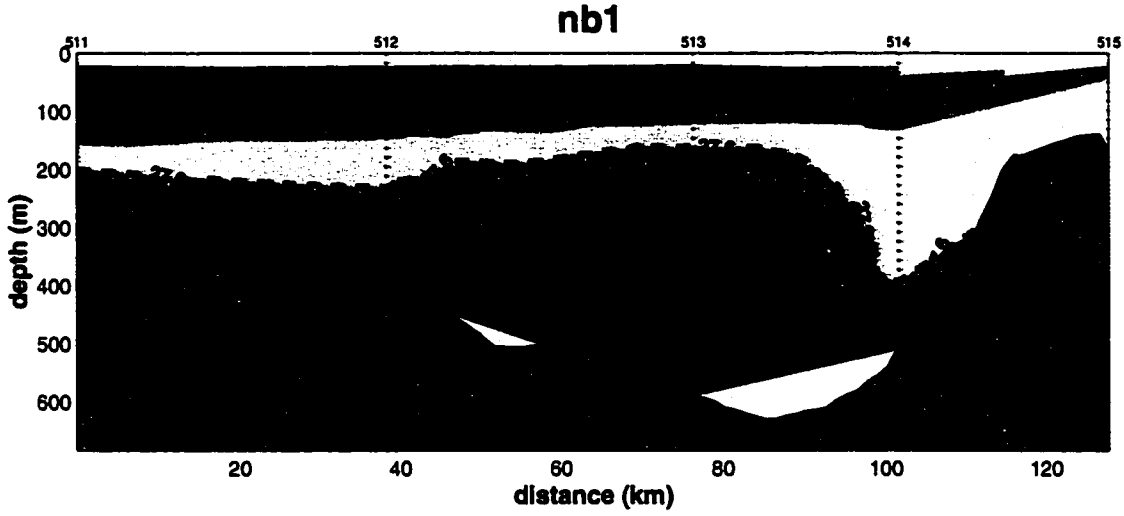

Greenland
Iceland

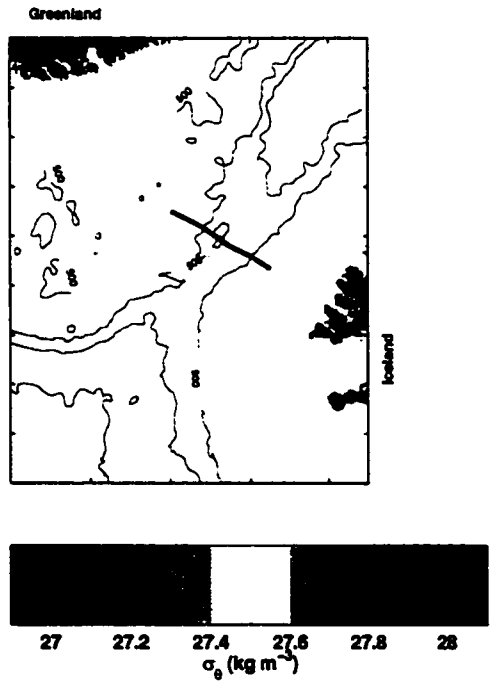

27
27.2
27.4
27.6
27.8
28
σθ (kg m-3)

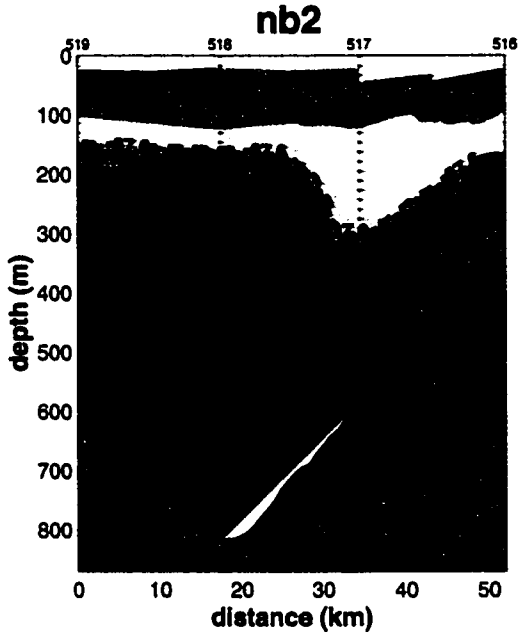

init
464
465
466
467
0
200
400
600
800
1000
depth (m)
0
10
20
30
40
50
distance (km)

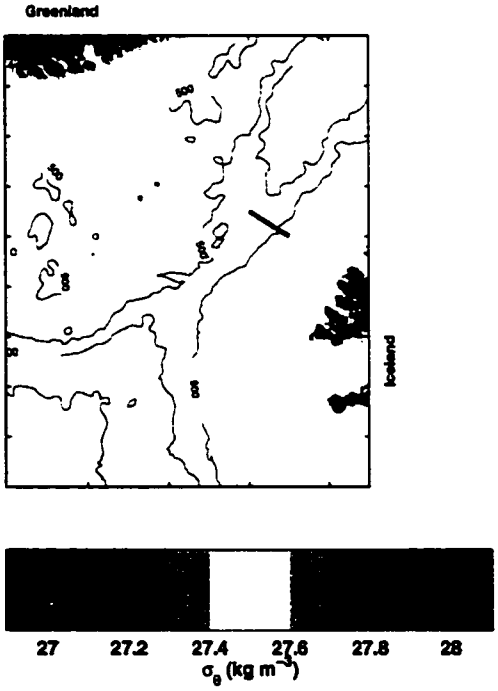

Greenland
Iceland


27
27.2
27.4
27.6
27.8
28
σθ (kg m-3)

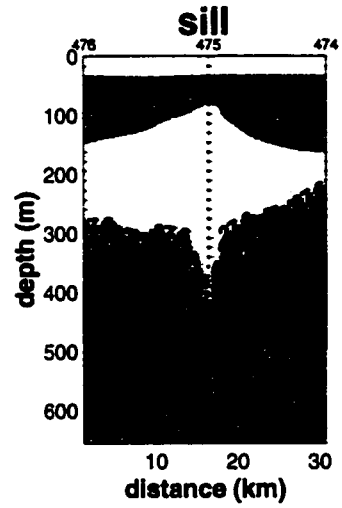

nb1
511
512
513
514
515
0
100
200
300
400
500
600
depth (m)
20
40
60
80
100
120
distance (km)

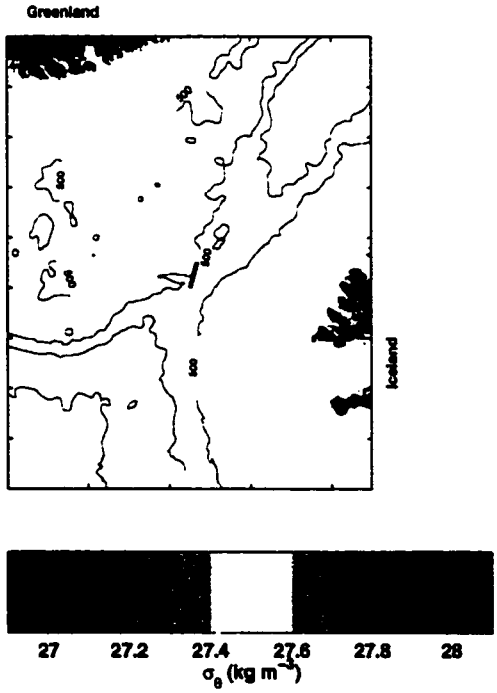

Greenland
Iceland
27
27.2
27.4
27.6
27.8
28
σ_θ (kg m^{-3})

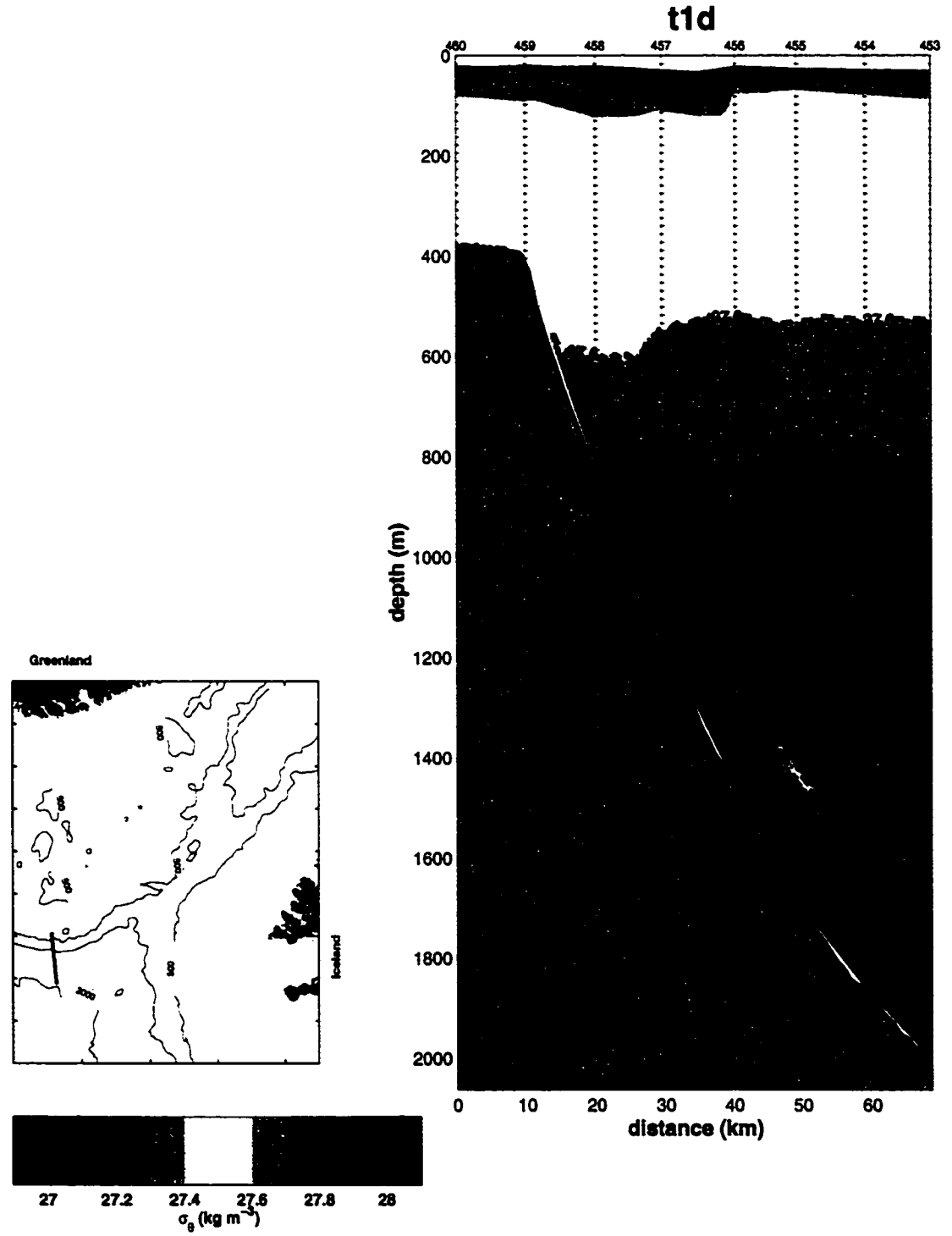

nb2
519
518
517
516
0
100
200
300
400
500
600
700
800
depth (m)
0
10
20
30
40
50
distance (km)

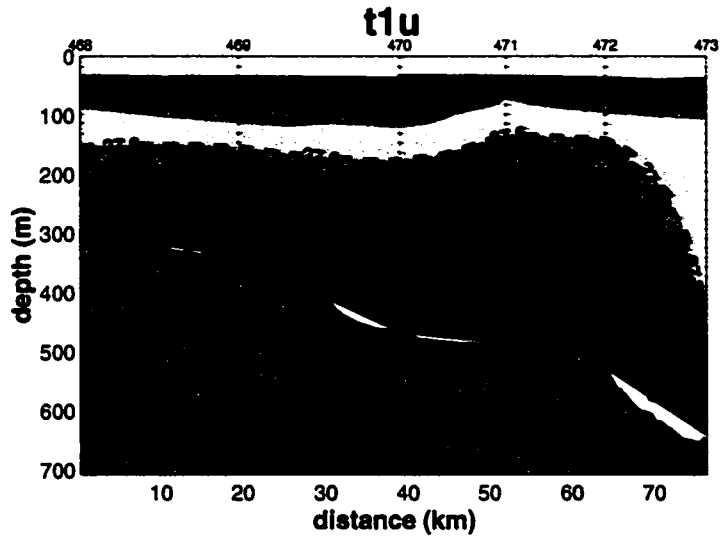

Greenland
Iceland

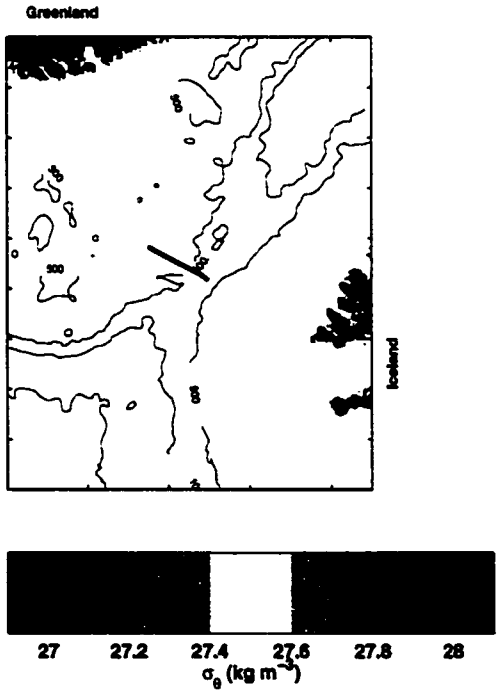
27
27.2
27.4
27.6
27.8
28
σθ (kg m-3)

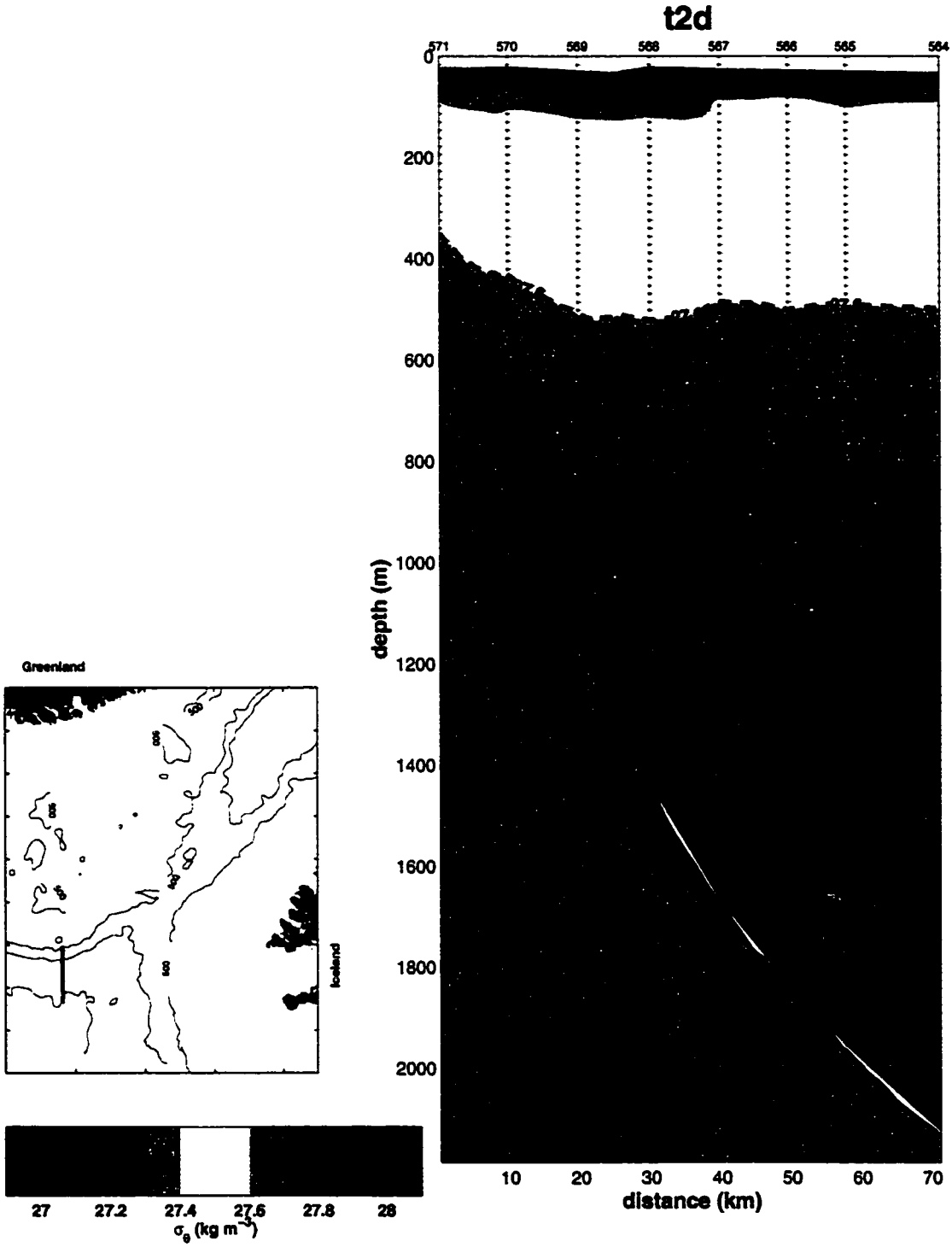

sill
476
475
474
0
100
200
300
400
500
600
depth (m)
10
20
30
distance (km)

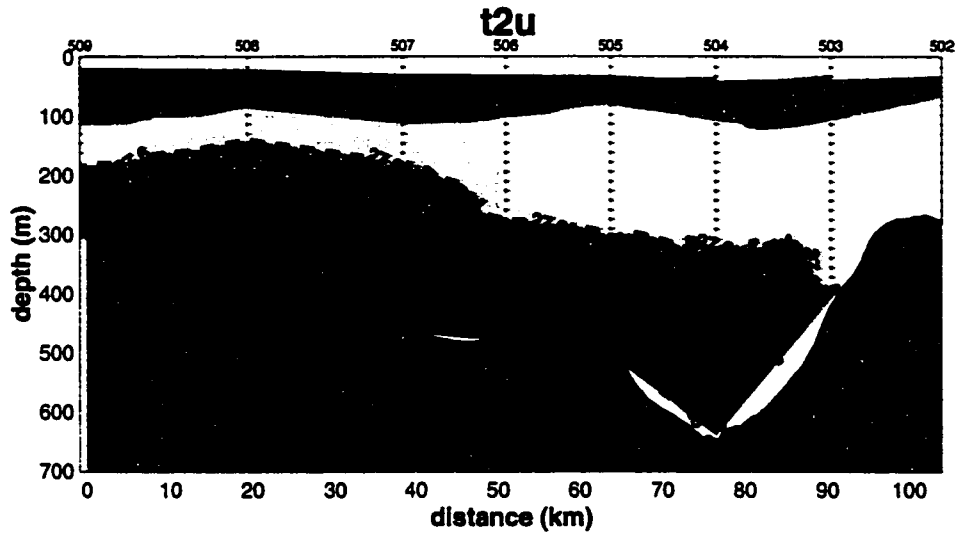

Greenland
Iceland
27
27.2
27.4
27.6
27.8
28
σθ (kg m⁻³)

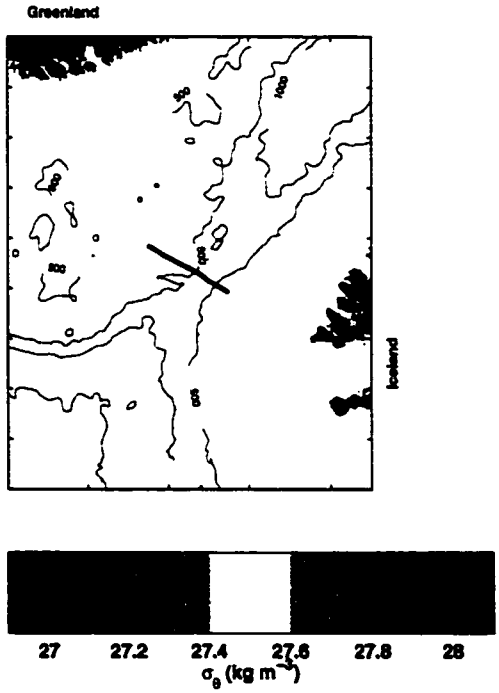

t1d
460
459
458
457
456
455
454
453
0
200
400
600
800
1000
1200
1400
1600
1800
2000
depth (m)
0
10
20
30
40
50
60
distance (km)
Greenland
Iceland
27
27.2
27.4
27.6
27.8
28
σ_θ (kg m^{-3})


t1u
468
469
470
471
472
473
0
100
200
300
400
500
600
700
depth (m)
10
20
30
40
50
60
70
distance (km)

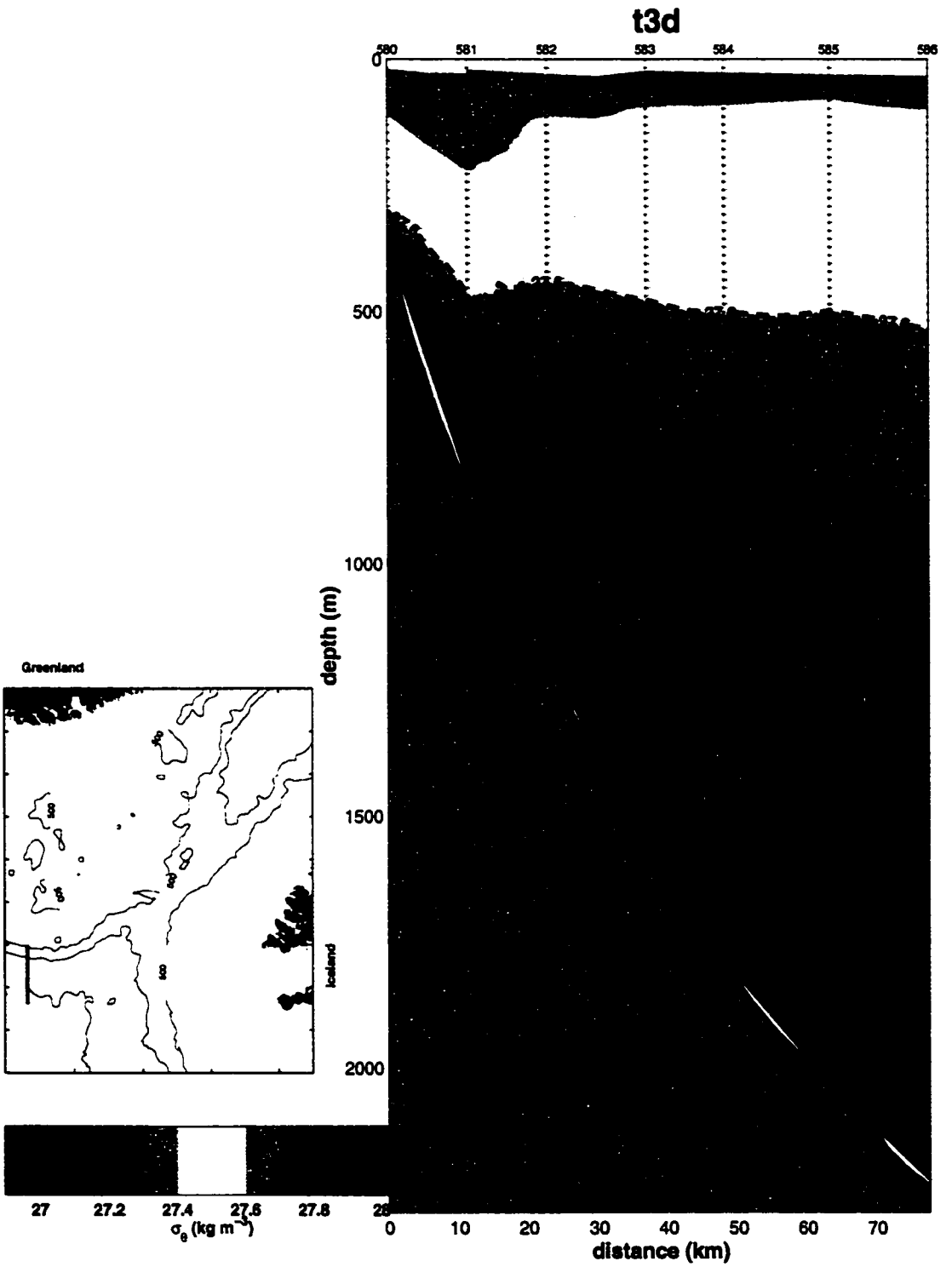

Greenland
Iceland
27
27.2
27.4
27.6
27.8
28
σ_θ (kg m^{-3})

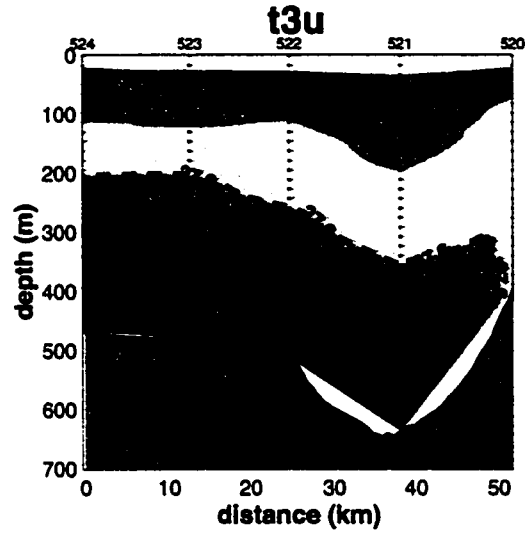

t2d
571
570
569
568
567
566
565
564
0
200
400
600
800
1000
1200
1400
1600
1800
2000
depth (m)
10
20
30
40
50
60
70
distance (km)
Greenland
Iceland
27
27.2
27.4
27.6
27.8
28
σθ (kg m-3)

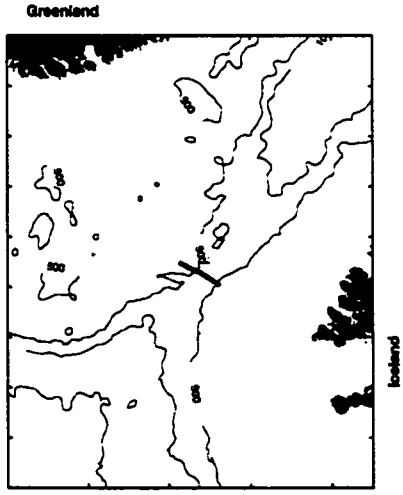

t2u
509
508
507
506
505
504
503
502
0
100
200
300
400
500
600
700
depth (m)
0
10
20
30
40
50
60
70
80
90
100
distance (km)

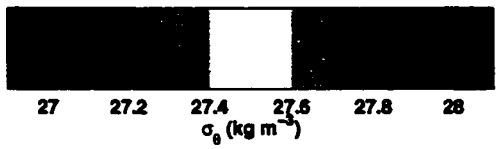

Greenland
Iceland

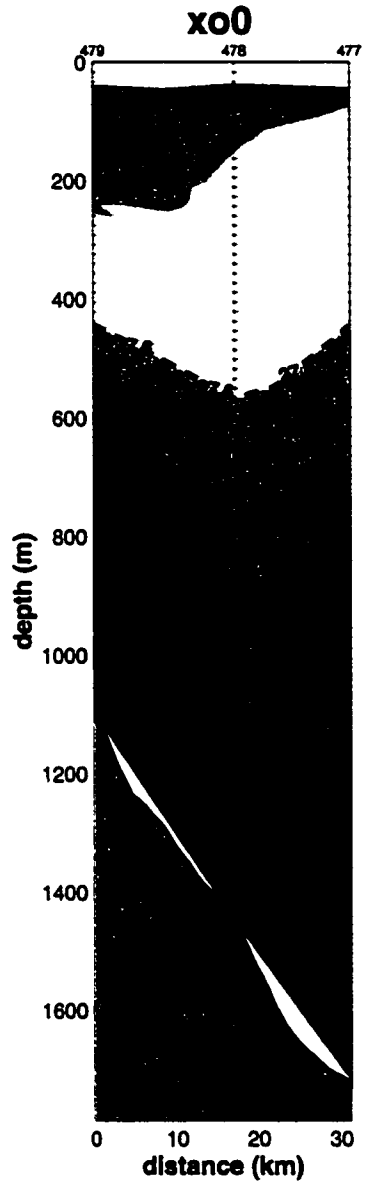
27
27.2
27.4
27.6
27.8
28
σθ (kg m-3)

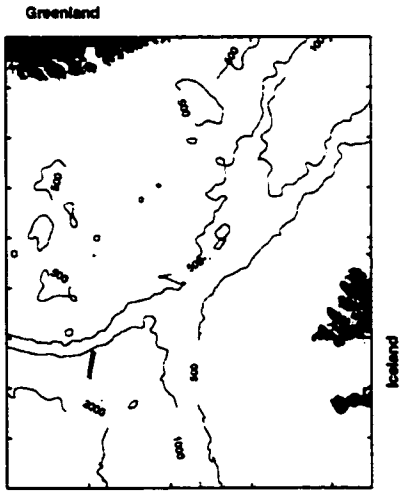

t3d
580
581
582
583
584
585
586
0
500
1000
1500
2000
depth (m)
Greenland
Iceland
27
27.2
27.4
27.6
27.8
28
σ_θ (kg m^{-3})
0
10
20
30
40
50
60
70
distance (km)

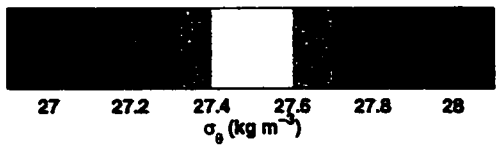

t3u
524
523
522
521
520
0
100
200
300
400
500
600
700
depth (m)
0
10
20
30
40
50
distance (km)

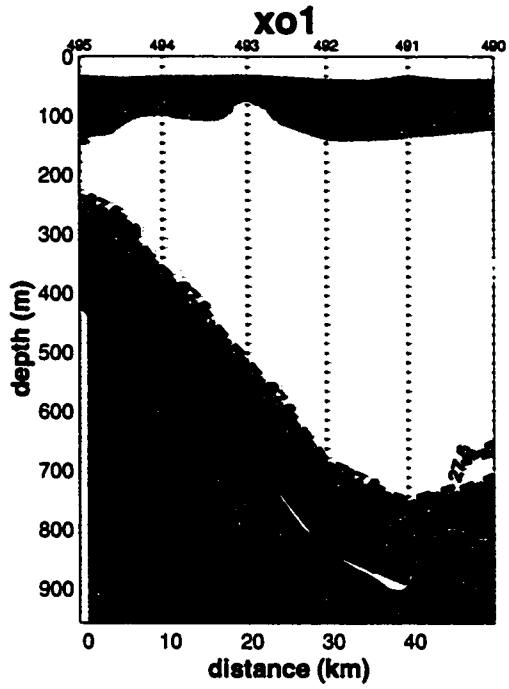

Greenland
Iceland

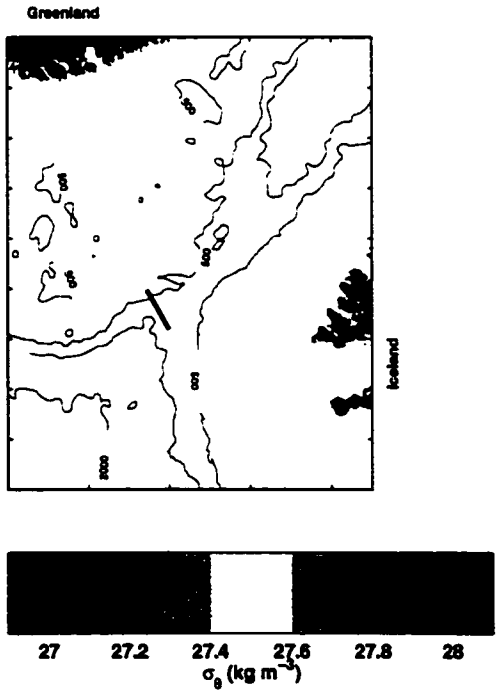

27
27.2
27.4
27.6
27.8
28
σθ (kg m-3)

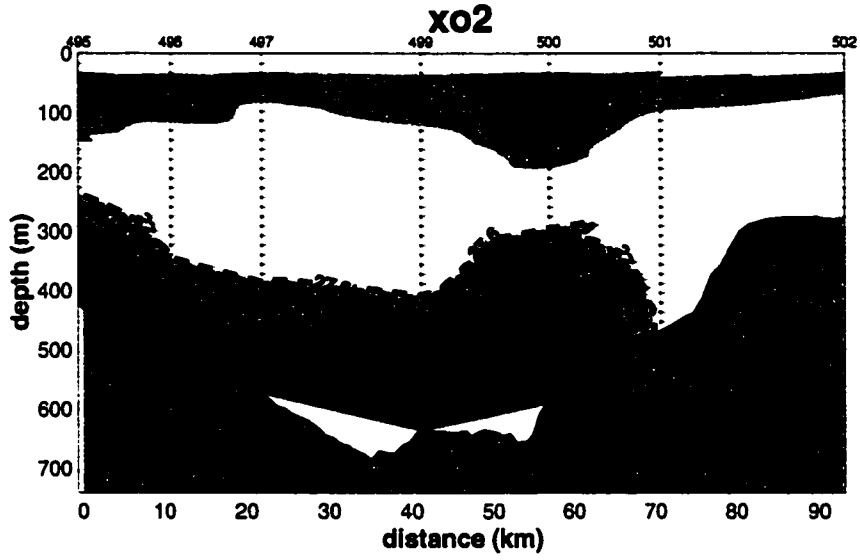

xo0
479
478
477
0
200
400
600
800
1000
1200
1400
1600
depth (m)
0
10
20
30
distance (km)

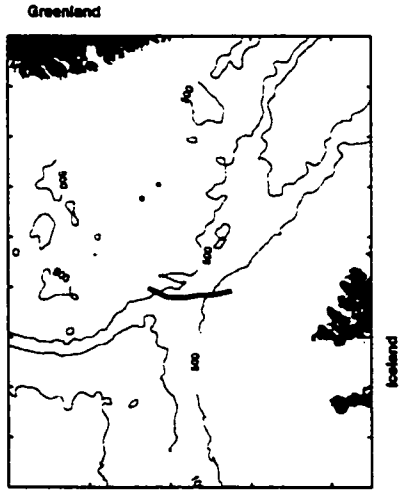

Greenland
Iceland

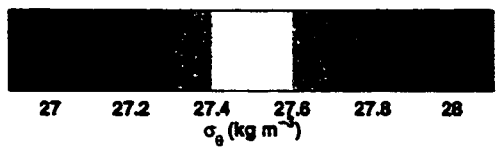

27
27.2
27.4
27.6
27.8
28
σθ (kg m⁻³)

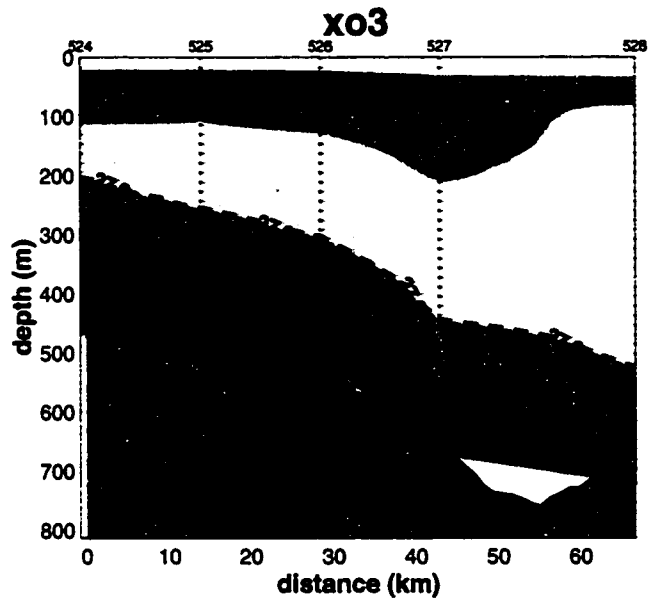

XO1
495
494
493
492
491
490
0
100
200
300
400
500
600
700
800
900
depth (m)
0
10
20
30
40
distance (km)
27.4

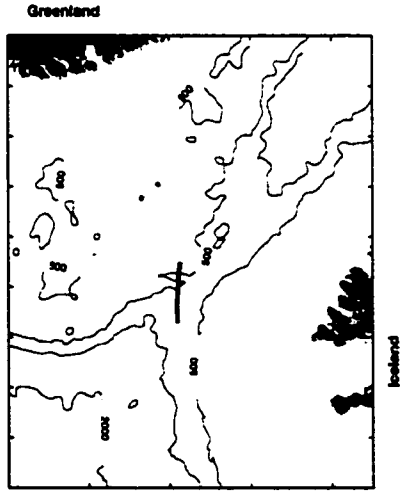

Greenland
Iceland
2000
27
27.2
27.4
27.6
27.8
28
σ_θ (kg m^{-3})

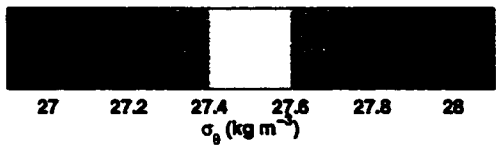

xo2
495
496
497
499
500
501
502
0
100
200
300
400
500
600
700
depth (m)
0
10
20
30
40
50
60
70
80
90
distance (km)

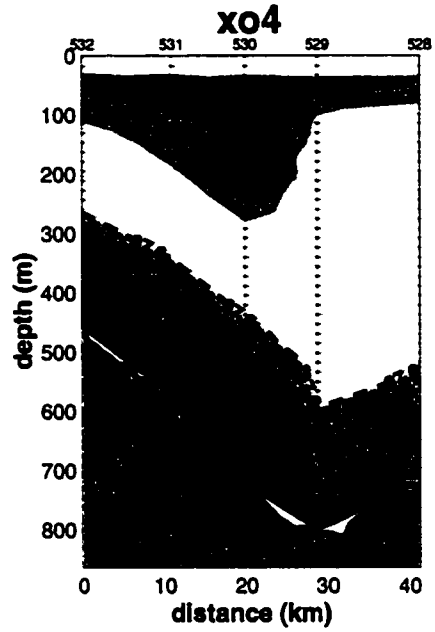

Greenland
Iceland

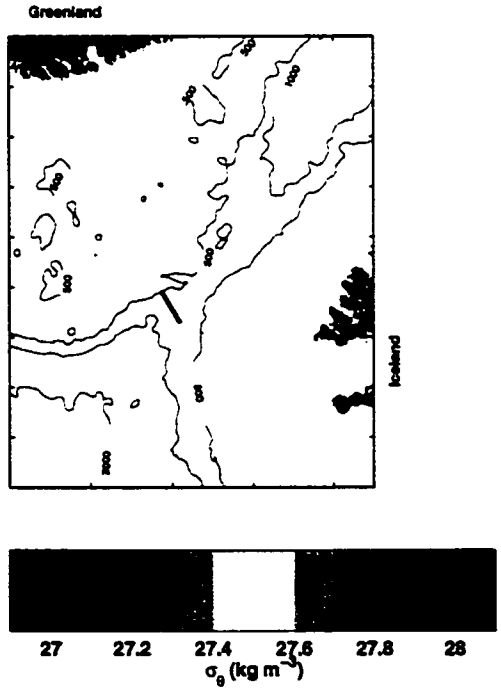

27
27.2
27.4
27.6
27.8
28
σθ (kg m⁻³)

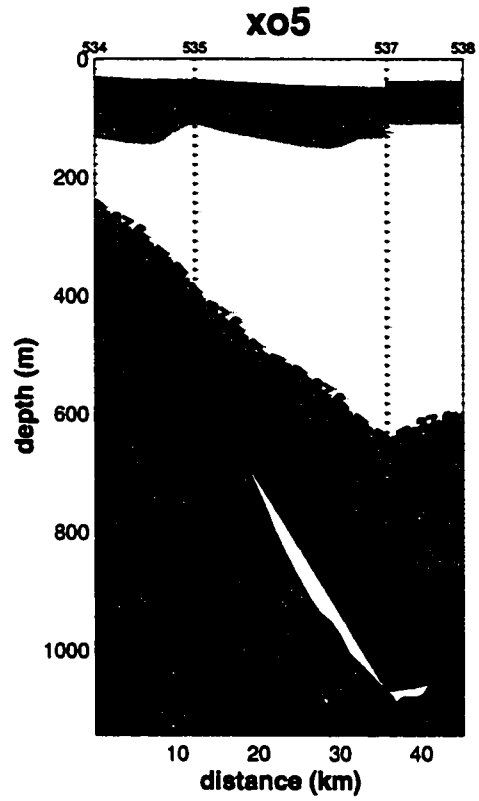

xo3
524
525
526
527
528
0
100
200
300
400
500
600
700
800
depth (m)
0
10
20
30
40
50
60
distance (km)

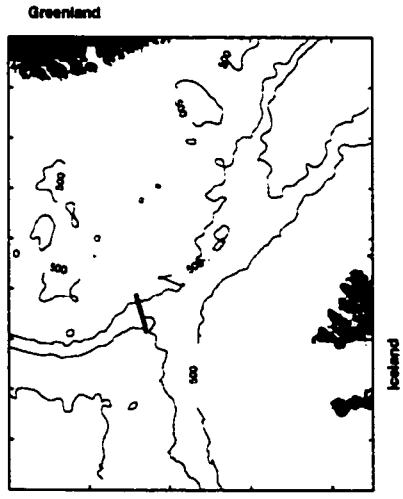

Greenland
Iceland

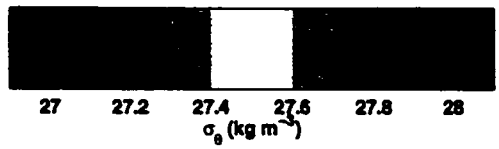

27
27.2
27.4
27.6
27.8
28
σθ (kg m-3)

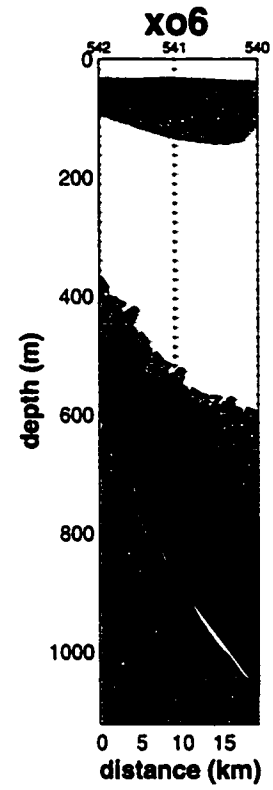

xo4
532
531
530
529
528
0
100
200
300
400
500
600
700
800
depth (m)
0
10
20
30
40
distance (km)

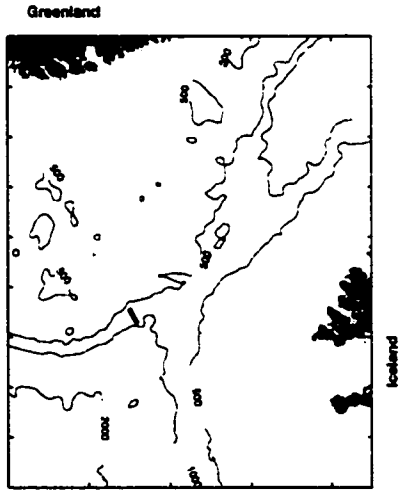

Greenland
Iceland
27
27.2
27.4
27.6
27.8
28
σθ (kg m-3)

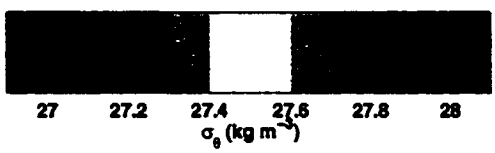

xo5
534
535
537
538
0
200
400
600
800
1000
depth (m)
10
20
30
40
distance (km)

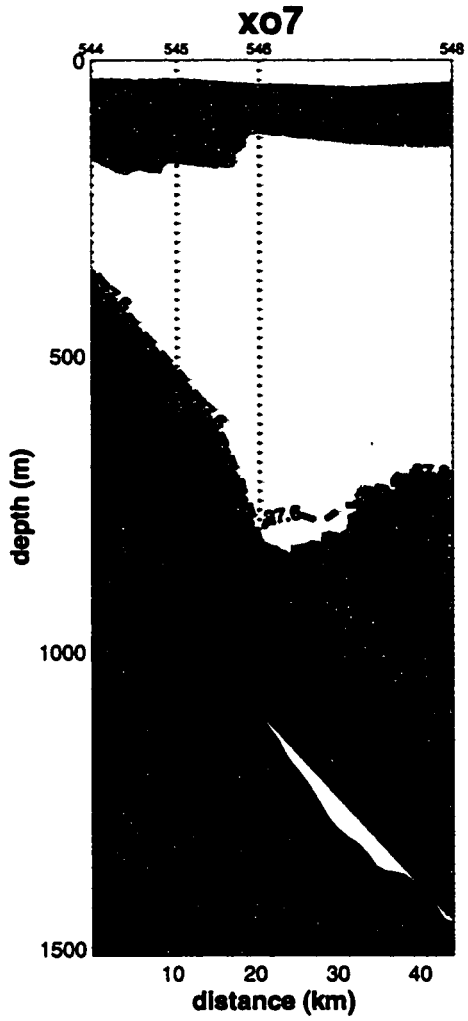

Greenland
Iceland

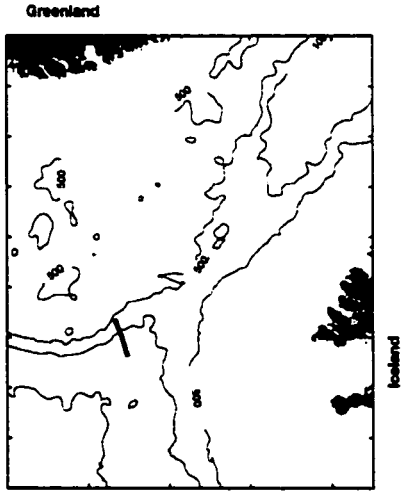

27
27.2
27.4
27.6
27.8
28
σθ (kg m-3)

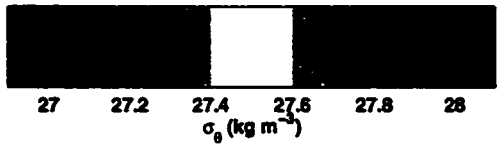

xo6
542
541
540
0
200
400
600
800
1000
depth (m)
0 5 10 15
distance (km)

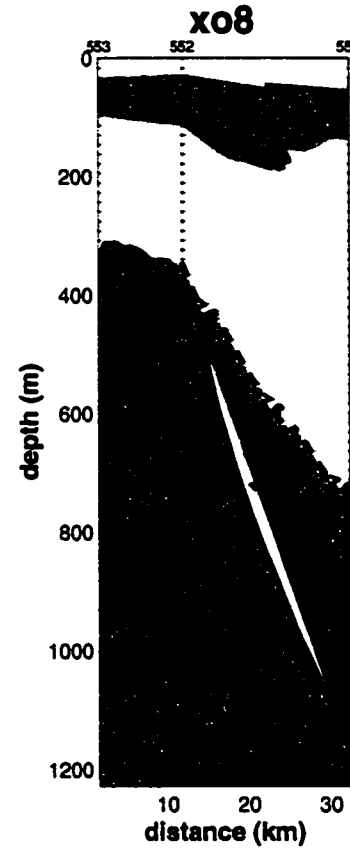

Greenland
Iceland

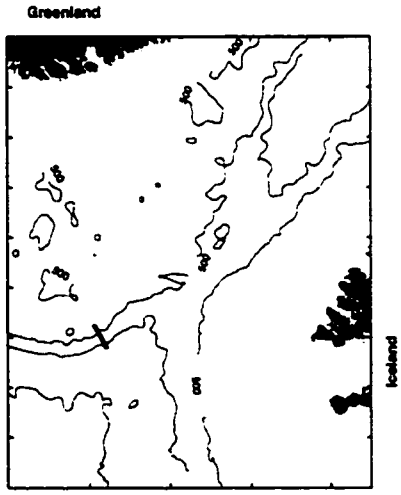

27
27.2
27.4
27.6
27.8
28
σθ (kg m-3)

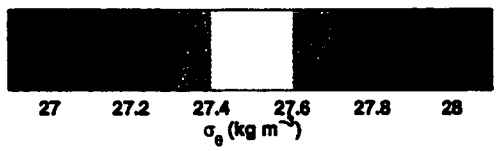

XO7
544
545
546
548
0
500
1000
1500
depth (m)
27.6
10
20
30
40
distance (km)

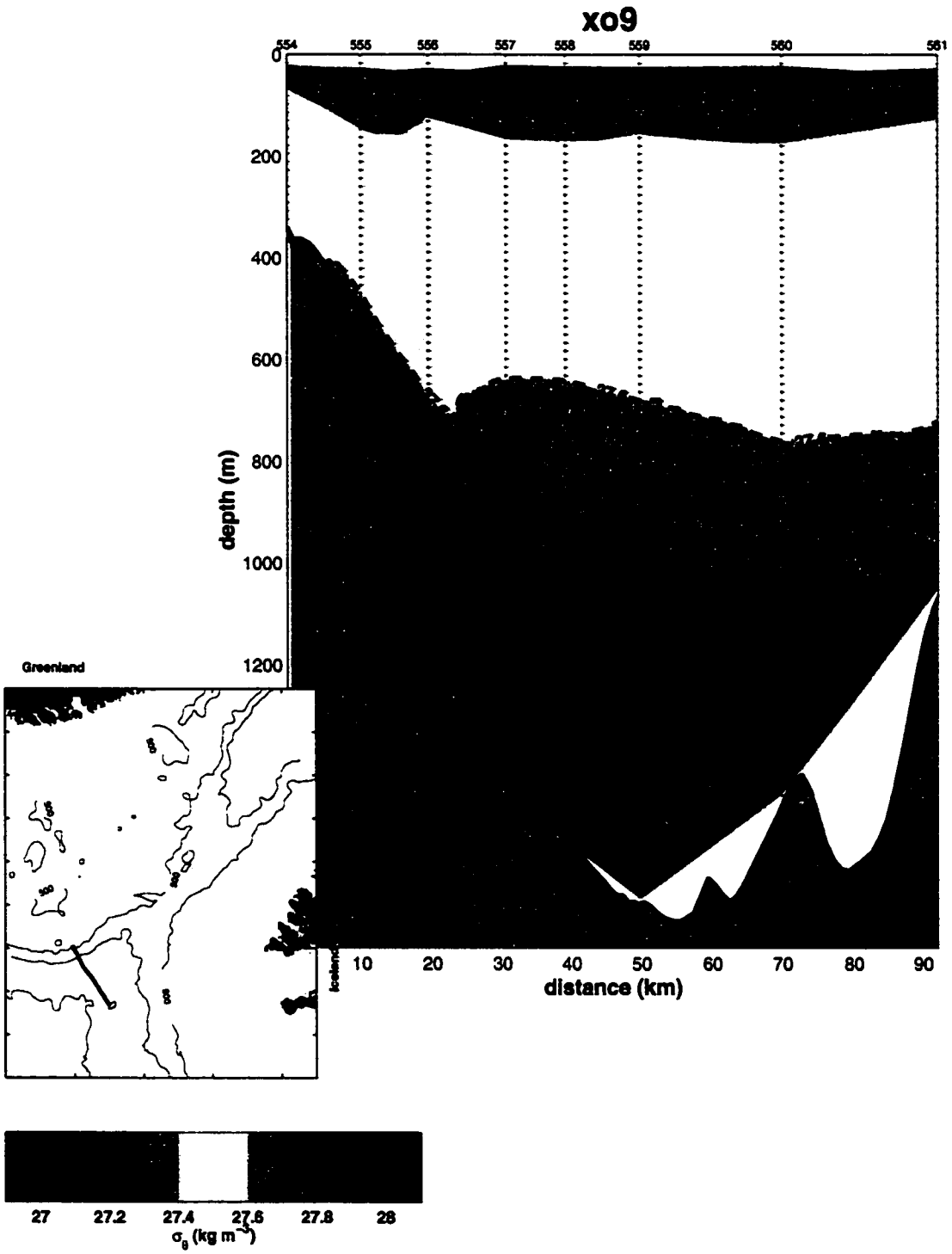

Greenland
Iceland

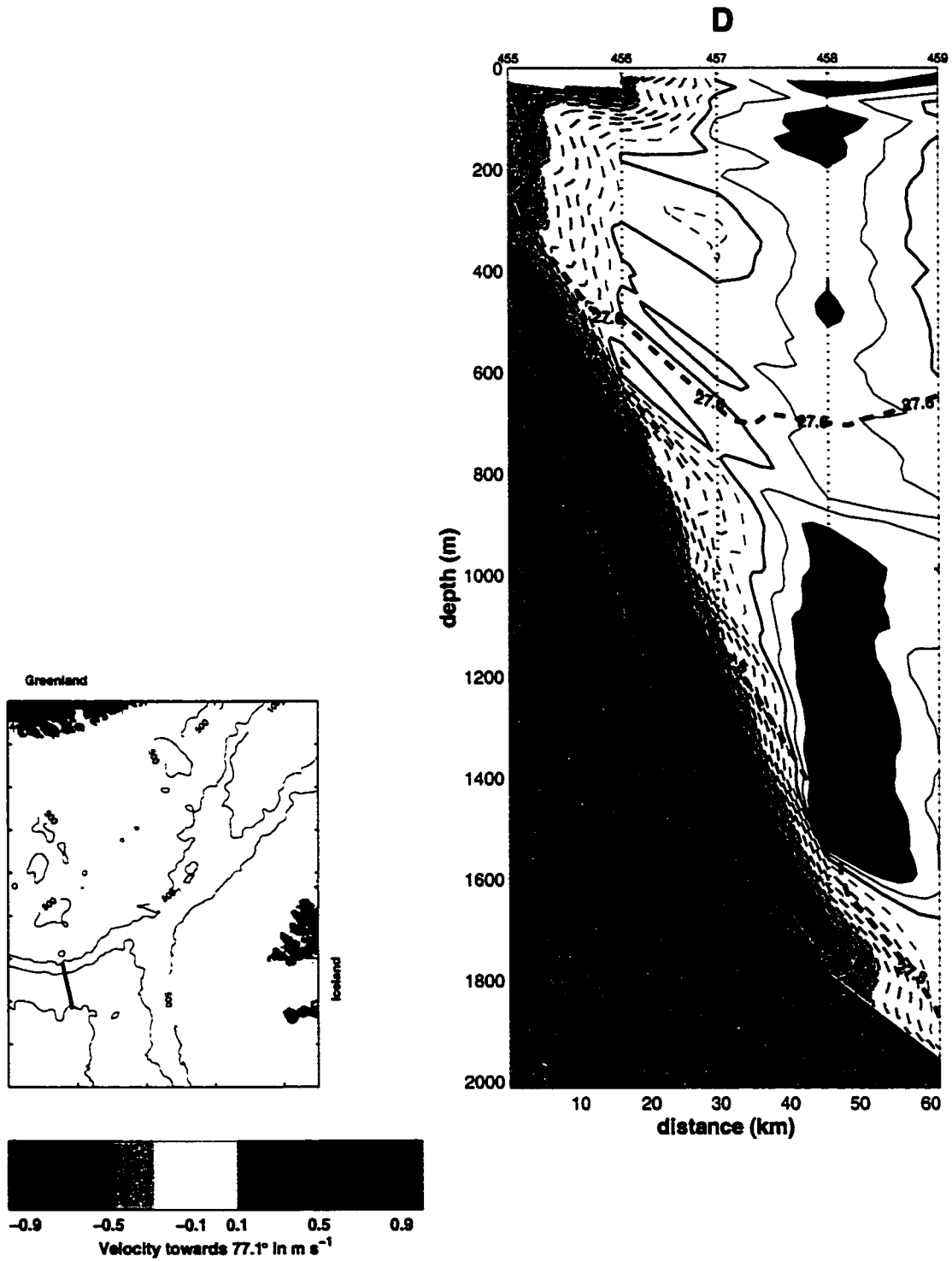

27
27.2
27.4
27.6
27.8
28
σθ (kg m-3)

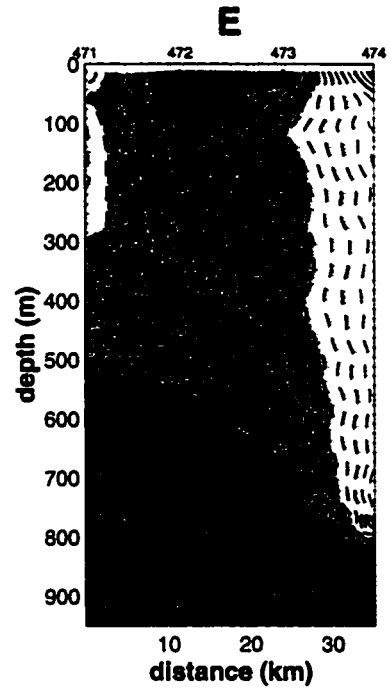

XO8
553
552
550
0
200
400
600
800
1000
1200
depth (m)
10
20
30
distance (km)

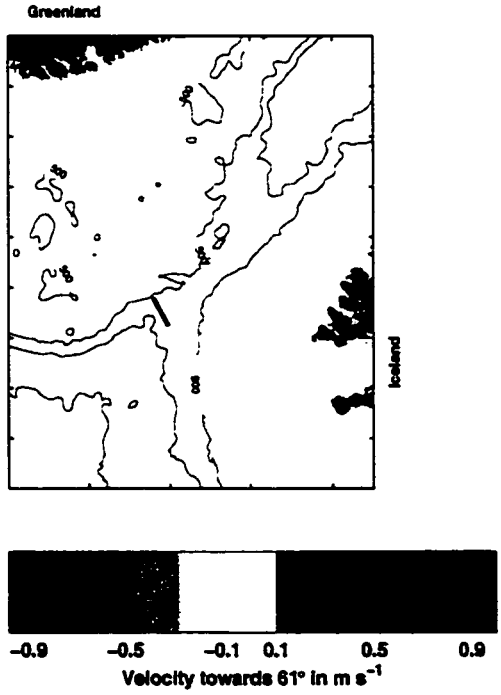

Greenland
Iceland

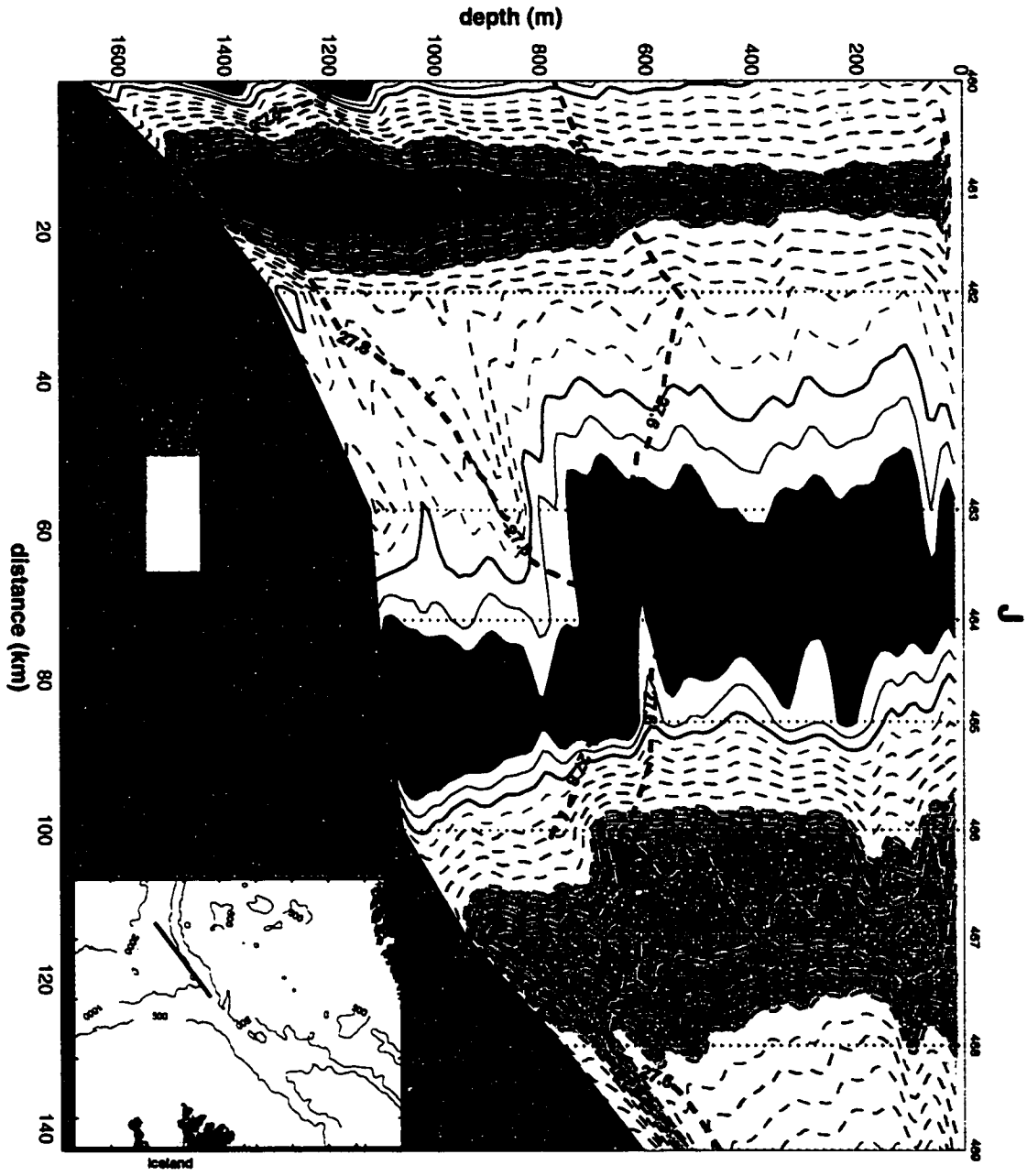

27
27.2
27.4
27.6
27.8
28
σ_θ (kg m^{-3})

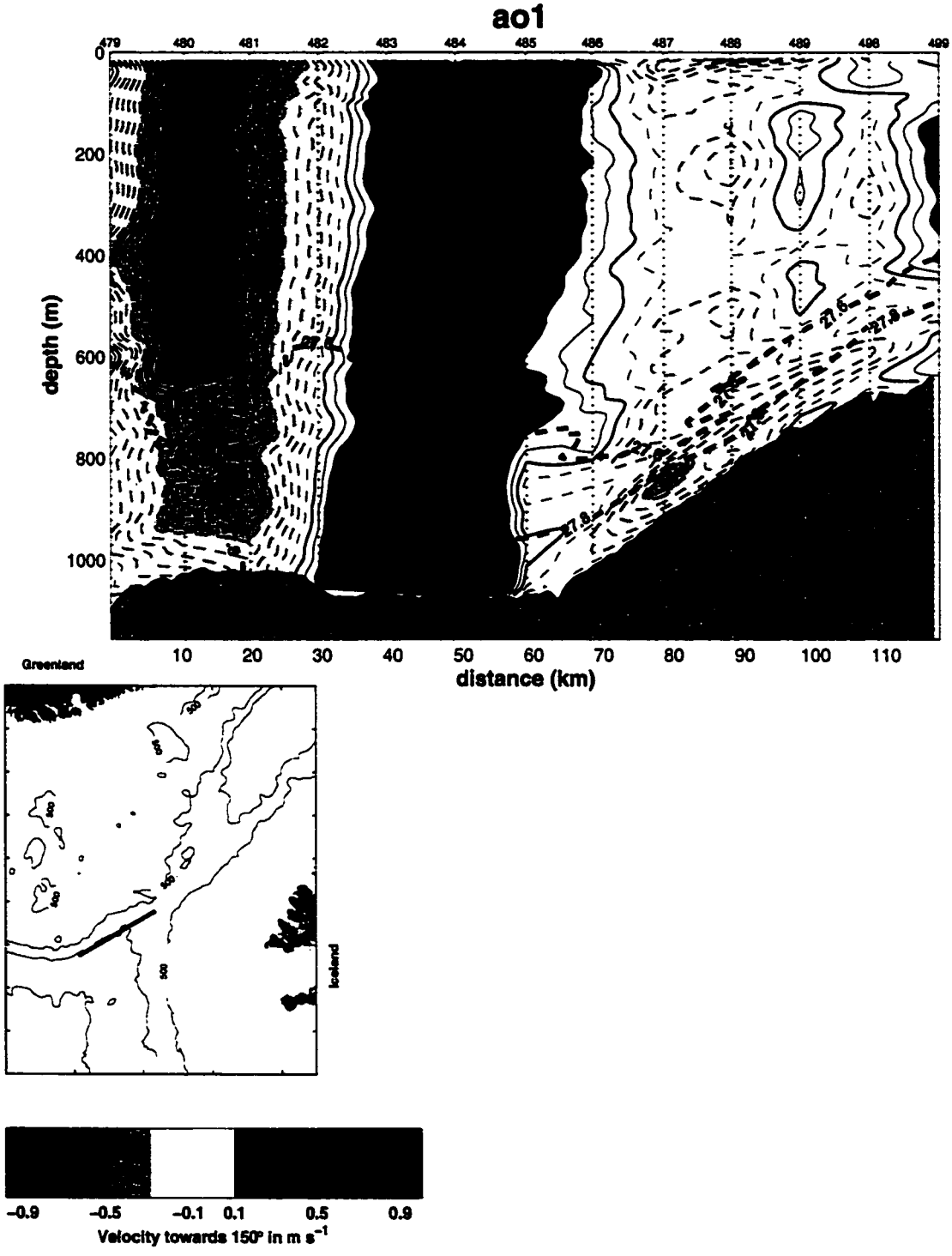

xo9
554
555
556
557
558
559
560
561
0
200
400
600
800
1000
1200
depth (m)
10
20
30
40
50
60
70
80
90
distance (km)
Greenland
Iceland
27
27.2
27.4
27.6
27.8
28
σ_θ (kg m^{-3})

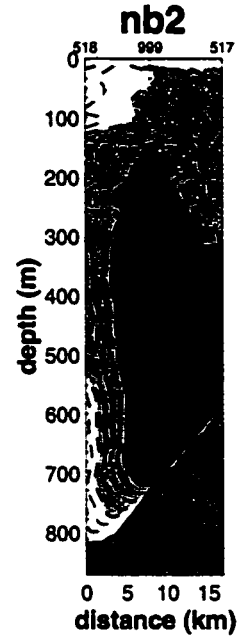

D
455
456
457
458
459
0
200
400
600
800
1000
1200
1400
1600
1800
2000
depth (m)
27.6
27.6
27.6
27.6
10
20
30
40
50
60
distance (km)
Greenland
Iceland
−0.9
−0.5
−0.1
0.1
0.5
0.9
Velocity towards 77.1° in m s^{-1}

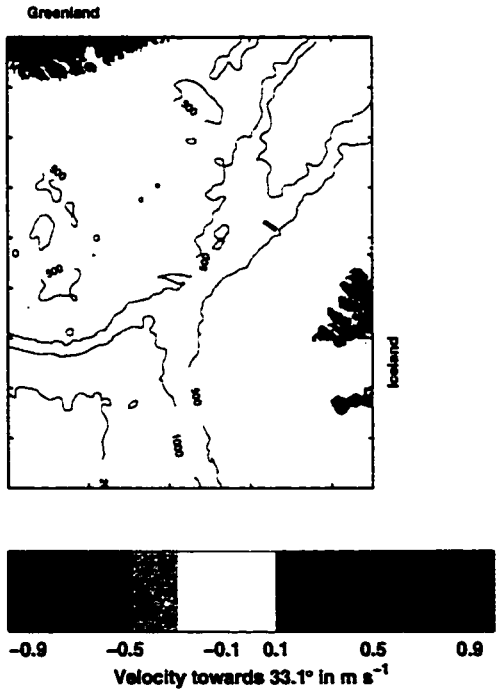

E
471
472
473
474
0
100
200
300
400
500
600
700
800
900
depth (m)
10
20
30
distance (km)

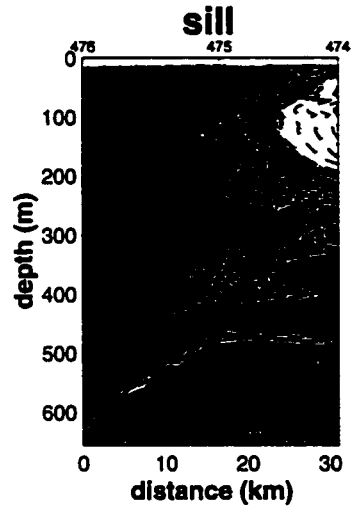

Greenland
Iceland
-0.9
-0.5
-0.1
0.1
0.5
0.9
Velocity towards 61° in m s-1

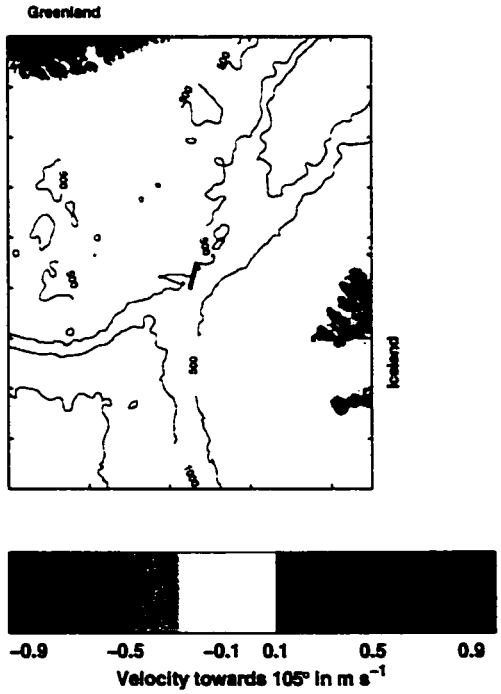

depth (m)
1600
1400
1200
1000
800
600
400
200
0
distance (km)
20
40
60
80
100
120
140
Iceland
J

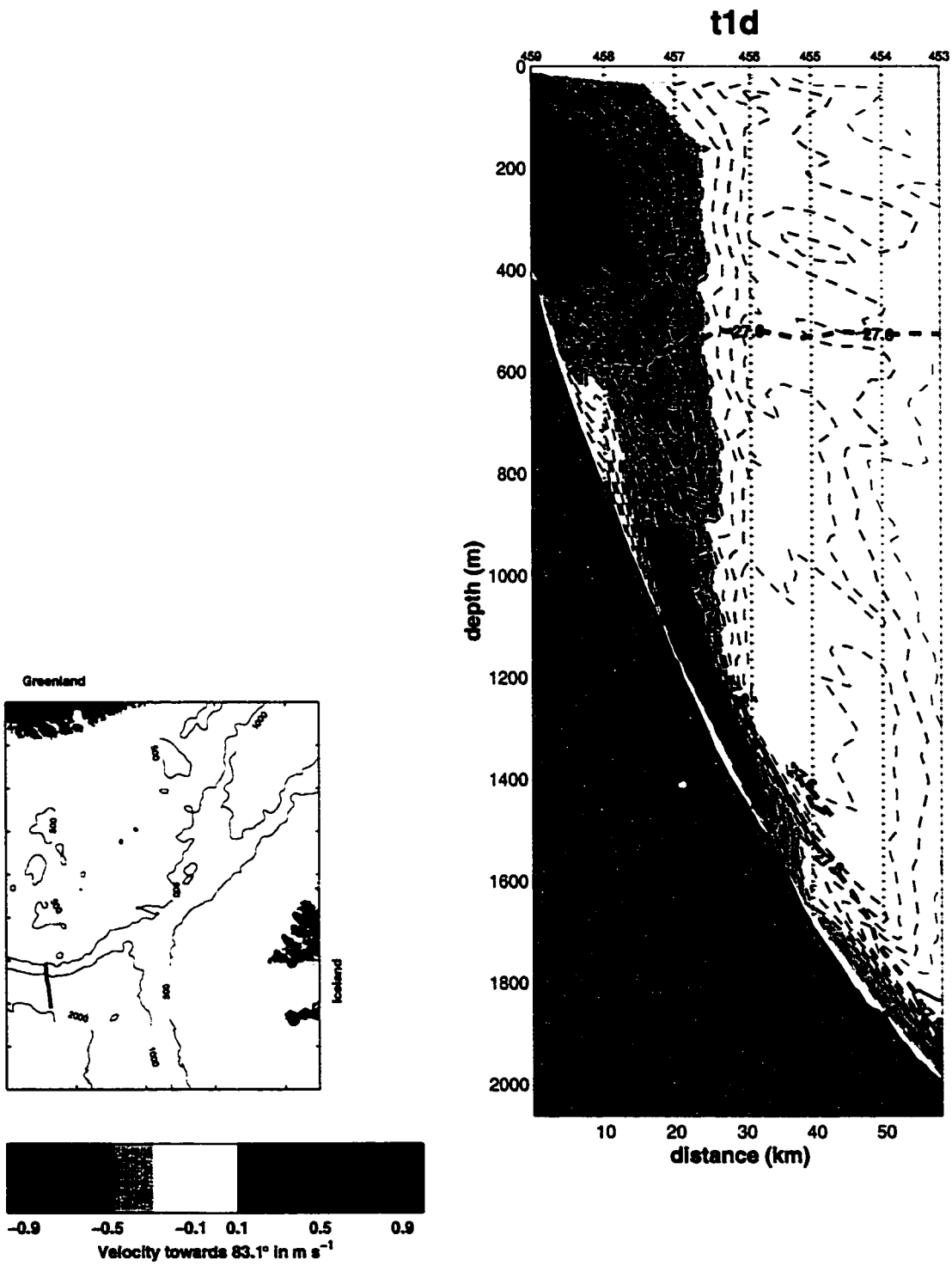

ao1
depth (m)
distance (km)
Greenland
Iceland
-0.9
-0.5
-0.1
0.1
0.5
0.9
Velocity towards 150° in m s⁻¹

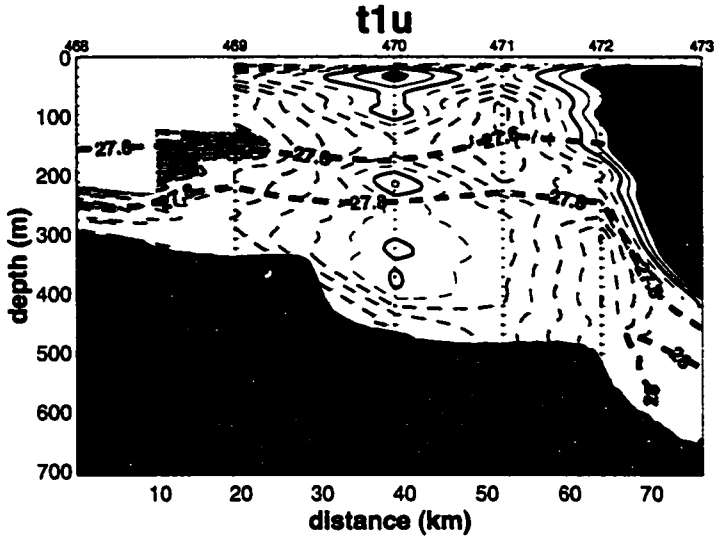

nb2
518
999
517
0
100
200
300
400
500
600
700
800
depth (m)
0 5 10 15
distance (km)

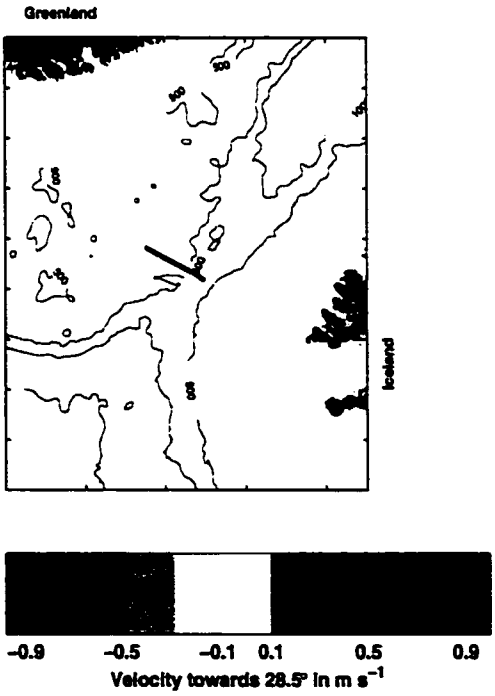

Greenland
Iceland
-0.9
-0.5
-0.1
0.1
0.5
0.9
Velocity towards 33.1° in m s-1


sill
476
475
474
0
100
200
300
400
500
600
depth (m)
0
10
20
30
distance (km)

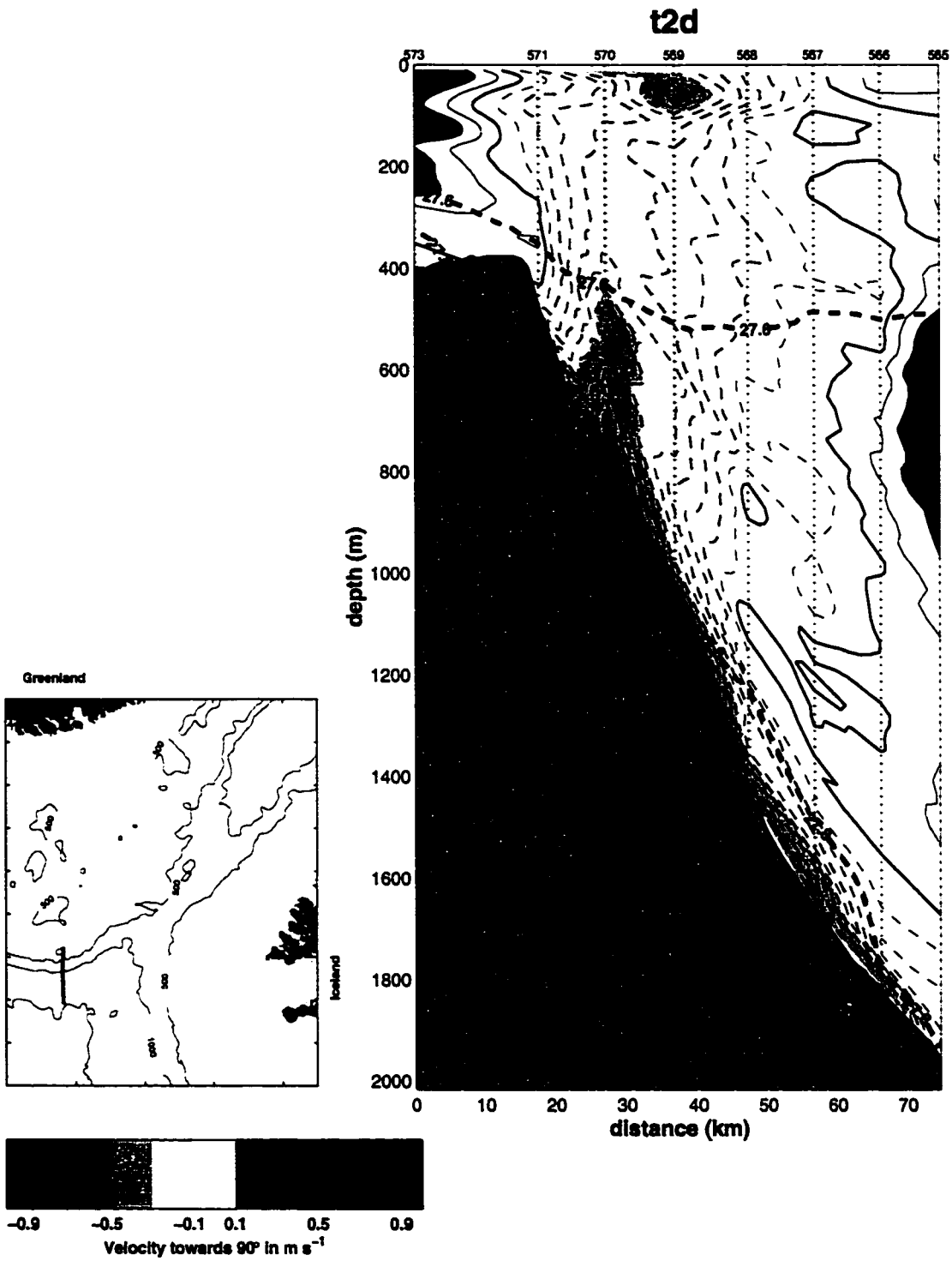

Greenland
Iceland
-0.9
-0.5
-0.1
0.1
0.5
0.9
Velocity towards 105° in m s^{-1}

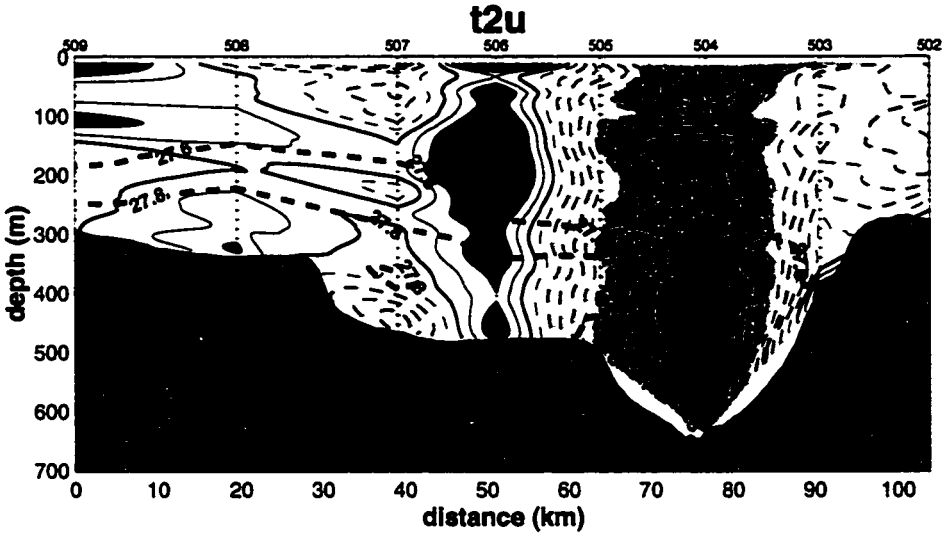

t1d
459
458
457
456
455
454
453
0
200
400
600
800
1000
1200
1400
1600
1800
2000
depth (m)
27.6
27.6
10
20
30
40
50
distance (km)
Greenland
Iceland
-0.9
-0.5
-0.1
0.1
0.5
0.9
Velocity towards 83.1° in m s^{-1}

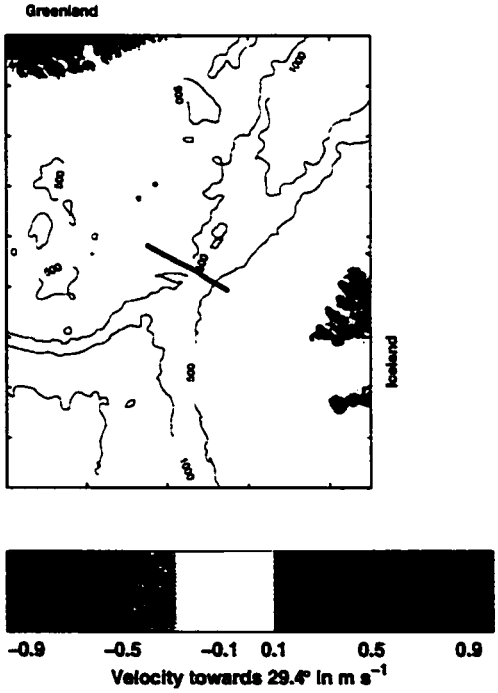

t1u
468
469
470
471
472
473
0
100
200
300
400
500
600
700
depth (m)
27.8
10
20
30
40
50
60
70
distance (km)

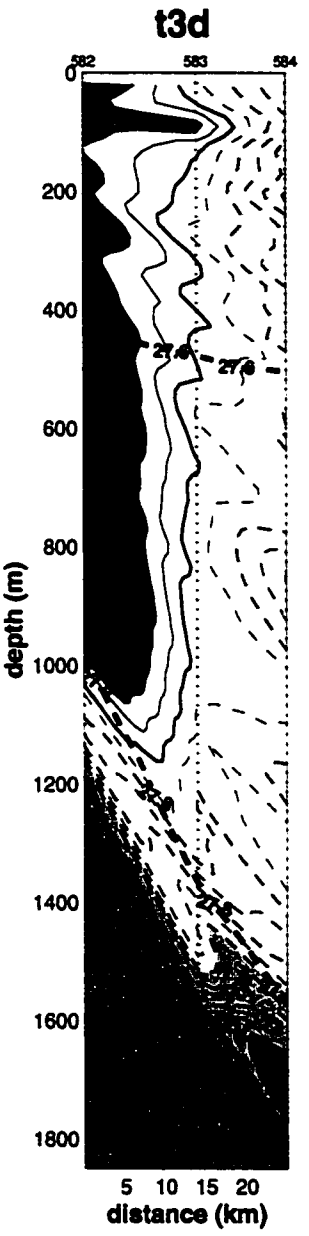

Greenland
Iceland

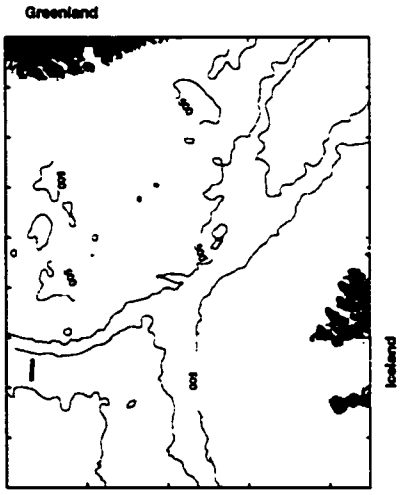
-0.9
-0.5
-0.1
0.1
0.5
0.9
Velocity towards 28.5° in m s^{-1}

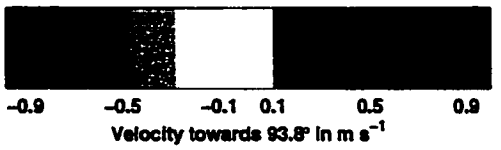

t2d
573
571
570
569
568
567
566
565
0
200
400
600
800
1000
1200
1400
1600
1800
2000
depth (m)
27.6
27.6
27.6
0
10
20
30
40
50
60
70
distance (km)
Greenland
Iceland
−0.9
−0.5
−0.1
0.1
0.5
0.9
Velocity towards 90° in m s^{-1}

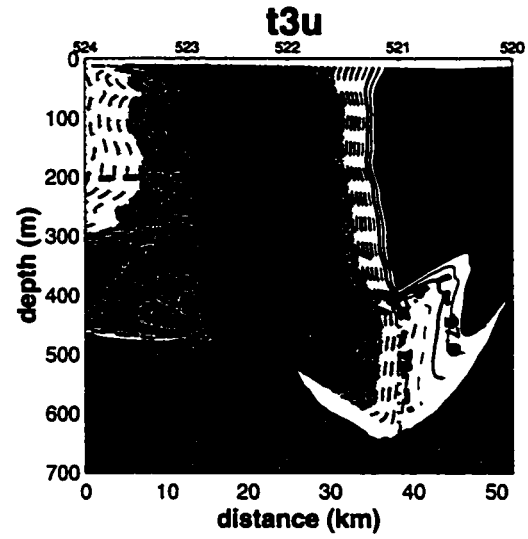

t2u
509
508
507
506
505
504
503
502
0
100
200
300
400
500
600
700
depth (m)
27.6
27.8
0
10
20
30
40
50
60
70
80
90
100
distance (km)

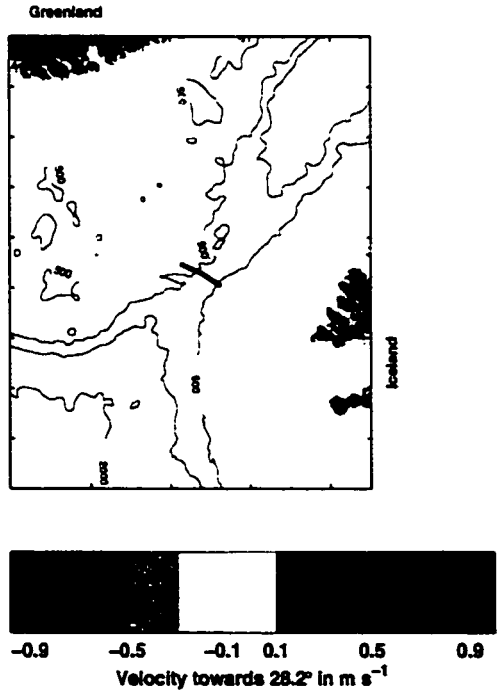

Greenland
Iceland
-0.9
-0.5
-0.1
0.1
0.5
0.9
Velocity towards 29.4° in m s^{-1}

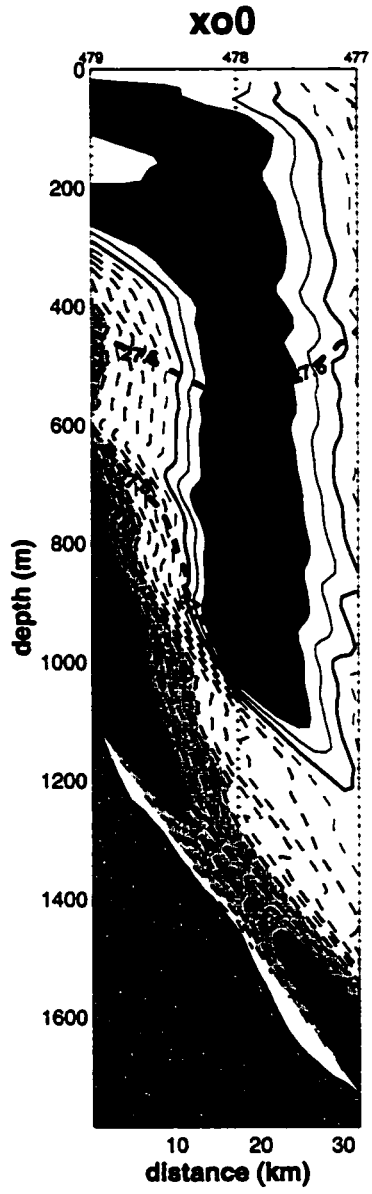

t3d
582
583
584
0
200
400
600
800
1000
1200
1400
1600
1800
depth (m)
5
10
15
20
distance (km)

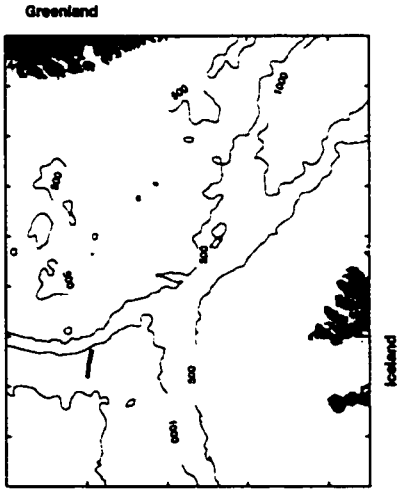

Greenland
Iceland

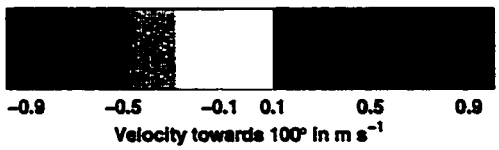

-0.9
-0.5
-0.1
0.1
0.5
0.9
Velocity towards 93.8° in m s^{-1}

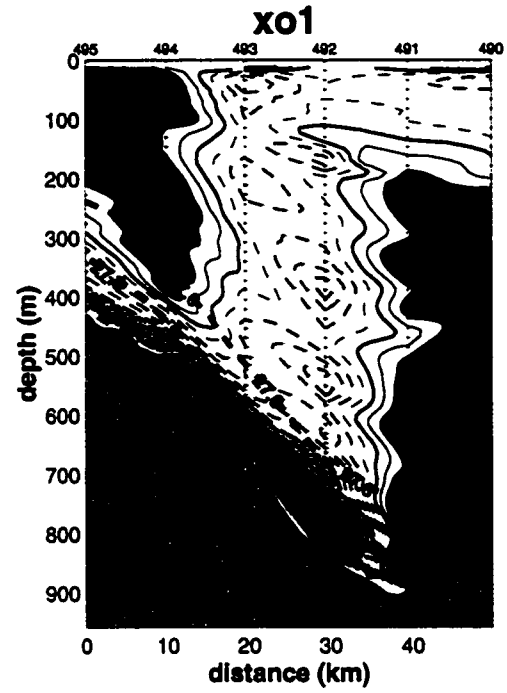

t3u
524
523
522
521
520
0
100
200
300
400
500
600
700
depth (m)
0
10
20
30
40
50
distance (km)

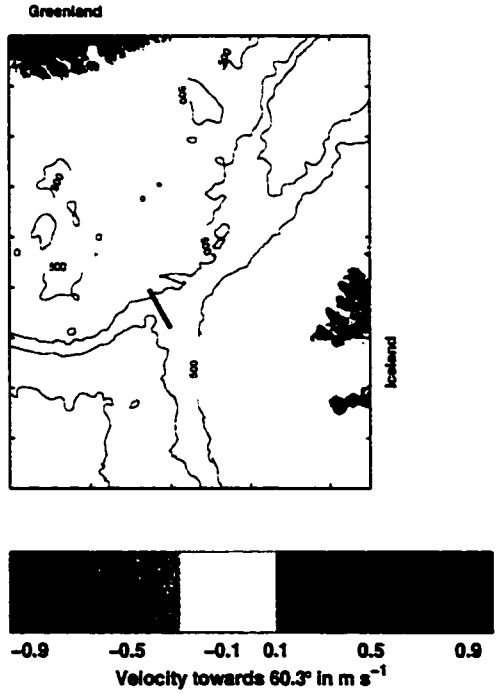

Greenland
Iceland
−0.9
−0.5
−0.1
0.1
0.5
0.9
Velocity towards 28.2° in m s^{-1}

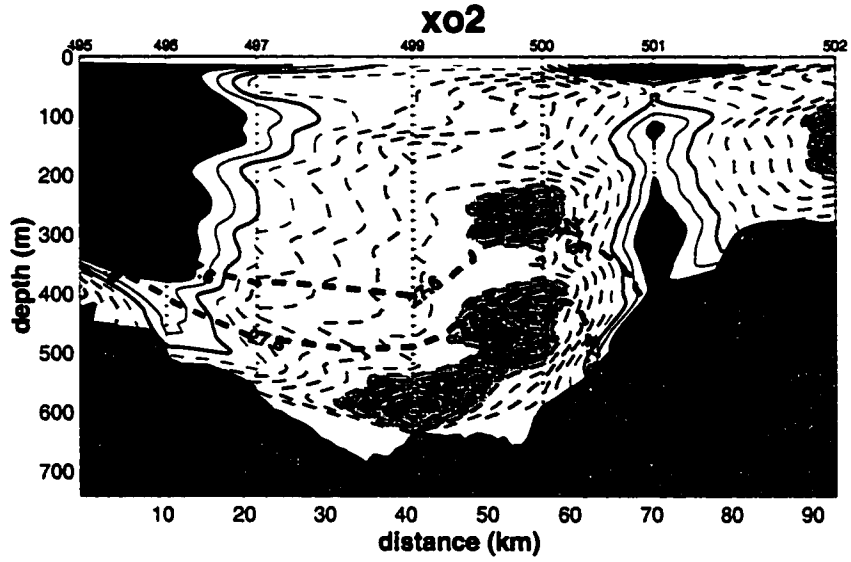

xo0
479
478
477
0
200
400
600
800
1000
1200
1400
1600
depth (m)
10
20
30
distance (km)

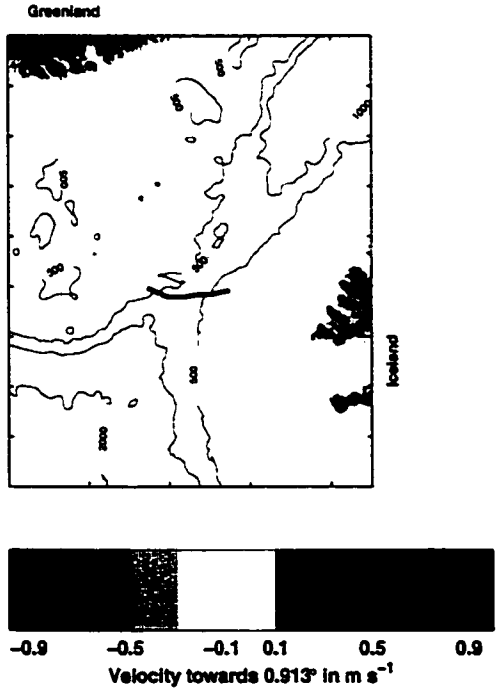

Greenland
Iceland

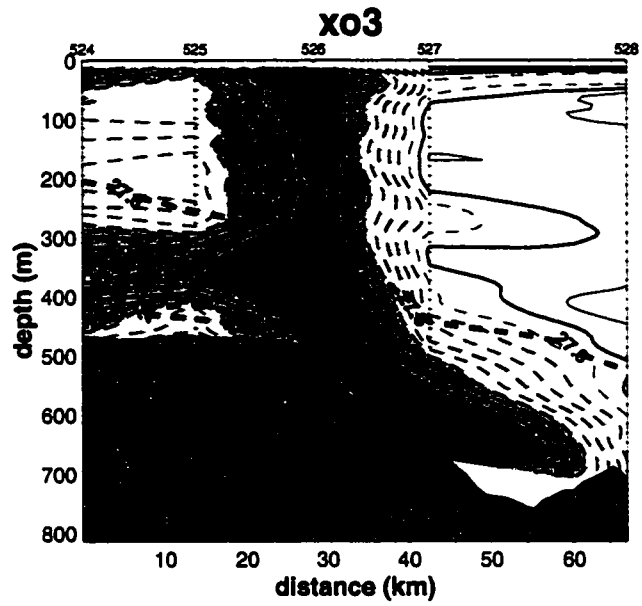

-0.9
-0.5
-0.1
0.1
0.5
0.9
Velocity towards 100° in m s^{-1}

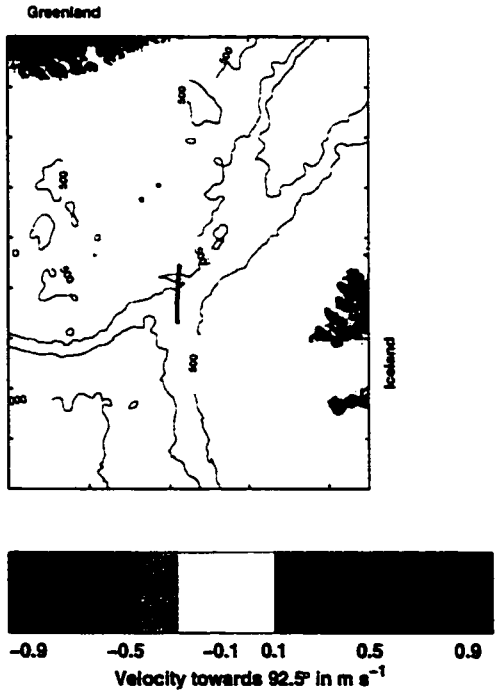

xo1
495
494
493
492
491
490
0
100
200
300
400
500
600
700
800
900
depth (m)
0
10
20
30
40
distance (km)

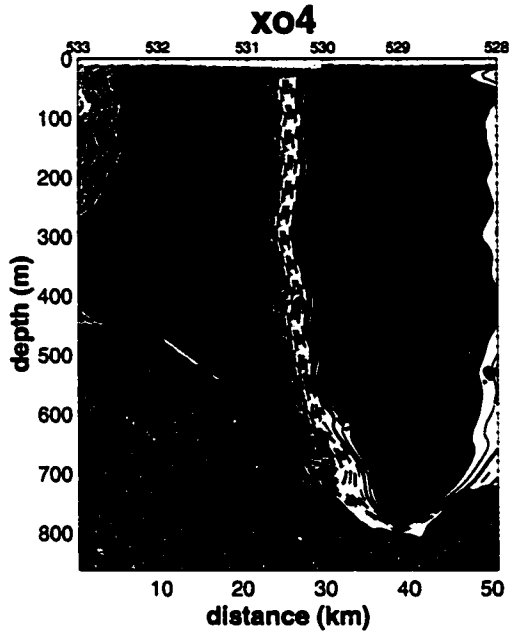

Greenland
Iceland
-0.9
-0.5
-0.1
0.1
0.5
0.9
Velocity towards 60.3° in m s^{-1}

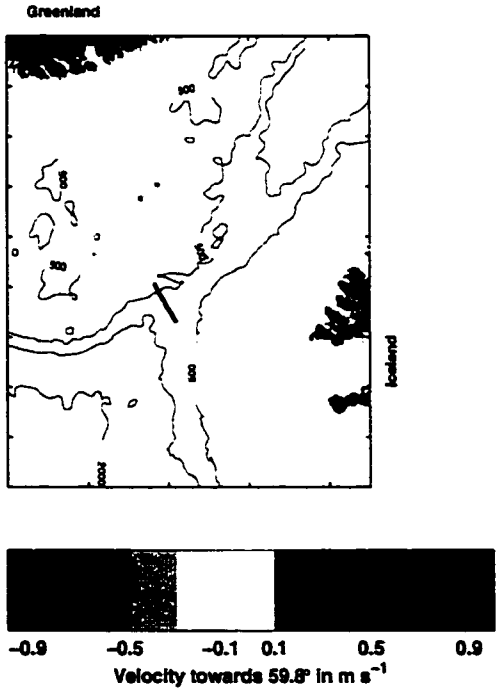

xo2
495
496
497
499
500
501
502
0
100
200
300
400
500
600
700
depth (m)
10
20
30
40
50
60
70
80
90
distance (km)

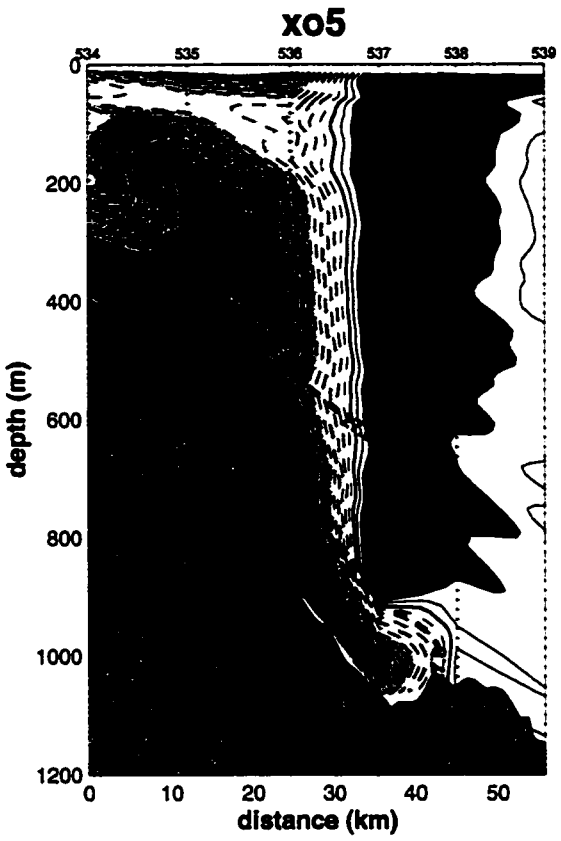

Greenland
Iceland
-0.9
-0.5
-0.1
0.1
0.5
0.9
Velocity towards 0.913° in m s^{-1}

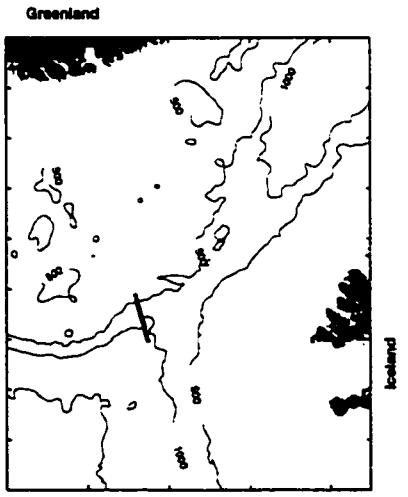

xo3
524
525
526
527
528
0
100
200
300
400
500
600
700
800
depth (m)
10
20
30
40
50
60
distance (km)

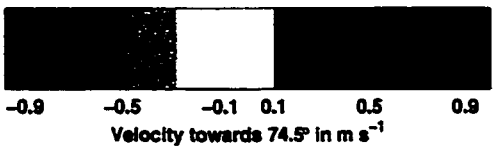

Greenland
Iceland
−0.9
−0.5
−0.1
0.1
0.5
0.9
Velocity towards 92.5° in m s⁻¹

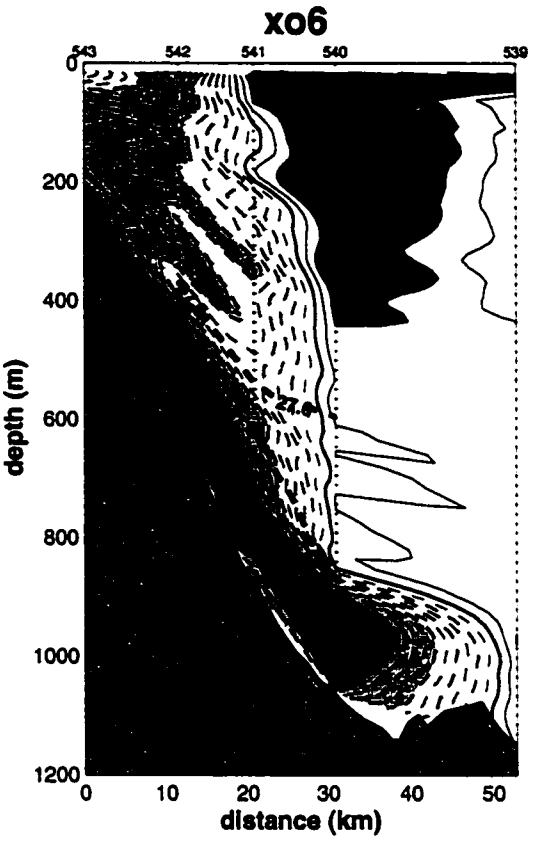

xo4
533
532
531
530
529
528
0
100
200
300
400
500
600
700
800
depth (m)
10
20
30
40
50
distance (km)

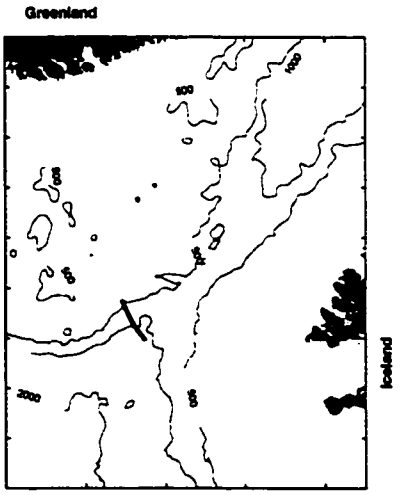

Greenland
Iceland
-0.9
-0.5
-0.1
0.1
0.5
0.9
Velocity towards 59.8° in m s^{-1}

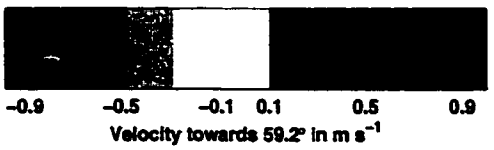

xo5
534
535
536
537
538
539
0
200
400
600
800
1000
1200
depth (m)
0
10
20
30
40
50
distance (km)

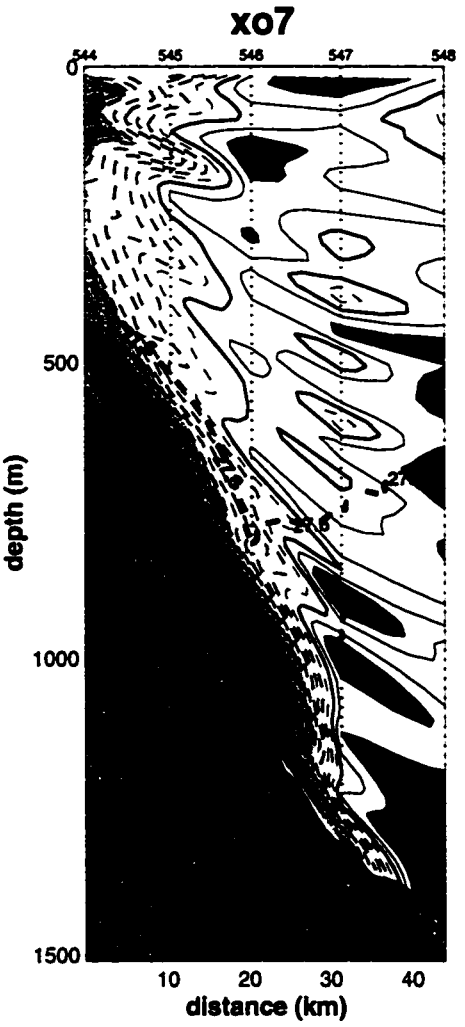

Greenland
Iceland

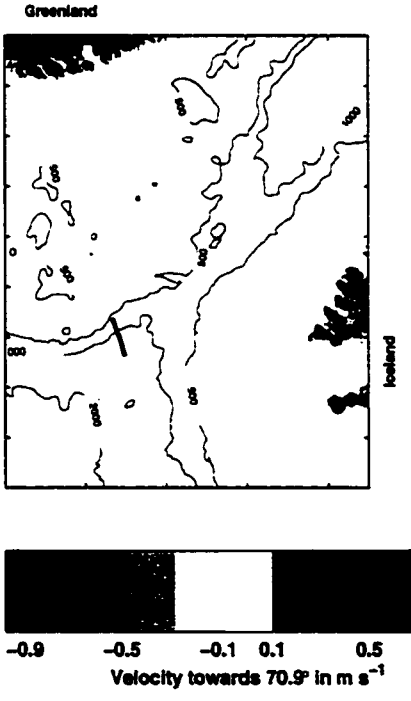

-0.9
-0.5
-0.1
0.1
0.5
0.9
Velocity towards 74.5° in m s-1

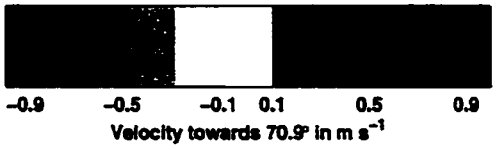

XO6
543
542
541
540
539
0
200
400
600
800
1000
1200
depth (m)
0
10
20
30
40
50
distance (km)

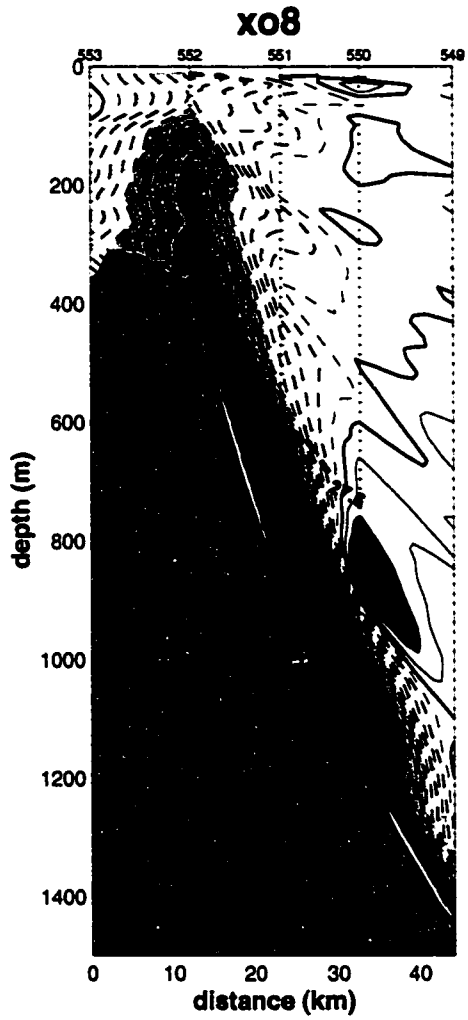

Greenland
Iceland

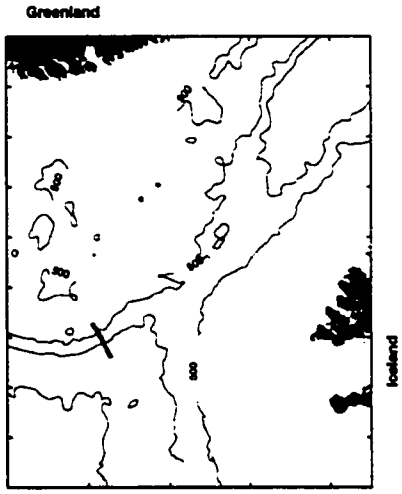

−0.9
−0.5
−0.1
0.1
0.5
0.9
Velocity towards 59.2° in m s⁻¹

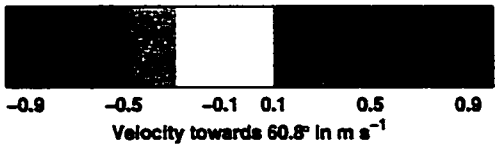

xo7
544
545
546
547
548
0
500
1000
1500
depth (m)
10
20
30
40
distance (km)

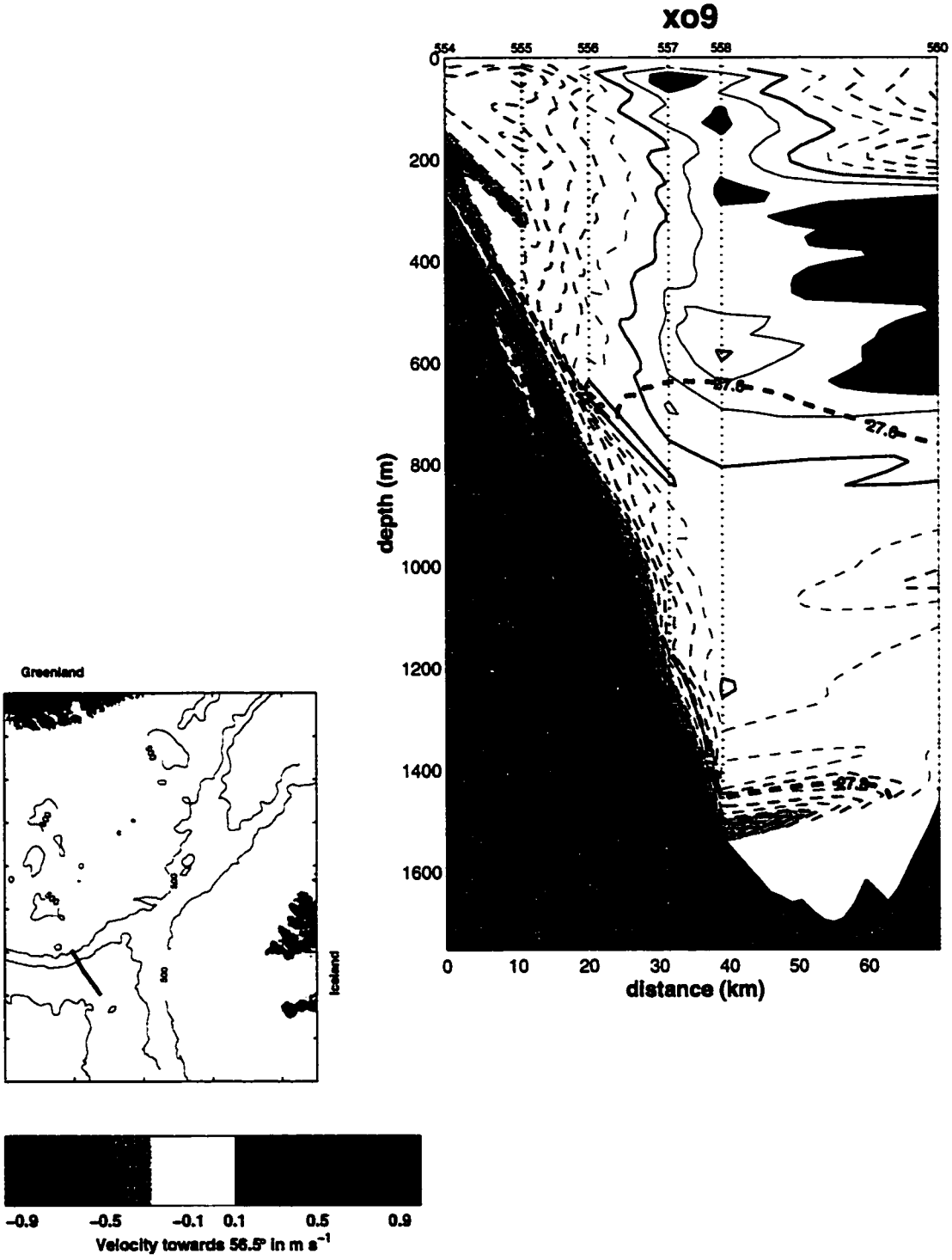

Greenland
Iceland

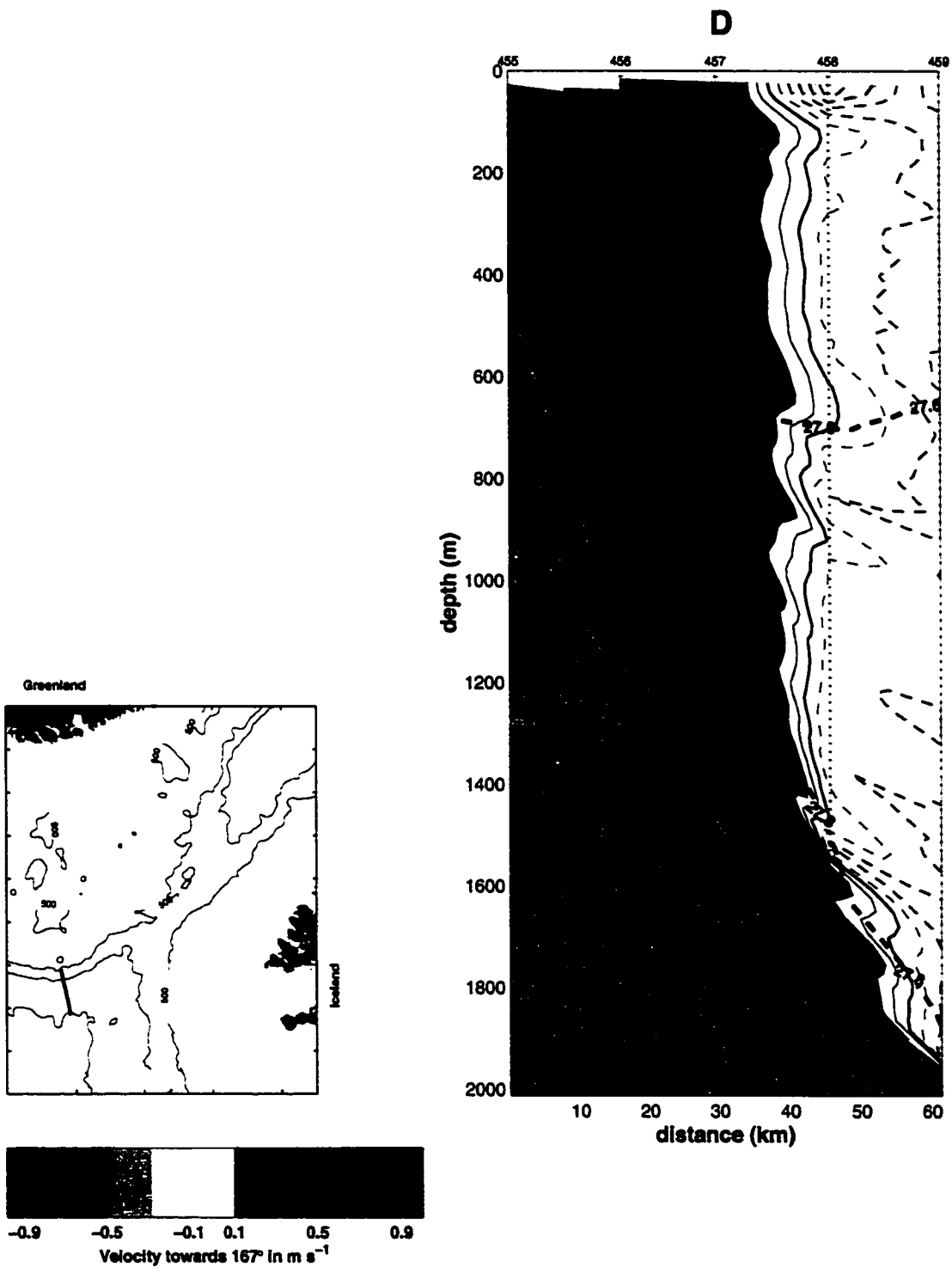

-0.9
-0.5
-0.1
0.1
0.5
0.9
Velocity towards 70.9° in m s-1

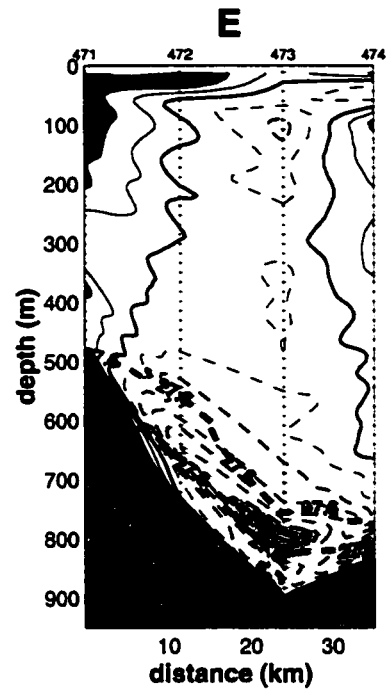

xo8
553
552
551
550
549
0
200
400
600
800
1000
1200
1400
depth (m)
0
10
20
30
40
distance (km)

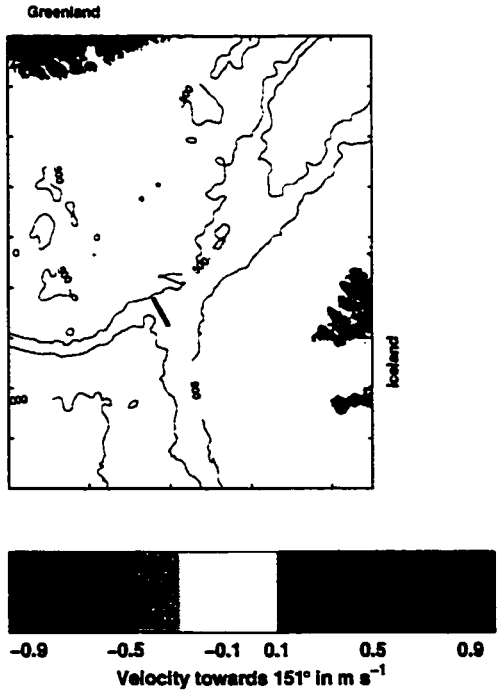

Greenland
Iceland

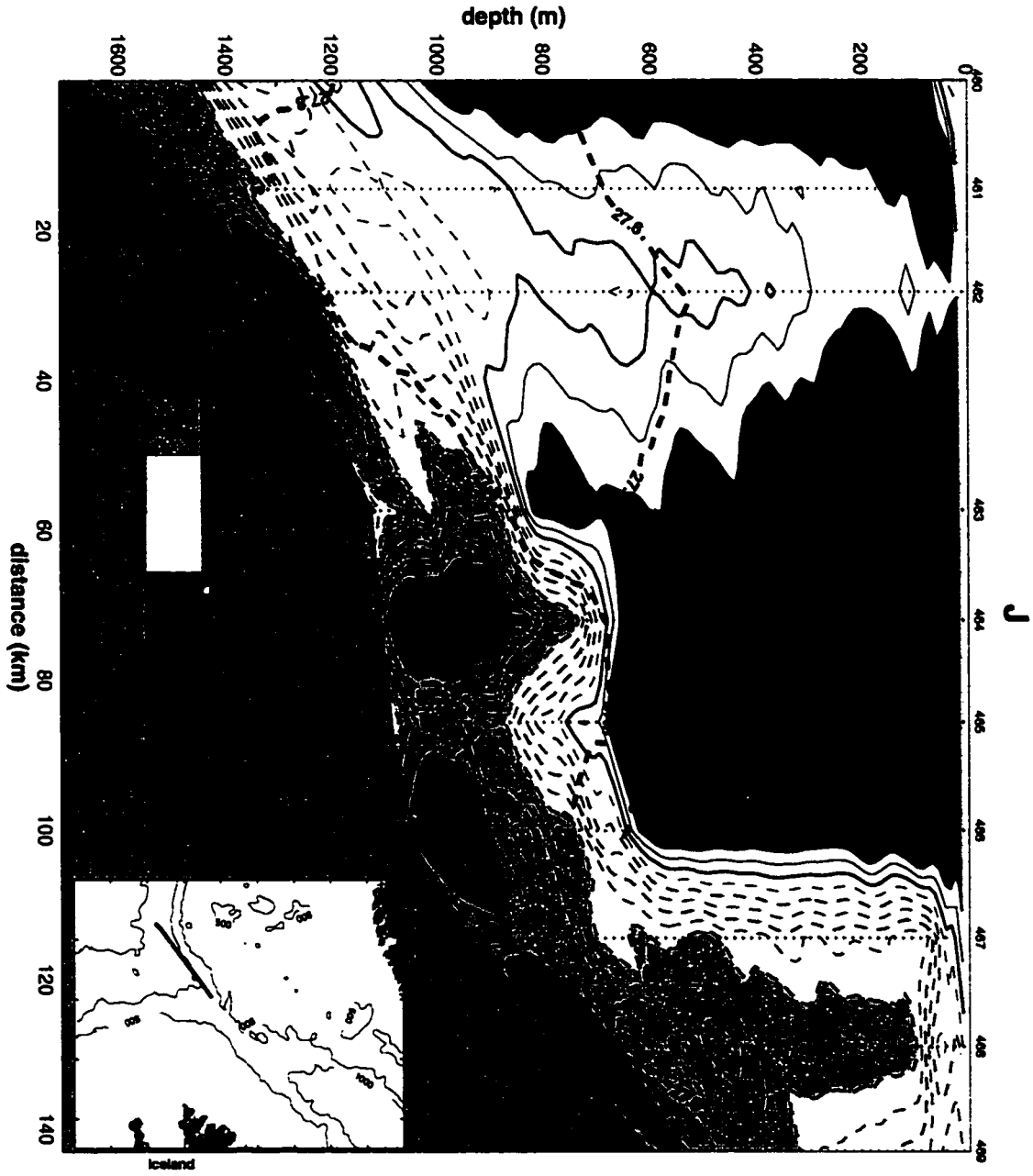

-0.9
-0.5
-0.1
0.1
0.5
0.9
Velocity towards 60.8° in m s^{-1}

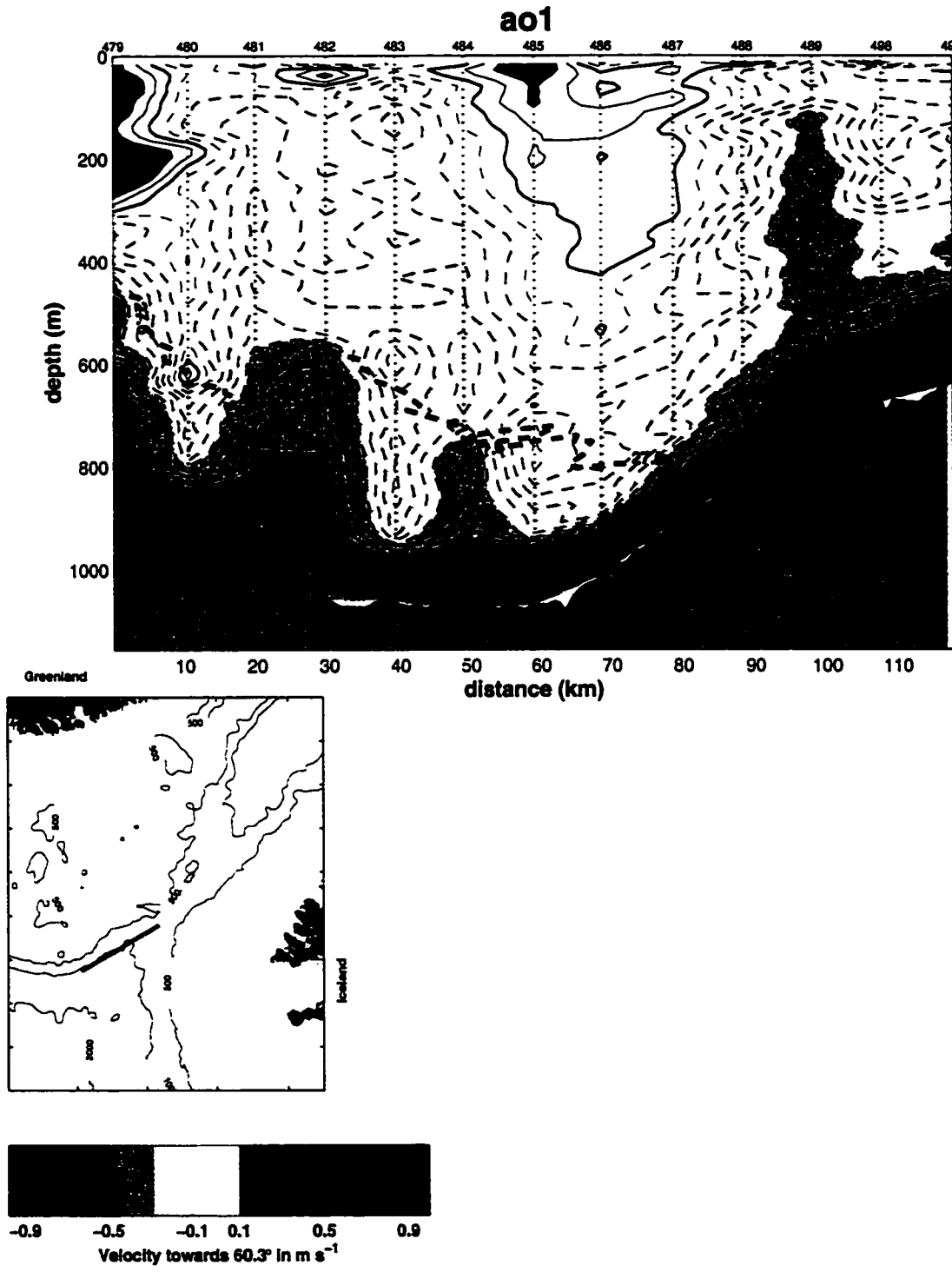

xo9
554
555
556
557
558
560
0
200
400
600
800
1000
1200
1400
1600
depth (m)
27.6
27.6
27.6
0
10
20
30
40
50
60
distance (km)
Greenland
Iceland
-0.9
-0.5
-0.1
0.1
0.5
0.9
Velocity towards 56.5° in m s-1

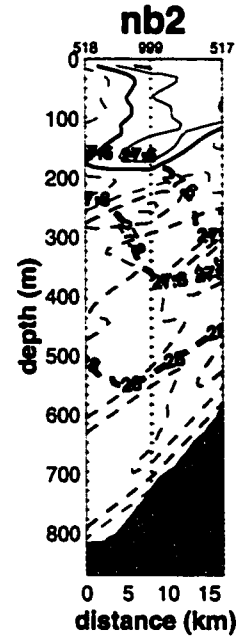

D
455
456
457
458
459
0
200
400
600
800
1000
1200
1400
1600
1800
2000
depth (m)
10
20
30
40
50
60
distance (km)
27.6
27.8
Greenland
Iceland
-0.9
-0.5
-0.1
0.1
0.5
0.9
Velocity towards 167° in m s^{-1}

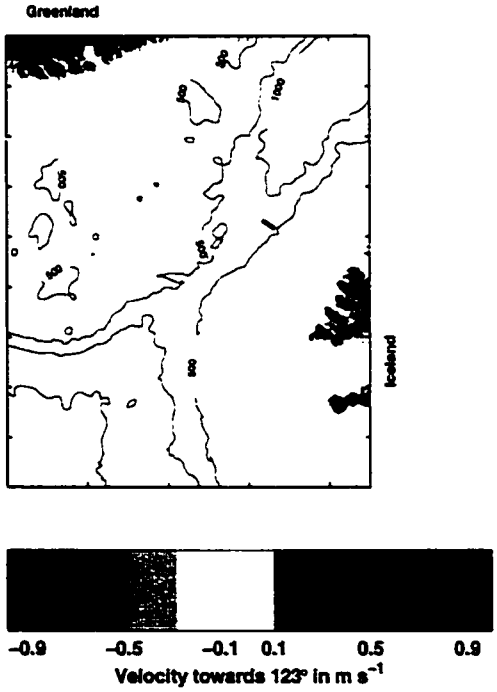

E
471
472
473
474
0
100
200
300
400
500
600
700
800
900
depth (m)
10
20
30
distance (km)

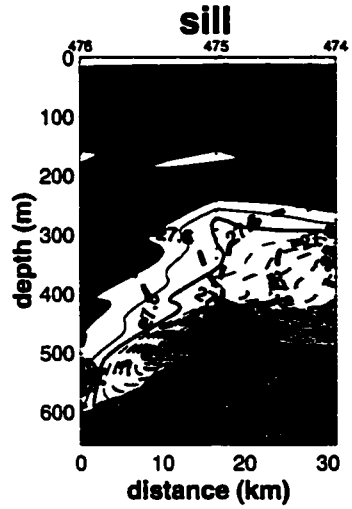

Greenland
Iceland
-0.9
-0.5
-0.1
0.1
0.5
0.9
Velocity towards 151° in m s^{-1}

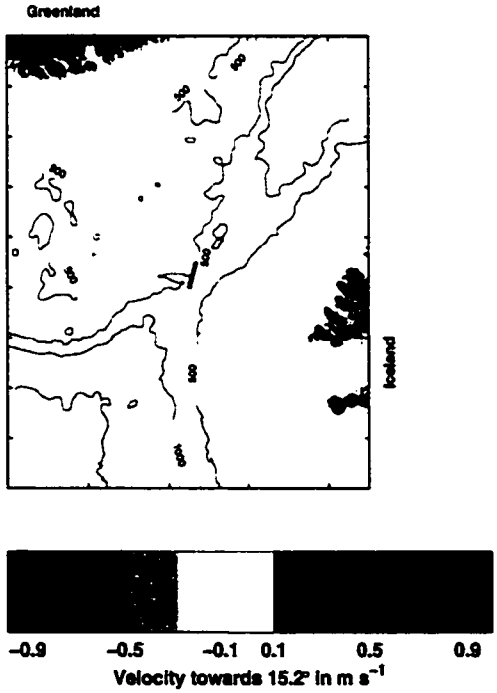

depth (m)
1600
1400
1200
1000
800
600
400
200
0
distance (km)
20
40
60
80
100
120
140
27.8
27.8
Iceland
J

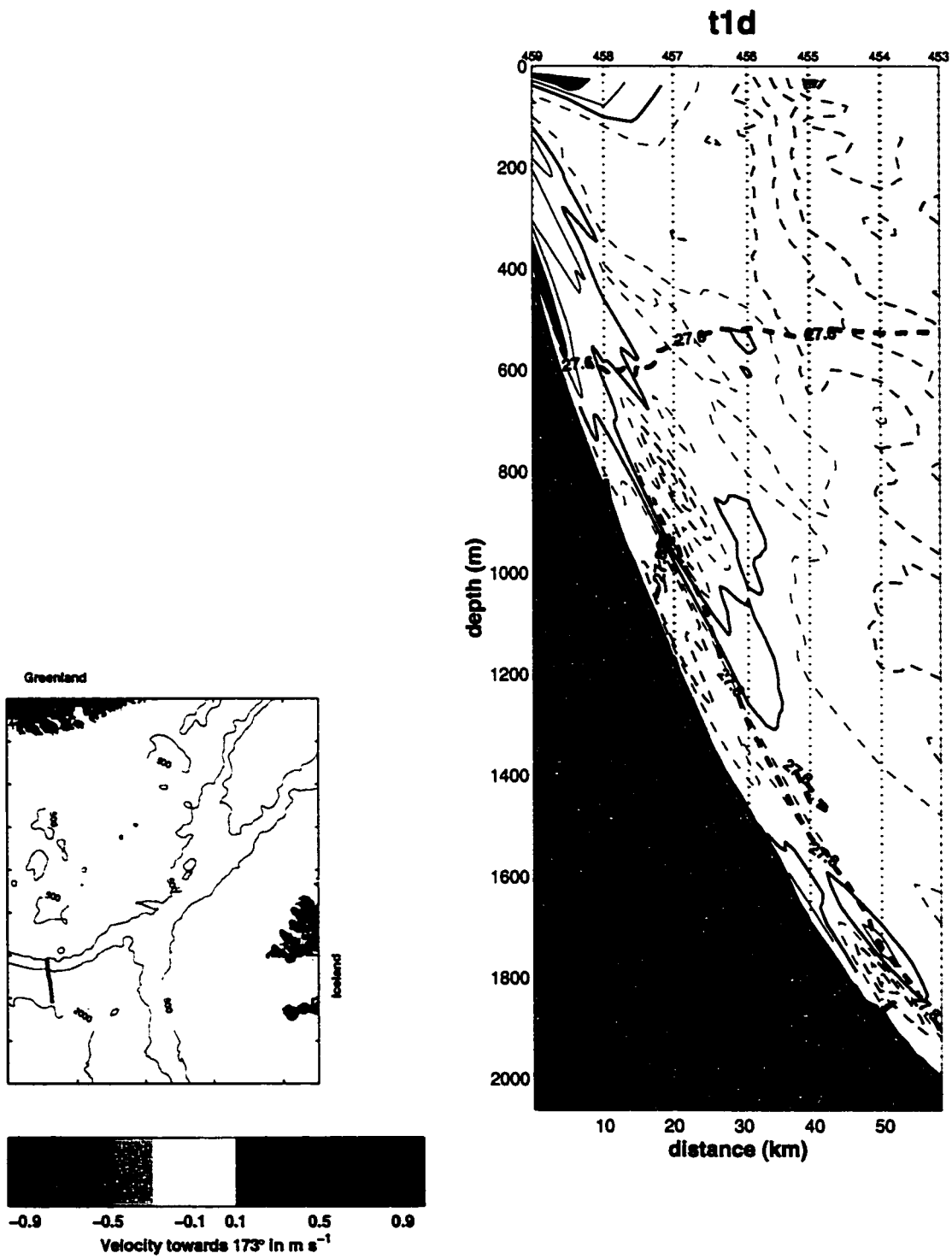

ao1
depth (m)
distance (km)
Greenland
Iceland
-0.9
-0.5
-0.1
0.1
0.5
0.9
Velocity towards 60.3° in m s⁻¹

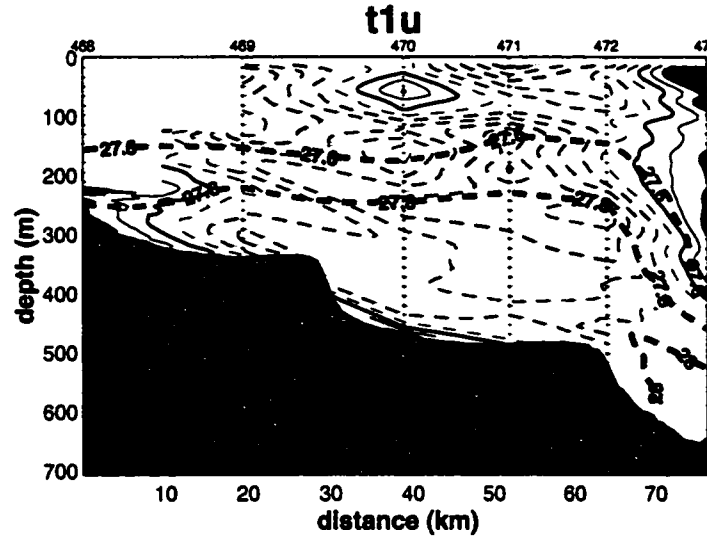

nb2
518
999
517
0
100
200
300
400
500
600
700
800
depth (m)
0 5 10 15
distance (km)

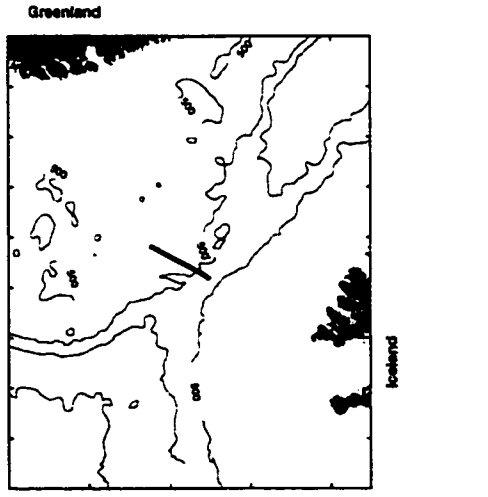

Greenland
Iceland
-0.9 -0.5 -0.1 0.1 0.5 0.9
Velocity towards 123° in m s^{-1}

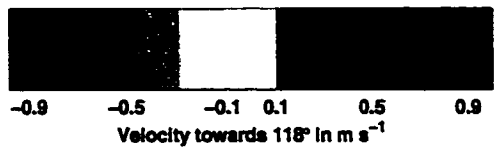

sill
476
475
474
0
100
200
300
400
500
600
depth (m)
0
10
20
30
distance (km)

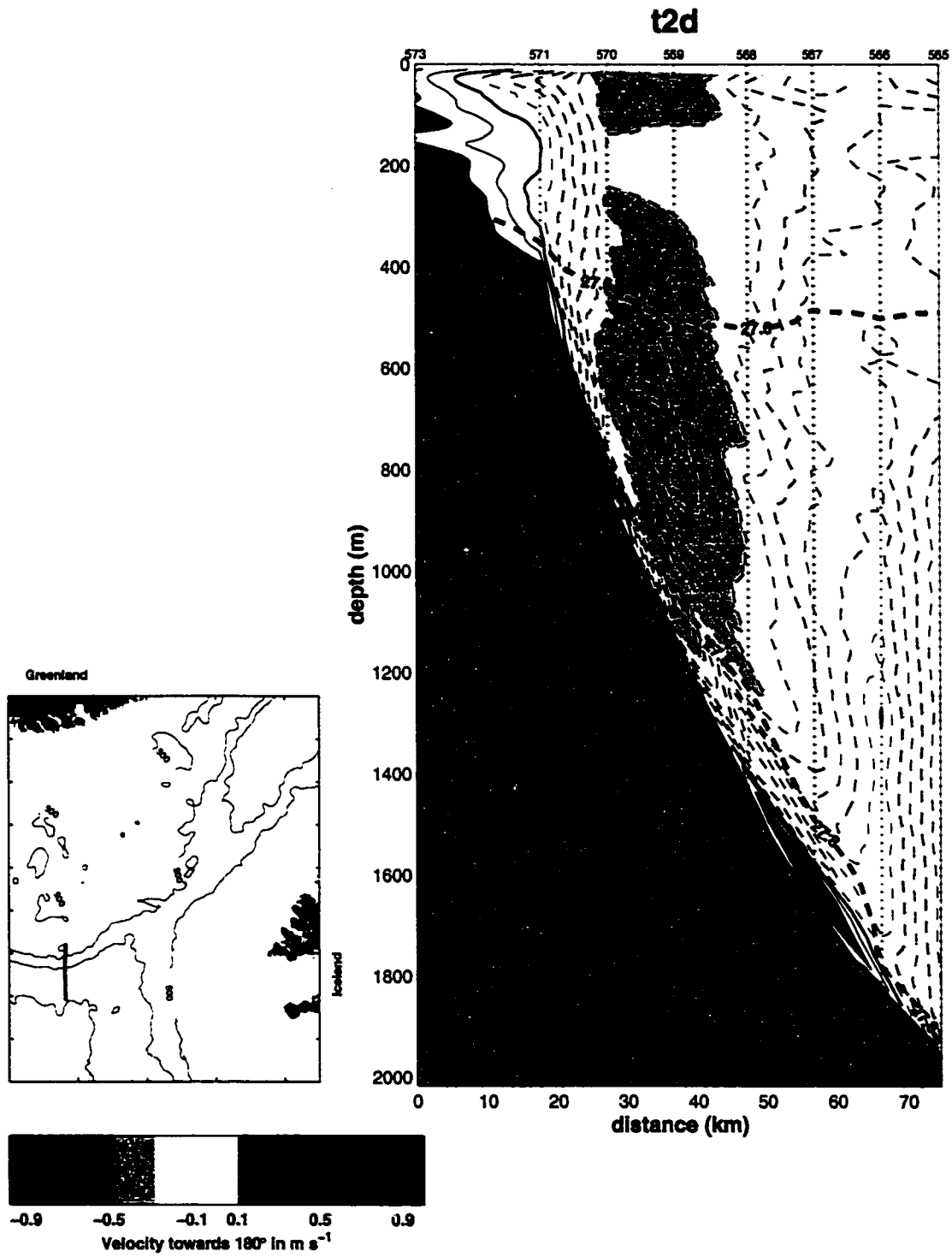

Greenland
Iceland
-0.9
-0.5
-0.1
0.1
0.5
0.9
Velocity towards 15.2° in m s^{-1}

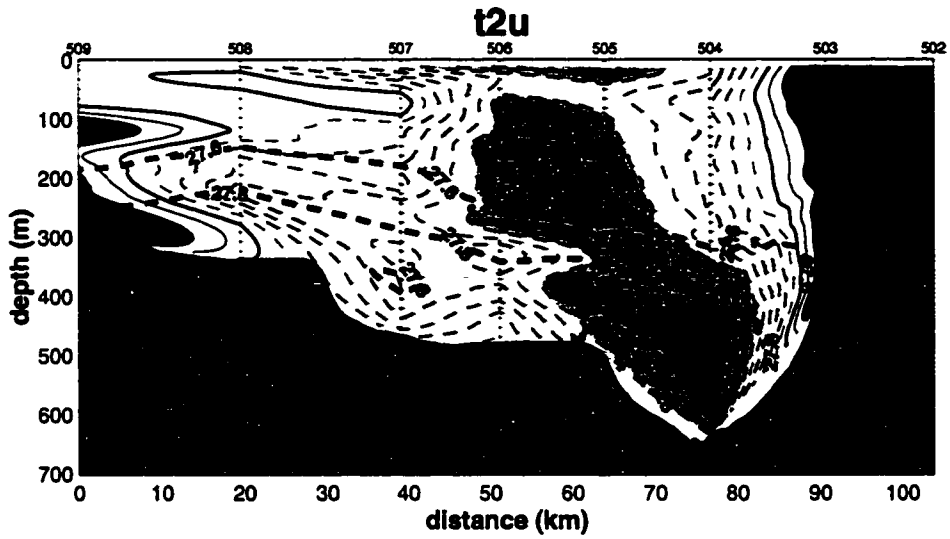

t1d
459
458
457
456
455
454
453
0
200
400
600
800
1000
1200
1400
1600
1800
2000
depth (m)
27.6
27.5
10
20
30
40
50
distance (km)
Greenland
Iceland
−0.9
−0.5
−0.1
0.1
0.5
0.9
Velocity towards 173° in m s^{-1}

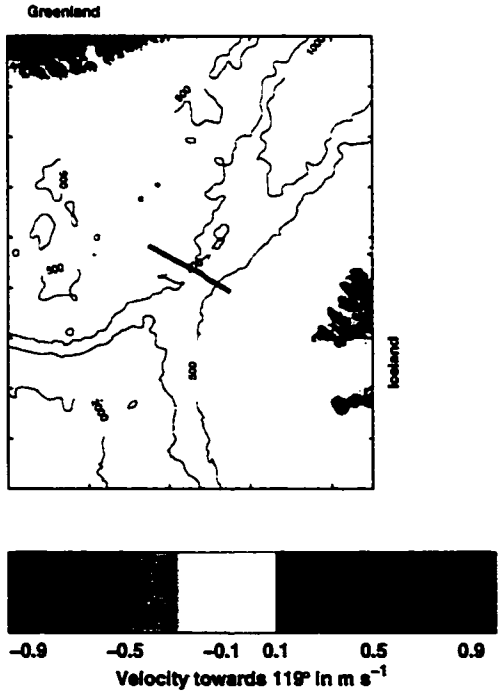

t1u
468
469
470
471
472
473
0
100
200
300
400
500
600
700
depth (m)
27.8
27.6
27.4
27.2
10
20
30
40
50
60
70
distance (km)

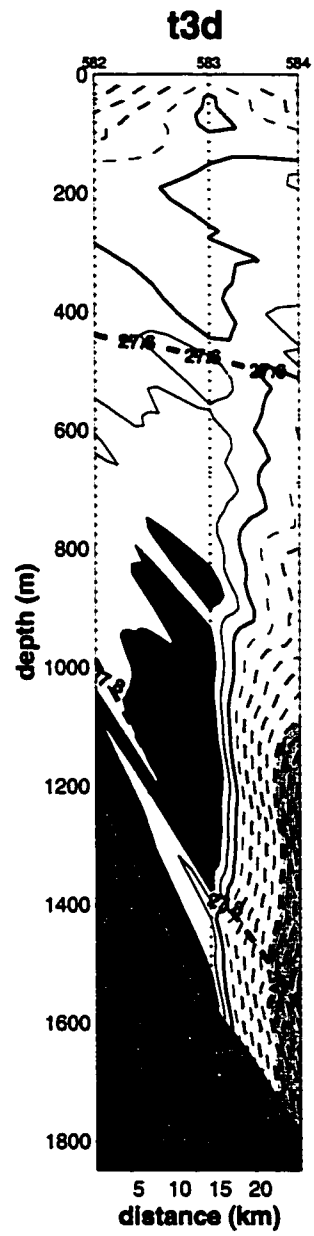

Greenland
Iceland

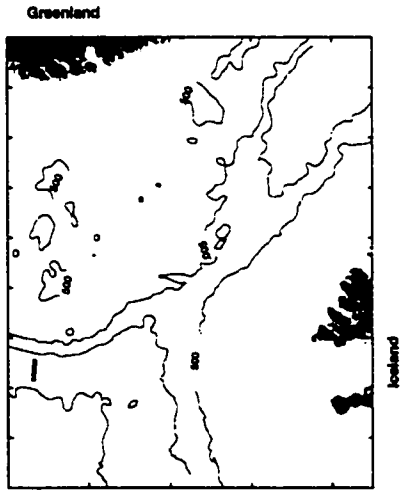

-0.9
-0.5
-0.1
0.1
0.5
0.9
Velocity towards 118° in m s^{-1}

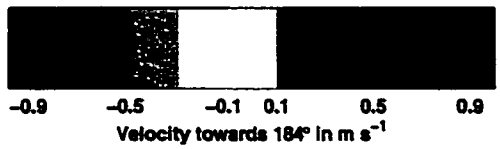

t2d
573
571
570
569
568
567
566
565
0
200
400
600
800
1000
1200
1400
1600
1800
2000
depth (m)
0
10
20
30
40
50
60
70
distance (km)
Greenland
Iceland
-0.9
-0.5
-0.1
0.1
0.5
0.9
Velocity towards 180° in m s-1

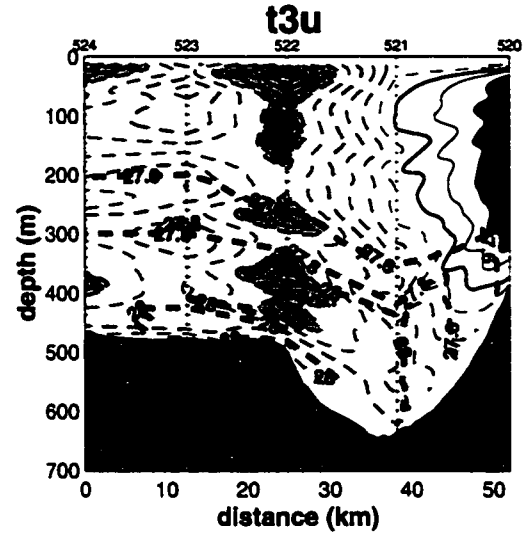

t2u
509
508
507
506
505
504
503
502
0
100
200
300
400
500
600
700
depth (m)
27.8
27.9
0
10
20
30
40
50
60
70
80
90
100
distance (km)

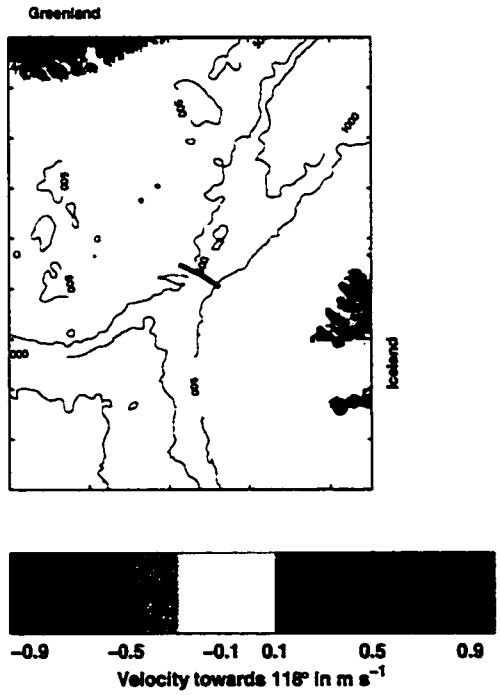

Greenland
Iceland
-0.9
-0.5
-0.1
0.1
0.5
0.9
Velocity towards 119° in m s^{-1}

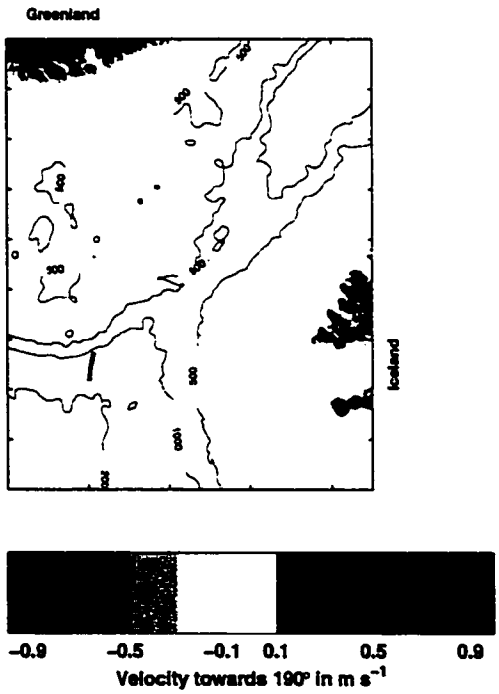

t3d
582
583
584
0
200
400
600
800
1000
1200
1400
1600
1800
depth (m)
5
10
15
20
distance (km)

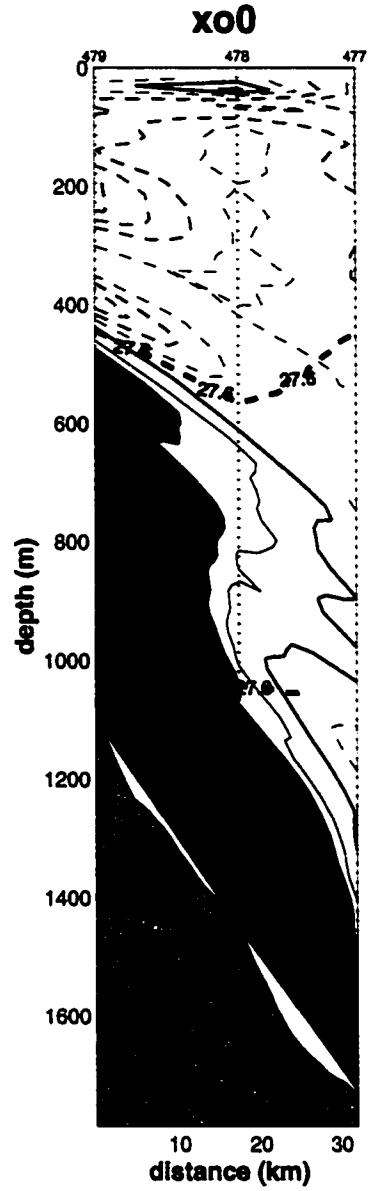

Greenland
Iceland

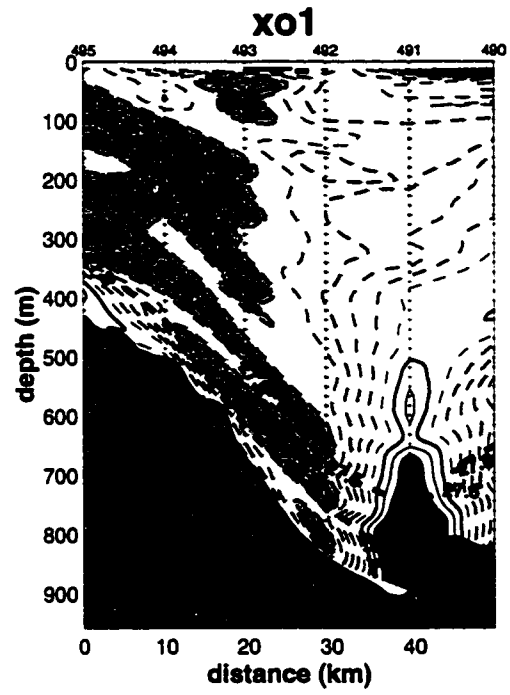

-0.9
-0.5
-0.1
0.1
0.5
0.9
Velocity towards 184° in m s-1

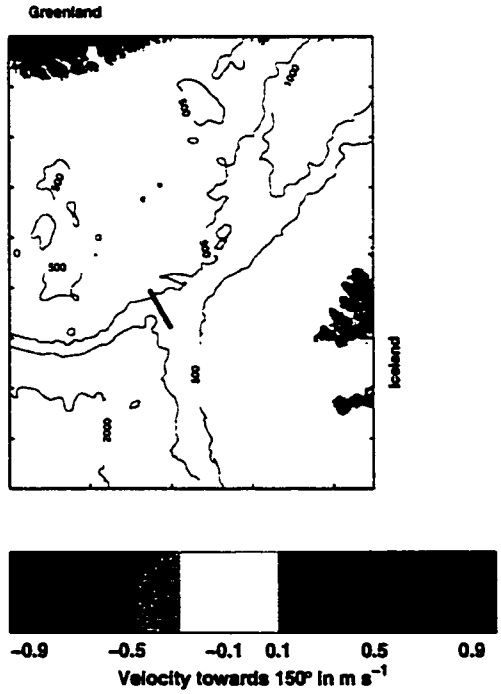

t3u
524
523
522
521
520
0
100
200
300
400
500
600
700
depth (m)
0
10
20
30
40
50
distance (km)

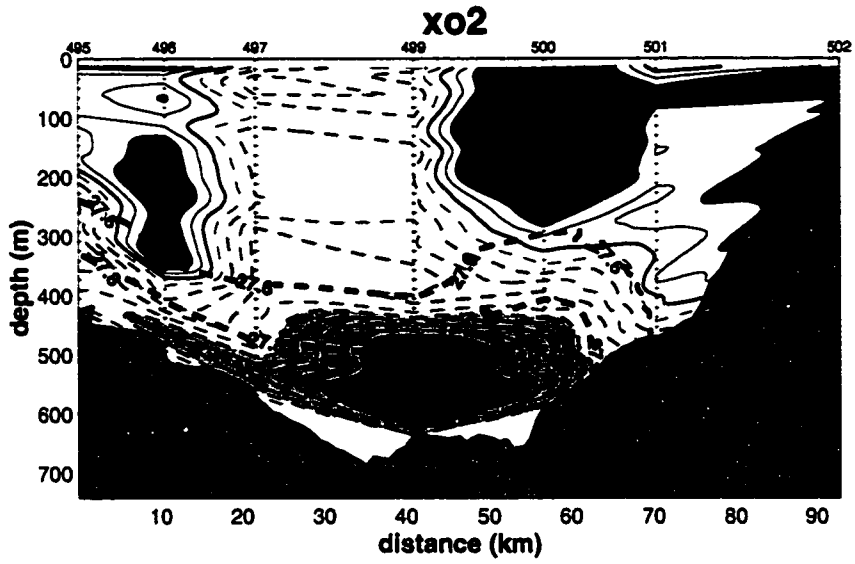

Greenland
Iceland
−0.9
−0.5
−0.1
0.1
0.5
0.9
Velocity towards 116° in m s^{-1}

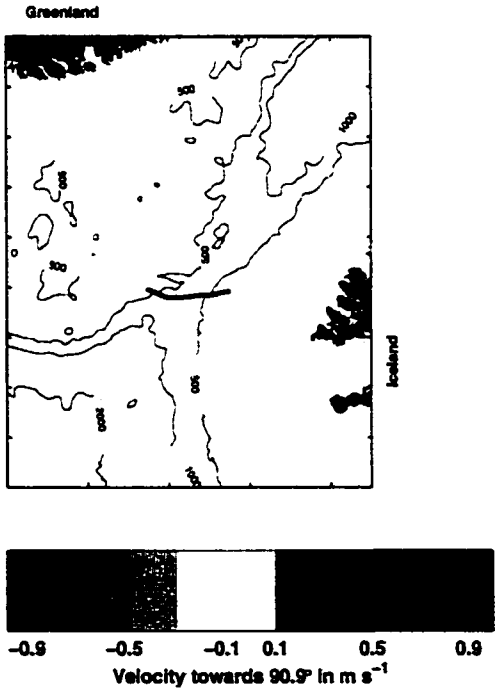

Greenland
Iceland
-0.9
-0.5
-0.1
0.1
0.5
0.9
Velocity towards 190° in m s^{-1}


xo0
479
478
477
0
200
400
600
800
1000
1200
1400
1600
depth (m)
27.6
27.6
27.6
10
20
30
distance (km)

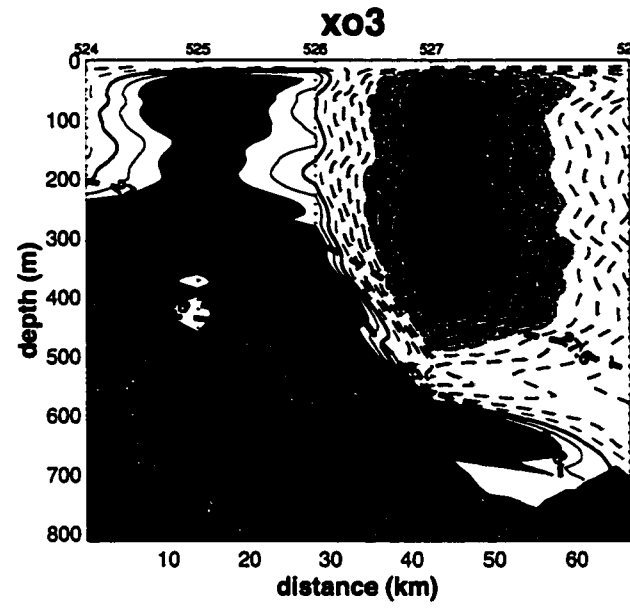

xo1
495
494
493
492
491
490
0
100
200
300
400
500
600
700
800
900
depth (m)
0
10
20
30
40
distance (km)

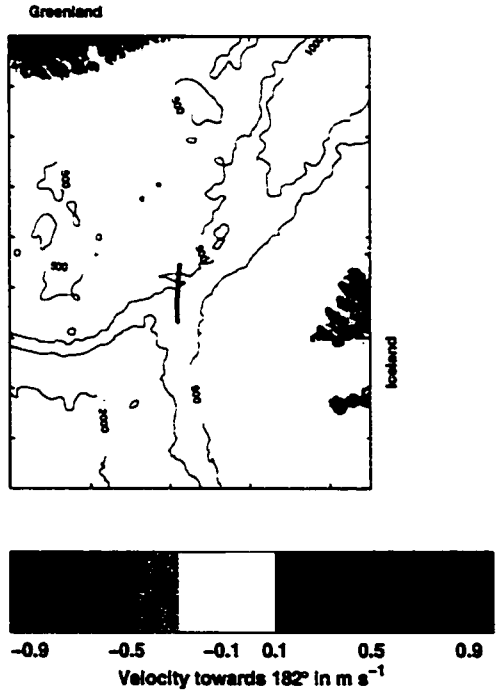

Greenland
Iceland
-0.9
-0.5
-0.1
0.1
0.5
0.9
Velocity towards 150° in m s-1

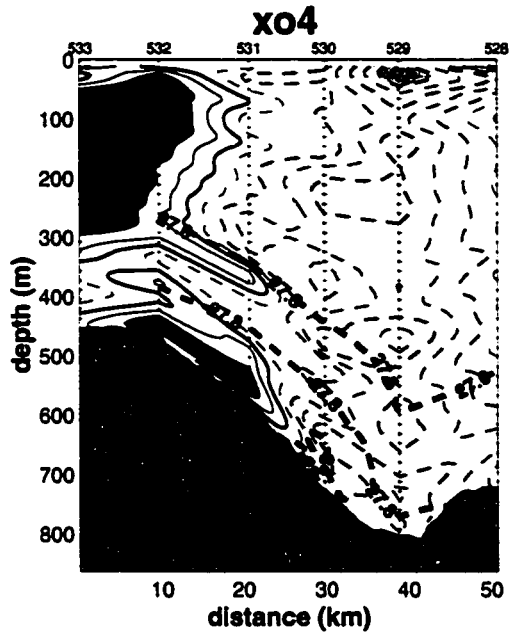

xo2
495
496
497
499
500
501
502
0
100
200
300
400
500
600
700
depth (m)
10
20
30
40
50
60
70
80
90
distance (km)

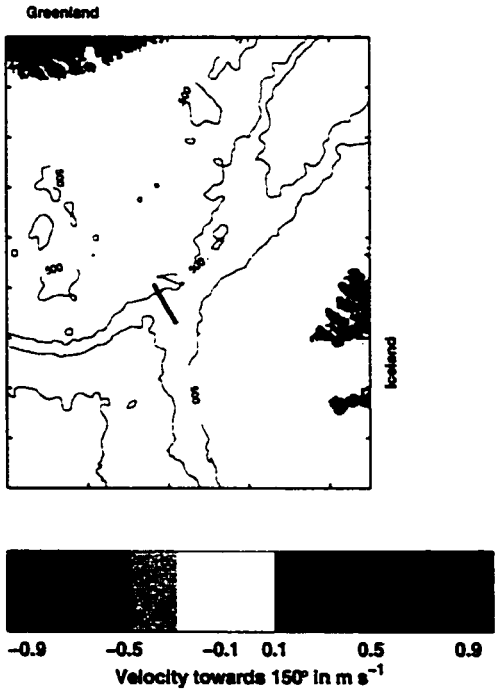

Greenland
Iceland

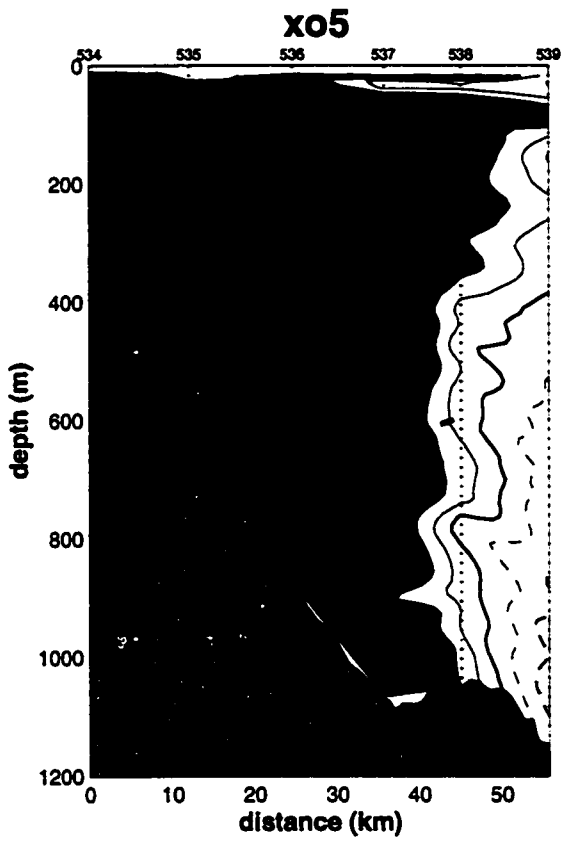
-0.9
-0.5
-0.1
0.1
0.5
0.9
Velocity towards 90.9° in m s-1

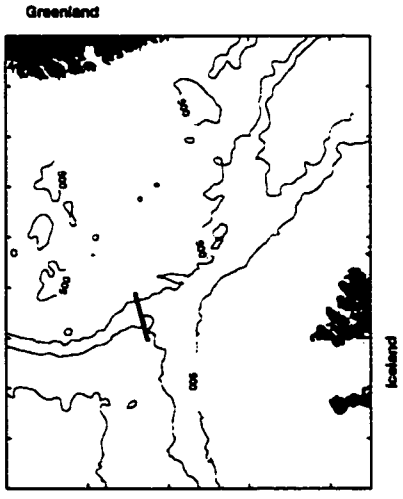

xo3
524
525
526
527
528
0
100
200
300
400
500
600
700
800
depth (m)
10
20
30
40
50
60
distance (km)

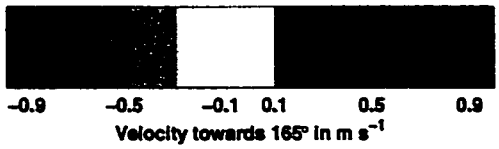

Greenland
Iceland
-0.9
-0.5
-0.1
0.1
0.5
0.9
Velocity towards 182° in m s^{-1}

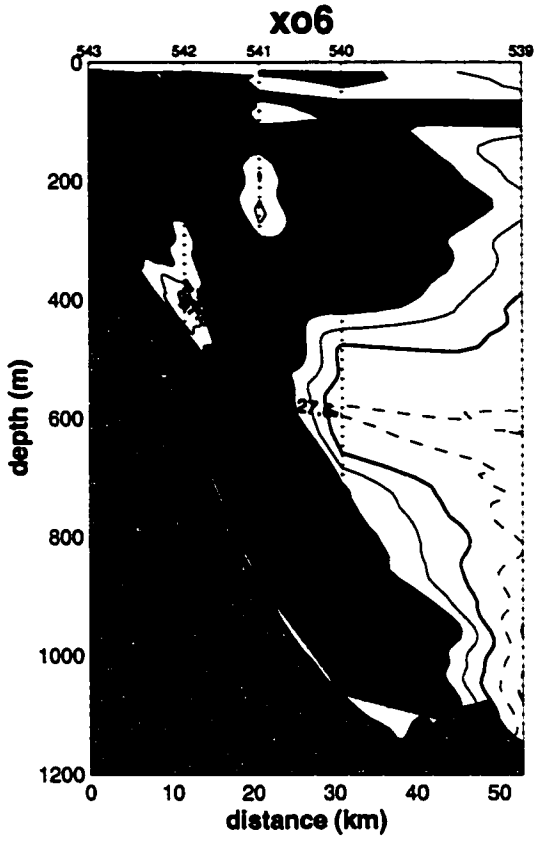

XO4
533
532
531
530
529
528
0
100
200
300
400
500
600
700
800
depth (m)
10
20
30
40
50
distance (km)

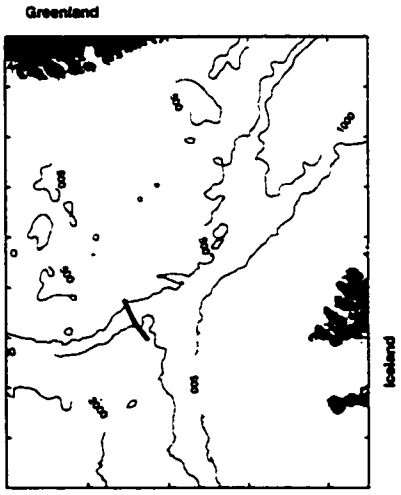

Greenland
Iceland
-0.9
-0.5
-0.1
0.1
0.5
0.9
Velocity towards 150° in m s^{-1}

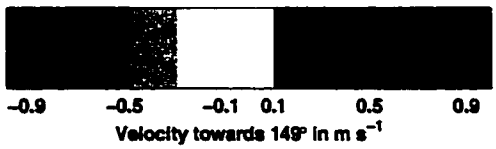

xo5
534
535
536
537
538
539
0
200
400
600
800
1000
1200
depth (m)
0
10
20
30
40
50
distance (km)

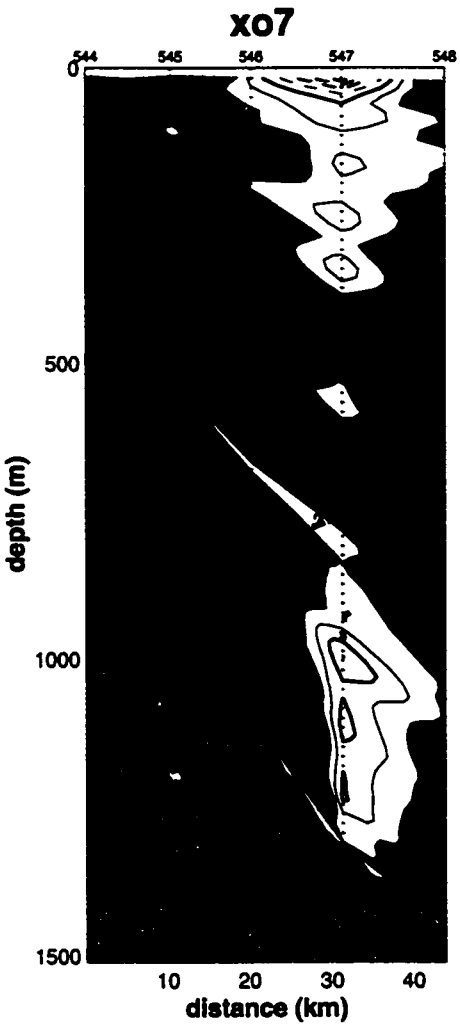

Greenland
Iceland

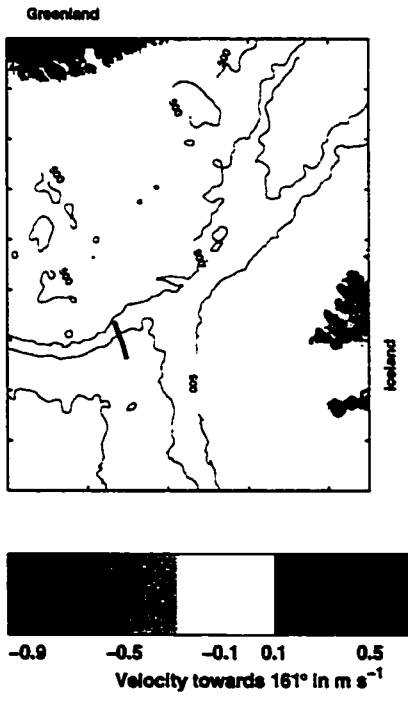

-0.9
-0.5
-0.1
0.1
0.5
0.9
Velocity towards 165° in m s-1

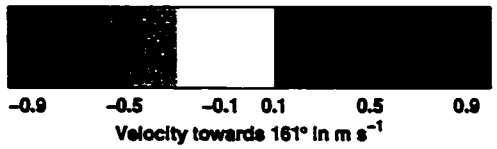

xo6
543
542
541
540
539
0
200
400
600
800
1000
1200
depth (m)
27.4
0
10
20
30
40
50
distance (km)

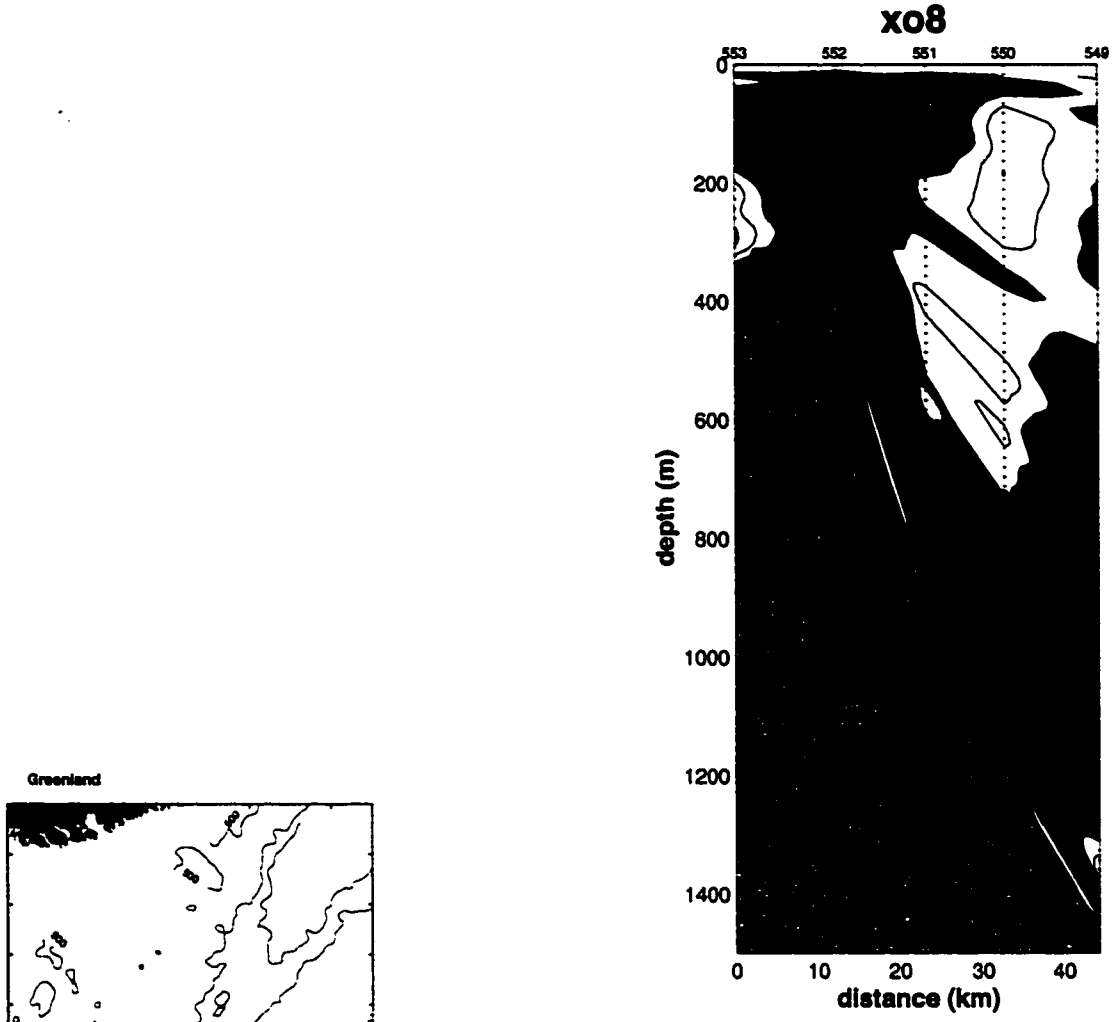

Greenland
Iceland

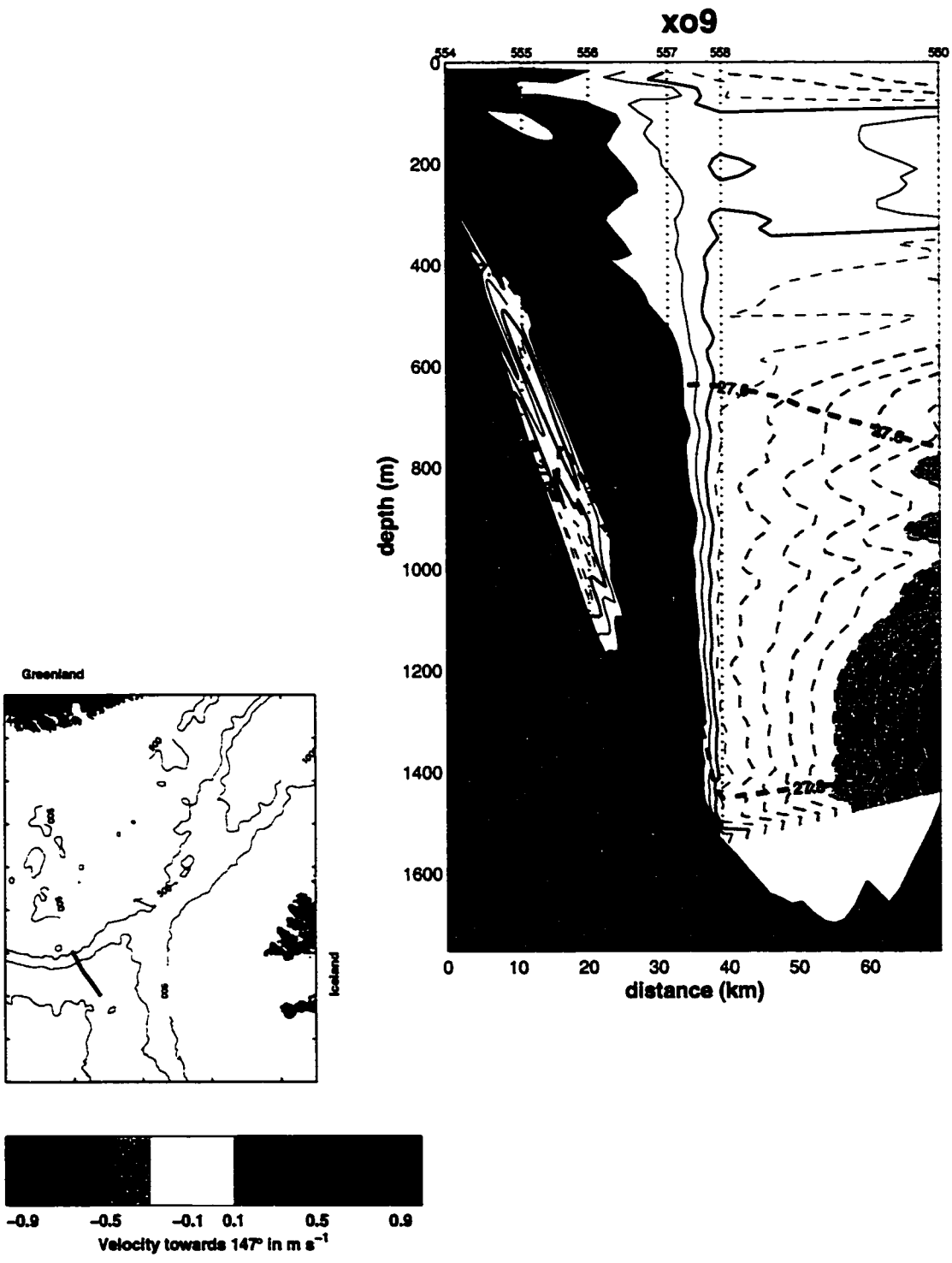

-0.9
-0.5
-0.1
0.1
0.5
0.9
Velocity towards 149° in m s⁻¹


xo7
544
545
546
547
548
0
500
1000
1500
depth (m)
10
20
30
40
distance (km)


Greenland
Iceland


-0.9
-0.5
-0.1
0.1
0.5
0.9
Velocity towards 161° in m s^{-1}


xo8
553
552
551
550
549
0
200
400
600
800
1000
1200
1400
depth (m)
0
10
20
30
40
distance (km)
Greenland
Iceland
-0.9
-0.5
-0.1
0.1
0.5
0.9
Velocity towards 151° in m s-1


xo9
554
555
556
557
558
560
0
200
400
600
800
1000
1200
1400
1600
depth (m)
27.8
27.8
27.8
0
10
20
30
40
50
60
distance (km)
Greenland
Iceland
-0.9
-0.5
-0.1
0.1
0.5
0.9
Velocity towards 147° in m s^{-1}

VITA

James B. Girton

Education

Spring 2001	Ph. D. in Oceanography, University of Washington, Seattle, WA
	Dissertation: Dynamics of Transport and Variability in the Denmark Strait Overflow
	Advisor: Thomas B. Sanford
1993	B.A. in Physics with Honors, Swarthmore College, Swarthmore, PA

Honors/Affiliations

1993–1996	Office of Naval Research Graduate Fellowship
1989–1993	National Scholarship, Swarthmore College
1996–present	American Geophysical Union
1996–present	The Oceanography Society
1993–present	Sigma Xi, the Scientific Research Society
1993–1995	IEEE Ocean Engineering

Publications

Girton, J. B., T. B. Sanford and R. H. Käse, Synoptic sections of the Denmark Strait Overflow, *Geophys. Res. Lett.*, **28** (8), 1619–1622, 2001.

Girton, J. B., and T. B. Sanford, Velocity profile measurements of the Denmark Strait Overflow, *Int. WOCE Newslett.*, **37**, 28-30, 1999.

Dunlap, J. H., J. A. Carlson, T. B. Sanford and J. B. Girton, Electrode and Electric Field Sensor Evaluation, Tech Report prepared for SAIC/NRaD, 1995.

Meeting Abstracts

Girton, J. B., T. B. Sanford and R. H. Käse, Transport and variability of the Denmark Strait Overflow, AGU Ocean Sciences, San Antonio, TX, 2000.

Girton, J. B., R. H. Käse and T. B. Sanford, Velocity structure of the Denmark Strait Overflow: New measurements and models, WOCE North Atlantic Workshop, Kiel, Germany, 1999.

Girton, J. B., T. B. Sanford , J. H. Dunlap, R. H. Käse and J. Hauser, Velocity surveying of the Denmark Strait Overflow and eddies, WOCE North Atlantic Workshop, Kiel, Germany, 1999.

Girton, J. B., and T. B. Sanford, Velocity profile measurements in the Denmark Strait, AGU Ocean Sciences, San Diego, CA, 1998.

Girton, J. B., and T. B. Sanford, Velocity measurements from an electric field float in the California Current, AGU Ocean Sciences, San Diego, CA, 1996.

REPORT DOCUMENTATION PAGE

Form Approved
OPM No. 0704-0188

Public reporting burden for this collection of information is estimated to average 1 hour per response, including the time for reviewing instructions, searching existing data sources, gathering and maintaining the data needed, and reviewing the collection of information. Send comments regarding this burden estimate or any other aspect of this collection of information, including suggestions for reducing this burden, to Washington Headquarters Services, Directorate for Information Operations and Reports, 1215 Jefferson Davis Highway, Suite 1204, Arlington, VA 22202-4302, and to the Office of Information and Regulatory Affairs, Office of Management and Budget, Washington, DC 20503.

1. AGENCY USE ONLY *(Leave blank)*	2. REPORT DATE	3. REPORT TYPE AND DATES COVERED
	August 2001	Technical

4. TITLE AND SUBTITLE
Dynamics of Transport and Variability in the Denmark Strait Overflow

5. FUNDING NUMBERS
NSF OCE9712313
NSF OCE0099275

6. AUTHOR(S)
James B. Girton

7. PERFORMING ORGANIZATION NAME(S) AND ADDRESS(ES)
Applied Physics Laboratory
University of Washington
1013 NE 40th Street
Seattle, WA 98105-6698

8. PERFORMING ORGANIZATION REPORT NUMBER
APL-UW TR 0103

9. SPONSORING / MONITORING AGENCY NAME(S) AND ADDRESS(ES)
National Science Foundation
4201 Wilson Boulevard
Arlington, VA 22230

10. SPONSORING / MONITORING AGENCY REPORT NUMBER

11. SUPPLEMENTARY NOTES
Approved for public release; distribution is unlimited.

12a. DISTRIBUTION / AVAILABILITY STATEMENT
Approved for public release; distribution is unlimited.

12b. DISTRIBUTION CODE

13. ABSTRACT *(Maximum 200 words)*

The overflow of dense water from the Nordic Seas through the Denmark Strait is one of the primary sources of the deep water in the world's oceans. In 1998, a rapid high-resolution survey on the F/S *Poseidon* with expendable profilers (XCP/XCTD) collected velocity, temperature, and salinity data from the region of the Denmark Strait sill to study the initial descent of the overflow into the deep North Atlantic. The major results from this and an earlier, more modest, survey in 1997 on the R/V *Aranda*, along with additional analysis of satellite and current meter data, can be summarized as follows:

- The flow near the sill is characterized by a strongly barotropic structure associated with a nearly-vertical temperature front. As the denser water descends the Greenland slope, it develops the bottom-intensified structure characteristic of a gravity current.
- Initial transport of $\sigma_\theta > 27.8$ water at the sill is measured by the synoptic sections to be 2.7 ± 0.6 Sv, essentially identical both in mean and variability to that measured in 1973 by a 5-week current meter array deployment.
- Despite large spatial and temporal variability in velocity, thickness, and transport, the overflow's pathway and descent with distance from the sill are remarkably steady.
- Measurements of near-bottom shear stress (from logarithmic velocity fits) confirm the importance of bottom friction in controlling the rate of overflow descent.
- Satellite sea-surface temperature images confirm the birth and downstream propagation of cyclonic eddies starting at approximately 125 km southwest of the sill. This same point is also marked by a change in the rate of overflow entrainment and a maximum in overflow speed.
- The presence of subsurface eddies upstream of the appearance of the surface features suggests a geographical separation between the region of flow instability and the site of eddy generation and vortex stretching. These two distinct processes occur in the approach to the sill and over the steepest descent, respectively.

14. SUBJECT TERMS
Denmark Strait Overflow, rotating gravity currents, ocean eddy formation, streamtube model, North Atlantic deep water, thermohaline circulation, physical oceanography

15. NUMBER OF PAGES
212

16. PRICE CODE

17. SECURITY CLASSIFICATION OF REPORT	18. SECURITY CLASSIFICATION OF THIS PAGE	19. SECURITY CLASSIFICATION OF ABSTRACT	20. LIMITATION OF ABSTRACT
Unclassified	Unclassified	Unclassified	SAR